Fritz-Haber Institute
der
Max-Planck Gesellschaft

Freie Universität

Berlin

# Theory of Adsorption, Diffusion and Spinpolarization of Mn on Si(001) and Si(111) Substrates

Submitted by
Master–Physics
Mahboubeh Hortamani

In the Faculty of Physik
at the Freie Universität Berlin
to obtain the degree
DOCTOR RERUM NATURALIUM

Thesis accepted

Committee:

| | |
|---|---|
| Head of committee: | Prof. Dr. D. Stehlik |
| Referee: | Prof. Dr. M. Scheffler |
| Referee: | Prof. Dr. P. Fumagalli |
| Referee: | Prof. Dr. E. K. U. Gross |

Exam date: 20 June 2006

Berlin 2006

Fritz-Haber Institute
der
Max-Planck Gesellschaft

Freie Universität

Berlin

# Theorie der Adsorption, Diffusion und Spinpolarization von Mn auf Si(001) und Si(111) Substraten

vorgelegt von
Master–Physikerin
Mahboubeh Hortamani

Im Fachbereich Physik
der Fereien Universität Berlin
zur Erlangung des akademischen Grades
Doktor der Naturwissenschaften
DOCTOR RERUM NATURALIUM

angenommene Dissertation

Promotionsausschuss:

| | |
|---|---|
| Vorsitzender: | Prof. Dr. D. Stehlik |
| Berichter: | Prof. Dr. M. Scheffler |
| Berichter: | Prof. Dr. P. Fumagalli |
| Berichter: | Prof. Dr. E. K. U. Gross |

Tag der wissenschaftlichen Aussprache: 20. Juni 2006

Berlin 2006

# List of Figures

1.1 Electronics with spin: current research and future possibility. Figure is adapted from "http://www. spintronics.inha.ac.kr" . . . . . . . . 2

2.1 Schematic figure of variation principle for $\langle\Phi_0|\ H\ |\Phi_0\rangle$ and $E_v[n(\mathbf{r})]$. Figure is adapted from [1] . . . . . . . . . . . . . . . . . . . . . . . . . . 10

2.2 The Self-consistent field approach for solving Kohn-Sham equations. 12

2.3 Division of the unit cell into two parts: the Muffin-Tin spheres, with radius $R$, around the nucleus and an interstitial region. . . . . . . . . . 16

2.4 Schematic dependence of $u_l(r, \epsilon_l)$ (a) and DOS (b) on the energy $\epsilon$. . . 18

2.5 Radial solution, $u_l$, of the l-composition and its behavior at MT-sphere boundaries in an APW (a) and LAPW (b) basis function are compared. 20

2.6 Schematic shape of the full potential (a) and the Muffin-Tin potential (b). . . . . . . . . . . . . . . . . . . . . . . . . . . . . . . . . . . . . . 21

2.7 Side view of a slab model containing 8 layers Si(001)$(2 \times 2)$ with alterating dimer reconstruction and vacuum. . . . . . . . . . . . . . . . 24

2.8 Flow chart of SCF cycle in WIEN2k compter code. . . . . . . . . . . 26

3.1 Energy-volume curve for bulk diamond and $\beta$-tin Si using GGA (red line) and LDA (blue line) functionals. The dashed lines are the common tangents, the slope of the common tangents is the pressure for the phase transition from the diamond to the $\beta$-tin structure. . . . . . 31

3.2 Band structure and DOS plot for bulk Si at equilibrium volume with a $(10 \times 10 \times 10)$ **k**-point grid in the Brillouin-Zone using GGA (solid lines) and LDA (dash lines) functionals. The energy zero is taken to be the top of the valence band. . . . . . . . . . . . . . . . . . . . . . . 34

3.3 The plot of total energy per atom versus unit cell volume, (E-V), with GGA (a) and LSDA (b). the circles, squares and triangle were used for antiferromagnetic, ferromagnetic and non-magnetic, respectively. The AFM ordering has lowest energy at equilibrium volume in GGA. The magnetovolume effect is not significant with LSDA. Magnetic and non-magnetic calculation have nearly the same E-V curve . . . . 36

3.4 Magnetic moment in ferromagnetic (red lines) and antiferromagnetic (blue lines) states from GGA (a) and LSDA (b) calculations. . . . . . . 38

3.5 Possible epitaxial structures of 1:1 stoichiometry of MnSi. The natural phase has FeSi structure (a) which is called B20 structure. The B2 struture (b), is the second lowest structure. The tungsten carbid, nickel arsenic and rocksalt structure are other possible epitaxial structures. . . . . . . . . . . . . . . . . . . . . . . . . . . . . . . . 39

3.6 Energy-volume curves for different epitaxy structures of MnSi are shown in the plot above. The FeSi (blue line), the CsCl (red line) and the NiAs (brown line) structures are stable in equilibrium, compressed and expanded volume, respectively. The WC (green line) and NaCl (purple line) structures are unstable. . . . . . . . . . . . . 41

3.7 Density of states ($N$) for MnSi in the B2 structure using a ($12\times12\times12$) **k**-point grid in the Brillouin-Zone. The filled blue (red dash) line is the DOS for the B2 in the majority (minority) spin channel (a). The black line is the DOS of the non-magnetic phase for both spin channels (b, c). The Fermi level is taken as the energy zero. . . . . . . 44

3.8 Density of states ($N$) for MnSi in the B20 structure using a ($12 \times 12 \times 12$) **k**-point in the Brillouin-Zone. The blue filled (red dash )line is the DOS of the majority (minority) spin channel (a). The black line is the DOS of the B20 structure in the non-magnetic phase for both spin channels (b). The Fermi level is referred to the energy zero level. 45

4.1 Top view of different unit cells at the (001) surface for which we have calculated the surface energy. White circles show atoms in the surface layer and black circles represent atoms in the second layer but big white and small gray circles are used to show upward and downward buckled dimer atoms on the surface, respectively. The non-reconstructed surface (a), the $(2\times1)$ symmetric dimer reconstruction (b), the $p(2\times1)$ buckled dimer reconstruction (c), the $p(2\times2)$ alternating buckled dimer reconstruction (d), the $c(4\times2)$ reconstruction (e). . . . . . . . . . . . . . . . . . . . . . . . . . . . . . . . . . . . . 51

4.2 Bond length of symmetric dimer structure (a), the bond length and the angle of the buckled dimer structure (b). . . . . . . . . . . . . . . 53

4.3 Band structure and density of states for $(2\times1)$ symmetric (a) and asymmetric (b) dimer. The band structure and DOS of the symmetric dimer has metallic character while the Fermi level cuts the tail of DOS and touches the top of valence band. The shaded areas in the band structure correspond to the highest valance band or the lowest conduction band in the slab. . . . . . . . . . . . . . . . . . . . . . . . 54

4.4 Bond length and the angle of the alternating buckled dimers structure in p(2×2) (a), and c(4×2) (b) supercells. . . . . . . . . . . . . . . . 56

4.5 Calculated energy difference between all possible surface reconstructions of the Si(001) surface. . . . . . . . . . . . . . . . . . . . . . . . 57

4.6 Band structure and density of states for $p(2 \times 2)$ (a) and $c(4 \times 2)$ (b) reconstruction. The band structure of the $c(4 \times 2)$ reconstruction was calculated using a $(4 \times 2)$ unit cell. . . . . . . . . . . . . . . . . . . . 58

4.7 Simulated and experimental empty states images for $c(4 \times 2)$ structure (a, c) and $p(2 \times 2)$ structure (b, d). The experimental images are measured with a positive sample bias of 1.3 eV and 2 eV for the mentioned structures. . . . . . . . . . . . . . . . . . . . . . . . . . . 59

4.8 Top view of $(2 \times 4)$ (a) and $(4 \times 2)$ (b) surface unit cell containing one dimer vacancy. . . . . . . . . . . . . . . . . . . . . . . . . . . . . . . 60

4.9 Side view of the bare Si(111) surface. It has two possible terminations, the single-dangling-bond (SDB) which is called shuffle-terminated face (a), triple-dangling-bond (TDB) which is called glide-terminated face (b). . . . . . . . . . . . . . . . . . . . . . . . . . . . . . . . . . 61

5.1 Schematic top view of the Si(001) surface, with various binding sites for a Mn adatom indicated (a). Side view, with sub-surface binding sites of Mn indicated (b). Top view illustrating substitutional adsorption of Mn, the arrows indicating various alternative positions for the expelled Si atom (c). Filled circles indicate possible binding sites for Mn, white circles Si atoms. . . . . . . . . . . . . . . . . . . 66

5.2 Top view (upper panel) and side view (lower panel) of adsorption of Mn impurity at tetrahedral interstitial site (a), hollow site (b) and substitutional site (c). . . . . . . . . . . . . . . . . . . . . . . . . . 69

5.3 Band structure of up-spin channel (a, b, c) and spin down channel (d, e, f) of a Mn impurity at the hollow, interstitial and substitutional site, respectively. . . . . . . . . . . . . . . . . . . . . . . . . . . . 71

5.4 DOS of the $t_{2g} = d_{z^2} + d_{xz} + d_{yz}$ and $e_g = d_{x^2-y^2} + d_{xy}$ sub-levels of partial $d$-orbitals of a Mn impurity at the tetrahedral interstitial site (a,b), hollow site (c, d) and substitutional site (e, f). Black solid lines are for the majority spin channel and red dashed lines belong to the minority spin channel. The energy zero refers to the Fermi level. . . . 72

5.5 Electron density in the (100) plane containing the adatom for single Mn atom adsorption on substitutional site (a), hollow site (b) and interstitial site (c). The electronic density for the (001) plane (at a certain $z$ above surface) for hollow site (d) and interstitial site (e). The bigger (smaller) white circles in every figure are the places of Mn (Si) atoms. . . . . . . . . . . . . . . . . . . . . . . . . . . . . 74

5.6 Simulated STM images for single atom adsorption on: substitutional site (a), hollow site (b), interstitial p(2×2) unit cell (c), interstitial c(2×4) unit cell (d), and the experimental STM (e) Ref. [2]. . . . . . . 75

5.7 Experimental STM image (a) and theoretical STM simulation (b) for $c(4 \times 2)$ unit cell. Curves (c) and (d) show the height difference in a linescan which runs across the bright part of the STM images. The linescans are indicated in the STM images. (e) ball-stick model of the c$(4 \times 2)$ structure. . . . . . . . . . . . . . . . . . . . . . . . . . . . . 76

5.8 STM simulation of Mn impurity at the position of a dimer vacancy in a $(4 \times 2)$ unit cell matched with a ball-and-stick model. . . . . . . . 77

5.9 Schematic of potential energy surface. $x$ and $y$ are coordinates of adatom and $z$ axis is adsorption energy. . . . . . . . . . . . . . . . . . 79

5.10 The PES and diffusion pathway on the Si(001) surface. The diffusion barriers for hopping to the next on-surface minimum are in the range of 0.6 eV. H and M are global and local minimum, $T_1$, $T_2$ and $T_3$ are saddle points. The white region are maximum and the dark parts are minimum in the potential energy surface. The space between contour lines is 0.2 eV. . . . . . . . . . . . . . . . . . . . . . . . . . . . 81

5.11 PES plot and diffusion barrier for penetration to the sub-surface site (a). The energy barrier is about 0.3 eV. The dark region is the global minimum and the bright part is the place of maximum in the PES. Structure of minimum and saddle points are shown in figure (b). The space between contour lines is 0.125 eV. . . . . . . . . . . . . . . . . . 82

5.12 Energy profile for a Mn atom approaching the Si(001) surface from the vacuum along the path shown in the left panel, breaking the Si dimer and inserting itself via the stable sub-surface site $I_1$ into the third-layer interstitial site $I_3$. The energy barrier for the last step, from $I_1$ to $I_3$, is about 1.3 eV. . . . . . . . . . . . . . . . . . . . . . . . 83

5.13 Different possible structures for adsorption of 1/2 ML of Mn on Si(001), shown in top view (upper panels) and side view (lower panels). (a) relaxed structure resulting from Mn in on-surface sites only (b) in sub-surface sites (c) in sub-surface and cave sites. . . . . . . . . . . . 85

5.14 Structures for adsorption of 3/4 ML of Mn on Si(001), shown in top view (upper panels) and side view (lower panels). (a) relaxed structure resulting topmost layer (b) sub-layer with Si-capping layer (c) from 1/2 ML in on-surface sites plus 1/4 ML in sub-surface sites. . . 86

6.1 Side view for two different directions of several configurations with 1 ML Mn coverage. Big black circles represent Mn and small white circles Si. . . . . . . . . . . . . . . . . . . . . . . . . . . . . . . . . . . 92

6.2 Density of states for spin up and down $d$-orbitals of the Mn atoms in the a dense layer of the Mn-overlayer (left panel) and the Mn-sublayer (right panel). . . . . . . . . . . . . . . . . . . . . . . . . . . . 94

6.3 Side view of structures with 2 ML coverage Mn / Si(001). Big black circles represent Mn atoms and small white circles represent Si atoms. 96

6.4 The overlayer-resolved DOS of the FM 2(Si-Mn) / Si(001) film. The overlayers are shown from surface (top) to interface (bottom). Full lines show the majority spin, dashed lines the minority spin component. The considerable spin polarization of carriers at Fermi level (zero energy) is evident. . . . . . . . . . . . . . . . . . . . . . . . . . 98

6.5 Formation energy of pure Mn films and MnSi films in the B2(001) structure as a function of the film thickness. The zero of the energy scale refers to the surface energy of the clean reconstructed Si(001) surface. The green line corresponds to the pure Mn overlayer-film, the purple line corresponds to the Mn thin film with a Si capping layer and the red line to the MnSi sandwich film in the B2(001) structure. . . . . . . . . . . . . . . . . . . . . . . . . . . . . . . . . . . 99

6.6 The overlayer-resolved DOS of the interlayered AFM 3(Si-Mn) / Si(001) film. See Fig. 6.4 for other notes. . . . . . . . . . . . . . . . . . . . . . 100

6.7 Ferromagnetic (A), interlayer antiferromagnetic (B) and intralayer antiferromagnetic (C) structure of B2(001) / Si(001). . . . . . . . . . . 101

6.8 Formation of films with B2 structure of Mn-mono-silicide on Si(001) in equilibrium with some Mn-silicide structures. The surface energy of the clean (001) reconstruced surface is considered as zero point. Formation of these films on the surface is unstable in equilibrium with Mn-poor compounds. . . . . . . . . . . . . . . . . . . . . . . . . 102

7.1 Top-view (left figure in each structure) and side-view (right figure in each structure) for five configurations of Mn adsorbed on the Si(111) surface. The big yellow circles represent Mn atoms, while all the small circles depict Si atoms in different layers. $O_1$ is an overlayer site with one-fold coordination to a surface atom. $C_3$ is a 3-fold mono-atomic chain and $H_3$ is the 3-fold hollow sites. $T_4$ is a 4-fold atop site and $S_3$ is a 3-fold substitutional site. . . . . . . . . . . . . . . 106

7.2 Side view of structures with hollow, atop and substitutional site adsorption and a Si-covering layer. In most of the structures, the surface dangling bonds are saturated and the Mn atoms below the surface are highly coordinated. . . . . . . . . . . . . . . . . . . . . . . . . 107

7.3 Formation energy for all the considered structures in eV per (1×1) cell.The six-fold substitutional site, $S_6$ on the SDB surface with a Si capping layer is the most stable adsorption site for Mn on this surface. . . . . . . . . . . . . . . . . . . . . . . . . . . . . . . . . . . . 108

7.4 Total density of states plot for Mn atom in $S_6$, $S_3$, $H_3$, $H_6^I$, $T_4$ and $T_7^I$ configurations. The solid (dashed) lines indicate the projection of the spin up(down) wave function onto the $d$ orbitals of manganese. . . . 110

7.5 The structures of a pure Mn film (a), a Mn-mono silicide with nickel arsenide structure (b) and a cesium chloride structure (c) are compared.111

7.6 B2 structure on Si(001) substrate (a) and Si(111) surface (b) and the film with $Mn_3Si$ structure on Si(111) (c) at coverage of 3 ML. . . . . . 113

7.7 DOS plot for the B2(111) structure on the Si(111) substrate at 3 ML coverage for Mn and Si atoms at interface and surface layer. Solid lines represent majority and dashed lines indicate minority spin channel, the dotted line shows the Fermi level. . . . . . . . . . . . . . . . . 114

7.8 Formation energy of film for B2 structure of Mn-mono-silicide on Si(001)(red lines) and Si(111)(black lines) substrates as a function of film thickness. Film formation is in equilibrium with bulk B20 structure of Mn-mono-silicide (circle signs), B2 structure of Mn-mono-silicide (triangle signs) and Mn (square signs). Surface energy of bare surface (dashed line) is considered as zero point. . . . . . . . . . . . 115

7.9 Structure of four possible terminations of MnSi(111) in the B20 structure. . . . . . . . . . . . . . . . . . . . . . . . . . . . . . . . . . . . 116

7.10 Surface energy of the four terminations of MnSi(111) as a function of the chemical potential of Mn. The dotted vertical lines indicate the limit of the Mn chemical potential for Mn-rich and -poor conditions. 117

7.11 Side view of the Si-termination of MnSi in B2 structure for a (111) surface (a) and a (001) surface (b). Small white (big black) circles are Si (Mn) atoms. . . . . . . . . . . . . . . . . . . . . . . . . . . . . 118

7.12 Top view (a) and side view (b-c) of B20 of Mn-mono-silicide structure at coverage of $\theta = 2/3$ ML. . . . . . . . . . . . . . . . . . . . . . . . . 119

7.13 Formation energy of ultrathin film for B2 (black lines) and B20 (red lines) structure of Mn-mono-silicide on Si(111) substrates as a function of film thickness. The energy of film formation is calculated by assuming equilibrium either with the B20 bulk structure of Mn-mono-silicide (circles), or the B2 structure of Mn-mono-silicide (triangles) or Mn bulk (squares). The surface energy of the bare Si(111)($1\times1$) surface (dotted line) is considered as zero point. . . . . . . . . . . 120

7.14 Schematic illustration of different growth modes of heteroepitaxial growth. . . . . . . . . . . . . . . . . . . . . . . . . . . . . . . . . . . 121

7.15 Schematic illustration of film formation with thickness $d$ (a) and island formation with island base length $a$. On the Si(111) substrate, the tetrahedral-shaped-islands with B2(001) facets (b) will form and on the Si(001) substrate, the pyramid islands with B2(111) facets (c). The iceberg island (d) with B2 structure can form on both Si substrates. . . . . . . . . . . . . . . . . . . . . . . . . . . . . . . . . 122

A-1 The cohesive energy as a function of (a) the cutoff of wave function, (b) the number of **k**-points in the 1BZ. . . . . . . . . . . . . . . . . . . 136

A-2 The surface free energy versus (a) the energy cutoff, (b) the number of **k**-points in the 1BZ for a slab of six Si layers and a vacuum of 15 Å. 137

A-3 The surface energy as a function of the number of layers in the slab (a) and the vacuum thickness (b), using $E_{cut}^{pw}$=13.8 Ry and a ($8\times8\times1$) **k**-point set. . . . . . . . . . . . . . . . . . . . . . . . . . . . . 137

B-4 Crystal structure of $Mn_3Si$ in the fcc lattice (a). The green small circles are Si and big blue circles are Mn. Energy-volume curves for non-magnetic, ferromagnetic and antiferromagnetic structures for $Mn_3Si$ (b). The antiferromagnetic structure has the lowest energy curve. . . . . . . . . . . . . . . . . . . . . . . . . . . . . . . . . . . . . 140

B-5 Band structure of non-magnetic $Mn_3Si$ shows metallic behavior. The contributions of $Mn_I$ (a), $Mn_{II}$ (b) and Si (c) atoms are shown separately. . . . . . . . . . . . . . . . . . . . . . . . . . . . . . . . . . . . . 141

B-6 Band structures for $Mn_I$, $Mn_{II}$ and Si atoms in majority spin direction (a, b, c)and for minority spin channel (d, e, f) of $Mn_3Si$ in the AFM phase. The majority spin band structure has the Fermi level crosses the top of the conduction band at the high symmetry point $\Gamma$ which produce a few hole in this band. . . . . . . . . . . . . . . . . . . . . . . . 142

B-7 The DOS plot of $Mn_3Si$ for both ferromagnetic and antiferromagnetic phases. The plots are total density of states of $Mn_3Si$ (a), Si (b), $Mn_I$ (c), and $Mn_{II}$ (d). The minority spin channel has character similar to a semiconductor. . . . . . . . . . . . . . . . . . . . . . . . . . . . . . . . 143

C-8 The negative tip bias probes empty substrate states (a) and positive tip bias probes filled states of the substrate (b). . . . . . . . . . . . . . . 146

# List of Tables

3.1 Comparison of the calculated lattice constant ($a_0$), bulk modulus ($B_0$), pressure derivative of the bulk modulus ($B_0^{'}$), and cohesive energy ($E_{\mathrm{coh}}$) for Si diamond and $\beta$-tin structures using LDA, GGA-PBE and GGA-PW. The transition presure between the two phases, as well as their volumes $V_t^d$ and $V_t^\beta$ at the transition point are given . The experimental values are taken from Ref. [3] and [4] and for the GGA-PW values the results of Moll *et al* [5]. . . . . . . . . . . . . . . . . . . . 33

3.2 Electronic energies of Kohn-Sham equation for Si bulk. . . . . . . . . . 35

3.3 Comparison of the cohesive energy $E_{\mathrm{coh}}$, the lattice parameter $a_0$ and the bulk modulus $B_0$ of different magnetic ordering of manganese in fcc-$\gamma$ structure. . . . . . . . . . . . . . . . . . . . . . . . . . . . . . . . 37

3.4 Lattice parameter ($a_0$), formation enthalpy ($\Delta H$), bulk modulus ($B_0$) and magnetic moment ($m$) for all epitaxial structures as calculated with both GGA and LDA functionals. . . . . . . . . . . . . . . . . . . 42

3.5 Density of states per Mn at the Fermi level for both spin channels ($n_\uparrow(\epsilon_F)$, $n_\downarrow(\epsilon_F)$), total density of states at the Fermi level for the non-magnetic case ($n_{\mathrm{nm}}(\epsilon_f)$), the exchange splitting ($\Delta_{ex}$), the magnetic moment $m$, the Stoner parameter ($I$), the Pauli susceptibility ($\chi$) and the Curie temperature ($T_C$) calculated by Mohn-Wohlfarth theory. . 46

3.6 Energy difference in DFT-GGA between FM and AFM order per formula unit and calculated Curie temperature for B20 and B2 structures. 47

5.1 Bond length of Mn and Si, absolute adsorption energy (eV) and magnetic moment for different adsorption sites for low coverage, $\theta_{\mathrm{Mn}} = 1/8$. Note that the Mn-Si distances are in the range of bond distances known from Mn-monosilicide. . . . . . . . . . . . . . . . . . . . . . . 67

5.2 Average adsorption energies per Mn atom of ordered monolayer structures at various Mn coverages $\theta$ with respect to bulk Mn and bulk Si. The left column is for all Mn atoms occupying on-surface (H) sites, and the middle column is for all Mn atoms in sub-surface ($I_1$) sites, the right column is for structures where sub-surface ($I_1$) and on-surface (H) sites are alternatingly populated. . . . . . . . . . . 87

6.1 Spin moments (in $\mu_\mathrm{B}$) of the Mn-overlayer, sub-layer and mixed MnSi layer at their respective magnetic ground states. $\mathrm{Si}^\mathrm{S}$ is substrate atom, $\mathrm{Si}^\mathrm{I}$ is an atom in the interface and $\mathrm{Si}^\mathrm{T}$ is a Si-capping atom. Note that a non-negligible spin moment is induced on the Si atoms in surface and interface Mn. . . . . . . . . . . . . . . . . . . . . . . . . 95

6.2 Formation energy (eV / cell) for different magnetic ordering and interlayer distances (Å) for the three structures with 2 ML coverage, shown in Fig. 6.3. . . . . . . . . . . . . . . . . . . . . . . . . . . . . 97

7.1 The distance between Mn and Si in the first ($\mathrm{Si}_1$) and the second ($\mathrm{Si}_2$) substrate layer in Å , Mn magnetic moment and first layer Si magnetic moment (in $\mu_\mathrm{B}$) for different adsorption sites of Mn on Si(111). 109

7.2 Formation energy, magnetic moment and spin polarization of different epitaxial structures of Mn-mono silicide on Si(111) at 1.5 ML coverage. . . . . . . . . . . . . . . . . . . . . . . . . . . . . . . . . . 112

7.3 Surface energy, $\gamma_\mathrm{surface}$ (meV / Å $^2$ ) of non-reconstructed Si and MnSi surfaces. Bulk MnSi in the B2 structure is considered as a reservoir for the chemical potential of Mn. The calculated surface energies from Stekolnikov and Bechstedt (S-B) [6] are for a Si(001)c($4 \times 2$) and a Si(111)($7 \times 7$) reconstruction. . . . . . . . . . . . . . . . . . . . . . 124

7.4 Film thickness, $d$, facet area $A_\mathrm{facet}$ energy of film formation per area, $\gamma_\mathrm{film}$, and surface energy of the bare surface. For Si, the reconstructed surfaces are considered while for MnSi, the non-reconstructed surface is considered. . . . . . . . . . . . . . . . . . . . . . . . . . . . . 125

7.5 Area of interface and volume of islands, interface energy per area, $\gamma_\mathrm{interface}$ and stable island size $a_0$ for island formation. Bulk MnSi in B2 structure is considered as reservoir for calculating the chemical potential of Mn. . . . . . . . . . . . . . . . . . . . . . . . . . . . . . . 126

B-1 Formation enthalpy ($\Delta H$) (cf. Eq. **??**), lattice parameter ($\mathrm{a}_0$) and magnetic moments ($\mathrm{m}_\mathrm{I}$, $\mathrm{m}_\mathrm{II}$) of $\mathrm{Mn}_\mathrm{I}$ and $\mathrm{Mn}_\mathrm{II}$ in different layers for $\mathrm{Mn}_3$ Si. . . . . . . . . . . . . . . . . . . . . . . . . . . . . . . . . . . . . . 140

# Contents

1 **Introduction** **1**

1.1 Goal and Outline . . . . . . 3

2 **Theoretical Background** **5**

2.1 Many-Body Problem . . . . . . 5

2.2 Approximation for the Hamiltonian . . . . . . 6

2.3 Density-Functional Theory (DFT) . . . . . . 8

2.3.1 Basic Principles . . . . . . 8

2.4 Approximation to The Exchange Correlation Potential . . . . . . 13

2.5 Approximation for Solving The Kohn-Sham Equations . . . . . . 15

2.5.1 Basis Functions: APW, LAPW, APW + lo . . . . . . 16

2.5.2 Representation of The Potential . . . . . . 21

2.6 **k**-point Sampling . . . . . . 22

2.7 The Slab Model and The Supercell Approach . . . . . . 24

2.8 The WIEN2k Code . . . . . . 25

3 **Bulk Properties** **29**

3.1 Introduction . . . . . . 29

3.2 Bulk Silicon . . . . . . 31

3.2.1 Structural Properties and Thermodynamical Stability . . . . . . 31

3.2.2 Electronic Properties . . . . . . 32

3.3 Bulk Manganese . . . . . . 35

3.3.1 Structural Properties . . . . . . 35

3.3.2 Magnetic Properties . . . . . . 38

3.4 Manganese-Silicide Compounds . . . . . . 38

3.4.1 Bulk MnSi . . . . . . 39

4 **Bare Si Surfaces** **49**

4.1 Introduction . . . 49
4.2 Si(001) Plane . . . 50
4.2.1 (1×1) Non-Reconstructed . . . 52
4.2.2 (2×1) Dimer Model: Symmetric / Asymmetric Si Dimers . . . 53
4.2.3 Alternating Buckled Dimers: $p(2 \times 2)\,/\,c(4 \times 2)$ Supercells . . . 55
4.2.4 Dimer Vacancy . . . 59
4.3 Si(111) Surface . . . 61

**5 Initial Mn Adsorption and Diffusion Pathways 63**
5.1 Introduction . . . 63
5.2 Computational Details . . . 64
5.3 Stable and Non-Stable Adatom Positions on The Si(001) Surface . . . 65
5.4 Influence of The Si-Dimer Vacancy . . . 77
5.5 Potential Energy Surface for Mn on Si(001) . . . 78
5.5.1 PES and Diffusion Pathway on The Surface . . . 80
5.5.2 PES and Diffusion Barrier for Penetration to The Sub-Surface (site $I_1$) . . . 81
5.6 Effect of Adatom Interaction : Submonolayer, Overlayer, or Bilayer Structures . . . 84

**6 Thin Film Growth on Si(001) 89**
6.1 Introduction . . . 89
6.2 Coverage of 1ML on Si(001) . . . 90
6.2.1 Thermodynamics, and Structural Stability . . . 90
6.2.2 Electronic and Magnetic Structure . . . 93
6.3 Coverage of 2ML on Si(001) . . . 95
6.3.1 Thermodynamical and Structural Stability . . . 95
6.3.2 Magnetic Structure . . . 97
6.4 Coverage of 3ML on Si(001) . . . 99
6.4.1 Thermodynamical and Structural Stability . . . 99
6.4.2 Electronic and Magnetic Structure . . . 100
6.5 The Thermodynamic Stability . . . 102

**7 Epitaxial Growth of Mn on Si(111) 105**
7.1 Introduction . . . 105
7.2 Low Coverage Adsorption . . . 105

7.3 Morphology of Epitaxial Film on Si(111) . . . . . . . . . . . . . . . . . . 111
7.4 Comparison of B2 Structure of MnSi Film on Si(001) and Si(111) . . . 112
7.5 MnSi Surfaces . . . . . . . . . . . . . . . . . . . . . . . . . . . . . . . . 116
7.6 MnSi Films with B20 Structure . . . . . . . . . . . . . . . . . . . . . . . 118
7.7 Growth Mode of Mn-Monosilicide in B2 Structures on Si Substrates 120
7.7.1 Formation of MnSi Nano-Structures on Si Substrates . . . . . 122

**8 Conclusion and Outlook 127**

**Zusammenfassung 131**

**Appendix A 135**

A-1 Convergence Test for Bulk Si . . . . . . . . . . . . . . . . . . . . . . . . 135
A-2 Convergence Test for The Si(001) Surface . . . . . . . . . . . . . . . . . 136

**Appendix B 139**

Bulk $Mn_3Si$ . . . . . . . . . . . . . . . . . . . . . . . . . . . . . . . . . . . 139
B-1 Structural and Magnetic Properties . . . . . . . . . . . . . . . . . . . . 139
B-2 Electronic Properties . . . . . . . . . . . . . . . . . . . . . . . . . . . . 141

**Appendix C 145**

Theory of Scanning Tunneling Microscopy (STM) . . . . . . . . . . . . . . . 145

**Bibliography 149**

**Acknowledgment 157**

# Chapter 1

# Introduction

The electron was discovered in 1897 by J.J. Thomson as an elementary particle embodying a finite amount of charge. The charge property makes a (moving) electron in free space interact with electromagnetic fields via the Coulomb and Lorentz forces and enables metals and semiconductors to carry an electrical current.

The observation of the Zeeman effect in 1896 and fine structure anomalies in the line spectra of atoms led to the suggestion that the electron also has a spin. The electron spin provides another degree of freedom for the electron to interact with a magnetic field. The most direct experimental proof of the existence and quantized nature of the electron spin ($S_z = 1/2$) was obtained by Stern and Gerlach in 1922. The concept of spin for electrons was introduced in 1925 by Uhlenbeck and Goudsmit [7]. They suggested that the electron spin acts like an intrinsic angular momentum (S) with a magnetic moment associated to it.

The quantization of the spin of a free electron imposes that, whenever it is measured, it can have only one of two possible values: spin-up and spin-down.

Using the spin of the electron besides its charge, creates a remarkable new generation of microelectronic devices. This field of research has been labelled with the term spintronics and has seen a rapid growth over the past few years. The most well known examples of spin dependent electron transport phenomena is the giant magnetoresistance (GMR) effect in metallic multilayers [8–12] and tunneling magnetoresistance (TMR) of magnetic tunnel junctions [13, 14].

Heterojunctions between a semiconductor and a ferromagnetic metal have attracted attention in the context of spintronics. The study of magnetism in thin films and low-dimensional systems is one of the most prospering areas of modern solid state physics. As a matter of fact the magnetic properties of these structures differ from those of the constituent bulk materials in many different ways. The research in this field revealed some new interesting phenomena like the anti-ferromagnetic coupling in magnetic / non-magnetic multilayered structures, which leads to the giant magnetoresistance effect.

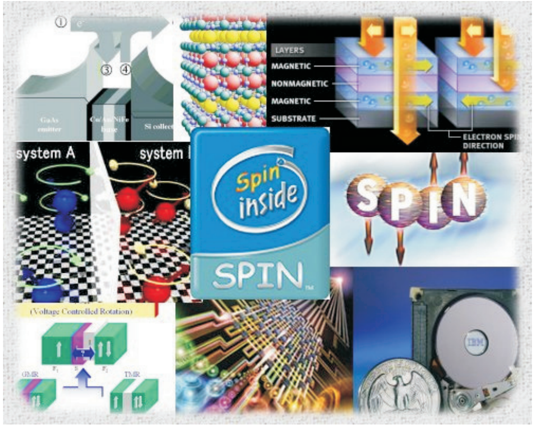

Fig. 1.1: Electronics with spin: current research and future possibility. Figure is adapted from ”http: / / www. spintronics.inha.ac.kr”

Metal-semiconductor heterojunctions hold great promise for fabrication of spintronics devices, because of the possibility to inject a spin current from a ferromagnetic metal into a semiconductor. For computational materials science, this poses the challenge of designing materials that are suitable to inject a spin-polarized current into a semiconductor.

The spin-injection efficiency into semiconductors could be produced either by using a diluted magnetic semiconductor or, by fabrication of magnetic metal films on a semiconductor. Epitaxial growth of transition metal monosilicide ferromagnetic films on a Si substrate can be used as a source of spinpolarized carrier injection to semiconductors which can be applied for spintronics devices. The requirements for such a material are i) it should show (preferably ferro-)magnetic ordering above room temperature, ii) have a high spin polarization of carriers at the Fermi level, and iii) be structurally compatible with silicon. Here, we want to put forward magnetic intermetallic compounds grown epitaxially on Si as promising candidate materials. Epitaxial Mn-silicide compounds are promising candidates for the components of microelectronic and spintronic devices applications. The high magnetization of Mn and compatible lattice match of Mn and Si make it suitable to create a magnetic interface of Mn (-silicide) on a Si substrate. Most of the experiments about Mn deposition on Si report about formation of a Mn-silicide compound. In 1985 the epitaxial growth of (001)$MnSi_{1.7}$ / Si(001) and $(1\bar{1}0)MnSi_{1.7}$ / Si(111) was reported by analysis of electron diffraction patterns [15] and recently, flat islands of MnSi and three-dimensional islands with $Mn_5Si_3$ structure on Si(001) [16] as well as (relatively) big islands consisting of MnSi were observed on Si(111) [17]. Moreover, among the known bulk phases of Mn silicides, $Mn_3Si$ in the $D0_3$ structure appears to be compatible with pseudomorphic thin film growth on Si surfaces

The epitaxial growth of a film of Mn-silicide on Si(111) with the help of a Bi surfactant layer [18–21] has been reported. The nearly closed film at higher coverage (more than 5 ML) was observed with the scanning tunneling microscopy (STM) and low-energy electron diffraction (LEED) [22].

## 1.1 Goal and Outline

The aims of this thesis are to investigate the structure and magnetic interactions in multilayer systems and how these affect their magnetic properties.

In an attempt of ’computational materials design’, we investigate the stability and magnetic properties of Mn on the Si substrate in both Si(001) and Si(111) orientations.

We have studied Mn incorporation at Si(001) and Si(111) surfaces within density functional theory using the full-potential augmented plane wave plus local orbital method (FP-LAPW+lo). The basis set of this method (i.e. choosing angular momentum eigen functions around atomic positions and plane waves in the interstitial region), make it a suitable tool to study the behavior of transition metals with localized $d$ orbitals. The detailed features of the method and computer package which is used in this thesis are described in **Chapter 2**.

To understand the mechanisms of the nanoscale structures such as thin films and to contrast the different properties of the film with its constituents in intermetallic multilayers, one needs to have good information about the bulk phases. In **Chapter 3**, bulk properties of plausible compounds which could be grown on Si surfaces are studied. Structure and thermodynamic stability as well as electronic and magnetic properties of bulk crystals are the quantities to compare with epitaxial films grown on the surface.

One requirement needed to simulate the growth on surfaces, the morphology of films and the properties of interfaces and surfaces is a sufficient knowledge about the surface on which the growth take place. In **Chapter 4** the morphology of Si(001) and Si(111) surfaces as well as the surface reconstructions for Si(001) are discussed.

The initial step which one needs to know the starting point for simulating the growth process is finding stable adsorption sites on the surface and surface diffusion. We show in **Chapter 5** that the sub-surface second layer is the most stable adsorption site for Mn with an adsorption energy of 3.8 eV. Besides, we calculated the adsortion energy at the substitutional site and also the adsorption on a surface defect site. In this chapter, we also estimate the energy barrier for diffusion on the surface and for penetration to the sub-surface site.

The morphology and stability of films on Si surfaces, magnetic properties of interfaces and surfaces are presented in **Chapter 6** and in the first part of **Chapter 7**. The stability of $\mathrm{Mn}_x\mathrm{Si}_y$ films on Si has been investigated for various stoichiometries and atomic structures of the films. We propose the formation of a film with with Mn-monosilicide in the cesium chloride (B2)(001) structure on Si(001). Due to suitable interface with Si(111) the natural phase (B20) of MnSi stabilizes on this substrate. Additionally, the formation energy of these films versus coverage is also discussed.

Finally in the second part of **Chapter 7**, we focus on the film stability against island formation and we calculate the energy associated with island formation of a certain size as a function of film thickness and coverage.

# Chapter 2

# Theoretical Background

## 2.1 Many-Body Problem

A significant part of condensed matter physics would be solved if the electronic structure of atoms, molecules and solids could be determined exactly. The starting point to investigate properties of materials is to solve the many-body Schrödinger equation. The problematic issue concerns the number of particles that are involved and the coupling and interactions of the particles ($10^{23}$ particles per cm$^3$). This problem can be overcome using approximate methods.

The $N$-electron quantum system is described by a function of the spatial (**r**) and spin ($\sigma$) coordinates of each electron, as well as the spatial coordinates $\mathbf{R}$ of the nuclei, $\Psi(\mathbf{r}_1\sigma_1, ..., \mathbf{r}_n, \sigma_n, \mathbf{R}_1, ..., \mathbf{R}_N)$. The properties of any (non-relativistic) time-independent quantum system are determined by the Schrödinger equation:

$$H\Psi(\mathbf{r}_1\sigma_1, ..., \mathbf{r}_n, \sigma_n, \mathbf{R}_1, ..., \mathbf{R}_N) = E\Psi(\mathbf{r}_1\sigma_1, ..., \mathbf{r}_n, \sigma_n, \mathbf{R}_1, ..., \mathbf{R}_N)\ , \tag{2.1}$$

$H$, $\Psi$ and $E$ are the Hamiltonian, many-body wave-function and total energy of the system.

The Hamiltonian for a solid system is given by

$$\begin{aligned} H = &-\sum_{I=1}^{N} \frac{\hbar^2}{2M_I}\nabla^2_{\mathbf{R}_I} - \sum_{k=1}^{n} \frac{\hbar^2}{2m}\nabla^2_{\mathbf{r}_k} + \frac{1}{4\pi\epsilon_0}\sum_{I}^{N}\sum_{I>J}^{N} \frac{Z_I Z_J}{|\,\mathbf{R}_I - \mathbf{R}_J\,|} \\ &-\frac{1}{4\pi\epsilon_0}\sum_{k=1}^{n}\sum_{I=1}^{N} \frac{Z_I\, e}{|\,\mathbf{r}_k - \mathbf{R}_I\,|} + \frac{1}{4\pi\epsilon_0}\sum_{k=1}^{n}\sum_{k'>k}^{n} \frac{e^2}{|\,\mathbf{r}_k - \mathbf{r}'_k|}\ , \end{aligned} \tag{2.2}$$

where $N$, $M_I$ , $Z_I$ and $\mathbf{R}_I$ represent the number, mass, charge and position of the nuclei and $n$ , $m$, $e$ and $\mathbf{r}_k$ are the number, mass, charge and position of an electron.

The first two terms are the kinetic energy contributions from the nuclei, $T_i$ and the electrons, $T_e$. The remaining terms are Coulombic potential energy terms arising from the ion-ion repulsion, $V_{ii}$, ion-electron attraction, $V_{ie}$ and the electron-electron repulsion, $V_{ee}$.

Although in principle everything is known exactly, the Schrödinger equation with this Hamiltonian is too difficult to be solved directly. Hence, the quantum many-body problem is centred upon finding intelligent approximations for the Hamiltonian and the many body wave-function that keep the correct physics and are computationally tractable.

This problem can be solved using three different levels of approximations:

## 2.2 Approximation for the Hamiltonian

### The adiabatic (Born-Oppenheimer)/static approximations

The first simplification of the many-body problem is to eliminate the dependency of the electron's and nuclear dynamics by breaking it down into two sub-systems, one for the electrons and one for the nuclei.

The electrons move so fast that they follow the ionic (lattice) geometries almost without delay. In fact, from the electron point of view, the ions are fixed. The concept behind this approximation comes from the fact that the mass of a nucleus is much larger than the mass of an electron ($M \sim 10^3 \times m_e$). If we assume that $\frac{m}{M_I} \to 0$, the many-body equation 2.1 for each ionic configuration, $\mathbf{R}_I$, turns to the electron equation:

$$H^e(\{\mathbf{R}_I\})\Phi_v(\{\mathbf{R}_I\},\{\mathbf{r}_k,\sigma\}) = (T^e + V^{e-ion} + V^{e-e})\Phi_v = E^e\Phi_v \,. \tag{2.3}$$

Please note that the $\{\mathbf{R}_I\}$ in the wave function are not variables but parameters. Now we expand the solution of the many-body Hamiltonian, $\Psi$, into a sum of eigenfunctions of the electron Hamiltonian, $\Phi_v$ :

$$\Psi = \sum_v \Lambda_v(\{\mathbf{R}_I\})\Phi_v(\{\mathbf{R}_I\},\{\mathbf{r}_k,\sigma\}). \tag{2.4}$$

Therefore, one can consider $H^e$ and $\Phi_v$ for a certain ionic geometry, and the dependence of the many-body Hamiltonian, $H$ and and wavefunction $\Psi$ on $\{\mathbf{R}_I\}$ enters only through the coefficients $\Lambda_v(\{\mathbf{R}_I\})$.

Using the above definition of the many-body wave function in equation (2.1) and multiplying from the left hand side by $\Phi_\mu^*$, one can get the ground state energy for a certain lattice geometry and electron wave function, $\Phi_\mu$, and the integration over all electronic coordinates gives the ground state energy of the many-body system. Equation 2.1 turns to:

$$(T^I + V^{I-I} + E_\mu^e)\Lambda_\mu = E\Lambda_\mu + \text{electron \& phonon interaction terms.} \qquad (2.5)$$

Up to now everything is exact. In order to decouple the electron and ion dynamics, we assume that (i) the electron-phonon interaction is negligible, (ii) the electronic wave function belonging to different eigenstates of the nuclear system are independent from each other (*i.e.* $\langle\Phi_v|\Phi_\mu\rangle = 0$ for $v \neq \mu$). In other words, the electrons are always in the ground state. This is the *adiabatic principle* or *Born-Oppenheimer approximation* (BO).

With multiplying the Eq. 2.5 from the left with $\Lambda_0$, the ground state energy will be obtained:

$$E_0 = E^e + V^{I-I} + \text{kinetic energy of the lattice vibrations} \qquad (2.6)$$

The kinetic energy of the lattice vibrations is given by $\langle\Lambda_0|T^I|\Lambda_0\rangle$. The many-body wave function of the ground state is

$$\Psi_0 = \Lambda_0(\{\mathbf{R}_I\})\Phi_0(\{\mathbf{R}_I\}, \{\mathbf{r}_k, \sigma\}). \qquad (2.7)$$

In the BO approximation, the solution of Eq. 2.3 is the ground state energy of the electronic system for a specific configuration and motion of the ions that follows from Eq. 2.5.

In the *static approximation* we assume that the nuclei are fixed at their equilibrium positions (their average positions), $\{\mathbf{R}_I^0\}$. In the other words, the nuclei are considered to be at rest with respect to the electrons $\Psi_0(\{\mathbf{r}, \sigma\}, \{\mathbf{R}_I^0\}) = \Phi_0(\{\mathbf{r}, \sigma\}, \{\mathbf{R}_I^0\})\,\Lambda_0(\{\mathbf{R}_I^0\})$.

The static and the adiabatic (BO) approximations come from different assumptions about the position of the nuclei. In the adiabatic (BO) approximation the wavefunction of the electrons is defined by the momentary configurations, $\{\mathbf{R}_I\}$, of the nuclei while in the static approximation the nuclei are in their equilibrium positions, $\{\mathbf{R}_I^0\}$. Therefore, in the adiabatic (BO) approximation these instantaneous nuclear configurations appear as parameters. These parameters are no longer fixed, but they are variables that the energy and wave function depend on.

Solving the Schrödinger equation with the above Hamiltonian is however still too complex for most cases, since the many-electron wave-function contains $3N$ variables.

One approach to solve the many-electron problem is using the electron density as the central unknown variable, rather than the many-electron wave-function. This approach was proposed initially by Thomas and Fermi in the 1920s [23, 24]. This model simplifies the problem considerably since the density contains only three degrees of freedom.

A significant leap in electronic structure theory was made in the remarkable theorems of '*density functional theory*' (DFT), proved by Hohenberg and Kohn [25]. DFT allows the ground-state properties of a many-electron system to be determined exactly through the electron density.

## 2.3 Density-Functional Theory (DFT)

### 2.3.1 Basic Principles

As mentioned previously, Thomas and Fermi were the first who suggested the model for the electron many-body problem based on the electron density. Due to the some shortcomings of this method, it could not describes the properties of molecules or solids quantitatively. However, almost forty years later, Hohenberg and Kohn proposed a powerful and exact theory which is based on the original idea by Thomas and Fermi. In the following section this theory will be discussed briefly. For a more comprehensive discussion one of the many review articles and books (e.g. review by Jones & Gunnarsson [26] and books by Parr & Yang [27] and Dreizler & Gross [28]) can be consulted.

In two remarkably powerful theorems Kohn and co-workers formally established the electron density as the central quantity describing electron interactions, and so devised the method which determines the ground state density exactly, known as density functional theory (DFT). The ground state density determines many body Hamiltonian and therefore all properties of the system.

**• The Hohenberg-Kohn Theorems**

The Hohenberg-Kohn theorems relate to any system consisting of electrons (fermions) moving under the influence of an external potential . These theorems are as follows:

**THEOREM 1.** *There is a one-to-one mapping between a specific external potential,* $V_{\mathrm{ext}}(\boldsymbol{r})$, *and certain electron density, $n(\mathbf{r})$.*

In the other words: The density determines the complete Hamiltonian and ground state energy, since the lowest eigenvalue of this Hamiltonian gives the ground state energy. Therefore, the ground state energy is obtained as a functional of the density.

$$E_v = \langle\Phi|\ H^e\ [n(\mathbf{r})]\ |\Phi\rangle = \langle\Phi|\ \underbrace{T[n(\mathbf{r})] + V_{int}[n(\mathbf{r})]}_{F_{HK}[n(\mathbf{r})]} + V_{\text{ext}}[n(\mathbf{r})]\ |\Phi\rangle\ . \tag{2.8}$$

The sum of $T[n(\mathbf{r})]$ and $V_{int}[n(\mathbf{r})]$ is a *universal functional* of the electron density. The expression for this unknown functional is the same for every system and is independent from the external potential. Therefore, a specific kind of system is determined only by $V_{\text{ext}}[n(\mathbf{r})]$.

The density, $n(\mathbf{r})$ which is a summation of the density of spin up $n_\uparrow(\mathbf{r})$, and spin down $n_\downarrow(\mathbf{r})$, is defined as:

$$n(\mathbf{r}) = n_\uparrow(\mathbf{r}) + n_\downarrow(\mathbf{r}) = \langle\Phi|\ \sum_{i=1}^{N} \delta(\mathbf{r} - \mathbf{r}_i)\ |\Phi\rangle\ . \tag{2.9}$$

The total energy can be written as a functional of the density in terms of the external potential and the universal functional in the following way,

$$\begin{aligned} E_v[n(\mathbf{r})] &\equiv \langle\Phi|\ H^e\ [n(\mathbf{r})]\ |\Phi\rangle \\ &\equiv \int V_{\text{ext}}(\mathbf{r})\ n(\mathbf{r})\ d^3\mathbf{r} + \mathcal{F}[n(\mathbf{r})]\ , \end{aligned} \tag{2.10}$$

where $\mathcal{F}[n(\mathbf{r})] = \langle\Phi|\ F_{HK}[n(\mathbf{r})]\ |\Phi\rangle$.

**THEOREM 2.** *The ground state energy can be obtained variationally, the density that minimises the total energy is the exact ground state density.*

This means, that $E_v[n_0]$ is the ground-state energy if and only if the true ground-state density $n_0(r)$ is inserted. For any other density $n(r)$ (which is solution of Eq. 2.8 and satisfies the constraint of the constant number of electrons, $\int n(\mathbf{r})\ d\mathbf{r} = N$), the obtained energy is larger than $E_v[n_0]$

$$E_v[n_0] = \min_{n(\mathbf{r})}\ (E_v\ [n(\mathbf{r})])\ \leq\ E_v[n]\ . \tag{2.11}$$

The ground state energy can be obtained from the variation principle, under the

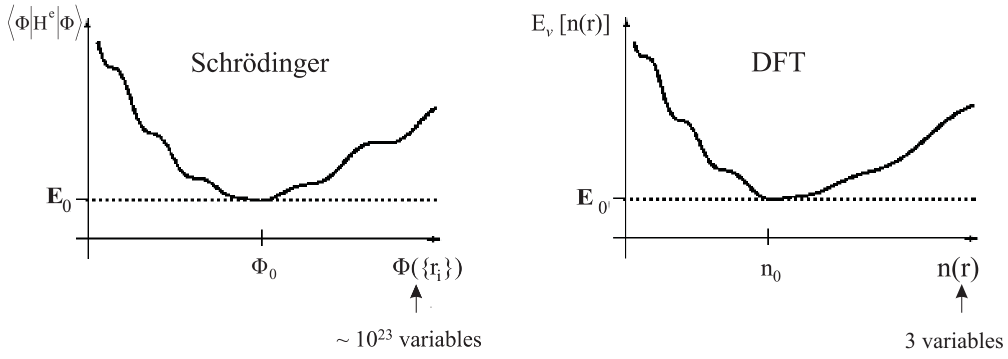

Fig. 2.1: Schematic figure of variation principle for $\langle\Phi_0|\ H\ |\Phi_0\rangle$ and $E_v[n(\mathbf{r})]$. Figure is adapted from [1]

constraint of conserving the number of electrons of the system. In other words:

$$\delta\langle\Phi|\ H^e\ [n(\mathbf{r})]\ |\Phi\rangle\ = \delta\ \{E_v[n(\mathbf{r})] - \mu\ (\int n(\mathbf{r})\ d^3\mathbf{r} - N)\} = 0\ . \tag{2.12}$$

Hence the constraint of a constant total number of electrons being equal to $N$ is taken into account by the method of Lagrange multipliers. The important physical conditions which have to be satisfied is that $n(\mathbf{r}) \geq 0$ and the assumption of continuous $n(\mathbf{r})$.

$$\int n(\mathbf{r})\ d^3\mathbf{r} = N, \tag{2.13}$$

Solving the equation above leads to the following Euler-Lagrange equation

$$\mu = \frac{\delta E_v[n]}{\delta n(\mathbf{r})} = V_{\text{ext}} + \frac{\delta F_{HK}[n(\mathbf{r})]}{\delta n(\mathbf{r})}\ , \tag{2.14}$$

where the Lagrange multiplier, $\mu$, is known as a chemical potential of the electrons.

The second Hohenberg-Kohn theorem states that there is a one to one correspondence between the ground-state wave function and the $v$-representable electron densities [1].

Now the many-electron problem with $10^{23}$ variable in three-dimensions turn into a problem with just one variable in three-dimensions.

Figure 2.1 is a schematical comparison of the solution of the Schrödinger equation using the wave function of electrons ($10^{23}$ wave functions) and the DFT approach using the electron density[2]. The significant advantage is achieved in DFT. In the treatments which are based on the wave function, one has to insert $10^{23}$ variables to the functional while in the DFT approach the functional depends only on one variable with three coordinates. One must use a separate wave function of each electron which sums up to $10^{23}$ variables.

---

[1] A density is v-representable, if it is associated with the electronic ground-state wave function of a Hamiltonian in form of $H = F_{KH} + V_{\text{ext}}$.

[2] Figure is taken from the presentation of Prof. M. Scheffler in density-functional theory workshop at Los Angeles, IPAM, (2005).

### • The Kohn-Sham Equations

The Kohn-Sham equations published in 1965, turn DFT into a practical tool for obtaining the ground state energy [29]. The Kohn-Sham formulation centres on mapping the full interacting system, onto a virtual non-interacting system. The Kohn-Sham method gives an exact solution since the virtual system yields the same ground state density as the real system. The kinetic energy functional of the non-interacting system, $T_s[n]$ (which is known), is not the same as the unknown kinetic energy of the real system. Therefore the difference between them contributes to the *correlation energy*, $E_c$ . The potential energy of the real system contains two terms: the classic part or Coulomb interaction, $V_H$, (which is known) and the unknown quantum part. The difference between these two parts is named *exchange energy*, $E_x$ . Therefore the functional $E_v[n(\mathbf{r})]$ can be written as a function of known quantities, kinetic energy ($T_s$) and Coulomb (Hartree) energy ($E^H$) of a non-interacting classical system and the unknown $E_c$ and $E_x$ functional,

$$E_v[n(\mathbf{r})] = T_s[n(\mathbf{r})] + \int V_{\text{ext}}(\mathbf{r})\, n(\mathbf{r})\, d^3\mathbf{r} + E^H[n(\mathbf{r})] + E_{xc}[n(\mathbf{r})] \,, \tag{2.15}$$

here, $E_{xc} \ = \ E_c + E_x$.

With the assumption above the Hamiltonian of the real system turns into the following formalism which is called *Kohn-Sham Hamiltonian*:

$$H_{KS}[n(\mathbf{r})] = T_s[n(\mathbf{r})] + V_H[n(\mathbf{r})] + V_{xc}[n(\mathbf{r})] + V_{\text{ext}}[n(\mathbf{r})]. \tag{2.16}$$

Here, $V_{xc}$ is called exchange-correlation potential. It is a variational derivative of the exchange-correlation energy, $E_{xc}$,

$$V_{xc} = \frac{\delta E_{xc}[n(\mathbf{r})]}{\delta n(\mathbf{r})} \ . \tag{2.17}$$

The Kohn-Sham Hamiltonian transforms the many-electron Schrödinger equation into a set of one-particle Kohn-Sham equations which are much easier to solve than the Schrödinger equation.

$$H_{KS}\Phi^{oi}(\mathbf{r}) = \epsilon_{oi}\Phi_{oi}(\mathbf{r}) \,, \tag{2.18}$$

here, $\Phi_{oi}$ 's and $\epsilon_{oi}$ 's are Kohn-Sham orbitals and eigenvalues. The Kohn-Sham equations are a set of equations which describe the behavior of non-interacting classical particles inside an external potential, $V_{\text{ext}}$. Please note that the eigenvalue of the single Kohn-Sham equations are not the energy of electrons but just mathematical objects and have no physical meaning.

The construction of Kohn-Sham equations guarantees that the ground state density of this virtual system is exactly the electron ground state density of the real system, $n(\mathbf{r}) = \sum_i \Phi^*_{oi}(\mathbf{r})\Phi_{oi}(\mathbf{r})$.

Since the Kohn-Sham Hamiltonian depends on the density, $n(\mathbf{r})$, which is driven from $\Phi_i$, a *' self consistency problem '* has to be considered to obtain a solution.

$$\underbrace{(-\frac{\hbar^2}{2m}\nabla_i^2}_{T_s[n]} + \underbrace{\frac{e^2}{4\pi\varepsilon_0}\int\frac{n(\mathbf{r})\,d^3\mathbf{r}}{|\mathbf{r}-\mathbf{r}'|}}_{V_H} + V_{xc} + V_{\text{ext}})\Phi_i(\mathbf{r}) = \epsilon_i\Phi_i(\mathbf{r})\ . \tag{2.19}$$

In the self-consistent field (SCF) approach (cf. Fig. 2.2), the solutions, $\Phi_i$, determine the Hamiltonian, and the equations cannot be solved before its solutions to be known. This paradox can be solved by an iterative procedure: a initial density, $n_i(\mathbf{r})$ is guessed and the Hamiltonian is constructed. The eq uations are solved and the resulting $\Phi_i$ lead to a new density, $n_1(\mathbf{r})$, which most probably is different from the initial density. Again, new Hamiltonian with new density is constructed which yields $n_2(\mathbf{r})$ and so on.

This procedure is set up in such a way that it converges this series to a final density, $n_f(\mathbf{r})$, which generates a Hamiltonian with the solution of previous density, $n_f(\mathbf{r})$, again. This final density is consistent with the Hamiltonian.

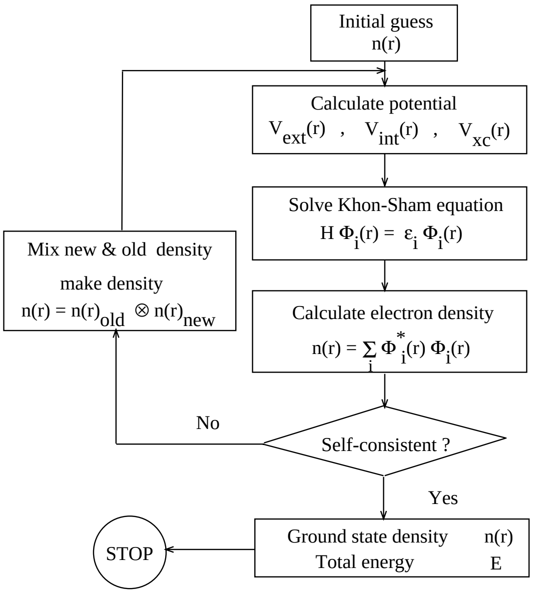
Initial guess
n(r)
Calculate potential
Vext(r) , Vint(r) , Vxc(r)
Solve Khon-Sham equation
H Φi(r) = εi Φi(r)
Calculate electron density
n(r) = Σi Φ*i(r) Φi(r)
Mix new & old density
make density
n(r) = n(r)old ⊗ n(r)new
No
Self-consistent ?
Yes
Ground state density n(r)
Total energy E
STOP

Fig. 2.2: The Self-consistent field approach for solving Kohn-Sham equations.

Kohn and Sham devised an ingeniously practical single-particle scheme for performing DFT calculations, which is still exact, in principle. An additional approximations must be made for the unknown component, $E_{xc}[n(\mathbf{r})]$, which accounts for electron many-body effects. The exchange and correlation energy is an important contribution since the binding energy of the systems is defined in an accurate description of $E_{xc}[n(\mathbf{r})]$ which is crucial for the prediction of binding properties.

Description of some present approximations for the exchange-correlation energy (potential) in DFT is the object of following part.

## 2.4 Approximation to The Exchange Correlation Potential

Hohenberg and Kohn in their original paper, considered the exchange-correlation potential for an inhomogeneous electron gas of almost constant density [25].

$$n(\mathbf{r}) = n_0 + \tilde{n}(\mathbf{r}) \ , \tag{2.20}$$

with $\tilde{n}(\mathbf{r})/n_0 \ll 1$ and $\int \tilde{n}(\mathbf{r})\, d\mathbf{r} = 0$. Then the exchange-correlation energy functional is expanded in terms of the assumed density:

$$E_{xc}[n] = \int \epsilon_{xc}^{homo}[n(\mathbf{r})]n(\mathbf{r})d\mathbf{r} \ , \tag{2.21}$$

where $\epsilon_{xc}^{homo}[n]$ is the exchange-correlation energy per electron of a uniform (homogeneous) electron gas of density $n$. The $\epsilon_{xc}$ is a functional of the local density, so that this approximation is known as *Local-Density Approximation* (LDA). The analogous formalism, in which it describes a spin-polarized system, is known as *Local -Spin -Density Approximation* (LSDA). The $E_{xc}$ is a functional of both spin up and spin down density. LDA predicts a too high cohesive energy and underestimates the equilibrium volume, due to overbinding.

There are several approximations for the $\epsilon_{xc}$. The most widely used approximations were proposed by:

Wigner [30]: $\epsilon_x = \frac{-0.09164}{r_s}$ and $\epsilon_c = \frac{-0.88}{7.8+r_s}$. $r_s = (4\pi n/3)^{-1/3}$ is the Wigner-Seitz radius.

Hedin and Lundqvist [31] : $\epsilon_x = \frac{-0.9164}{r_s}$ and $\epsilon_c = -0.045[(1 + (\frac{r_s}{21})^3)h(1 + \frac{21}{r_s} + \frac{r_s}{42} - (\frac{r_s}{21})^2 - \frac{1}{3})]$

Perdew and Wang [32]: which used the Ceperley and Alder [33] parameterization for $r_s \geq 1 : \epsilon_x = \frac{-0.4582}{r_s}$

$$\epsilon_c = \begin{cases} \frac{-0.1423}{1+11.0529\sqrt{r_s}+0.333\ r_s} & r_s \geq 1 \\ -0.0480 + 0.0311 \ln \mathrm{r_s} - 0.0166\ \mathrm{r_s} + 0.002\ \mathrm{r_s} \ln \mathrm{r_s} & 0 \leq r_s \leq 1 \end{cases}$$

For a system with smooth electron density LDA provides an accurate enough description, but for strongly inhomogeneous systems, in which the density variations are significant, the performance of an LDA-$E_{xc}$ functional is not satisfactory.

An Alternative to LDA can be obtained by letting $E_{xc}$ depend on the gradient of density as well, which allows for more flexibility in dealing with density fluctuations.

$$E_{xc}[n(\mathbf{r})] = \int n(\mathbf{r})\ \epsilon_{xc}(n(\mathbf{r}), \nabla n(\mathbf{r}))d^3\mathbf{r}\ . \tag{2.22}$$

This approach leads to the *Generalized Gradient Approximation*(GGA).

The idea of using the gradient of density beside density, was found for the first time in Kohn and Sham original paper from 1965 [29]. They used a gradient expansion of the density as a correction:

$$E_{xc}[n] = \int \epsilon_{xc}[n(\mathbf{r})]n(\mathbf{r})d\mathbf{r} + \int \epsilon_{xc}^2[n(\mathbf{r})]|\nabla n|^2 d\mathbf{r}\ +\ ... \tag{2.23}$$

There is not a unique generalized gradient approximation for the exchange- correlation functional. Indeed, there are several modifications and some of the most popular functionals, implemented also in the WIEN2k code are: the PW91 formalism, proposed by Perdew and Wang [32] and the modified version, PBE-96 by Perdew-Burke-Ernzerhof [34]. The latter one is used throughout the present work.

In the PBE-96 functional, a correction term, $h(n, r_s, t)$ is added to the correlation part, $\epsilon_c$. The correlation energy is a functional of the relative spin polarization density, $\bar{n} = (n_\uparrow - n_\downarrow)/(n_\uparrow + n_\downarrow)$ ,

$$E_c^{GGA}[n_\uparrow, n_\downarrow] = \int n(\mathbf{r})(\epsilon_c^{homo}(\bar{n}, r_s) + H(\bar{n}, r_s, t))d^3\mathbf{r}\ , \tag{2.24}$$

where $t \propto |\nabla n|/n$.

The functional $h$ has a logarithmic shape and obeys the following conditions [34]:
i) For a slowly varying density gradient, $h$ is given by its (the densities) second-order gradient expansion.
ii) For a rapidly varying density gradient, $h \longrightarrow -\epsilon_c^{homo}$.

iii) Under uniform scaling $h$ is a constant.

The exchange energy is constructed as:

$$E_x^{GGA} = \int n(\mathbf{r})\epsilon_x^{homo}(n)F_x(s)d^3\mathbf{r} \ , \tag{2.25}$$

where $s = |\nabla n|/(2k_f n)$ and $k_f = (9\pi/4r_s^3)^{-1/3}$. $F_x$ is given as:

$$F_x(s) = 1.804 - \frac{0.804}{1 + 0.235s^2/0.804} \ . \tag{2.26}$$

Note that the energy in the PBE formalism is given in Hartree unit.

The last level of approximation is applied to solve the Kohn-Sham equation.

## 2.5 Approximation for Solving The Kohn-Sham Equations

A most important step for solving Kohn-Sham equations is to find a suitable basis set for the expansion of wave function. Using the suitable basis set that describes the behavior of the electrons leads to a solution of Kohn-Sham equations, not be computationally very demanding but still accurate. For example, the behavior of an electron in a constant potential can be described quite well by a set of plane waves.

The DFT orbital wave functions, $\Phi_i$s, are then expanded in terms of a basis set, $\varphi^i$,

$$\Phi_{oi} = \sum_{\mathbf{K}}^{M} c_{\mathbf{K}}^i \, \varphi_{\mathbf{K}}^i \qquad , \qquad \mathbf{K} = \mathbf{k} + \mathbf{G} \ , \tag{2.27}$$

where **k** is the crystal momentum vector in the irreducible Brillouin zone and **G** is a reciprocal lattice vector.

In order to find the density, one must set up the basis set and determine the $c_K^i$ coefficients. In principle, the expansion of the wave functions should be infinite, but in practice they are truncated at some point. The choice of the truncation value, $M$, turns the infinite number of the basis functions into a finite set of those. This represent the third level in a hierarchy of approximations necessary to solve a many-body system Hamiltonian, discussed in the beginning of this chapter.

There are several different methods to define the orbital wave function and solve the DFT equations. One of the common used methods is the pseudo-potential plane waves (PP-PWs) method. They are quite suitable for describing periodic solids when using pseudo-potentials, but are an inefficient basis for describing the rapid variations of wave-functions close to the nucleus.

One solution for this difficulty is using the pseudopotential concept, in which the oscillations of the electron wave-function near a nucleus are considered in a pseudised fashion. Another possibility, used in the calculations presented in this work, is to augment the plane waves basis set in the vicinity of a nucleus.

In the following sections, the augmented plane waves (APW), the linearized augmented plane waves (LAPW) method and the effect of local orbitals on the efficiency of the basis set will be discussed.

### 2.5.1 Basis Functions: APW, LAPW, APW + lo

**• The Augmented Plane Wave Method (APW)**

Slater was the first to introduce Augmented Plane Waves (APW) as possible basis functions to solve one-electron equations [35]. In this method the unit cell is divided into two regions: i) the rigion around the nuclei, which is a sphere with radius $R$, the so called ' *Muffin-Tin* ' sphere (MT). ii) the remaining part of the unit cell which is called ' *interstitial* ' region (IR), see Fig. 2.3. Loucks describes this methods in detail [36].

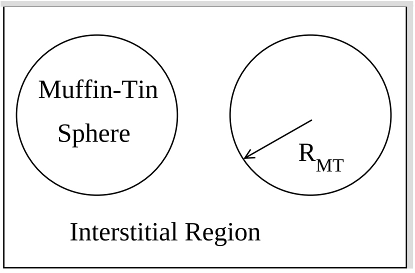

Fig. 2.3: Division of the unit cell into two parts: the Muffin-Tin spheres, with radius $R$, around the nucleus and an interstitial region.

The idea behind APW is that the potential in the interstitial region is almost constant. This means, that the behavior of electrons can be efficiently described by a plane waves basis set[3]. Close to the nuclei it is assumed that electrons behave like in a free-atom. The atomic like functions are efficient to describe the behavior of the electrons in this region. Therefore, the wave function of electron over the whole unit cell can be obtained as below:

$$\varphi_{\mathbf{K}}(\mathbf{r}) = \begin{cases} \frac{1}{\sqrt{V}} e^{i\mathbf{K}.\mathbf{r}} & \mathbf{r} \in IR \\ \sum_{l,m} A_{lm}^{\mathbf{K}} \, u_l(r,E) \, Y_{lm}(\hat{\mathbf{r}}) & \mathbf{r} \in MT \end{cases} \tag{2.28}$$

Here, $V$ is the unit cell volume, $Y_{lm}$ are spherical harmonics and $u_l$ is the numerical solution to the radial Schrödinger equation at the energy $\epsilon$:

---

[3] The solution of a Hamiltonian with constant potential is plane waves.

$$\{-\frac{1}{r^2}\frac{d}{dr}(r^2\frac{d}{dr})+[\frac{l(l+1)}{r^2}\ +\ V_{\text{eff}}(r)\ -\ \epsilon]\}\ u_l(r,\epsilon)=0\ . \tag{2.29}$$

The coefficients $A^{\mathbf{K}}_{lm}$ are chosen in such way that satisfy the boundary conditions. The only boundary condition in the APW method is that the basis functions must be continuous at the MT-sphere boundaries [4]. Therefore, with expanding the plane wave into Bessel functions and matching the basis functions inside and outside the sphere, the coefficients are

$$A^{\mathbf{K}}_{lm}\ =\ 4\pi i^l Y^*_L(\hat{\mathbf{K}}_{\mathbf{G}})\frac{j_l(\mathbf{K}_{\mathbf{G}}R)}{u_l(R,E)}\ , \tag{2.30}$$

where $j_l(\mathbf{K}_{\mathbf{G}}r)$ are Bessel functions and $R$ is radius of MT sphere.

The Kohn-Sham eigenstates are expressed as linear combination of APW functions, $\varphi_{\mathbf{K}}(\mathbf{r})$:

$$\Phi_{oi}(\mathbf{r})=\sum_{\mathbf{K}} C^i_{\mathbf{K}}\ \varphi_{\mathbf{K}}(\mathbf{r})\ . \tag{2.31}$$

The expansion coefficients $C^i_{\mathbf{K}}$, can be determined variationally [36]. This requires a variational expression for energy with respect into the linear combination of APW basis set:

$$\frac{\delta\langle\Phi_o\ |H|\ \Phi_o\rangle}{\delta C_{\mathbf{K}}}=0\ . \tag{2.32}$$

Although the APW basis set can describe the behavior of the electron near the nuclei, there are two shortcomings for this method:
i) First, the coefficients $A^{\mathbf{K}}_{lm}$ are not defined for the energies that yield a radial solution equal to zero at MT-sphere boundaries, $u_l(E,R)=0$. In this case, the basis sets are decoupled, since the boundary conditions would not be satisfied [37].
ii) Second, the Kohn-Sham wave functions, $\Phi_i(r)$ can be described by the APW basis set only if the radial solutions are evaluated at Kohn-Sham eigenvalues,($E=\epsilon_i$). Therefore a different energy-dependent set of APW basis functions must be found for each Kohn-Sham eigenenergy. One should start with a guessed energy value, solve the radial Schrödinger equation to construct the APW basis and set up the matrix elements . Then the determinant $|H-ES|$ must be computed, where $S$ is the overlap matrix [5]. So in order to find the root of the determinant, several trial energies have to be tested. A similar procedure is repeated to determine all matrix

---

[4] The kinetic energy is not well-defined for discontinuous basis functions.

[5] Since the APW basis sets are not orthogonal, overlap matrix would not vanish from the secular equation.

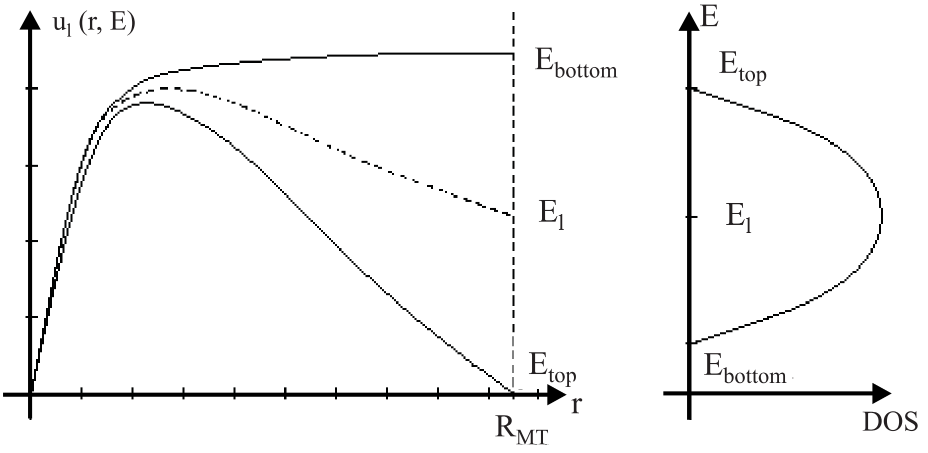

Fig. 2.4: Schematic dependence of $u_l(r, \epsilon_l)$ (a) and DOS (b) on the energy $\epsilon$.

elements. This is computationally very expensive [38].

### • The Linearized Augmented Plane Wave Method (LAPW)

In 1975 Andersen [39] and Koelling and Arbman [40] in two different works, improved the APW methodology and solved the problem of energy-dependence of the basis set. In this modified method which is called *' Linearized Augmented Plane Wave '* (LAPW), an energy independent radial solution is expanded in a Taylor-like series around a fixed energy. Such a Taylor expansion of $u_l$ around fixed energy value[6] $E_l$ is given by:

$$u_l(r,\epsilon) = u_l(r,\epsilon_l) + (\epsilon_l - \epsilon) \underbrace{\frac{\partial u_l(r,\epsilon)}{\partial \epsilon}\Big|_{\epsilon=\epsilon_l}}_{\dot{u}_l(r,\epsilon_l)} + O(\epsilon_l - \epsilon)^2 \, . \tag{2.33}$$

The basis functions in the interstitial region are considered to be PW while the basis set inside the MT-spheres are taken as a linear combination of a radial solution, $u_l$, at fixed linearization energy, $E_l$, and its energy derivative ,$\dot{u}_l$, at the same energy. Note that both $u_l$ and $\dot{u}_l$ are regular at the origin. $E_l$ should be chosen in such a way that its value is close to the center of the energy band with the appropriate $l$-character.

---

[6] It is not essential that $E_l$ is equal to the Kohn-Sham eigenvalues.

$$\varphi_{\mathbf{K}}(\mathbf{r}) = \begin{cases} \frac{1}{\sqrt{V}} e^{i\mathbf{K}.\mathbf{r}} & \mathbf{r} \in IR \\ \\ \sum_{l,m} \left( A_{lm}^{\mathbf{K}}\, u_l(r, E_l) \;+\; B_{lm}^{\mathbf{K}}\, \dot{u}_l(r, E_l) \right) Y_{lm}(\hat{\mathbf{r}}) & \mathbf{r} \in MT \end{cases} \tag{2.34}$$

The coefficients $A_{lm}^{\mathbf{K}}$ and $B_{lm}^{\mathbf{K}}$ will be determined by requiring that the basis function as well as its derivative are continuous at the boundary of the MT-sphere.

Since the shape of the radial solution $u_l(r, \epsilon)$ depends on the $\epsilon_l$, choosing the suitable linearization energy $\epsilon_l$ is quite important. The most simple way for doing this is the Wigner-Seitz method. In this method the linearized energy is chosen to be the average of two energies $\epsilon_{top}$ and $\epsilon_{bottom}$, i.e. $\epsilon_l = (\epsilon_{top} + \epsilon_{bottom})/2$, see Fig. 2.4 [7]. $\epsilon_{top}$ is the highest antibonding energy state, i.e. the top of the band. It is also an energy, for which the radial solution becomes zero at the MT-sphere boundaries, $u_l(R, E_{top}) = 0$. The other energy is chosen in a similar fashion: $E_{bottom}$ is the lowest bonding energy state, i.e. the bottom of the band and for it the derivative of the radial solution becomes zero at the MT-sphere boundaries, $\dot{u}_l(R, E_{top}) = [\partial u_l(r, E_{bottom})/\partial r]_R = 0$, see Fig. 2.4-a.

Solutions to the radial Schrödinger equation, $u_l$, for *s*, *p*, *d* and *f* orbitals are shown for an APW basis set in Fig. 2.5-a and an LAPW basis function in Fig. 2.5-b. The Figure is taken from work by Sjöstedt *et al.* [37]. As mentioned before and can be seen from the figure, due to the discontinuous behavior of the slopes of the functions in the APW approach, it possesses a kink at the MT-sphere boundary. In contrast, the LAPW functions have smooth behavior at the MT-sphere boundary.

The LAPW basis set can provide sufficient basis functions for Kohn-Sham eigenstates in the energy range around the linearization energy. Therefore, all the Kohn-Sham eigenvalues can be found with just a single diagonalization of the secular matrix. However, the number of basis functions in LAPW is larger than in the APW method, thus the secular matrix of LAPW is enlarged in comparison to APW.

### • The Augmented Plane Wave plus local orbital Method (APW+lo)

In an alternative approach to LAPW one can combine advantages of both the APW and the LAPW method to optimized basis functions. It can be done by removing the energy dependence of the original APW basis functions (which is the characteristic of LAPW functions) but retaining the lower cutoff, i.e. smaller matrix associated with the original APW functions. In the so called APW+lo method (de-

---

[7] Figure is adapted from WIEN2k userguide (http://www.wien2k.at).

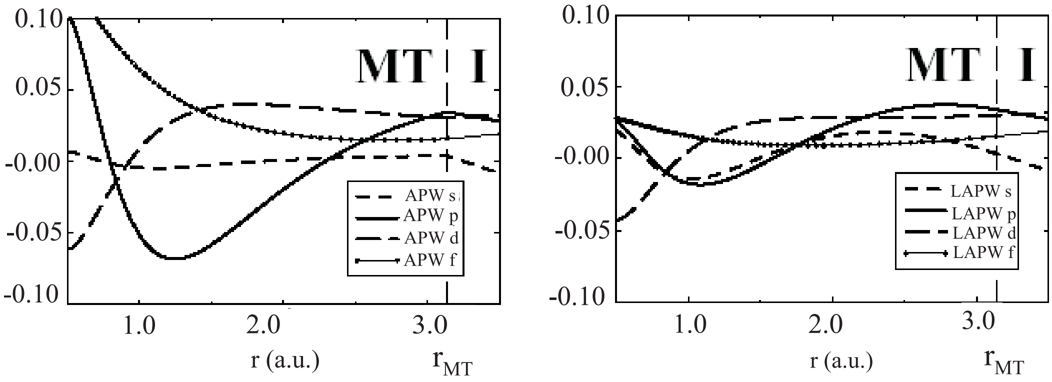

Fig. 2.5: Radial solution, $u_l$, of the l-composition and its behavior at MT-sphere boundaries in an APW (a) and LAPW (b) basis function are compared.

veloped by Sjöstedt *et al.*) Sjöstedt *et al.* proposed an energy-independent basis set of APW which combines with a new basis set in the MT-sphere which belongs to the local orbitals. This new basis set is called local orbital basis set (lo). It is applied in order to increase the flexibility of the basis set and to recover the effect of the missing derivative of the radial wave functions. They (the local orbitals), neither impose extera boundary condition of the APW basis set nor affect the number of basis functions in the interstitial region. This local orbitals are restricted only inside the MT-sphere, therefore the interstitial region will remain unaffected.

$$\varphi^{lo}_{lm}(\mathbf{r}) = \begin{cases} 0 & \mathbf{r} \in IR \\ \\ \sum_{l,m} \left( A^{lo}_{lm}\, u_l(r, E_l) \;+\; B^{lo}_{lm}\, \dot{u}_l(r, E_l)\right) Y_{lm}(\hat{\mathbf{r}}) & \mathbf{r} \in MT \end{cases} \tag{2.35}$$

For simplification, one can use the same linearization energy for the local orbital basis functions. The coefficient $A^{lo}_{lm}$ and $B^{lo}_{lm}$ are determined by normalization and using $\varphi^{lo}_{lm} = 0$ at the MT-sphere boundary. The APW and local orbital are continuous at the MT-sphere while their first derivatives are discontinuous (the slope of the local orbital has a non-zero value at the MT-sphere).

The new APW+lo basis set includes the radial solutions of the Schrödinger equation in their original APW form, which efficiently describes the eigenfunctions at energies close to $E_l$, but also a (less restricted) linear combination of $u_l(r, E_l)$ and $\dot{u}_l(r, E_l)$, which improves the description of states away from $E_l$.

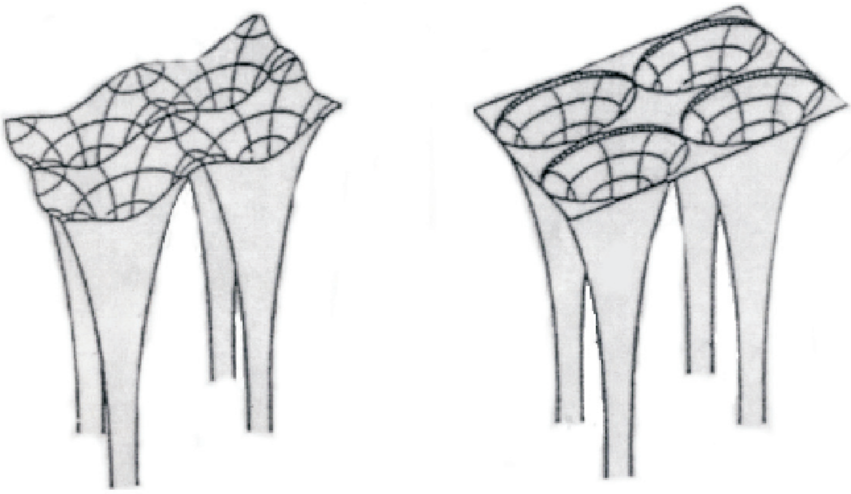

Fig. 2.6: Schematic shape of the full potential (a) and the Muffin-Tin potential (b).

### 2.5.2 Representation of The Potential

The (L)APW method allows an accurate description of the rapidly changing (oscillating) wave-functions, potential and electron density close to the nuclei as well as the smoother part of these quantities in between the atoms (interstitial region). Therefore the representation of the potential will be similar to the wave-functions, the potential is a hybrid of two adjacent regions of space.

M. Weinert [41] and E. Wimmer *et al.* [42] proposed a method to describe the all electron potential in the solid using the multipole potentials concept. As there is no shape approximation for the potential, such an approach is called a full-potential treatment. In this method the Poisson equation is solved for the general periodic potential, including the non-spherical contributions of the potential inside the MT-sphere to the Hamiltonian matrix elements.

The Hamiltonian , and hence the potential, contains three contributions:

$$V_{eff} \; = \; V_S + V_{NS} + V_{IR} \; , \tag{2.36}$$

where the $V_S$, $V_{NS}$ and $V_{IR}$ terms are due to the spherical and non-spherical part of the potential in the MT-sphere and the potential in interstitial regions [43].

The potential in the interstitial region is described by the Fourier representation (of the smooth interstitial charge density), which means that the full potential has then the following form:

$$V(\mathbf{r}) = \begin{cases} \sum_{\mathbf{G}} V_{\mathbf{G}}\, e^{i\mathbf{G}.\mathbf{r}} & \mathbf{r} \in IR \\ \\ \sum_{L,M}\; V_{LM}(\hat{\mathbf{r}})\, Y_{LM}(\hat{\mathbf{r}}) & \mathbf{r} \in MT \end{cases} \tag{2.37}$$

Here, **G** is a reciprocal vector and its maximum value is required to be larger than the one of a reciprocal vector in the PW expansion in the interstitial region, $\mathbf{K}$. This is due to the fact that the Fourier expansion represents the potential while the quadratic form of the wave functions determine the density.

$Y_{LM}$s are lattice harmonics represent the point group symmetry which is applied to the spherical harmonics. The quality of the full-potential is controlled by the cutoff parameter **G** which truncates the sum over lattice vectors in the interstitial region and $L, M$ which restricts the number of the non-spherical terms inside the MT-sphere which contributes to the potential.

Neglecting non-spherical terms, ($l \neq 0$), in the expansion of the potential inside a MT-sphere and considering just a constant potential in the interstitial region ($G = 0$) leads to an approximate crystal potential called Muffin-Tin (MT) potential. The MT-potentials are a reasonable approximation to describe the potential for bulk materials but for reduced symmetry solid (such as films or interface) it is not a very useful treatment. The schematic shape of the full potential and the MT-potential is shown in Fig. 2.6.

## 2.6 k-point Sampling

According to Bloch's theorem [44], any real-space integral over a periodic system with infinite extent can be replaced by an integral in reciprocal-space over the (finite) first Brillouin zone. Thus in order to study the properties of crystals, one needs to calculate the integration of the periodic functions over the first Brillouin-zone (1BZ) in the reciprocal space in [45]; For a example quantity $I$ can be defined as:

$$I = \int_{BZ} F(\mathbf{K})\, d^3\mathbf{k}\,, \tag{2.38}$$

where the periodic function, $F(\mathbf{k}) = \sum_R f(\mathbf{R})\, e^{i\mathbf{k}.\mathbf{R}}$ is the Fourier transform of a periodic function in real space. In practice for the numerical evaluation, this integral turns into the sum over a large number of discrete points. To make calculations feasible only a finite set of such points in the BZ is used to compute these functions.

Such a set of special points is called $'\mathbf{k}-point'$ set. [46]:

$$\Omega^{-1}\int_{BZ} F(\mathbf{k})\, d^3k = \sum_n w_n F(\mathbf{k}_n)\ . \tag{2.39}$$

Here $\Omega$ is the unit cell volume in the real space and $w_n$ is a weight factor [8] and the sum over all weights is equal to one.

$$\sum_n w_n \ = 1 \tag{2.40}$$

The error introduced by using a discrete **k**-point set can be reduced by increasing the density of the **k**-point mesh.

The symmetries of a crystal allow further reduction of the number of **k**-points used for an actual calculation. There are several methods to find such set of points [47–49]. The most applicable and famous approach is that of Monkhorst and Pack, [49] which is employed for the calculations in this work. This scheme contains equispaced grid points which are distributed homogeneously throughout the BZ with rows and columns parallel to the reciprocal vectors. These equispaced grid of **k**-points are constructed as follows:

$$\mathbf{k} = x_1\mathbf{b}_1 + x_2\mathbf{b}_2 + x_3\mathbf{b}_3\ , \tag{2.41}$$

where $\mathbf{b}_i$s are the reciprocal lattice vectors, and the coefficients are obtained:

$$x_i = \frac{(2i-q-1)}{2q} \qquad , \qquad i = 1, 2, ...q \tag{2.42}$$

$q$ is an integer number that determines the number of special points in the set.

Typically, the point-group symmetry of the crystal is used to produce a smaller subset of the full **k**-point set, containing points located within the irreducible part of the Brillouin zone. The values of the weighting factors will be adjusted according to this new **k**-point set. This **k**-point in the irreducible BZ results in a significant reduction in the computational expense since a smaller number of **k**-points is used in the summations.

Choosing a sufficiently dense mesh of integration points is crucial for the convergence of the results. Therefore, it is one of the major parameters for which one should perform convergence tests before setting up the calculations.

---

[8] A weight factor, $w_n$, is defined as a fraction of **k**-points equivalent under symmetry consideration.

## 2.7 The Slab Model and The Supercell Approach

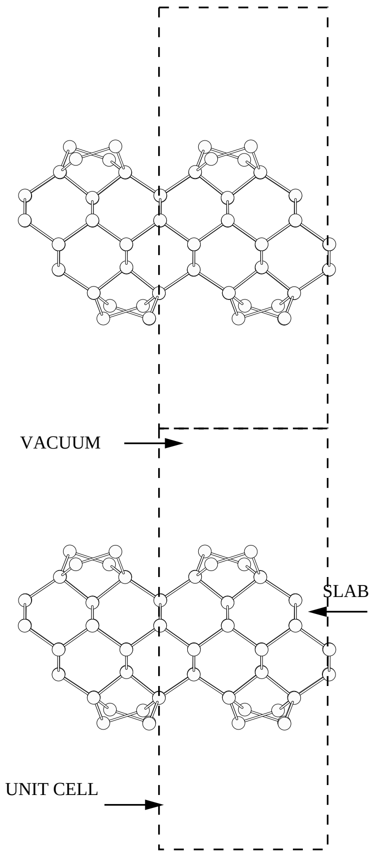

Fig. 2.7: Side view of a slab model containing 8 layers Si(001)($2 \times 2$) with alterating dimer reconstruction and vacuum.

The goal of this work is to predict and simulate the behavior of magnetic adatoms (such as adatom adsorption, diffusion pathways and thin film growth ) on semiconductor surfaces. To perform such calculations, one needs a proper model that describes the system reasonably well and is computationally not (too) expensive.

Normally, in the bulk material with three dimensional periodicity, the periodic boundary conditions of solids can be satisfied in the surfaces. However, due to the lack of the translation symmetry in the direction normal to the surface, the periodicity will be reduced to two dimensions. The slab approach is suitable for such a purpose and is utilized in this work to simulate the studied system. In the slab model the unit cell is described by a finite number of layers and a vacuum region is introduced into the unit cell. This leads to a reduction of the symmetry (compared to the bulk material) in $z$-direction, but also introduces a surface into the calculation. Periodic boundary conditions ensure that the slab is infinte in $x$ and $y$ direction, but also that there are periodically repeated slabs in $z$-direction, which are separated by the vacuum region. The slabs used in this work are constructed in such a way, that inversion symmetry is retained. The thickness of the slab and the vacuum region are chosen with the requirement that both surfaces would not have interaction with each other through the vacuum or the slab. The adequate value for slab and vacuum thickness must be determined in convergence tests.

There are two different interpretations and descriptions of the slab model within the (L)APW method and the shape of the full-potential:
i) **Film geometry approach**, in this model which was proposed by Krakauer *et al.* [42, 43, 50], the vacuum region is described by an alternative basis set and potential term. The basis function is considered to be a product of a two-dimensional planewave and a $z$-dependent function and its energy derivative. The $z$-dependent func-

tion is defined by the solution of the one-dimensional Schrödinger equation with $z$-dependent potential. The applied boundary condition requires that the basis function and its energy derivative are continuous across the slabs boundaries.
ii) **Supercell approach**: this model is used in the present work. It is based on the three dimensional periodicity of the unit cell. It means the periodic boundary conditions are applied for the slabs in $z$-direction as well as in $x$ and $y$ directions. The conditions of an adequate thickness of the vacuum and the slab, requires that the the electronic wave function of the slabs vanishes around the middle of the vacuum region. The middle layers of the slabs should have a bulk-like representation.
A side view ball-stick model of a supercell with an eight layer Si(001)($2 \times 2$) slab and a vacuum region, which is approximately 1.5 times as thick as the slab, is shown in Fig. 2.7.

## 2.8 The WIEN2k Code

The calculations in this work are performed using the **WIEN2k** computer package [51, 52]. This program contains several sub-programs, which are described briefly in the following parts. There are two major parts in the program, the **initialization** and the **self-consistent field** [(SCF)] cycle. The flow chart of the code is given in Fig. 2.8.

**• Initialization:**
**setting up the unit cell and generating the initial density**

In this sub-program, atomic densities are generated and superimposed to obtain a initial crystal density for the SCF calculation. Additionally, the atomic potentials and, optionally, atomic valence densities are created. Information about $l, m$ values of the lattice harmonics representation and number of Fourier coefficients of the interstitial charge density are inserted as input file in this part.

**• LAPW0:**
**Construction of the effective potential:**

The Poisson equation is solved and the total potential is computed as the sum of the Coulomb and the exchange-correlation potential in the LAPW0 program. The electron (spin) density is used as input and the spherical (l=0) and the non-spherical parts of the potential are generated. The Coulomb potential is calculated by a multipolar Fourier expansion introduced by Weinert [41]. The exchange-correlation

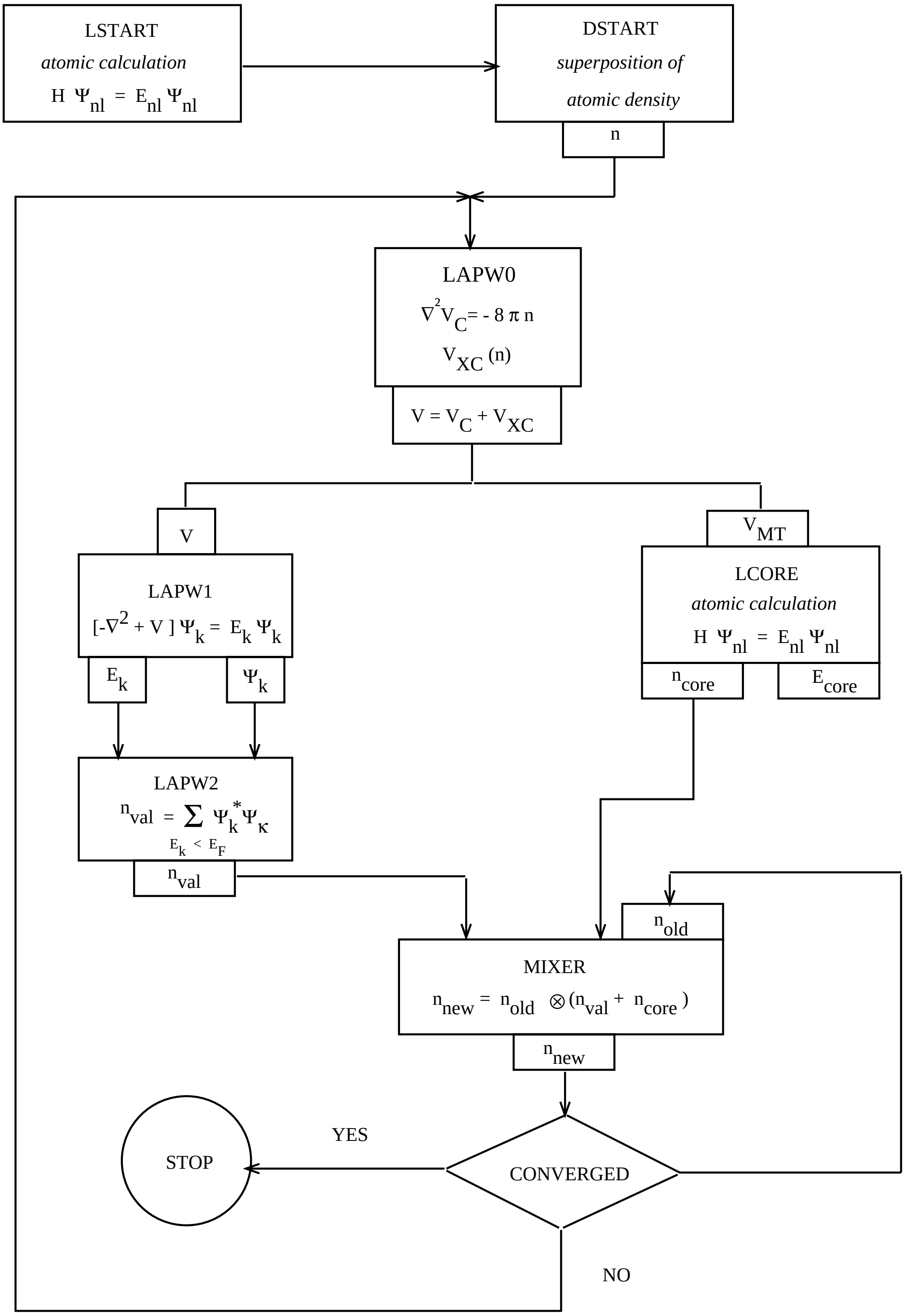
LSTART
atomic calculation
H Ψnl = Enl Ψnl
DSTART
superposition of
atomic density
n
LAPW0
∇²VC = - 8 π n
VXC (n)
V = VC + VXC
V
VMT
LAPW1
[-∇² + V ] Ψk = Ek Ψk
LCORE
atomic calculation
H Ψnl = Enl Ψnl
Ek
Ψk
ncore
Ecore
LAPW2
nval = Σ Ψk* Ψκ
Ek < EF
nval
nold
MIXER
nnew = nold ⊗ (nval + ncore )
nnew
STOP
YES
CONVERGED
NO

Fig. 2.8: Flow chart of SCF cycle in WIEN2k compter code.

potential is computed numerically on a grid. Additionally, the Hellmann-Feynman force contribution to the force is also determined [53].

**• LAPW1:**
**Solving the Kohn-Sham equations of valence electrons:**

The Hamiltonian and the overlap matrix [40] are set up in LAPW1. Their diagonalization provides the eigenvalues and eigenvectors. Both the LAPW and the APW+lo methods are supported. For maximum efficiency a mix of both is recommended, i.e. the APW+lo basis functions are used for physically meaningful $l$ values, while LAPW basis functions are employed to describe higher $l$-values functions.

**• LAPW2:**
**Construction of the new electron density**

The Fermi-energy is computed. The electronic charge densities are expanded according to the representation of Eq. 2.28 for each occupied state and each **k**-vector. Afterwards the corresponding (partial) charges inside the atomic spheres are obtained by integration. In addition, Pulay-corrections to the forces are calculated.

**• LCORE :**
**The treatment of the core electrons**

The potential and the charge density of the core electrons are computed.

**• LMIXER:**
**Generating the input density for the next iteration**

The electron densities of core, semi-core, and valence states are combined to yield the total new density. Taking only the new densities would, however, lead to instabilities in the iterative SCF process. To have a stable SCF cycle new and old densities need to be mixed, to obtain a new density.
$n_{new}^{m+1} = (1-\alpha) n_{new}^{m} + \alpha \, n_{old}^{m}$ , here $\alpha$ is a mixing parameter. In the WIEN2k code this is done (mainly) using the Broyden scheme.
The total energy and the atomic forces are computed in mixer, as well.

# Chapter 3

# Bulk Properties

## 3.1 Introduction

A surface is directly connected to the underlying bulk, which means that the properties of the bulk material will most probably influence the properties and behavior of the surface. This chapter is therefore devoted to the investigation of different bulk structures, in order to study their equilibrium atomic structure, relative stability, electronic and magnetic properties. The results are then used to obtain the surface energy and formation energy of films at the surface. Additionally, it is the basis for comparing the theoretical results with experimental data.

The starting point of any investigation is the determination of the theoretical lattice parameter. Thermodynamic properties will be important as well for the following discussion of the surfaces.

To obtain the equilibrium bulk structure, the total energy is minimized with respect to the unit cell volume. The lattice parameters and bulk modulus are determined by fitting a set of data points to the Murnaghan equation of state, [54]:

$$E(V) = E(V_0) + \frac{B_0}{B_0^{'}} \left[ \frac{V_0 \, (V_0/V)^{B_0^{'}-1}}{B_0^{'} - 1} + V(1 - \frac{(V_0/V)}{B_0^{'} - 1}) \right] \qquad , \tag{3.1}$$

where $V_0$ is the equilibrium volume at zero temperature, $E(V_0)$ is the minimum energy of the system, $B_0$ is the bulk modulus, defined as

$$B_0(T,p) = -V \, \frac{\partial p}{\partial V} \, |_T \qquad , \tag{3.2}$$

and $B_0^{'}$ is the pressure derivative of bulk modulus at $p = 0$ and constant temperature:

$$B_0^{'} = -\frac{\partial}{\partial p}\,(\,V\frac{\partial p(T,V)}{\partial V}\,)_{T,p=0} \qquad . \tag{3.3}$$

The cohesive energy is always defined as the energy needed to form a crystal from the individual free atoms [1] which form the crystal. For example, the cohesive energy for MnSi is obtained as:

$$E_{\mathrm{coh}} = E_{\mathrm{tot}}^{\mathrm{MnSi-bulk}} - E_{\mathrm{tot}}^{\mathrm{Mn-atom}} - E_{\mathrm{tot}}^{\mathrm{Si-atom}} \qquad . \tag{3.4}$$

where $E_{\mathrm{tot}}^{\mathrm{MnSi-bulk}}$, $E_{\mathrm{tot}}^{\mathrm{Mn-atom}}$ and $E_{\mathrm{tot}}^{\mathrm{Si-atom}}$ are the total energies of MnSi bulk, Mn and Si free atoms.

The energy difference between a crystal and it's constituent parts as solid phases is called the formation enthalpy of the solid at zero temperature, which is given by:

$$\Delta H(\mathrm{MnSi}) = E_{\mathrm{tot}}^{\mathrm{MnSi-bulk}} - E_{\mathrm{tot}}^{\mathrm{Mn-bulk}} - E_{\mathrm{tot}}^{\mathrm{Si-bulk}} \qquad . \tag{3.5}$$

where $E_{\mathrm{tot}}^{\mathrm{MnSi-bulk}}$, $E_{\mathrm{tot}}^{\mathrm{Mn-bulk}}$ and $E_{\mathrm{tot}}^{\mathrm{Si-bulk}}$ are the total energies of the bulk phases of MnSi, Mn and Si, respectively.

The first-principles calculations are performed using density-functional theory (DFT). For non-magnetic cases the exchange-correlation functional is treated with the local-density approximation (LDA) [55]. In the spinpolarized calculations, the generalized gradient approximation in the parameterization of Perdew, Burke, and Ernzerhof (GGA-PBE 96) [34] for the exchange-correlation potential, is used [2]. It has been demonstrated and confirmed by test calculations that GGA gives a much better description for bulk Mn than the local-spin-density approximation (LSDA). The Kohn-Sham equations were solved applying the full-potential augmented plane wave plus local orbital (FP-APW + lo) method [37].

This chapter presents ab initio total energy calculations of Si, Mn, MnSi. The effects of pressure on structure, bonding and electronic structures are also discussed.

---

[1] The total energy for a spin-polarized free atom is calculated. Due to the periodic boundary conditions the self-consistent calculations for the atom are performed using a large cubic supercell, so that interactions between the atoms are negligible.

[2] The convergence test are presented in Appendix A.

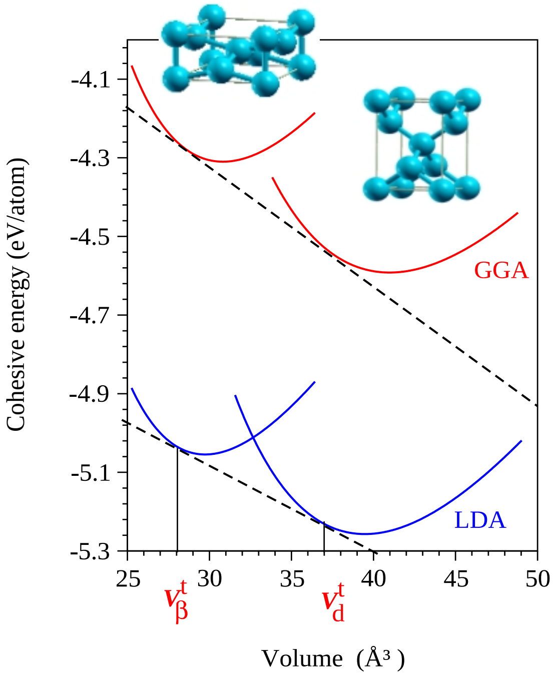

Fig. 3.1: Energy-volume curve for bulk diamond and $\beta$-tin Si using GGA (red line) and LDA (blue line) functionals. The dashed lines are the common tangents, the slope of the common tangents is the pressure for the phase transition from the diamond to the $\beta$-tin structure.

## 3.2 Bulk Silicon

### 3.2.1 Structural Properties and Thermodynamical Stability

Silicon with the atomic number 14 belongs to the group-IV elements in the periodic table. It has 4 unpaired electrons in the outer shell which leads to the formation of 4 bonds with neighboring atoms in the diamond structure of the Si-bulk phase. The conventional cell of Si-bulk is a fcc lattice type with two basis atoms at (0 , 0 , 0 ) and $(\frac{1}{4}, \frac{1}{4}, \frac{1}{4})$. The primitive lattice vectors are $\mathbf{a_1} = \frac{a}{2}\hat{\mathbf{i}} + \frac{a}{2}\hat{\mathbf{k}}$ , $\mathbf{a_2} = \frac{a}{2}\hat{\mathbf{i}} + \frac{a}{2}\hat{\mathbf{j}}$ and $\mathbf{a_3} = \frac{a}{2}\hat{\mathbf{j}} + \frac{a}{2}\hat{\mathbf{k}}$ , where $\hat{\mathbf{i}}$ , $\hat{\mathbf{j}}$ , $\hat{\mathbf{k}}$ are the unitary vectors along the $x$ , $y$ , $z$ directions, respectively. There is a structural phase transition from four-fold-coordinated diamond structure to a tetragonal six-fold-coordinated $\beta$-tin phase at pressure of 99 GPa [56]. The $\beta$-tin has a bcc lattice with atoms at (0, 0, 0) and $(\frac{1}{2}, 0, \frac{3}{4})$ positions.

To obtain the lattice parameter, a sequence of calculations are performed for bulk Si in both diamond and $\beta$-tin phases in nine separate calculations for volumes varying between -20 % and +20 % of the experimental volume. The volume corresponding to the minimum energy identifies the equilibrium lattice parameter, $a_0$. The cohesive energy versus volume curves calculated with GGA and LDA functional for both diamond and $\beta$-tin are shown in Fig. 3.1. The blue curves are LDA and the red curves are GGA results, the dashed lines are common-tangents, the slope of these lines indicate the phase transition pressure.

For the diamond structure, the LDA calculations show the well-known overbinding effect value with a cohesive energy overestimated by +11.4% and lattice parameter underestimated by -0.37 %, as compared to the experimental results.

In GGA, on the other hand, the equilibrium volume is overestimated by 0.74 % and the cohesive energy, $E_{\mathrm{coh}}$, is underestimated by -0.86 %. Here, we do not consider the zero point vibrations of lattice. Therefore, the calculated lattice constant in this work is smaller than that, including zero point vibrations. The order of magnitude of the zero point vibrations can be estimated from the uncertainty relation [57]. Taking into account the zero point vibrations increase the lattice constant up to 0.5%. Our results are compared to GGA-PW 91 functional [58] and experimental data in Tab. 3.1. The lattice parameter (a$_0$), bulk modulus ($B_0$), and derivative of bulk modulus, $B_0'$ calculated using LDA are in good agreement with the experimental results. The difference in the GGA-PBE 96 and GGA-PW 91 results are just a few percent.

The pressure of the phase transition is obtained via the Gibbs common tangents construction using the energy versus volume plot for the two phases, i.e.,

$$p_t = -\frac{E_t^d - E_t^\beta}{V_t^d - V_t^\beta} \qquad , \tag{3.6}$$

where $P_t$ is phase transition pressure, $E_t^d$ and $E_t^\beta$ are energy at the transition for diamond and $\beta$-tin structures, $V_t^d$ and $V_t^\beta$ are the transition volume for the mentioned structures.

In the prediction of the transition pressure, the LDA results are significantly lower than the experimental value, whereas the GGA increases the transition pressure, leading to a value that is close to the experimental value. The transition pressure is a sensitive quantity, since it depends not only on the energy but also on its first derivative with respect to the volume. The pressures calculated with both GGA PBE / PW functional are 4 % - 5 % smaller than the experimental value while this is 22 % smaller for LDA.

### 3.2.2 Electronic Properties

The diamond structure of silicon is found to be the ground state structure at zero pressure and temperature, therefore only the electronic properties of this structure

Table 3.1: Comparison of the calculated lattice constant ($a_0$), bulk modulus ($B_0$), pressure derivative of the bulk modulus ($B_0^{'}$), and cohesive energy ($E_{\mathrm{coh}}$) for Si diamond and $\beta$-tin structures using LDA, GGA-PBE and GGA-PW. The transition presure between the two phases, as well as their volumes $V_t^d$ and $V_t^\beta$ at the transition point are given . The experimental values are taken from Ref. [3] and [4] and for the GGA-PW values the results of Moll *et al* [5].

| | | LDA | GGA PBE | GGA PW | EXP. |
|---|---|---|---|---|---|
| **Diamond** | | | | | |
| | $a_0$(Å) | 5.41 | 5.47 | 5.59 | 5.43 |
| | $B_0$(GPa) | 94.9 | 87.8 | 85.2 | 98.8 |
| | $B_0'$ | 4.25 | 4.25 | 3.70 | 4.09 |
| | $E_{\mathrm{coh}}$(eV / atom) | 5.26 | 4.59 | 4.64 | 4.63 |
| **$\beta$-tin** | | | | | |
| | $a_0$(Å) | 4.73 | 4.78 | 4.82 | — |
| | $B_0$(GPa) | 115 | 106 | 106 | — |
| | $B_0'$ | 4.89 | 4.25 | 4.10 | — |
| | $E_{\mathrm{coh}}$(eV / atom) | 5.06 | 4.31 | — | 4.63 |
| | $c/a$ | 0.55 | 0.55 | 0.551 | 0.552 |
| | $V_t^d/V_0^d(exp.)$ | 0.926 | 0.937 | 0.928 | 0.918 |
| | $V_t^\beta/V_0^d(exp.)$ | 0.703 | 0.715 | 0.706 | 0.710 |
| | $p_t$ (GPa) | 70 | 95 | 106 | 99-101 |

will be discussed in the following. It can be seen from the band structure that silicon (in the diamond structure) is semiconductor. It has an indirect band gap of 1.17 eV [3].

The band gap calculated with DFT-LDA (GGA), which is determined by the energy difference between the top of highest occupied state (valence band) and bottom of lowest unoccupied state (conduction band), is almost half of the value of the experimental band gap. Having a value of 0.5 eV for the calculated band gap, agrees poorly with the experimentally observed band gap. The calculated band structure and density of states for both the LDA and GGA functionals at their equilibrium volume are shown in Fig. 3.2. The GGA and the LDA bandstructures are quite similar, but the conduction and the upper valence bands in LDA are shifted by 0.2 eV with respect to their GGA counterparts.

The electron density of states (DOS) is shown in Fig. 3.2. Three energy regions for the valence bands can be distinguished: the $s$ band's contribution is found in the range between -12 eV and -8 eV below the Fermi level; a hybridization of $s$ and $p$

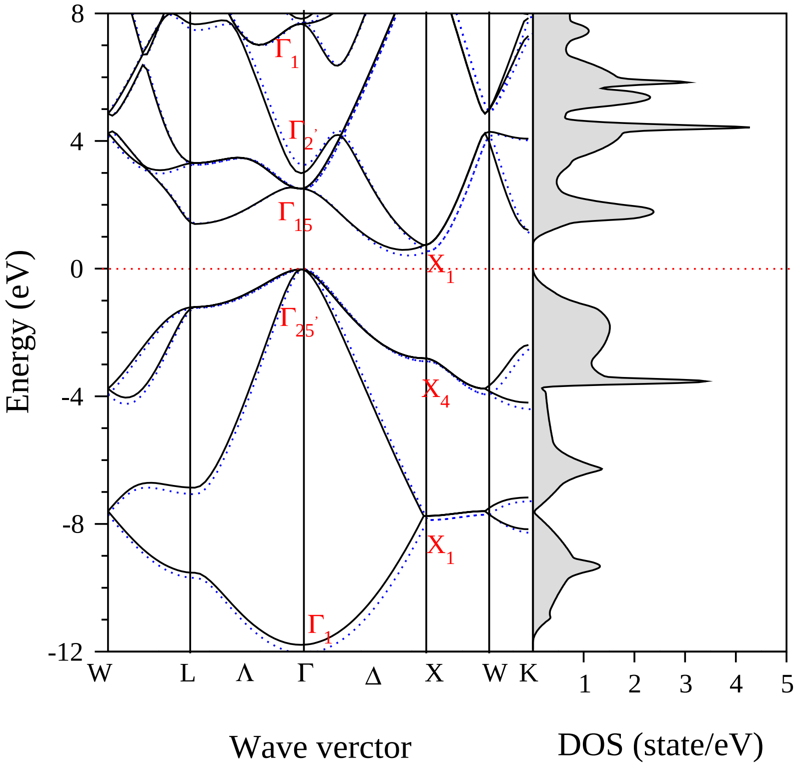

Fig. 3.2: Band structure and DOS plot for bulk Si at equilibrium volume with a $(10 \times 10 \times 10)$ **k**-point grid in the Brillouin-Zone using GGA (solid lines) and LDA (dash lines) functionals. The energy zero is taken to be the top of the valence band.

bands is found between -4 eV and -8 eV below the Fermi level; while $p$ bands are observed between zero to -4 eV below Fermi level.

It is known from photoemission experiments, that the top of the valence band is located at **k**=0, denoted $\Gamma_{25'}$ [61]. The minimum of the conduction band is found close to the $X$ point (**k**=$(2\pi/a)(\frac{1}{2},0,0)$) along the $\Delta$ symmetry line and has $p$-like character, cf. Fig. 3.2. The experimental optical gaps found at $\Gamma$ and $X$ points, respectively, are 3.4 eV and 4.4 eV, which is 1.0 eV and 0.9 eV higher than the values found in the present work. On the other hand, for deeper lying valence bands, the calculated band structure is in good agreement with the experiment, the relative error being less than 2 %. In Tab. 3.2.2 one can compare the eigenvalues of Kohn-Sham equations for Si bulk with photoemission measurement energy for some critical points in the Si-band structure. These value are calculated at theoretical lattice parameter. As one expects, the LDA results are closer to experimental observations.

Table 3.2: Electronic energies of Kohn-Sham equation for Si bulk.

| | $\Gamma_{1v}$ | $\Gamma_{25'v}$ | $\Gamma_{15c}$ | $\Gamma_{2'c}$ | $\Gamma_{1c}$ | $X_{4v}$ | $X_{1c}$ |
|---|---|---|---|---|---|---|---|
| LDA | -12.1 | 0.0 | 2.3 | 3.2 | 7.7 | -3.1 | 0.6 |
| GGA | -12.0 | -0.2 | 2.5 | 2.8 | 7.5 | -3.0 | 0.55 |
| EXP | -12.5 [a] | 0.0 [a] | 3.4 [a] | 4.15 [b] | 7.6 [b] | -2.9 [a] | 1.13 [a] |

(a) Ref. [59]
(b) Ref. [60]

## 3.3 Bulk Manganese

Manganese (Mn) is one of the interesting and complex case in the metallic elements. According to Hund's rule, the magnetic moment of the free atom is as large as 5 $\mu_B$ which is the highest magnetic moment among transition metal elements. The stable phase under normal temperature and pressure condition is $\alpha$-manganese (space group $\mathrm{T_d^3}$—$I\bar{4}3m$) [62], which has complex cubic structure with 29 atoms per unit cell and shows non-collinear magnetism.

The Mn atoms in the $\alpha$ phase have magnetic moments between 0 and more than 3 $\mu_B$ [63]. The $\alpha$-Mn phase undergoes a phase transition from antiferromagnetic (AFM) to non-magnetic (NM) at a Neél temperature of $T_N$ = 95 K. This magnetic transition is coupled to a tetragonal crystal structure for the non-magnetic phase.

In the temperature interval from 1000 K to 1368 K the $\beta$ phase will form. It has a cubic structure with twenty atoms per unit cell, the space group $P4_132$ [64] and a small magnetic moment [65, 66] . The fcc-$\gamma$ phase exists in the temperature region from 1368 K to 1406 K and has an antiferromagnetic low-spin ground state. For high temperatures up to the melting point (1517 K) the non-magnetic bcc-$\delta$ structure is found. Under compression a phase transition to the antiferromagnetic hexagonal $\epsilon$-structure [63] occurs.

### 3.3.1 Structural Properties

The calculations which are performed in this part are for fcc-$\gamma$ structures with different magnetic ordering (PM, FM, AFM). The AFM ordering is considered as planes in (100) direction containing parallel magnetic moments ($i.e.$ in-plane FM). Extensive convergence test showed that an energy cutoff of 16 Ry and $(15 \times 15 \times 15)$ **k**-points in the Brillouin zone are sufficient to describe this structure. In order to do calculation for AFM phase, a body-centered-tetragonal structure with lattice parameters, $a = b = \sqrt{2}\,c$ and $c = a_{fcc}$ is considered.

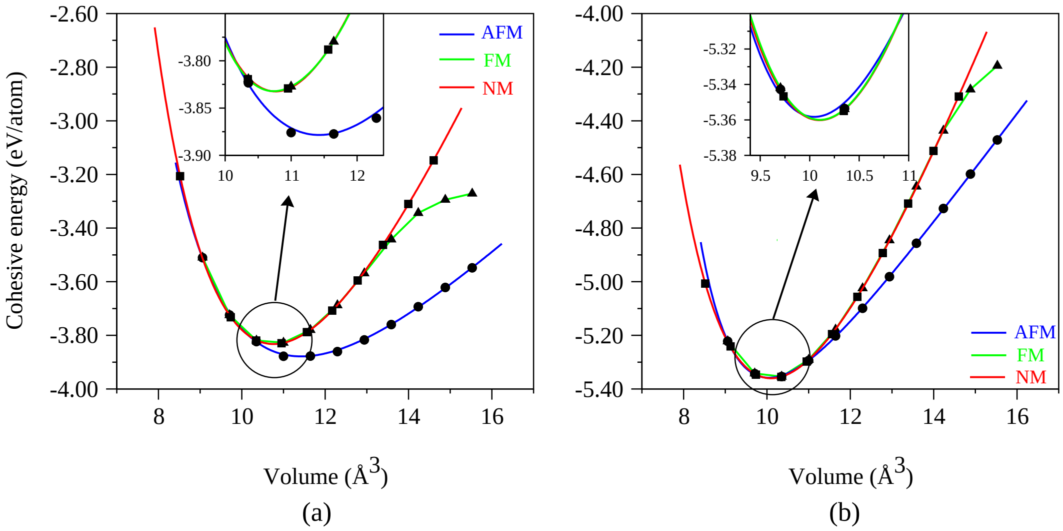

Fig. 3.3: The plot of total energy per atom versus unit cell volume, (E-V), with GGA (a) and LSDA (b). the circles, squares and triangle were used for antiferromagnetic, ferromagnetic and non-magnetic, respectively. The AFM ordering has lowest energy at equilibrium volume in GGA. The magnetovolume effect is not significant with LSDA. Magnetic and non-magnetic calculation have nearly the same E-V curve

In Fig. 3.3 the total energy is given as a function of volume for both GGA and LSDA functionals. The antiferromagnetic fcc-$\gamma$ phase structure is energetically the ground state for GGA calculations. The lattice constant is 4% smaller than the $\alpha$-Mn and the cohesive energy is lower than non-magnetic state by at least 50 meV. In the LSDA all calculations converge to a non-magnetic ground state at a volume interval in ±10 % around equilibrium volume. GGA, on the other hand, predicts an increased equilibrium volume. This means a smaller deviation of the theoretical lattice parameter from the experimental result in GGA, compared to LSDA. In addition, LSDA increases the magnetovolume effect: an antiferromagnetic solution exists for expanded volume which is about 11 Å$^3$ while the AFM order found at volume around at 10 Å$^3$, for GGA.

The results for the cohesive energy, lattice constant and bulk modulus for the non-magnetic, ferromagnetic and antiferromagnetic ordering are summarized in Table 3.3 for GGA, LSDA and the experimental results. Some prominent details in this comparison that should be emphasized are:

(I) Use of different exchange-correlation functionals has a stronger influence on the total energy and equilibrium volume, than the magnetovolume effect.

(II) The difference between LSDA and GGA results for the magnetic cases are more

Table 3.3: Comparison of the cohesive energy $E_{\text{coh}}$, the lattice parameter $a_0$ and the bulk modulus $B_0$ of different magnetic ordering of manganese in fcc-$\gamma$ structure.

| fcc-$\gamma$ structure | Magnetic Phase | $E_{\text{coh}}$ (eV / atom) | $a_0$ (Å / atom) | $B_0$ (Mbar) |
|---|---|---|---|---|
| | AFM | 3.87 | 3.59 | 1.35 |
| Present work (GGA) | FM | 3.82 | 3.47 | 2.76 |
| | NM | 3.83 | 3.50 | 2.72 |
| | AFM | 5.36 | 3.42 | 3.07 |
| Present work (LSDA) | FM | 5.38 | 3.42 | 4.19 |
| | NM | 5.36 | 3.43 | 3.25 |
| US-PP (GGA)$^{(a)}$ | AFM | — | 3.65 | 0.95 |
| US-PP (LSDA) | NM | — | 3.43 | 3.10 |
| LMTO (GGA)$^{(b)}$ | — | — | 3.61 | 2.81 |
| LMTO (LSDA) | — | — | 3.49 | 3.14 |
| EXP. | AFM | 2.92$^{(c)}$ | 3.73 | 1.31 |

(a) Ref. [67]
(b) Ref. [68]
(c) Ref. [69], value was obtained by extrapolation of high-temperature data to room temperature.

pronounced than for the non-magnetic phases.

(III) The lattice parameter for both GGA and LSDA is smaller than experimental value, but the discrepancy between theory and experiment is reduced in GGA.

(IV) The compressibility [3], which is the reciprocal of the bulk modulus, is overestimated in LSDA. This leads to a shorter bondlength and stronger bonding compared to GGA. Therefore the cohesive energy in LSDA is also larger than in GGA.

Table 3.3 shows that the full-potential LSDA calculations are in good agreement with ultrasoft-pseudopotential (US-PP) [67] and linear-muffin-tin-orbital (LMTO) [68] calculations. All methods using GGA calculations show a thermodynamically stable AFM phase for bulk Mn.

---

[3] The compressibility is defined as the inverse of bulk modulus: $\kappa = \frac{1}{B_0}$.

### 3.3.2 Magnetic Properties

The dependence of the FM and AFM states on the volume are shown in Fig. 3.4. A high-spin state at the expanded volume is found for each of these magnetic phases and the magnetic moment is underestimated in both calculations. In the GGA calculations, the magnetic moment for the AFM state at equilibrium volume is as large as 1.9 $\mu_B$ but its value is quenched to almost zero for the FM state. The LSDA predicts the non-magnetic states as the ground state at the equilibrium volume. All in all, LSDA poorly describes the magnetization at the equilibrium volume and fails to give the experimental magnetic moment of the fcc-$\gamma$ structure, which is about 2.3 $\mu_B$ .

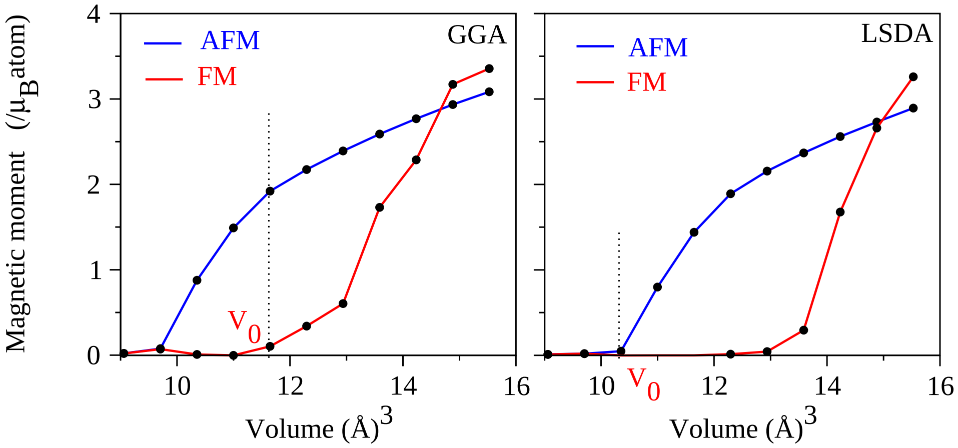

Fig. 3.4: Magnetic moment in ferromagnetic (red lines) and antiferromagnetic (blue lines) states from GGA (a) and LSDA (b) calculations.

## 3.4 Manganese-Silicide Compounds

Studies of Mn covered Si substrates show that Mn has the tendency to form manganese-silicide alloys on the surface [15, 16]. Our studies of the growth process of manganese on Si show that the strong covalent bond between Mn and Si lead to the formation of islands or films of Mn-Si on the Si surfaces. This makes it essential to first study the properties of some Mn-Si compounds, before turning to the films. In this chapter, the structural, magnetic and electronic properties of MnSi which could form on Si are studied (The bulk properties of $Mn_3Si$ will be discussed in Appendix B).

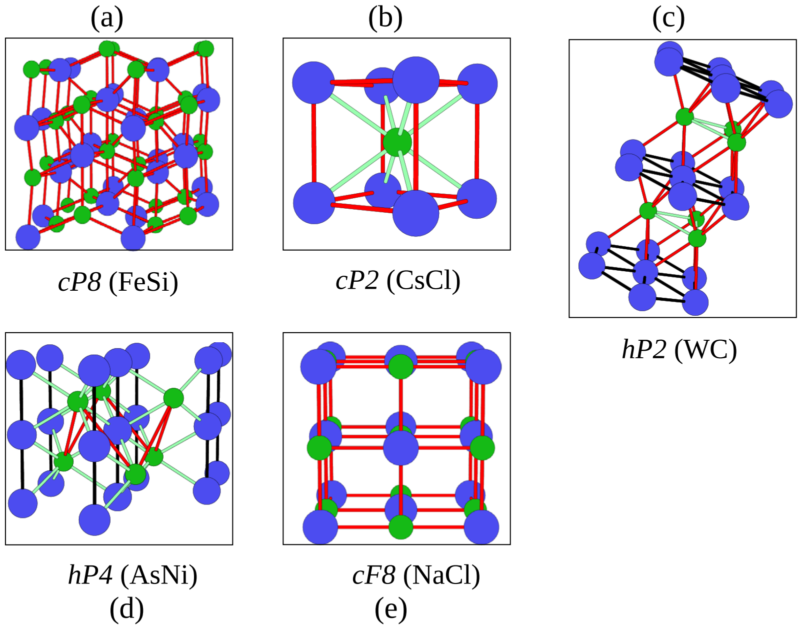

*cP8* (FeSi)
*cP2* (CsCl)
*hP2* (WC)
*hP4* (AsNi)
*cF8* (NaCl)

Fig. 3.5: Possible epitaxial structures of 1:1 stoichiometry of MnSi. The natural phase has FeSi structure (a) which is called B20 structure. The B2 struture (b), is the second lowest structure. The tungsten carbid, nickel arsenic and rocksalt structure are other possible epitaxial structures.

### 3.4.1 Bulk MnSi

Manganese mono-silicide is a magnetic intermetallic compound with B20 structure that is isostructural to non-magnetic transition metal silicides like FeSi, CoSi and CrSi. It contains four Mn and four Si atoms in a simple cubic structure with Pearson symbol $cP8$ and a lattice parameter of $a_0 = 4.558$ Å [70]. Mattheiss *et al.* [71] described the B20 structure as a rocksalt structure containing four MnSi in the unit cell where the atoms are displaced along the [111] direction. This distortion eliminates the inversion symmetry and changes the space group from $Fm3m$ to $P2_13$ [71]. The position of four Mn or Si in the unit cell are $(u, u, u)$, $(\frac{1}{2} + u, \frac{1}{2} - u, -u)$, $(-u, \frac{1}{2} + u, \frac{1}{2} - u)$ and $(\frac{1}{2} - u, -u, \frac{1}{2} + u)$ where $u_{Mn} = 0.137$ and $u_{Si} = 0.845$ [72]. Mn is coordinated to one Si at 2.11 Å along [111] direction, three Si neighbors at a distance of 2.35 Å and three neighbors at 2.69 Å. In the absence of a magnetic field and below $T_c = 29$ K, it has a helical magnetic structure with a long spiral period of 180 Å [72]. The lack of inversion symmetry is the reason of the spiral magnetic structure in the B20 crystal structure [73]. At the temperature of zero K, there is a spontaneous magnetic moment of 0.4 $\mu_B$ per Mn atom which forms a conical order phase in the magnetic field of 0.1 T [74]. The spins align as a ferromagnetic structure at 0.6 T external magnetic field [72]. The temperature increases spin fluctuation of Mn, which is called thermal excitations of spin fluctuations (SFs). This induces a large magnetic moment of 2.2 $\mu_{\mathrm{B}}$ [73]. The Curie temperature drops with pressure until the magnetic ordering disappears at the pressure of 1.46 GPa [75].

The growth of some mono-silicide compounds on Si substrates introduces new crystal structures which do not exist in bulk form [76]. They are formed by epitaxy and cannot be reached by external changes in pressure or temperature of bulk phase. The epitaxial stabilization of CsCl-structure of FeSi and CoSi was first observed in Si(111) surface [76].

In the following, the energy-volume curves of the epitaxial structures are compared which might conceivably form on the Si surface. In particular, the CsCl, WC, AsNi and NaCl crystal structures, Fig. 3.5, are considered which are the starting point of the forthcoming surface calculations. The optimized volume and other primitive structural properties are determined using both GGA and LSDA functionals, an energy cutoff $E_{\mathrm{cut}}$ =13.8 Ry and 12×12×12 **k**-points in the Brillouin zone.

- **Structural, Electronic and Magnetic Properties**

To assess the stability of various phases of manganese mono-silicide compound, the energy vs. volume curves are calculated for each structure. The curves for each structure, fitted using the Murnaghan equation, are shown in Fig. 3.6. These curves show that the stable phase is the simple cubic lattice with 4 Mn and 4 Si which corresponds to the previously mentioned B20 (or $P2_13$) structure. The calculated lattice parameter is 0.9 % smaller than the experimental value and the calculated Mn-Si bond lengths are 2.28 Å , 2.37 Å and 2.52 Å. The structural properties for all calculated phases are collected in Tab. 3.4. A FM ordering with a magnetic moment of more than 1.0 $\mu_{\mathrm{B}}$ per atom is predicted for the $P2_13$ structure, which is larger than the experimental value. However, this is comparable to previous calculations done by Jeong *et al.* using the full-potential nonorthogonal local orbital (FP-LO) method [77].

The density of states of MnSi in Fig. 3.8-a shows metallic behavior for both spin channels. For the majority spin channel there is a narrow gap of about 0.2 eV above the Fermi level. An indirect narrow gap was also reported by Nakanishi *et al* [78] for the iso-structure alloy FeSi. Due to four more valence electrons per unit cell in this latter structure, its Fermi level lies in the gap, i.e. it is a normal semiconductor.

The CsCl or B2 structure appears in the regimes of high pressure. The calculations with GGA (LDA) show a phase transition from B20 structure to B2 structure at the pressure of 45 (22) GPa. This pressure is larger than the quantum critical pressure where the magnetism vanishes. Therefore it is not surprising to find the cubic B2

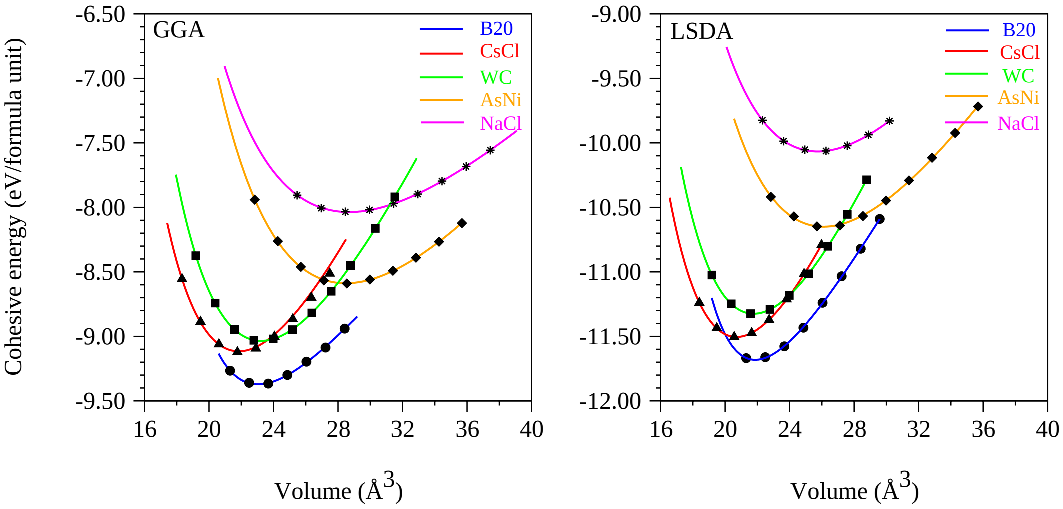

Fig. 3.6: Energy-volume curves for different epitaxy structures of MnSi are shown in the plot above. The FeSi (blue line), the CsCl (red line) and the NiAs (brown line) structures are stable in equilibrium, compressed and expanded volume, respectively. The WC (green line) and NaCl (purple line) structures are unstable.

structure with a non-magnetic phase. This structure undergoes to ferromagnetic order in a tetragonal cell. The ferromagentic structure is found upon a small distortion of the lattice, leading to an elongation of 5 % in the **c** direction. The calculated magnetic moment is about 0.7 $\mu_{\rm B}$ in this tetragonal structure, the exchange splitting due to magnetization is 0.35 eV and the spinpolarization at the Fermi level is around 37 % [4]. The density of states for cubic and tetragonal structure are compared in Fig. 3.7. A difference of 0.25 eV between the cohesive energy of the B2 and the B20 structures is found, which is smaller than similar results for FeSi (0.54 eV) and CoSi (0.75 eV) [76].

The WC structure is not stable structure according to the energy-volume plot, c.f. Fig. 3.6. The lattice parameters in **a** and **b** directions are just 0.15 % shorter than in the B20 structure but an elongation of almost 20 % in the **c** direction is found. The space group of the tungsten carbide structure is $P6$m2; it is an *hcp* structure (i.e. *ABAB*... stacking) with Mn at (0, 0, 0) and Si ($\frac{2}{3}$, $\frac{1}{3}$, $\frac{1}{2}$), c.f. Fig. 3.5. The magnetic moment is 1.5 $\mu_B$ and the polarization at the Fermi level is about 13 %.

The AsNi structure is a metastable structure which exists in the expanded volume of 35 % compared to the equilibrium volume of the $P2_13$ structure. It has the space group $P6_3mmc$ and hexagonal structure with four basis atoms at (0,0,0) and (0, 0, $\frac{1}{2}$) for Mn and ($\frac{1}{3}$, $\frac{2}{3}$, $\frac{1}{4}$) and ($\frac{2}{3}$, $\frac{1}{3}$, $\frac{3}{4}$) for Si. The stacking is *ABACABAC*... with Mn in *A* site and Si in *B* and *C* sites. The environment of Mn atom is *fcc*-like and environment of Si atom is *hcp*-like. The cohesive energy is 0.4 eV / atom less than cohesive

---

[4] spin polarization at Fermi level is defined as : $(n_f^{\uparrow} - n_f^{\downarrow})/(n_f^{\uparrow} + n_f^{\downarrow})$.

Table 3.4: Lattice parameter ($a_0$), formation enthalpy ($\Delta H$), bulk modulus ($B_0$) and magnetic moment ($m$) for all epitaxial structures as calculated with both GGA and LDA functionals.

| | structure | $a_0$<br>Å | $\Delta H$<br>eV / formula unit | $B_0$<br>Mbar | $m$<br>$\mu_B$ / atom |
|---|---|---|---|---|---|
| | MnSi | 4.517 | 0.879 | 2.00 | 0.26 |
| | CsCl | 4.437 | 0.623 | 2.23 | 0.0 |
| (GGA) | WC | 4.524 | 0.542 | 1.19 | 1.5 |
| | AsNi | 4.483 | 0.077 | 2.06 | 1.5 |
| | NaCl | 4.859 | -0.457 | 0.92 | 0.0 |
| | MnSi | 4.439 | 6.522 | 2.94 | 0.26 |
| | CsCl | 4.359 | 6.345 | 2.61 | 0.0 |
| (LSDA) | WC | 4.410 | 5.500 | 1.46 | 1.7 |
| | AsNi | 4.197 | 6.165 | 2.44 | 1.6 |
| | NaCl | 4.687 | -4.907 | 1.30 | 0.0 |
| EXP$^*$. | MnSi | 4.558 | | | 0.4 |

($*$) Ref. [78]

energy of B20 structure and the manganese atoms have AFM spin alignment with a magnetic moment of 1.5 $\mu_B$. The magnetic moment in this structure and the WC crystal structure can be attributed to a distortion of cubic cell to tetragonal cell.

The NaCl structure is considered as an undistorted variant of the B20 structure [79]. This non magnetic structure is energetically unstable with a cohesive energy of almost 1.4 eV per formula unit higher than in the B20 structure. This structure has the largest equilibrium volume and compressibility of all considered structures.

Due to the deviation of the atomic positions from the structure with $O_h$ symmetry, the B20 structure has magnetic order with a considerable magnetic moment.

In the following calculations, due to the second highest stability (after the natural B20 phase) of the B2 structure, the magnetic properties of the B2 structure will be compared with the B20 structure.

- **Curie Temperature**

A good magnetic material, in addition to a high magnetization, should have a high Curie temperature. In order to estimate the Curie temperature of the B2 structure, two simplest models are considered:

(i) Mohn-Wohlfarth approach:

This model is based on band theories of magnetism (the Stoner model). The features of this model are that it has a good description for the itinerant electrons, involves spin fluctuation and introduces an exchange energy which is proportional to the magnetization [80,81]. The constant of proportionality is the so-called Stoner parameter [5].
(ii) Heisenberg approach: This model usually is used for the systems with well-localized electrons.

**Mohn-Wohlfarth approach:** The MnSi is considered to be in the group of *weak itinerant-electron ferromagnetism* because of [83]:

I) a low saturation magnetic moment at the temperature of zero K (0.4 $\mu_\mathrm{B}$ / Mn) [74].

II) a low magnetic order-disorder phase transition temperature ($T_C \sim$ 29K) [72].

Since MnSi is an itinerant ferromagnet, the existence of magnetism could be evaluated by the *Stoner criterion* [84] which states:

$$I \cdot N(\epsilon_F) > 1 \qquad , \tag{3.7}$$

where $I$ is the Stoner parameter and $N(\epsilon_F)$ is the density of states at the Fermi level in the non-magnetic phase.

The Stoner parameter is obtained from the following definition:

$$\Delta_{ex} = Im \qquad , \tag{3.8}$$

where $\Delta_{ex}$, the exchange splitting, is the band splitting between spin up and spin down channel due to magnetization. The exchange splitting is calculated directly from the total DOS of the B20 structure. $m$ is the total magnetic moment per atom. The calculated $\Delta_{ex}$ = 0.55 eV and $m$ = 1.0 $\mu_\mathrm{B}$ yield a Stoner parameter of $I$ = 0.5 eV / $\mu_\mathrm{B}$.

From the Stoner model, the magnetic phase appears when the gain in the exchange energy is larger than the loss in kinetic energy. Additionally, this model allows us to understand the structural dependence of the magnetic moment in the structures. This dependency is explained by comparing the DOS of the B2 and the B20 structures (Fig. 3.7 and 3.8) :
The non-magnetic B20 DOS has several peaks which belong to itinerant electrons. The Fermi level in MnSi DOS lies on one of the peaks which results in a higher density of states than for the cubic B2 structure. On the other hand in the cubic B2 DOS

---

[5] The Stoner parameter is an intra-atomic quantity that does not depend on the crystal environment and structure [82].

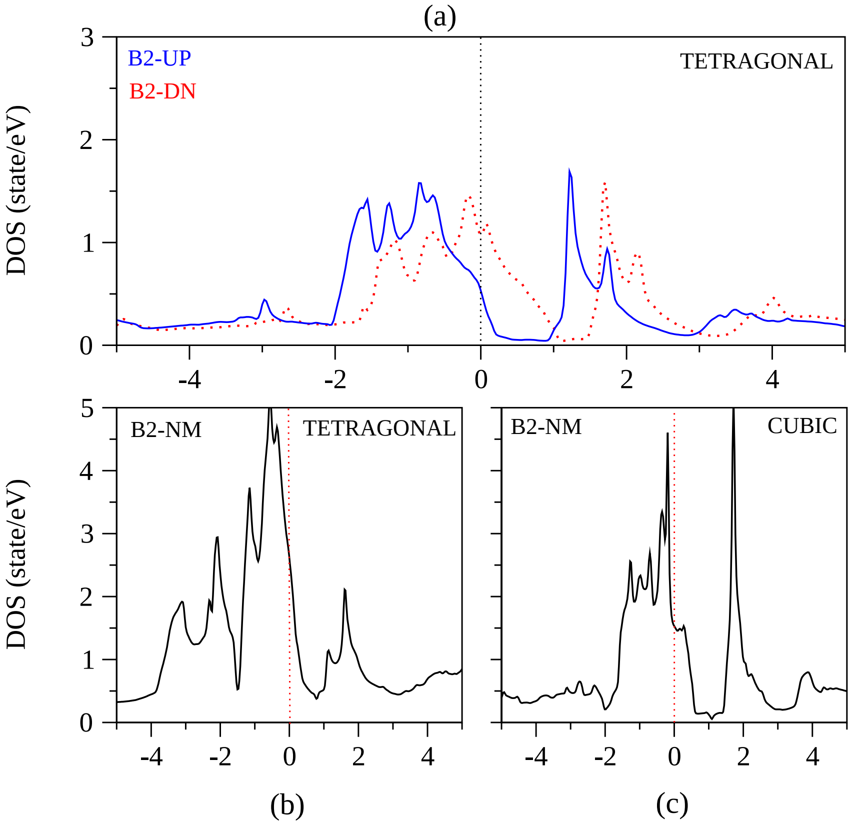

Fig. 3.7: Density of states ($N$) for MnSi in the B2 structure using a ($12 \times 12 \times 12$) **k**-point grid in the Brillouin-Zone. The filled blue (red dash) line is the DOS for the B2 in the majority (minority) spin channel (a). The black line is the DOS of the non-magnetic phase for both spin channels (b, c). The Fermi level is taken as the energy zero.

the Fermi level is in the shoulder of the peak, c.f. Fig. 3.8. In the DOS of the cubic B2 structure, there are several occupied peaks for the $t_{2g}$ band and one peak which has $e_g$ character. The Fermi level is in the shoulder of the lower peak which results in a low density of states at the Fermi level ($\sim$ 1.5 state / eV), see Fig. 3.7-c. As the Stoner parameter is the same for both structures [82], the Stoner criterion is fulfilled for B20 but not for the cubic B2 structure. These results are in agreement with the thermodynamical stability of the non-magnetic phase of the B2 cubic structure and the magnetic ground state order of the B20 structure. However, with distortion of the B2 structure in **c** direction (at constant volume), one can get a magnetic structure [85]. In the present work with the lattice distortion of 5 % in **c** direction, we get a magnetic moment of 0.7 $\mu_B$ / Mn atom. The density of states for cubic and tetragonal structure in non-magnetic and magnetic order are shown in Fig. 3.7-b, c. The density of states at the Fermi level in the non-magnetic cubic B2 structure is about 1.5 state / eV but rises up to 2.6 state / eV in the tetragonal structure, c.f. Fig. 3.7-b, c and leads to satisfy the Stoner criterion.

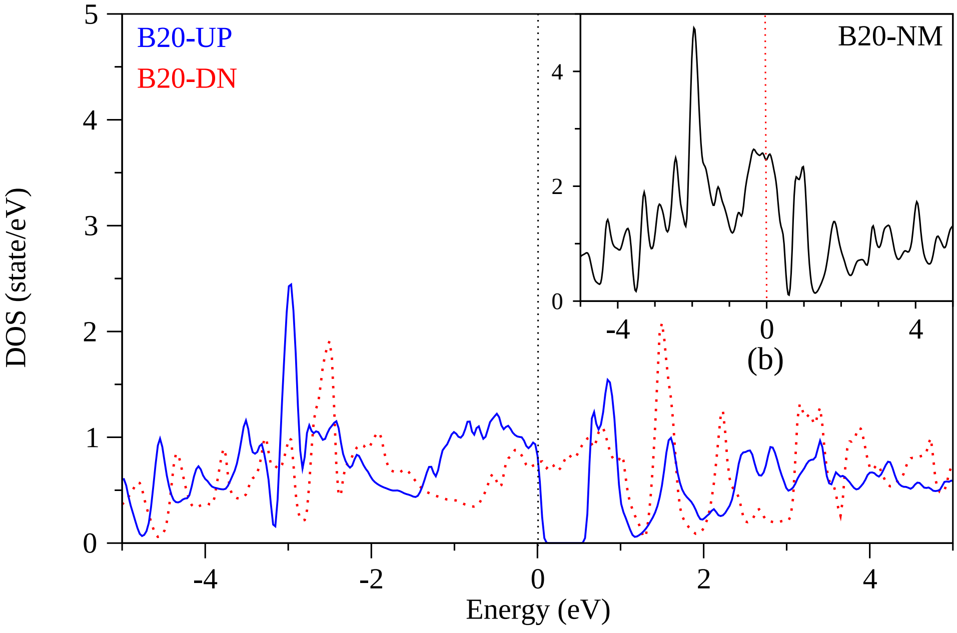

(a)

Fig. 3.8: Density of states ($N$) for MnSi in the B20 structure using a $(12 \times 12 \times 12)$ **k**-point in the Brillouin-Zone. The blue filled (red dash )line is the DOS of the majority (minority) spin channel (a). The black line is the DOS of the B20 structure in the non-magnetic phase for both spin channels (b). The Fermi level is referred to the energy zero level.

The simplest approach to estimate the Curie temperature of itinerant magnets is to consider Stoner excitations. The Stoner excitations lead to a reduced magnetic moment with raising the temperature, which finally vanishes at $T = T_C$ . The Curie temperature from the Stoner model, $T_S$, is defined as [81] :

$$I(\epsilon_F) \int_{-\infty}^{\infty} \frac{\partial f(\epsilon, T)}{\partial \epsilon}\, n_{\mathrm{nm}}(\epsilon)\, d\epsilon + 1 = 0 \qquad . \tag{3.9}$$

where $n_{\mathrm{nm}}(\epsilon) = 1/2\ N_{nm}(\epsilon)$ is the density of states per atom and spin in the non-magnetic state, and $f(\epsilon, T)$ is the Fermi distribution function which is a function of temperature. The solution of above equation gives the Stoner temperature ($T_S$).

However, the Stoner model yields a Curie temperature that is too high. There is the semiempirical approach developed by Mohn and Wohlfarth [80] which calculates the Curie temperature of a very weak itinerant ferromagnet involving spin fluctuations [86] . In this approach, long-wavelength spin fluctuations are made responsible for the Curie temperature.

Table 3.5: Density of states per Mn at the Fermi level for both spin channels (n$_\uparrow(\epsilon_F)$, n$_\downarrow(\epsilon_F)$), total density of states at the Fermi level for the non-magnetic case (n$_{\mathrm{nm}}(\epsilon_f)$), the exchange splitting ($\Delta_{ex}$), the magnetic moment $m$, the Stoner parameter ($I$), the Pauli susceptibility ($\chi$) and the Curie temperature ($T_C$) calculated by Mohn-Wohlfarth theory.

| | $n_\uparrow(\epsilon_F)$ | $n_\downarrow(\epsilon_F)$ | $N_{\mathrm{nm}}(\epsilon_F)$ | $\Delta_{ex}$ (eV) | $m$ ($\mu_{\mathrm{B}}$) | $I$ (eV / $\mu_{\mathrm{B}}$) | $\chi$ | $T_C^{SF}$ (K) |
|---|---|---|---|---|---|---|---|---|
| B20 | 0.5 | 0.6 | 2.5 | 0.52 | 1.0 | 0.5 | 1.6 | 609 |
| B2 | 0.6 | 1.2 | 2.6 | 0.35 | 0.7 | 0.5 | 2.7 | 225 |

This theory contains three parameters: saturation magnetization, Pauli susceptibility and Stoner parameter. Despite its theoretical shortcomings, this approach has been widely used to evaluate experimental data on intermetallic materials.

In the Mohn-Wohlfarth theory the mentioned parameters are related in this formula

$$\frac{T_C^2}{T_S^2}+\frac{T_C}{T_{SF}}=1 \qquad , \tag{3.10}$$

where $T_S$ is the Stoner-model Curie temperature, and the spin-fluctuation temperature $T_{SF}$ is given by:

$$T_{SF}=\frac{m^2}{20k_B\chi_0} \qquad , \tag{3.11}$$

where $\chi_0$ is the spin susceptibility at equilibrium and $m$ is the averaged magnetic moment per Mn (in units of $\mu_{\mathrm{B}}$).

$$\chi_0^{-1}=(1/2\mu_B^2)(\frac{1}{2n_\uparrow(\epsilon_F)}+\frac{1}{2n_\downarrow(\epsilon_F)}-I) \qquad . \tag{3.12}$$

Here $n_\uparrow(\epsilon_F)$ and $n_\downarrow(\epsilon_F)$ are the zero-temperature densities of states per atom at the Fermi level of the spin up and down bands, and $I$ is the Stoner parameter. Often the Stoner temperature, $T_S$ is much higher than the spin fluctuation temperature $T_{SF}$; therefore, the Curie temperature is estimated just by $T_{SF}$ ($T_C \sim T_{SF}$) .

The density of states at the Fermi level, the exchange splitting energy, the Stoner parameter, the Pauli susceptibility and finally the Curie temperature for both B2 and B20 structures are summarized in Tab. 3.5. As one sees, this approach still yields a very high Curie temperature for both structures.

**Heisenberg approach:** In this approach, the Curie temperature is calculated from the total energy difference of the ferromagnetic and the antiferromagnetic state in the nearest-neighbor Heisenberg model [87]. Here, one starts with the Heisenberg Hamiltonian

$$H = -J \sum_i \sum_j \mathbf{S}_i \mathbf{S}_j \qquad . \tag{3.13}$$

which describes the isotropic exchange interaction, $J$, between the spins located on a three-dimensional lattice. It is assumed that the exchange interaction between nearest-neighbor atoms is the dominant one, thus the summation runs over all nearest-neighbor sites.

The Curie temperature of the Heisenberg ferromagnet in the mean-field approximation is described in Ref. [88]:

$$T_C^{MF} = 2J \frac{\gamma}{3K_B} = 2 \frac{E_{\mathrm{AFM}} - E_{\mathrm{FM}}}{3k_B} \qquad . \tag{3.14}$$

Table 3.6: Energy difference in DFT-GGA between FM and AFM order per formula unit and calculated Curie temperature for B20 and B2 structures.

| | $E_{\mathrm{AFM}} - E_{\mathrm{FM}}$ (meV) | $T_C$ (K) |
|---|---|---|
| B20 | 11 | 85 |
| B2 | 11 | 85 |

The factor $\gamma$ is given by $S(S+1)/S^2$ for quantum spins and it equals to 1 for classical spins, $E_{\mathrm{AFM}}$ and $E_{\mathrm{FM}}$ are the energy of antiferromagnetic and ferromagnetic structures. Choosing the empirical value of $\gamma = 1$ leads to a good agreement with the experiment [88].

The energy of ferromagnetic and antiferromagnetic order and the calculated Curie temperature in the Heisenberg model are summarized in Tab 3.6. The Heisenberg model predicts the Curie temperature more realistic than the Stoner model, and shows low Curie temperature (below room temperature) for bulk structures of Mn-mono-silicide.

# Chapter 4

# Bare Si Surfaces

## 4.1 Introduction

Surfaces and interfaces of semiconductors play an important role in technological device applications. Their physical and chemical characteristics are responsible for the interesting properties and making them an active area in semiconductor research.

This chapter focuses on the low index (001) and (111) surfaces of silicon. The surface structure, surface free energy and the electronic properties of the clean surfaces are discussed.

Silicon with diamond structure is characterized by four strongly covalent bonds. Each bond holds two spin-paired electrons. The surface can be prepared by cutting the crystal in a certain orientation. During the surface creation, at least one bond per atom will be cut upon cleavage, which is called ”dangling bond”. The unsaturated dangling bonds make the surface unstable and are responsible for an increase in the surface free energy. A reduction in the number of dangling bonds minimizes this energy and is the driving force behind the surface relaxation and reconstruction. With the atomic displacement in surface relaxation and reconstruction this energy can be minimized. The atoms seek to find new positions which reduce the number of the dangling bonds.

Upon *relaxation* the atoms at the surface are displaced from their bulk positions, but there is no change in the surface periodicity or symmetry. The *reconstruction* of a surface, on the other hand, involves a change in the surface unit cell, compared to an ideal or bulktruncated surface, thereby leading to a change in the periodicity and symmetry at the surface.

There are two basic principles which can explain the surface reconstruction and relaxation. Duke [89] has presented them in detail for the tetrahedrally coordinated compound semiconductors:

*Principle 1: Reconstructions tend either to saturate surface dangling bonds via rehybridization or to convert them into non-bonding electronic states.*
Surface reconstructions minimize the number of the dangling bonds by the formation of new bonds between neighboring surface atoms via hybridization. This leads to a fully occupied or unoccupied energy state which in Si(001) transforms the metallic character of the unreconstructed surface to a semiconductor one.
*Principle 2. In many cases surfaces can reduce their energy by both atomic reconstruction and relaxation.*
For example in Si(001), the atom relaxed toward the bulk (with conserving the surface symmetry) donates the electronic charge in its dangling bond to couple with the dangling bond of a neighboring atom, which has relaxed away from the bulk. The atomic relaxation will not change the symmetry of the surface .

Different surfaces of a crystal have different surface free energies, depending on their orientations. The most stable surface is the one, which exhibits the lowest surface free energy. The surface free energy at zero temperature is given by:

$$\gamma^{\mathrm{SUR}} = \frac{E^{\mathrm{slab}} - \sum_i N_i \times \mu_i}{2 \times A} \tag{4.1}$$

where $E^{slab}$ is the total energy of a slab calculation with two identical surfaces, $\mu_i$ is the chemical potential of the surface constitute components, $N_i$ is the number of the $i$th kind of atoms per unit cell and $A$ is the unit cell area. There are two surfaces in the slab model therefore, the factore $\frac{1}{2}$ is applied.

## 4.2 Si(001) Plane

The Si(001) surface has received particular attention for two reasons. Firstly, most silicon devices are grown on this substrate and secondly, because it has the most simple reconstruction, compared to other silicon surfaces. The characteristic feature of this surface are the Si-dimers, which have been studied with a large variety of experimental and theoretical methods.

In 1959, Schlier and Farnsworth [90] used low energy electron diffraction (LEED) technique and were the first to observe a (2×1) periodicity (cf. Fig. 4.1-b) on the this surface. In such a periodicity, surface atoms come together to form dimers,

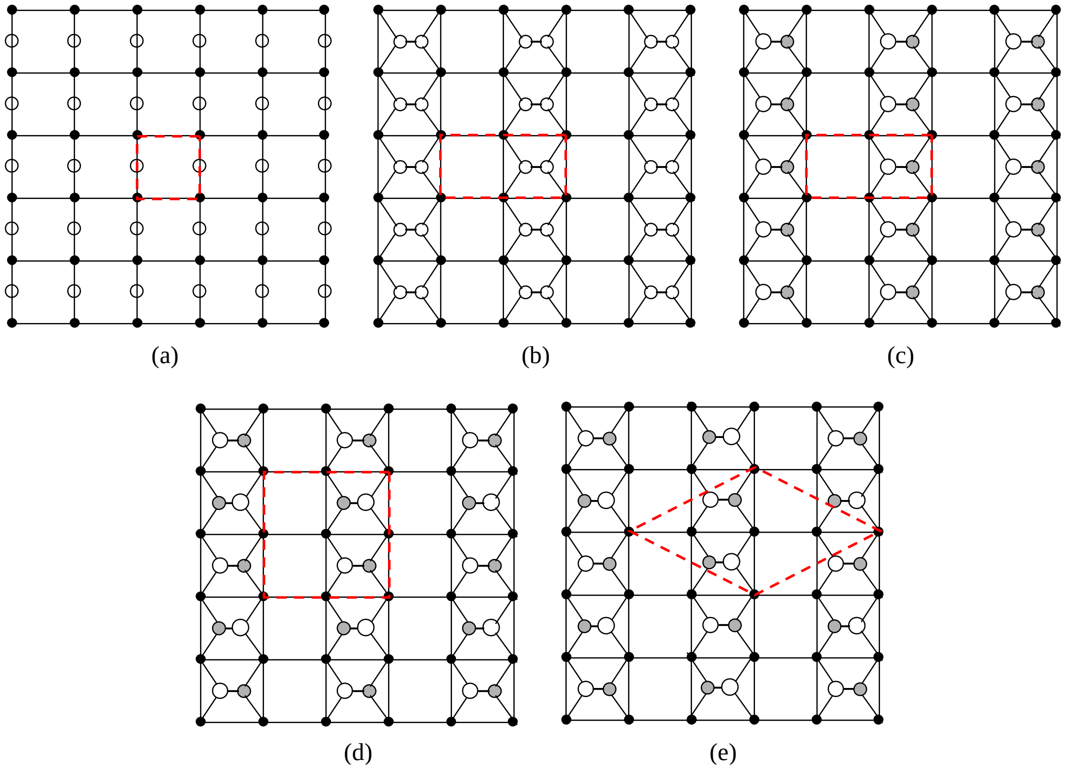

(a) (b) (c)

(d) (e)

Fig. 4.1: Top view of different unit cells at the (001) surface for which we have calculated the surface energy. White circles show atoms in the surface layer and black circles represent atoms in the second layer but big white and small gray circles are used to show upward and downward buckled dimer atoms on the surface, respectively. The non-reconstructed surface (a), the $(2 \times 1)$ symmetric dimer reconstruction (b), the $p(2\times1)$ buckled dimer reconstruction (c), the $p(2\times2)$ alternating buckled dimer reconstruction (d), the $c(4 \times 2)$ reconstruction (e).

thereby reducing the surface energy. The formation of dimers halves the density of dangling bonds compared to a bulk terminated surface. Dimerization, as a basic reconstruction, was observed also in photoemission experiments [91], optical observations [92], core-level spectroscopy [93] and scanning tunneling microscopy (STM) [94]. One of the first calculations on dimerized surface was performed by Appelbaum and Hamann in 1974 [95]. They showed that the dimer length are slightly shorter than the distance of atoms in the silicon bulk and that the subsurface distortion due to surface dimerization extends up to 4-5 layers into the bulk [95]. This model predicted a metallic band structure, contrary to experimental observations. The reason for this discrepancy is that in a symmetric dimer model, one dangling (or unsaturated) bond per surface atom remains, leading to a metallic surface.

The symmetric dimer in Si(001) is energetically unstable, therefore Chadi proposed that the buckled dimer surface is the most stable surface of Si(001) [96]. Support for the dimer buckling came from ion scattering measurements [97, 98] and STM [94], which confirmed Chadi's prediction. Apart from an energy gain, the buckling of the surface dimer is accompanied with the formation of a semiconducting electronic band structure [96]. The charge transfer between the dangling bonds causes one dangling bond per dimer to become completely filled while the other one is empty. This opens the gap in the band structure of the $(2 \times 1)$ asymmetric model. The bonding geometry of the Si atom relaxed towards the bulk becomes more planar. Therefore, its orbital hybridization changes from $sp^3$ to $sp^2$. Its dangling bond gains more $p$ character and becomes unoccupied. The dangling bond of the other Si dimer atom (the one relaxed outwards) becomes fully occupied [99]. The $\pi$ bond found between Si atoms of the symmetric dimer is partially destroyed by buckling, but the energy gain due to the rehybridization mechanism obviously overcompensates this energy cost [89].

Due to elastical coupling via the atoms in the second and deeper layers the buckling angle alternates along the dimer row. The lowest energy reconstruction is $p(2 \times 2)$ or, even slightly lower, $c(4 \times 2)$.

A top view of the various reconstructions on the Si(001) surface is shown in Fig. 4.1. The calculated geometric (atom displacement, dimer lengths, dimer angles) and electronic (surface free energy, bandstructure) properties of this structures, i.e. the $(1 \times 1)$ ideal, the $(2 \times 1)$ symmetric dimer, the $(2 \times 1)$ asymmetric dimer, the $p(2 \times 2)$ alternating buckled dimer and the $c(4 \times 2)$ reconstruction, cf. Fig. 4.1, are discussed in the following sections.

### 4.2.1 (1×1) Non-Reconstructed

In the ideal Si (1×1) surface termination, every silicon atom remains in its bulk position, but has only two-fold coordination. The calculated surface energy is 2.05 eV per (1×1) unit cell. The generation of this surface structure upon cleavage of the Si bulk leads to the formation of two surface state bands in the band gap of bulk silicon, that cut the Fermi level. These surface states are not localized and the bands is highly disperse, which shows significant overlap between states of surface atoms. These surface states are responsible for the metallic character of Si.

These two dangling bonds make the surface unstable, therefore the surface atoms move close to each other to form one bond which creates the dimerized $(2 \times 1)$ reconstructed surface.

### 4.2.2 (2×1) Dimer Model: Symmetric/Asymmetric Si Dimers

The surface energy for the symmetric and the asymmetric dimer reconstructions are 2.74 eV / dimer and 2.59 eV / dimer, respectively. They are 1.37 eV and 1.52 eV / $(1 \times 1)$ unit cell lower than the unrelaxed ideal surface. The dimer bond length is 2.30 Å for symmetric and slightly longer, 2.32 Å , for asymmetric dimer structure while the bond length of the bulk silicon is 2.37 Å . The vertical distance separation between the up and the down atom of the dimer is 0.74 Å and the angle of the buckled dimer is 18.7° which is comparable with the angle of 18.3°, reported by Ramstad, Brocks and Kelly [100] and 15° reported by Dabrowski and Scheffler [101]. The angle of the buckled dimer extracted from the analysis of transmission electron diffraction (TED) measurements, 7°, [102] and a X-ray diffraction, 5°, [103] are substantially smaller than calculated values. In contrary, low-energy electron diffraction (LEED) at low temperature (120 K) gave a value of 19° for the tilt of the dimer [104]. All bond lengths for these reconstruction are shown in Fig. 4.2.

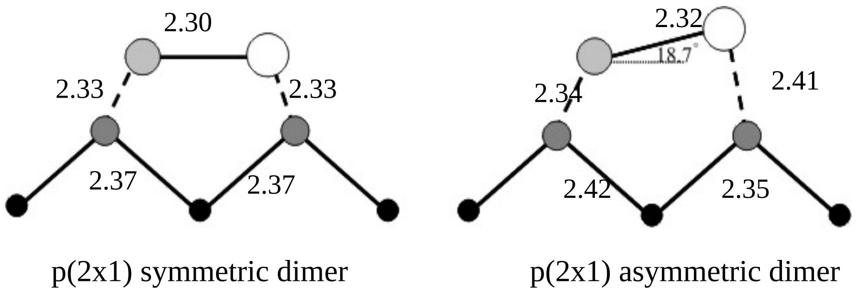

(a) (b)

Fig. 4.2: Bond length of symmetric dimer structure (a), the bond length and the angle of the buckled dimer structure (b).

The discussed results are for calculations performed at temperature of $0\,K$, therefore they should be compared to the low temperature experimental geometry. According to STM experiments at room temperature [94], the dimers appears to be symmetric. It has been suggested that the symmetric images are caused by the thermal flipping motion of the dimers between the left and the right tilted position [105]. In fact, asymmetric dimers have been observed in low temperature STM experiments [105, 106].

In the dimer model, the equivalent dangling bond orbital of each dimer atom are coupled by $\pi$ interaction. The bandstructure is shown in Fig. 4.3. The projected bulk band structure is shown as a gray shaded area. The $\pi$ states are split into a bonding $\pi$-band and an anti bonding $\pi^*$-band. One thing to notice in this figure is that all bands come in pairs. This is a consequence of using a slab model, i.e. there are actually two surfaces. In an infinite thick slab, these pairs would be degenerated.The small energy splitting remains because of the finite thickness. Simple solution to this problem, is to take the average of the split pairs. However, the features of the electronic structures is reasonable and will not substantially change when the thickness of slab is increased.

The rather strong interaction between neighboring dangling bonds in the symmetric dimer leads to a significant dispersion of the bands. In fact, the dangling bonds on the Si(001) surface have itinerant electron, which causes the metallic character in the band structure of this surface. The formation of an asymmetric dimer is associated with a charge transfer of 0.36 from the atom which moves downward to the atom which is shifted up [96]. This charge transfer from the down to the up atom in the asymmetric configuration results in the formation of a partly ionic $\pi$ bond between two atoms, leading to a downward shift of the $\pi$ and upward shift of the $\pi^*$ band.

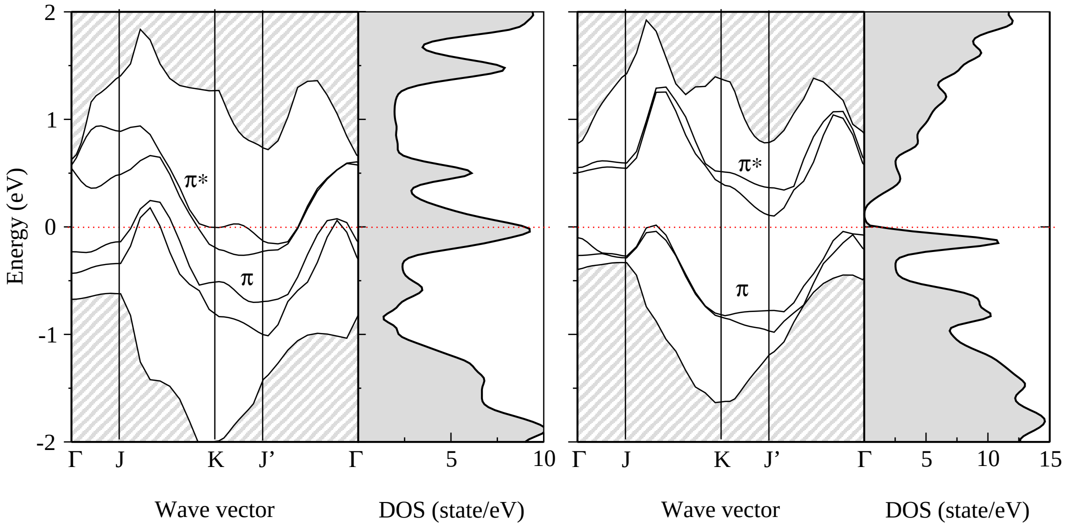

(a) (b)

Fig. 4.3: Band structure and density of states for $(2 \times 1)$ symmetric (a) and asymmetric (b) dimer. The band structure and DOS of the symmetric dimer has metallic character while the Fermi level cuts the tail of DOS and touches the top of valence band. The shaded areas in the band structure correspond to the highest valance band or the lowest conduction band in the slab.

The dispersion of surface bands is almost the same for both the symmetric and the asymmetric dimer. The band width is around 0.7 eV which is close to the experimental value of 0.65 eV [107]. There are large changes in the $\pi^*$ states mainly in

$K \rightarrow \mathrm{J}'$ direction which is parallel to the dimer bonds.

There is a pronounced splitting between the $\pi$ and $\pi^*$ energy bands in the asymmetric structure, leading to the formation of a band gap, slightly above the Fermi level. As can be seen in the DOS plot, the Fermi level cuts the tail of valance band. The width of the calculated band gap is 0.1 eV. It is significantly smaller than the experimentally measured band gap. A band gap of 0.9 eV (corresponding to the indirect gap from $\Gamma$ to **k** ) was measured using scanning tunneling spectroscopy [107, 108], while the value obtained from angle-resolved photoelectron spectroscopy (ARUPS) is 0.7 eV. On the other hand, a direct band gap of 1.7 eV was obtained by Rowe and Ibach with electron energy loss [109].

The underestimation of band gaps is a well-known shortcoming of LDA calculations. For Si surfaces, this flaw is also not corrected within GGA. To further understand if there is a relationship between the structural stability of different reconstructions and the existence of a band gap or region of low densities of states, the band structures of various reconstructions are compared.

### 4.2.3 Alternating Buckled Dimers: $p(2 \times 2)$/$c(4 \times 2)$ Supercells

It turns out that the formation of an asymmetric dimer leads to a significant amount of mechanical stress at the surface. This surface stress can be partially released if the dimers are buckled in alternating form which reduces the surface energy. Different orders of arrangements of these buckled dimers give the p(2×2) or c(4×2) reconstructions. These are the most stable reconstructions on the Si(001) surface. The buckled dimers alternate either in one direction with $p(2 \times 2)$ unit cell or in two directions with $c(4 \times 2)$ unit cell. In other words, in the $p(2 \times 2)$ structure, the direction of buckling alternates along the dimer rows while in the $c(4 \times 2)$ reconstruction they alternate both parallel and perpendicular to the dimer rows .

The buckled dimers first appear on the surface at 120 K and their number increases with decreasing temperature [110]. At low temperature (∼4 K) there is transition from the $p(2 \times 2)$ to the $c(4 \times 2)$ reconstruction. The occupied area by the $c(4 \times 2)$ phase is larger than the part with $p(2 \times 2)$. [106]. The barrier to flip the dimer is about 0.1 eV [48, 111].

The calculated surface energy for the buckled structure is 2.503 eV per dimer which is almost the same for both reconstructions. The surface energy of the $c(4 \times 2)$ reported in the literature is slightly ($\sim$ 2 meV / dimer) lower than for the $p(2 \times 2)$ structure [100, 112], which is not noticeable in theses calculations.

The dimer bond length of 2.38 Å is almost the same for both structures, while the tilt angle of the dimer in the $c(4\times2)$, 18.7°, is slightly larger than that in the $p(2\times2)$ structure, 18.3° (cf. Fig. 4.4). The up and down atom on the dimer are separate by a vertical distance of 0.73 Å in the $p(2\times2)$ and 0.96 Å in the $c(4\times2)$ structures, respectively. This is shorter than the vertical distance between atoms in the bulk which is 1.37 Å. The dimer bond lengths and the back-bond lengths (the bonds between the dimer atoms and those in the second layer) is given for each of these structures Fig. 4.4.

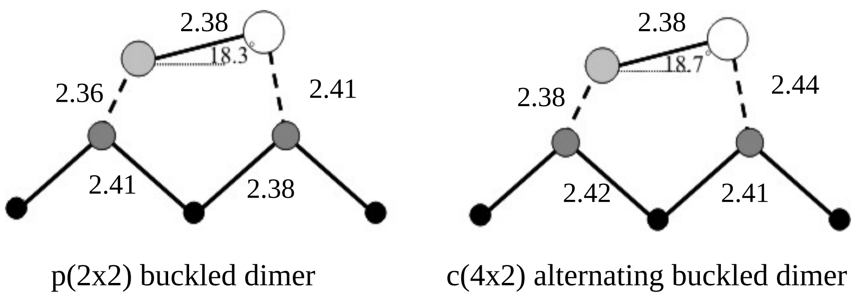

(a) (b)

Fig. 4.4: Bond length and the angle of the alternating buckled dimers structure in p(2×2) (a), and c(4×2) (b) supercells.

In the figure 4.5, we present our results of calculated surface energies of different reconstructions. A difference of 0.2 eV / dimer between the energy of symmetric and asymmetric dimer reported in the literature is the result of a pseudopotential calculation [100]. This value is larger than the one which is calculated here (cf. 4.5). Furthermore, the surface energy of the $p(2\times2)$ buckled structure is reported to be 0.02 eV / dimer lower than the $(2\times1)$ asymmetric dimer [100]. A small energy difference of 1-2 meV / dimer between the $p(2\times2)$ and the $c(4\times2)$ reconstruction is reported by Inoue *et al.* [112] and Ramstad *et al.* [100], but no such difference is observed in the present calculations.

In the following, the electronic structure of the alternating buckled dimer structures are discussed. The density of states and the band structure of the $p(2\times2)$ and $c(4\times2)$ structures are shown in Fig. 4.6.

The band structure of the $c(4\times2)$ reconstruction was calculated using a $(4\times2)$ unit cell, ensuring that there are eight surface atoms in the cell and corresponding eight surface bands in the band structure plot. Similarly, the four surface atoms per $p(2\times2)$ unit cell, are responsible for the appearance of four surface states in the bulk band gap for that reconstruction. These four states are derived from the four dangling bonds, two with $\pi$ character ($\pi_1$ , $\pi_2$), which are occupied, and two $\pi^*$ antibonding states ($\pi_1^*$ , $\pi_2^*$), which are empty.

Due to the buckling of the dimer in the $p(2\times2)$ and $c(4\times2)$ structures, the dispersion of the surface bands are about 0.6 eV for the occupied states and about 0.8 eV for unoccupied state compared to the $(2\times1)$ structure. The valence band of the $c(4\times2)$ is shifted downward by about 0.2 eV, increasing the band gap, and the surface bands become smoother compared to the $p(2\times2)$ structure.

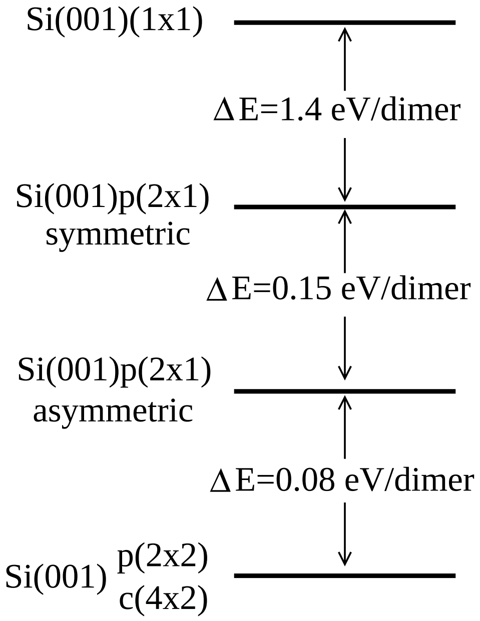

Fig. 4.5: Calculated energy difference between all possible surface reconstructions of the Si(001) surface.

The DOS plot and band structure of $p(2\times2)$ and $c(4\times2)$ structures are shown in Fig. 4.6. The significant changes appear in the occupied states (especially in the directions perpendicular to dimer rows). The less dispersion of the bands open larger gap in the band structure in comparison to asymmetric $(2\times2)$ reconstruction. In the alternating dimer reconstructions the bandwidth of $\pi$ band decrease which leads to a larger band gap. The lower energy of the $p(2\times2)$ and $c(4\times2)$ reconstruction can be associated with a increasing of the band gap.

The lowest energy of the $\pi^*$ band is 0.3 eV ( 0.1 eV) above the valence band maximum (VBM) for $c(4\times2)$ ( $p(2\times2)$ ) reconstruction. The corresponding experimental value obtained from optical absorption experiments is about 0.4 eV [92]. The two unoccupied states ($\pi_1^*$ and $\pi_1^*$) are separated by 0.5 eV in the $c(4\times2)$ structure and 0.7 eV in the $p(2\times2)$ structure at the $\Gamma$ point where the minima of unoccupied states are located. The dispersion in the $\Gamma \rightarrow$ J and $K \rightarrow$ J$'$ directions (along dimers bonds) is flat in both structures. The valence band at the $\Gamma$ point is 0.3 eV below the Fermi level, which is half of the value measured by ARUPS, being 0.6 eV [113].

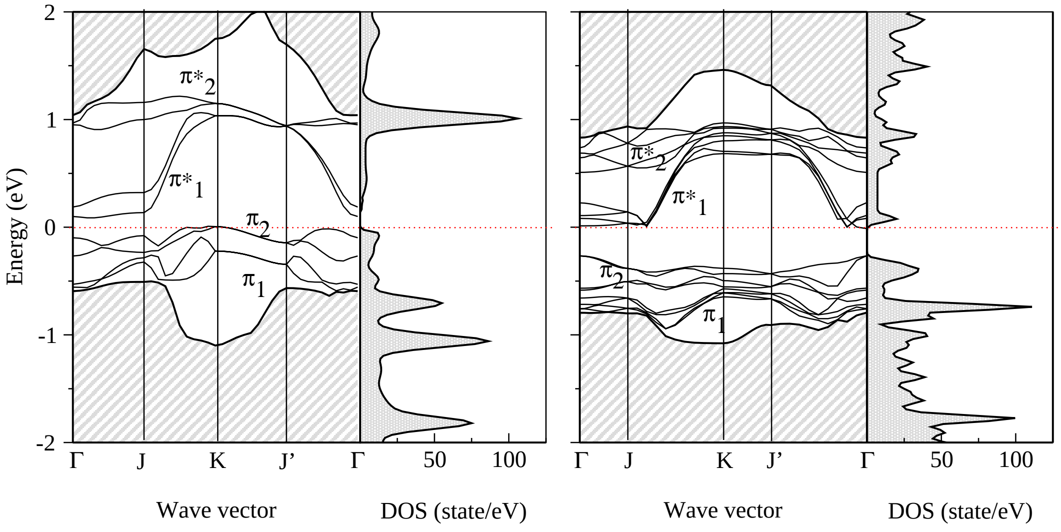

(a) (b)

Fig. 4.6: Band structure and density of states for $p(2 \times 2)$ (a) and $c(4 \times 2)$ (b) reconstruction. The band structure of the $c(4 \times 2)$ reconstruction was calculated using a $(4 \times 2)$ unit cell.

- **Scanning Tunneling Microscopy (STM)**

In order to compare simulations with experiment, the reconstructed structures of the Si (001) surface in the low temperature regime where the flip-flop motion of dimers is frozen, are considered. As is evident in Fig. 4.7, which shows the simulated and experimental STM pictures of the $c(4 \times 2)$ and $p(2 \times 2)$ reconstruction, the simulated images accurately reproduce the experimental result. The experimental images were produced at a temperature of 4.2 K, using a positive sample bias of 1.3 eV (2 eV) for the $c(4 \times 2)$ ( $p(2 \times 2)$ ) structure and a tunneling current of 30 nA .

As shown in Fig. 4.7, the simulated images can support the interpretation of the experimental STM images. The simulated images are generated from the electronic local density of states of $10^{-5}$ electrons / Å $^{3}$ ($0.5 \times 10^{-5}$ electrons / Å $^{3}$) for the $c(4 \times 2)$ ($p(2 \times 2)$) structure. The estimated distance from the surface at the mentioned charge density is at a height 4 – 4.7 Å above the surface in a $(2.3 \times 2.3)$ nm$^2$ scan region. The applied voltages are 0.5 eV above the surface Fermi level corresponding to the empty states of the surface. In these images the gray-scale range from bright to dark represents a height change of around 4 Å.

In the experimental $c(4 \times 2)$ image, Fig. 4.7-a, the buckled dimers form a honeycomb pattern while in the $p(2 \times 2)$, Fig. 4.7-d, the dimer rows have a zigzag shape. It is found, that at low temperature the out of phase $c(4 \times 2)$ arrangement is prefer-

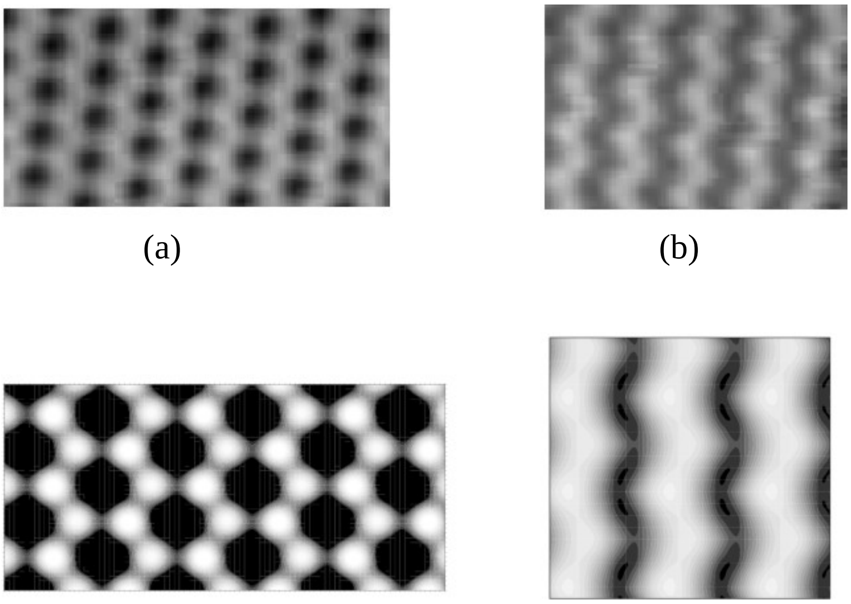

(a) (b)

(c) (d)

Fig. 4.7: Simulated and experimental empty states images for $c(4 \times 2)$ structure (a, c) and $p(2 \times 2)$ structure (b, d). The experimental images are measured with a positive sample bias of 1.3 eV and 2 eV for the mentioned structures.

entially formed. The domains with in-phase $p(2 \times 2)$ order are five times less than the $c(4 \times 2)$ areas [110].

Looking at the $p(2 \times 2)$ structure, one protrusion is clearly distinguished inside one buckled dime. This bright part belongs to the upper atom Fig. 4.7-d. The dark areas are surface depressions where the dangling bonds in the deeper layers are lacking. This bean-like shape of bright parts was reported for first time by Hamers $et\ al$ [105].

### 4.2.4 Dimer Vacancy

Thirty years ago it had been suggested that the energy of the Si(001) surface would be lowered if a small fraction of the dimers were removed from the surface. Due to the dimer vacancy, the atoms below could rebond, eliminating two dangling bonds for every dimer involved. Later on, it was shown by Robert and Needs, that the strain due to the dimer vacancy would prevent the atoms below to rebond [114]. In order to study the effect of a vacancy on the surface stability, calculations for one dimer vacancy were performed for $(2 \times 4)$ and $(4 \times 2)$ unit cells.

The two considered defect geometries are shown in Fig. 4.8. The energy cost to form a defect in the $(4 \times 2)$ and the $(2 \times 4)$ structure is 0.52 eV / dimer and 1.0 eV / dimer,

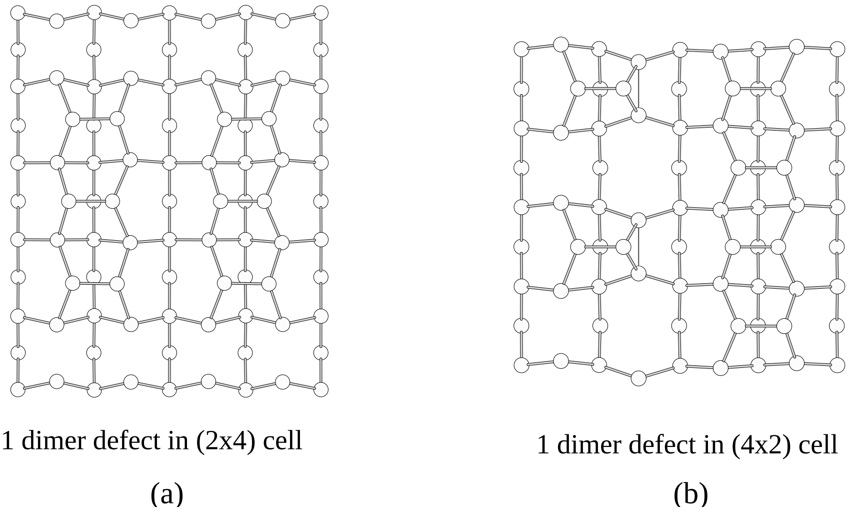

Fig. 4.8: Top view of $(2\times4)$ (a) and $(4\times2)$ (b) surface unit cell containing one dimer vacancy.

respectively. In the $(2 \times 4)$ geometry the vacancy structure is obtained by removing one dimer in every fourth dimer at the surface. This results in an ordered array consisting of one empty site and three dimers in each cell (cf. Fig. 4.8-a). The neighboring dimers become shorter in the $(2 \times 4)$ structure (by 0.08 Å), the angle of buckling is reduced to 15° and the atoms of these dimers are pulled downwards (by 0.3 Å) towards the defect. Simultaneously the exposed second-layer atoms beneath the defect move closer together until their sparation distance is 2.94 Å which is about of 1.22 Å (i.e. 30%) shorter than for the second-layer atoms located below the dimer rows.

The energy cost to form a defect in a $(4 \times 2)$ cell equals half that of the $(2 \times 4)$ geometry. In the $(4 \times 2)$ structure, Fig. 4.8-b, there is one full dimer row, while every second dimer is removed in the adjacent row. The strain in this geometry is smaller than in the previously discussed structure, there is an additional bond of 2.61 Å between the second-layer atoms (the triangle in Fig. 4.8-b). These atoms in the second layer are pulled downward by 0.3 Å (compared to the second-layer atom below the full dimer row). The other second-layer atoms (these are below the lower dimer atom) approach each other and move toward the defect until they reach a distance of 4.32 Å from each other. The angle of dimers increases to 20° and 22° for the full and the defect containing dimer rows, respectively.

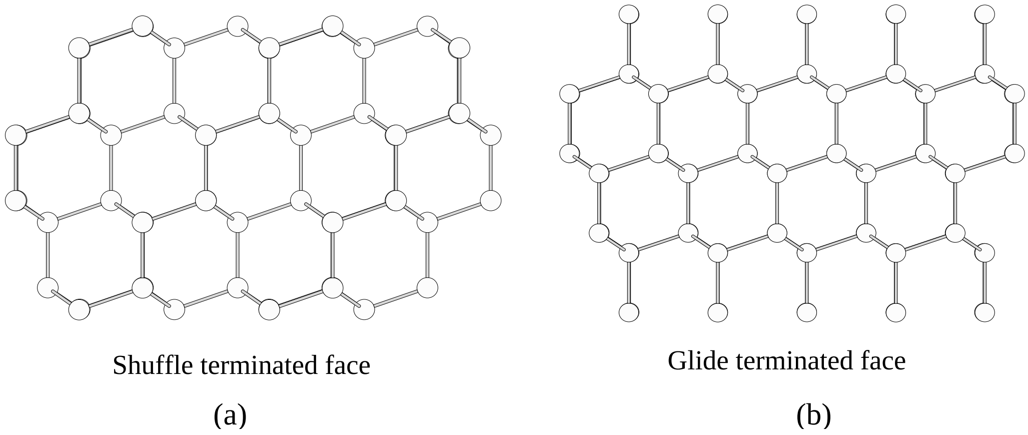

Fig. 4.9: Side view of the bare Si(111) surface. It has two possible terminations, the single-dangling-bond (SDB) which is called shuffle-terminated face (a), triple-dangling-bond (TDB) which is called glide-terminated face (b).

## 4.3 Si(111) Surface

The Si(111) surface is cleavage face of silicon for which the covalent bonds along [111] direction are cut. Depending on the number of layers, there are two surface terminations, see Fig. 4.9:

(a) Cleaving so that it has a single dangling bond (SDB) per surface atom which is called shuffle-terminated face [115, 116], see Fig. 4.9-a.

(b) Single coordination atop site, which has three dangling bonds (TDB) per surface atom which is called glide-terminated faces (cf. Fig. 4.9-b). Due to the degrees of freedom of the surface atom in all direction, this surface reconstructs.

It has been established that this surface has a 7×7 reconstruction as described by Takayanagi [1] [117]

There are also several surface reconstructions at different temperatures: Below T $\leq$ 600 K, cleavage produces a $(2 \times 1)$ structure, annealing this surface above 600 K generates a $(5 \times 5)$ structure which upon further heating to 870 K becomes a $(7 \times 7)$ structure [89, 118] . Still further heating to about 1120 K causes a phase transition to the $(1 \times 1)$ symmetry [119]. There are some studies which consider these structures and the transitions between them, that have been reviewed by Haneman [118]. Also the existence of metastable $(9{\times}9)$, $(2{\times}2)$, $c(4{\times}2)$ and $(\sqrt{3}{\times}\sqrt{3})$ reconstructions was observed by STM [120].

The triple-dangling-bond (TDB) face could theoretically be created upon cutting perpendicular to the (111) direction between the two narrowly spaced layers, in contrast to the single-dangling-bond (SDB) face, which separates the widely spaced bilayers at which the dangling bond is oriented exactly in the (111) direction. From this two possible cleavage planes, the SDB requires less energy since only one bond per atom has to be broken. Although cleaving along the TDB face involves the separation of three bonds, the surface energy is not three times as large as for the SDB surface. The present results for the surface energies confirm this trend. The calculations for the SDB and the TDB surface are performed using symmetric slabs of 12 and 10 atomic layers, respectively. Five (four) layers on each side are relaxed. Two layers in the middle of the slab are kept bulklike. The TDB termination is usually discarded for energetic reason since the cutting of three bonds needs more energy. The surface energy, $\gamma$, is 100.08 meV / Å$^2$ and 175.05 meV / Å$^2$ for the SDB and TDB, respectively. The surface energy for the TDB is only 0.98 eV / unit cell (1.75 times) higher than for the SDB surface.

---

[1] This model basically consists of 12 adatoms arranged locally in the 2×2 structure, nine dimers on the sides of the triangular subunits of the 7×7 unit cell and a stacking fault layer.

The surface energy for the SDB termination using pseudopotentials gives a value of 108.6 meV / Å$^2$ for the $(1 \times 1)$ relaxed unit cell which decreases to 85 meV / Å$^2$ for the $(7 \times 7)$ reconstructed surface [121]. Using molecular dynamics with empirical potentials or tight-binding calculations leads to a value of 88.0 meV / Å$^2$ [122].

The relaxed structure for SDB (TDB) has an inward relaxation of the first atomic layer by a vertical displacement of 0.144 Å (0.005 Å) and an outward relaxation of the second layer by a vertical displacement of 0.035 Å (0.005 Å). The energy gain in the relaxed structure is due to the short bond between the atoms in the first and the second sub-surface layer which is contracted by 0.18 Å (18% shorter than unrelaxed bulk terminated).

On the SDB surface there is only a very weak $\pi$-like interaction of the dangling bond orbital over second nearest neighbor distance. The surface is metallic for both SDB and TDB surfaces.

# Chapter 5

# Initial Mn Adsorption and Diffusion Pathways

## 5.1 Introduction

Spintronics has attracted much attention since it opens the possibility for building up a new class of multi-functional devices. Using the spin of the electron in addition to its charge, creates a remarkable new generation of microelectronic devices. Although this class of material seem very promising, the injection and controlling of spin in semiconductors is still a current topic of research.

Technologically, it would be desirable to grow heterostructures of a transition metal (Mn, Fe, Co, Ni) on the surface of silicon which is the most common semiconductor. This could be done either by depositing a structurally well-defined thin film of a ferromagnetic metal on silicon, or by turning silicon itself into a dilute magnetic semiconductor by adsorption of magnetic metal atoms on the Si. Due to the strong interaction between transition metals and Si surfaces, formation of the intermetallic silicide compounds is energetically preferred on a Si substrate. However, Fe, Co, and Ni silicide films are weakly magnetic or non-magnetic and therefore unsuitable for spintronic devices [85]. On the other hand, Mn displays a considerable magnetic moment in some of its phases. Moreover, both the Mn $\gamma$ phase and the Mn-silicide compounds have good lattice match to the Si-substrate (see Tab. IV in Chap. 3). Thus, we expect the growth of such films to produce suitable interfaces for spin injection in semiconductors. In analogy to Mn:Ge [123] the possibility to grow strongly doped Mn:Si, which could be ferromagnetic, has been explored theoretically [124, 125]. Recently, it has been shown experimentally that a ferromagnetic phase with a Curie temperature above room temperature can be formed by Mn ion implantation into Si at 0.8% and 0.5% Mn atom concentrations [126, 127].

Another interesting possibility is the growth of heterostructures of Si with Heusler alloy films, e.g., $Co_2MnSi$ or $Co_2MnGe$. Theses materials that are not only ferromagnetic at room temperature, but also display a high spin polarization of carriers at the Fermi level. Both these properties make this type of materials promising for efficient spin injection of the majority-spin carriers through the heterojunction.

While transition-metal silicide deposition has been studied intensively, only a few experimental studies of Mn-silicide films on Si have been performed. Both metallic MnSi and semiconducting $MnSi_{1.7}$ have been grown [128] on Si(001). Recently experiments also demonstrated the growth of two types of three-dimensional nanostructures on Si(001), which were attributed to MnSi and $Mn_5Si_3$ nano-crystallites [16]. On the theoretical side, studies of Mn diffusion on Si(001) have not appeared until very recently [124, 125]. However, there are a number of reports, both experimental and theoretical, for other metal atoms on Si(001) [129–131]. In all these cases, dimerization of the adatoms as well as formation of islands and clusters have been observed.

For all these approaches, it is crucial to better understand and control the adsorption, diffusion and nucleation of Mn on the silicon surface. Furthermore in order to identify the elementary growth processes which determine the junction quality, it is essential to have detailed information about the potential energy surface and the possible diffusion paths of Mn on Si.

The current chapter is organized as follows: First the behavior of single Mn adatoms on Si(001), atomic structure, stability, magnetic properties and diffusion pathways will be investigated. Subsequently, the initial growth process of Mn on Si(001) for coverages up to 1 monolayer (ML) will be studied.

## 5.2 Computational Details

The Si surfaces are modeled using a slab geometry consisting of eight or ten layers of Si atoms for Si(001) and ten or twelve layers for Si(111). Mn adatoms are always placed on both sides of the slab to preserve the inversion symmetry with respect to the middle of the slab. The $\theta$=1 monolayer (ML) coverage of Mn is defined in such a way that it corresponds to a space-filling arrangement of two Mn adatoms per $(1 \times 1)$ unit cell of the Si surface. For Mn coverages $\leq 1/2$ ML on Si(001), the calculations were performed in a $p(2 \times 2)$ unit cell using a surface reconstruction with alternating buckled Si dimers. For Si(111) we performed calculations in a hexagonal $(1 \times 1)$ unit cell containing 1 Mn, which corresponds to a coverage of 0.5 ML. In the case of Si(001), the periodic supercell contains a total of 32 Si atoms in a eight-layer-slab of Si, plus 1/8 or 1/4 ML of Mn, which corresponds to one or two Mn adsorbed on either side of the supercell. The successive slabs are separated by a vacuum space of 16.4 Å . The Brillouin zone sampling is done by a set of 8 $k$-points in the irreducible part of the Brillouin zone, derived from a $4\times4\times1$ $k$-point mesh. In all calculations, the muffin-tin sphere radius is chosen to be 1.11 Å for both Mn and Si. The cut-off energy for the plane-wave expansion in the interstitial region, $E^{wf}_{cut}$, is 13.8 Ry. The numerical accuracy of the present calculations has been checked by using a higher cut-off energy, *e.g.*, 21.8 Ry, indicating a maximum uncertainty of about 0.1 eV per (1×1) cell for formation energies but negligible change of the relative stability (relative energy difference). All Mn and Si atoms except for the two central-layer Si atoms, were relaxed until the calculated atomic force for each of them is smaller than 0.03 eV/Å.

## 5.3 Stable and Non-Stable Adatom Positions on The Si(001) Surface

In the following section, the adsorption energy of the single atom adsorption on the Si(001) surface will be reported. The effect of the position of the Mn impurity on the magnetic and electronic properties will be studied as well.

The reported dimer bond lengths is 2.38 Å and the angle of the buckled dimer is around 18.2°. Adsorption of a single Mn atom on this surface leads to the formation of a strong covalent bond, due to the overlap of the two surface states of the dangling bonds with the Mn-$d$ orbitals. This turns the semiconductor behavior of the band structure of the bare surface into a metallic band structure. According to our earlier calculations for bulk Si and Mn-monosilicide, the nearest neighbors interatomic distances are 2.37 Å for Si-Si and 2.38-2.4 Å for Si-Mn. The energy gain to form a Si-Si or a Mn-Si bond are 2.7 eV and 1.3 eV, respectively.

In order to find the binding sites of the Mn atom on the Si(001) surface, the adsorption energy of an adatom is defined as the difference between total energy of the adsorbate and substrate system, $E^{\rm tot}$, the bare Si(001) surface, $E^{\rm clean}_{\rm surface}$ and the free Mn atom, $E^{\rm free}_{\rm Mn}$, i.e.

$$E^{\rm ad} = \frac{1}{2}(E^{\rm tot} - E^{\rm clean}_{\rm surface} - 2E^{\rm free}_{\rm Mn}) \tag{5.1}$$

The fraction $\frac{1}{2}$ is considered to count two surfaces in the top and bottom of the slab model.

In Fig 5.1 the most stable adsorption sites on the Si(001) $2\times2$ reconstructed surface

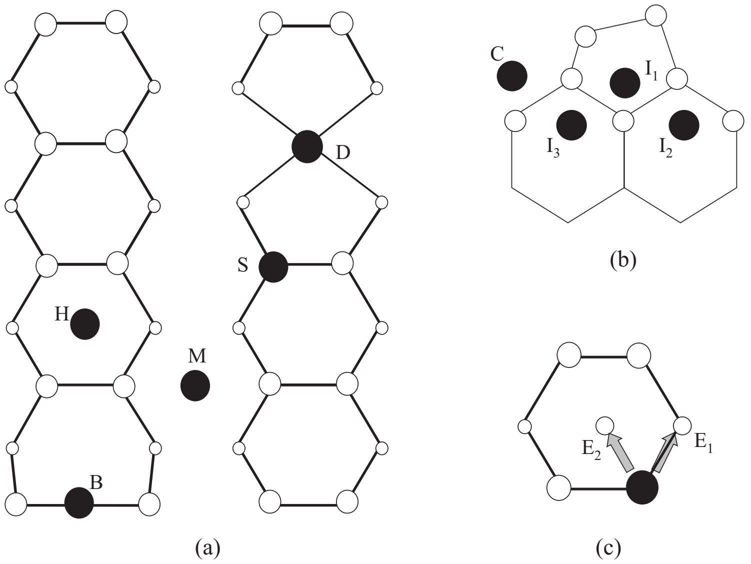

Fig. 5.1: Schematic top view of the Si(001) surface, with various binding sites for a Mn adatom indicated (a). Side view, with sub-surface binding sites of Mn indicated (b). Top view illustrating substitutional adsorption of Mn, the arrows indicating various alternative positions for the expelled Si atom (c). Filled circles indicate possible binding sites for Mn, white circles Si atoms.

are shown. In order to compare the present results to those reported in the literature, the adsorption energies, bonds length and magnetic moments for adatom at some high-symmetry sites of the PES, as well as for some other adsorption geometries are collected in Tab. 5.1. The sites are known as the interstitial ($I_1$), the third-layer sub-surface ($I_2$,$I_3$), the dimer vacancy (D), the cave site (C), the hollow site (H), the substitutional (S), the exchange ($E_2$,$E_3$) and the dimer short bridge site (B). The dimer vacancy, 3rd layer sub-surface and interstitial site are stable sites for Co, Ni and Ti adsorption on this surface, respectively [132–134] which induced the idea to include them in the present study[1]. The first three sites are capped by a Si layer. All these geometries which result from an exothermic process are found by fully relaxing the system. The energy of substitutional adsorption of Mn was calculated under the assumption that the replaced Si atom moves to the Si bulk.

The most stable site for Mn is the 2nd-layer tetrahedral interstitial site, $I_1$. The Mn is located 2 Å below the Si-dimer while it elongates the dimer and moves it up by 1 Å from the surface. This configuration is mentioned also as the lowest energy position in the work of Dalpian, da Silva and Fazzio [124]. In this position, the Mn bonds are completely saturated without disrupting the substrate bonds and the magnetic moment of Mn reduces to 2 $\mu_B$ . This is due to strong covalent bonds between

---

[1] In section 5.4 , the dimer vacancy will be discused in details.

Table 5.1: Bond length of Mn and Si, absolute adsorption energy (eV) and magnetic moment for different adsorption sites for low coverage, $\theta_{\mathrm{Mn}} = 1/8$. Note that the Mn-Si distances are in the range of bond distances known from Mn-monosilicide.

| site | Si-Mn Bond Å | $E_{ad}$ eV/atom | Magnetic Moment $\mu_B$ |
|---|---|---|---|
| $I_1$ | 2.3-2.6 | 3.80 | 2.4 |
| D | 2.5 | 4.29 | 2.9 |
| $I_3$ | 2.4-2.5 | 3.01 | 2.9 |
| H | 2.4 | 2.91 | 3.2 |
| S | 2.4-2.4 | 2.86 | 3.6 |
| B | 2.5-2.7 | 2.72 | 3.9 |
| $E_1$ | 2.3-2.4 | 2.69 | 3.0 |
| M | 2.4 | 2.63 | 4.1 |
| $E_2$ | 2.3-2.4 | 2.36 | 2.9 |
| C | 2.4 | 2.49 | 3.3 |

the adsorbate and substrate atoms. The presence of a Mn atom beneath the dimer, changes the buckled dimer surface into non-buckled and almost symmetric dimer surface. The charge density distribution of this Si-dimer is reduced significantly and is localized around the Mn atom. The dimer bond above Mn is stretched by approximately 16%, whereas the other Si-dimers shrink by about 4% in comparing to the usual Si dimer bond length in bare Si(001) surface. In this optimized atomic configuration, Mn forms 9 bonds with neighboring Si atoms with bond lengths in the range of 2.3 – 2.6 Å.

As seen from the table, the adsorption energy for Mn in the 3rd-layer is less favorable than in the second layer interstitial site. There are two different adsorption sites, $I_2$ and $I_3$, in the third layer. Since the dimers are buckled, these two site are not equivalent, i.e. they have different surrounding. The $I_2$ side is not a real adsorption site since there is no barrier from 3rd layer sub surface $I_2$ to 2nd layer interstitial, $I_1$. In this site Mn breaks the Si-dimer's back bonds and diffuses easily to the most stable site, the second layer tetrahedral interstitial site. Mn in the position below the lower Si atom of the dimer, $I_3$ , has an adsorption energy, $E^{ad}$, of 3.01 eV. Therefore, the third layer is a thermodynamically unstable place for Mn. From interatomic distances one can conclude that the adsorption in the third layer sites enhances the angle of dimers.

Another metastable adsorption site on the surface is the $pedestal$ or $hollowsite$ where the Mn is situated between Si-dimers in the same row (in the center of hexagon formed by the surface atoms). Adsorption of Mn on the surface reduces buckling of the dimer, therefore the surface has less distortion. In this metastable binding site, the Mn atom is in four fold coordination with nearly equally short bonds ($\sim$ 2.4 Å) with Si in the top most layer. The Si-dimers on the substrate still remain intact. The energy gain due to adsorption at this point is about 0.89 eV less compared to the adsorption in the interstitial site $\mathrm{I}_1$.

In the context of epitaxial growth of Mn-doped Si, incorporation of Mn at substitutional positions at the surface is particularly important. This process is likely to trigger silicide formation. On the other hand, it has been long known that the substitutional Mn impurity in Si act as an acceptor [135] with a large local magnetic moment. Hence one could speculate that Si can be turned into a dilute magnetic semiconductor. In the substitutional site, Mn incorporation with a high concentration could be achieved. Therefore, the feasibility of Mn replacing the lower Si atom of the Si surface dimer should be studied. With taking the chemical potential of bulk Si as an energy reference, the substitutional impurity is energetically less favorable than the impurity in the sub-surface interstitial site by 0.93 eV.

In an attempt to calculate the energy barrier for a surface exchange process of Mn and Si, we have calculated several geometries where Mn occupies the Si site, while the replaced Si atom sits at different neighboring positions. Specifically, we investigate the possibilities that the exchanged Si atom could move to an asymmetric position between two Si dimers (marked as $E_1$ in Fig. 5.1), or to the center of the surface Si-hexagon, the hollow site (marked as $E_2$ in Fig. 5.1). The adsorption energies for these two possibilities are 0.22 eV and 0.55 eV lower than for a Mn atom in the hollow site. Since the energies of these intermediate configurations can be considered as a lower bound for the energy barrier of substitution, it is concluded that a Mn impurity in the hollow site needs to overcome a barrier of at least 0.22 eV to create a substitutional Mn site at the surface.

However, once a Mn atom has reached the stable interstitial site $\mathrm{I}_1$, the activation energy for creating a substitutional Mn is increased by 0.89 eV. The barrier for reaching the interstitial site from the hollow site is 0.3 eV (see section 5.5.2). Hence we conclude that substitutional and interstitial adsorption of Mn are competing processes.

The Mn impurity at the dimer short bridge site, ($B$), has the same (x,y) coordinates as the tetrahedral interstitial site, but is located above the Si-dimer. This position is unstable because the Si-Si dimer is broken and the Mn bonds is not saturated. This will cause to diffused Mn to the ($H$) without any barrier. The impurity in this site is less stable than the $\mathrm{I}_1$ site by 1.07 eV.

The cave site, $C$, where the Mn atom is located in the trench between two dimer rows, has an adsorption energy of 2.69 eV which is less than for the hollow site impurity by 0.8 eV. In Mn / GaAs(001), where the cave site is a local minimum.

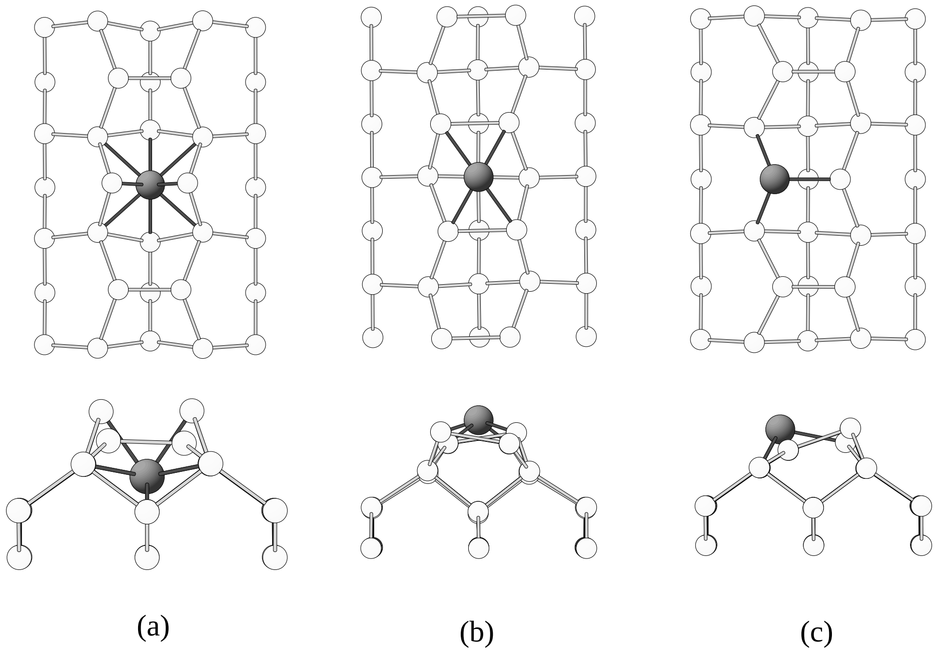

Fig. 5.2: Top view (upper panel) and side view (lower panel) of adsorption of Mn impurity at tetrahedral interstitial site (a), hollow site (b) and substitutional site (c).

In summary we conclude that, due to the strong Mn-Si covalent bonding, incorporation and penetration of a single Mn into silicon sub-surface site is energytically more favorable than adsorption on the surface.

We note that Dalpian *et al.* [124] have performed a similar study, using ultrasoft pseudopotentials and a $(4 \times 4)$ unit cell to describe the surface. In their results, the magnetic moments obtained in the pseudopotential calculations [125] are in fair agreement with ours, except for the second layer interstitial site, where the pseudopotential calculation yields a considerably smaller magnetic moment (0.92 $\mu_\mathrm{B}$) than our all-electron calculations (2.4 $\mu_\mathrm{B}$). While the reason of the discrepancy is yet unclear, we note that the magnitude of the magnetic moment may depend sensitively on core polarization effects.

Comparing to recent calculations by Zhu *et al.* for Mn / Ge(001), [123] we conclude that Mn shows very similar behavior on Ge(001) and on Si(001). For Mn on Ge(001), the interstitial sites in deeper layers, as well as the surface substitutional site, are also found to be less stable than the second layer interstitial site, in agreement with the behavior that we find for Mn / Si(001). In similar work by Dalpian *et al.*, the same results were found. In contrast, in Ge the substitutional impurity can diffuse easily to the interstitial impurity [123, 136, 137].

Similarly, calculations for Mn / GaAs(001) have identified the interstitial site below an As surface dimer to be the most stable site for Mn on GaAs(001). [138]

It is also interesting to compare our results with results for adsorption of other transition metals on Si(001). In a STM study of Cu deposition on Si(001), the Cu atoms form a dimer on top of the Si dimer rows and perpendicular to the Si dimer direction. The adatom dimerization, undimerizes the Si substrate [129]. In a study of the initial process of Ni adsorption, Ni can diffuse rapidly into Si and penetrate to the third sub -surface site [139]. A theoretical study of adsorption of Co on Si(001) predicts that the most stable site for Co is the dimer vacancy which is formed by removing the dimer above cobalt in the site below dimer [132]. For single atom adsorption of Ti, the interstitial site is the most stable site. The adatom adsorbs on a Si-dimer row, dives into the near-surface interstitial site, and the surface Si atoms adjacent to the Ti adatom are ejected on to the terrace [53].

In order to better understand the behavior of Mn in substitutional, tetrahedral interstitial site and hexagonal interstitial site (hollow site), the band structure, DOS and charge density of aforementioned structures will be discused in details.

- **Electronic structures :** For the discussion of the electronic and magnetic properties, it is helpful to look at the band structure of a Mn-impurity at the hollow site, tetrahedral interstitial site and substitutional site, Fig. 5.3. The band structures are plotted in the directions parallel ($\Gamma \rightarrow X$) and perpendicular ($\Gamma \rightarrow Y$) to the surface-dimer. The upper (lower) panel in the Fig. 5.3 are the band structures for the majority (minority) spin channel.

As expected, the magnetic phases are energetically more favorable than the paramagnetic phase. Since the exchange splitting (energy difference between spin up and down state) has a significant effect on the $d$ orbitals, the band structure for spin up and down channels are plotted near the Fermi level where the bands have mainly $d$ character. With comparing the DOS of both spin channels we see, the Si $sp$ orbitals contribute to the bonding state far from the Fermi level and their splitting due to the exchange field is almost negligible.

According to the band structure of the hollow site impurity, both spin channels have semiconductor behavior with a band gap of about 0.42 (0.33) eV for spin up (down) channel (cf. Fig. 5.3-a and d). In contrast, in the substitutional and interstitial site band structures, due to the surface state, the band crosses the Fermi level and is in the shoulder of the peaks. Their band structures have metallic character with spinpolarization of 7% and 51% at the Fermi level for the substitutional and the interstitial impurity, respectively.

Mn in the center of the surface hexagon, hollow site, saturates all surface dangling

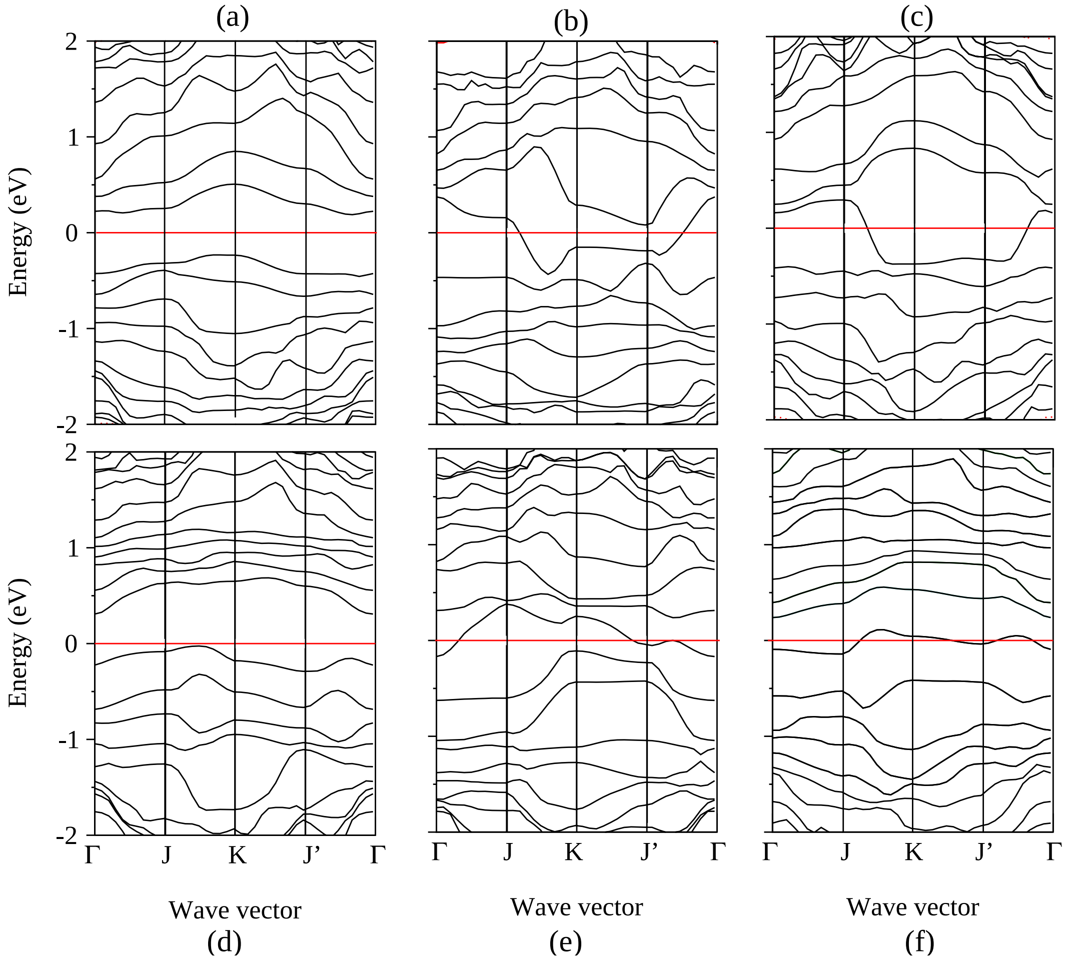

Fig. 5.3: Band structure of up-spin channel (a, b, c) and spin down channel (d, e, f) of a Mn impurity at the hollow, interstitial and substitutional site, respectively.

bounds and opens a gap. While in the interstitial and substitutional structures, the surface bands appear in the band gap where one of them is partially occupied. This band which has relatively large dispersion is responsible for the loss of the band gap.

Since coordination of Mn on the surface is lower than in the bulk, the magnetic moment in the surface becomes higher than bulk Mn. Whenever the exchange splitting is more than the crystal field splitting (energy difference between sub-level of atomic orbital, i.e. $d_{e_g}$ and $d_{t_{2g}}$), therefore a high spin state is observed in the top-most layer, which is in agreement with published calculations [124, 125].

The magnetic moments of Mn in the pedestal and in the substitutional topmost layer are 3.2 and 3.6 $\mu_{\rm B}$, respectively, but for the sub-surface this diminishes to 2.4 $\mu_{\rm B}$. The reduction of the magnetic moment from topmost layer to 2nd layer is due to the strong overlap between $sp$-hybridized orbitals of the topmost Si layer and the Mn $d$-orbitals in the interstitial site which reduces the exchange splitting and hence the magnetic moment. Moreover, due to the different structural environments of Mn atoms at different adsorbtion sites, the population of filled state of $d$-orbital down-spin channel below the Fermi level in interstitial site is 20% more than hollow and substitutional sites. This induces an increase of the exchange splitting and the magnetic moment in the substitutional (hollow) site in comparison to the interstitial site.

Furthermore, an estimate of the exchange splitting, $\Delta_x$, and the crystal field splitting, $\Delta_{e_g-t_{2g}}$, just for the $e_g$ state at the $\Gamma$ point in the case of the hollow, substitutional and interstitial site leads to a value of $\Delta_{e_g-t_{2g}} = 0.2, 0.2, 0.1$ eV and $\Delta_x = 3.95, 4.05, 3.25$ eV, respectively.

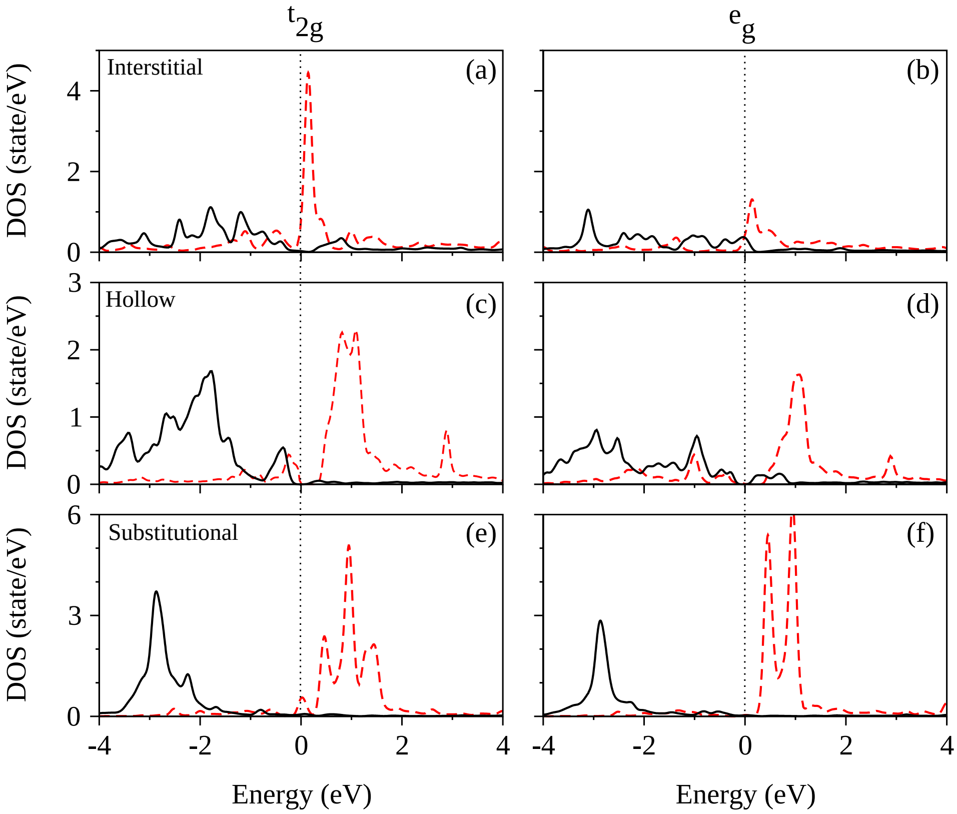

Fig. 5.4: DOS of the $t_{2g} = d_{z^2} + d_{xz} + d_{yz}$ and $e_g = d_{x^2-y^2} + d_{xy}$ sub-levels of partial $d$-orbitals of a Mn impurity at the tetrahedral interstitial site (a,b), hollow site (c, d) and substitutional site (e, f). Black solid lines are for the majority spin channel and red dashed lines belong to the minority spin channel. The energy zero refers to the Fermi level.

Further insights about magnetic properties can be gained from comparison of the DOS plot for the sub-level of the $d$-orbitals of Mn at different impurity sites, Fig. 5.4.

Due to the crystal field, the $d$-orbitals of a Mn atom which is five-fold degenerate splits into a two-fold in-plane $d_{e_g}$, and three-fold out-of-plane $d_{t_{2g}}$ orbitals. These two levels will be split by an exchange interaction into $d_{x^2-y^2}, d_{xy}$ in-plane and $d_{x^2}, d_{xz}, d_{yz}$ out-of-plane components. The metallic character of the substitutional impurity is mainly due to the out-of-plane $d_{t_{2g}}$ orbitals ( specifically $d_{xz}$ and $d_{yz}$ sub-levels), while in the interstitial site both the in-plane $d_{e_g}$ orbitals ($d_{x^2-y^2}$, $d_{xy}$) and out-of-plane $d_{t_{2g}}$ orbitals ($d_{yz}$ sub-level) are responsible for the metallic behavior.

Since the effect of Mn is evident only starting at about -4 eV below the Fermi level, The comparison of the DOS plots is discussed only in the most affected component at the valence region, near to the Fermi level.

In the interstitial impurity, the well-localized peak for the spin down channel is centered at 0.15 eV and has $d_{t_{2g}}$ character. Whereas in the majority spin channel, the delocalized peaks spread in an energy range from around -4 eV to the Fermi level and correspond to both $d_{t_{2g}}$ and $d_{e_g}$ orbitals.

In contrast, in the majority spin channel of the substitutional site, there is a sharp localized peak centered at 2.85 eV which belongs to $d_{t_{2g}}$ and $d_{e_g}$ sub-levels. The main peaks for minority spin channel are around 1 eV and correspond to both $d_{t_{2g}}$ and $d_{e_g}$ sub-levels.

The band structure for this structure still has metallic behavior which is due to the surface dangling bonds of the second dimer. However, a small gap ($\sim$0.4 eV) appears in the majority spin channel of the DOS of the Mn atom on top of the surface in hollow site. It has 100% spin polarization at the Fermi level.

- **Charge density contour plots :** Comparison of the contour plots of the charge densities for Mn at substitutional, hollow and interstitial sites are the subject of the following part. In Fig. 5.4. , plots (a), (b) and (c) show the contour plot of the charge density in a plane perpendicular to the surface and containing the Mn impurity, and plots (d) and (e) are plotted in a plane parallel to the surface. The white big and small circles are the place of Mn and Si atoms, respectively.

In Mn / Si(001) system, the tilt of the dimers is reduced when the Mn is adsorbed on the surface, especially in the interstitial site. The presence of Mn reduces charge distribution in 2nd, 3rd and fourth layers as well as topmost layer and removes part of the charge from the back bonds. The charge density is mostly confined to the Mn-Si bonds and concentrated around Mn atoms.

In the interstitial and hollow sites, there is still charge density distribution at the place of the upper Si atom which belongs to the dangling bonds.

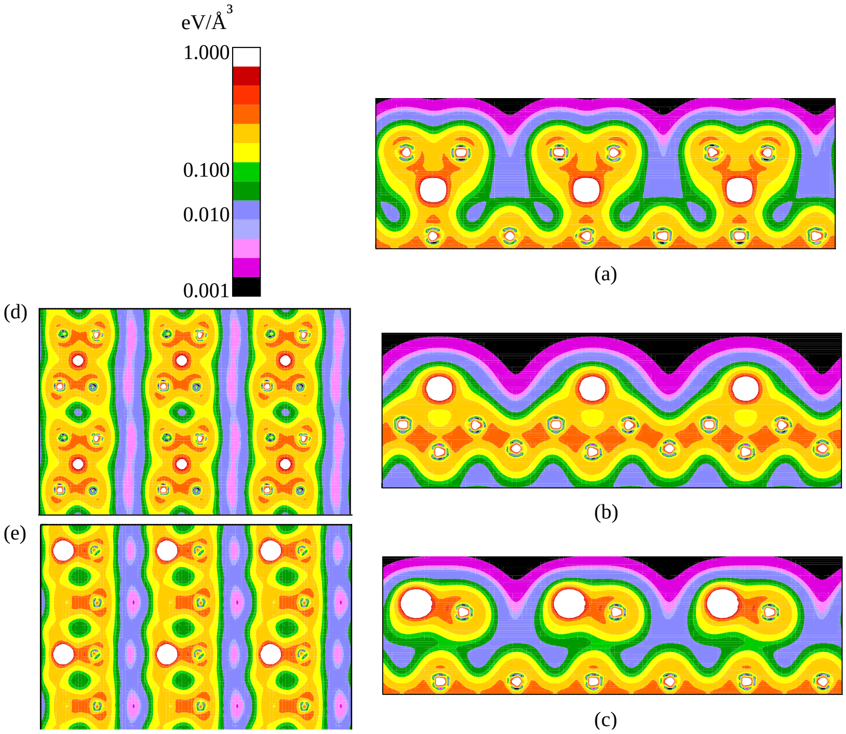

Fig. 5.5: Electron density in the (100) plane containing the adatom for single Mn atom adsorption on substitutional site (a), hollow site (b) and interstitial site (c). The electronic density for the (001) plane (at a certain $z$ above surface) for hollow site (d) and interstitial site (e). The bigger (smaller) white circles in every figure are the places of Mn (Si) atoms.

In the case of Mn adsorption on the substitutional site, the charge density contour plots are similar to those for the bare surface. The itinerant charge is distributed between Mn and the nearest Si and vanishes in the dangling bonds while in the other Si-dimer the dangling bonds are still occupied.

- **STM images :** In order to study the differences between various single Mn atom adsorption sites, the STM for adsorption of $\frac{1}{8}$ ML of Mn at hollow, interstitial in p(2×2) as well as c(4×2)and substitutional site on Si(001) are simulated.

In Fig. 5.6 the simulated STM images for a Mn impurity at the substitutional site(a), the hollow site (b), the tetrahedral interstitial site in a $(2 \times 2)$ cell (c), the tetrahedral interstitial site in a c$(4 \times 2)$ cell (d) and an experimental image (e) [2] are shown.

Besides the decrease of the dimer angle, which can also be seen in charge density contour plots, vanishing of the dangling bonds causes that the bean-like shape of dimers which are observed in the clean Si(001) surface are no longer visible (see Fig.4.10 Chap.4). In all simulated images, the occupied states have a maximum

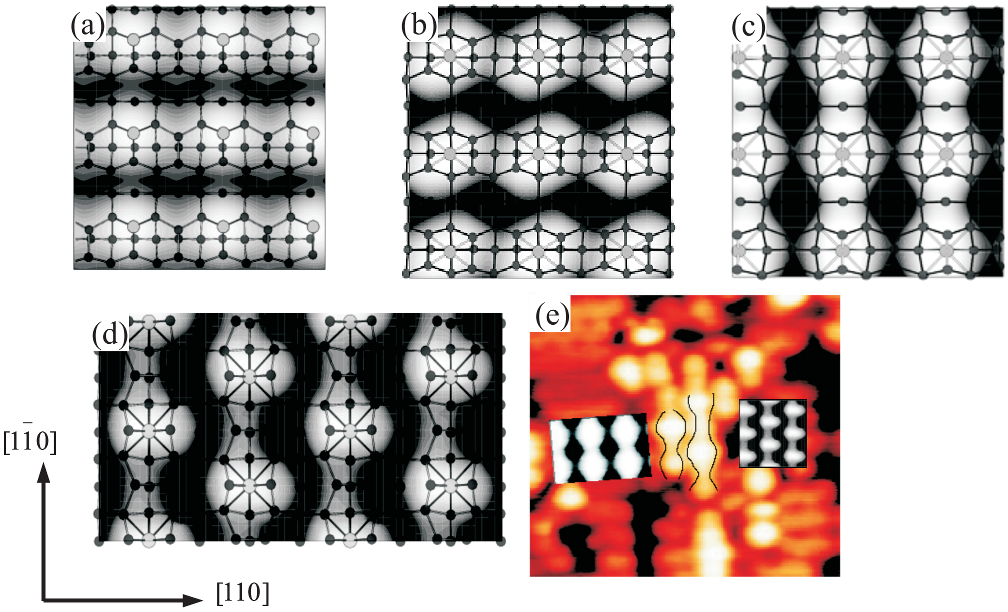

Fig. 5.6: Simulated STM images for single atom adsorption on: substitutional site (a), hollow site (b), interstitial p(2×2) unit cell (c), interstitial c(2×4) unit cell (d), and the experimental STM (e) Ref. [2].

between Mn-Si which appears as a bright protrusion in the STM image. The dark area is the region between dimer rows and the rest funnel-shape parts are $\pi$-states in the Si-Si dimers.

The simulated STM images for Mn in substitutional and hollow sites, Fig. 5.6-a and b, show bright and dark stripes in the [110] direction which are parallel to the surface dimer rows. The bright regions are always around Mn atoms and their shape depends on the bonds between Mn and the surface Si atoms. The substitutional site around Mn is protruded while the other dimer is recessed which is the effect of the charge distribution around Mn.

However, in the interstitial site, Fig. 5.6-c, the elongated dimer is shifted up, which causes the distribution of occupied states to be concentrated between dimers rows in the [1$\bar{1}$0] direction. Therefore the STM images show the upper dimer as a bright part while the position of other dimer appears dark, Fig. 5.6-c,d. In this structure there is no strong bond between the other Si-dimers and Mn.

In the c(4×2) interstitial model, Fig. 5.6-d, the strips are still in the [1$\bar{1}$0] direction but the protruding parts are shifted relative to each other which is similar to the experimental STM image, (see Fig. 5.6-e). The experimental image is obtained for a 2.4 V tip bias voltage and 0.03 ML coverage of Mn.

The STM pattern for Mn in the interstitial site looks symmetric in the direction parallel to dimer bonds in both $(2)$ and $c(4 \times 2)$ surface reconstructions.

More details of the bright part related to islands in experimental STM image and theoretical STM simulations are shown in Fig 5.7. A surface, where Mn sits in a c(4x2) structure below the Si-dimers, is clearly different from the STM picture of a clean, c(4x2) reconstructed Si surface, (see Fig. 4.10-a,c in Chap.4).

Figure 5.7-c and d, shows the experimental [2] and simulated curves of the height difference between the islands and the bare surface. A linescan is plotted which crosses the island in the STM images (see Fig. 5.7-a,b). In the experimental image, the island is built up on the bare surface and has a height of about 1.1-1.2 Å.

The three central peaks which are marked by A, B and C, are reproduced by the simulation. The central peak is the superposition of two peaks, which come from the two Si atoms which are located above Mn. This is the position of the Si-dimer which is lengthened and is higher than the surranding surface area.

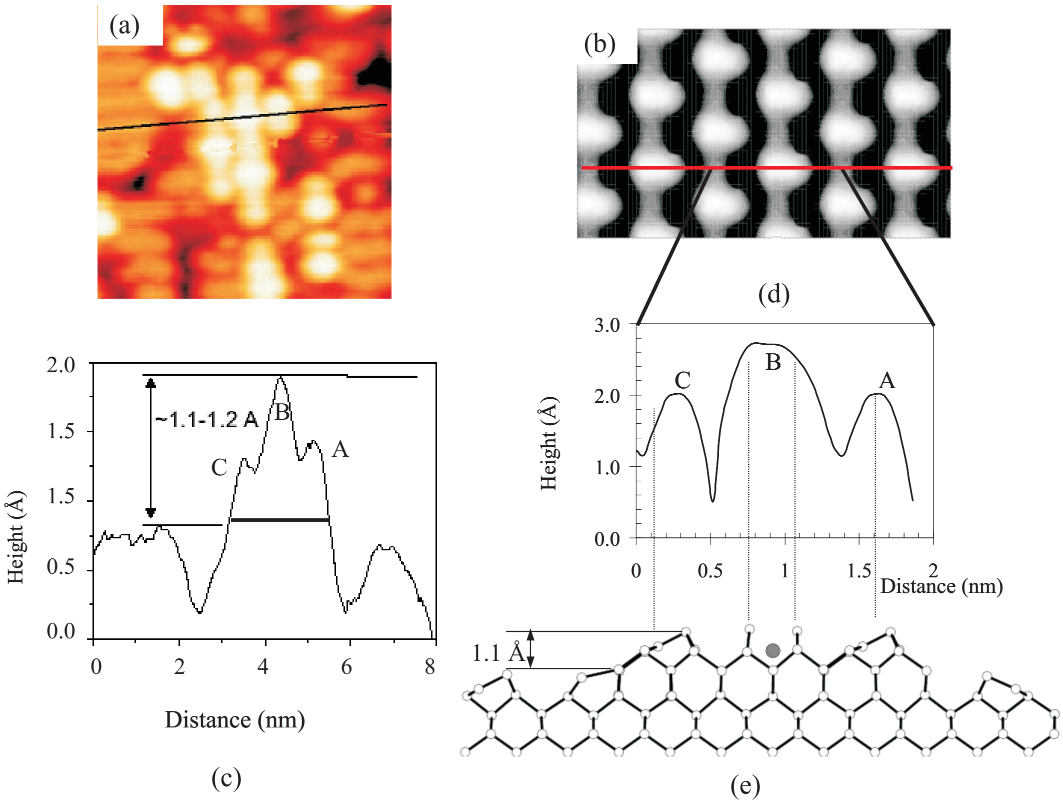

Fig. 5.7: Experimental STM image (a) and theoretical STM simulation (b) for $c(4 \times 2)$ unit cell. Curves (c) and (d) show the height difference in a linescan which runs across the bright part of the STM images. The linescans are indicated in the STM images. (e) ball-stick model of the c$(4 \times 2)$ structure.

The two smaller peaks on the right of and left are intact Si-dimers, which belong to the Si island, and do not contain any Mn (cf. Fig. 5.7-d). The difference in height between the large and the small peak amounts to about 0.6 Å which is in good agreement with the measurement.

The two regions on the right of and left of the central peaks in the linescan which appear approximately 1.1 Å lower than the maximum, belong to the substrate (cf. Fig. 5.7-c).

## 5.4 Influence of The Si-Dimer Vacancy

In the following part, the role of surface imperfections on Mn adsorption is investigated. The most abundant defect on a Si(001) surface is the missing-dimer defect [140]. It would be interesting to check the formation of a Mn-decorated missing-dimer defect.

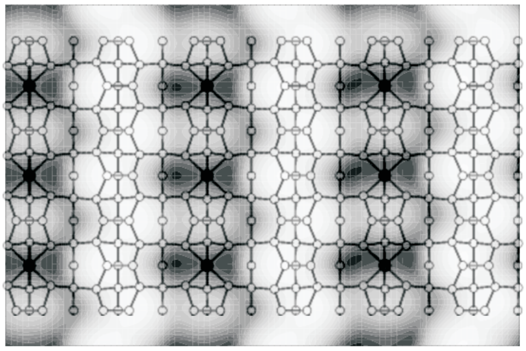

Fig. 5.8: STM simulation of Mn impurity at the position of a dimer vacancy in a $(4 \times 2)$ unit cell matched with a ball-and-stick model.

For Mn atoms occupying the dimer vacancy, first a Si-dimer must be removed, then Mn replaces it. In order to describe the surface with a missing-dimer defect, a larger unit cell is used, either $(2 \times 4)$ or $(4 \times 2)$. As it was discused before in Chap. 4, the first model is considered as a Si dimer row, consisting of blocks of three Si dimers, interrupted by a dimer vacancy. In the second case of the $(4 \times 2)$ unit cell, the surface consists of continuous rows of Si dimers, alternating with rows where a Si dimer and a dimer vacancy follow each other. The second type of dimer vacancies (single dimers alternating with vacant sites in a row) is more stable by 0.48 eV / unit cell. Therefore, this calculation has been performed in a $(4 \times 2)$ unit cell with $25\%$ dimer defects that means 1 / 16 ML Mn coverage. The adsorption energy of Mn at the dimer vacancy is calculated to be 4.29 eV for the $(4 \times 2)$ unit cell.

Formation of the defect site with Mn adsorbed becomes exothermic, if it is assumed that the two expelled Si atoms move to kink sites at steps (i.e., to a reservoir at the chemical potential of bulk Si).

In table 5.1, the thermodynamic stability of Mn adsorption on the Si-dimer vacancy structure are compared to the adsorption of Mn atom on the perfect Si surface. The

Mn adatom binds very strongly to vacancy site, with a binding energy of 1.4 eV larger than the binding energy at the hollow site. The Mn-atom binds clearly more strongly to the missing-dimer defect than to the normal Si surface. When it (the Mn atom) occupies the dimer vacancy, it comes very close to the surface and sits at about the same height as the Si dimers.

This case is similar to adsorption of Co on Si(001) [132]. Due to Mn-Si bonds the nearset Si-dimers become shorter and more horizontal. The Mn is rather highly coordinated with formation of 6 short Mn-Si bond. In this site Mn placed in the 2nd layer has a magnetic moment of 2.9 $\mu_{\mathrm{B}}$ which shows strong bonding between Mn and Si.

The STM image is simulated for the energy of $-0.5$ eV below the Fermi level (filled state), and an iso-surface is plotted with constant charge density of $10^{-6}$ / Å$^3$. The perfect dimer rows have a zig-zag shape protrusion pattern similar to the bare Si-surface. In the imperfect dimer rows, the white parts come from the Si-dimer while the dark parts belong to the Mn atom. The Si-dimer in the imperfect row is almost horizontal and about 0.7 Å higher than the Mn impurity.

## 5.5 Potential Energy Surface for Mn on Si(001)

In the previous section, the stable and meta-stable adsorption sites of Mn on Si(001) were discused. For a detailed study of adatom kinetics, the adatom diffusion pathways and energy barriers should be determined.

Diffusion of adatoms is one of the microscopic processes which controls epitaxial growth on the surfaces. The adsorbed atom binds on the surface at specific sites, exactly at the position of lowest potential energy for the adsorption. This adatom may be able to move from a binding site to an equivalent one without very much expenditure of energy. Therefore the adatom motion is stochastic in a two-dimensional random walk. The mean square displacement is proportional to the time and to the diffusion coefficient , $D$ ( $\langle r^2 \rangle \propto Dt$) [141, 142].

The rate of a microscopic process that may take place during diffusion which is proportional to the diffusion coefficient, can be calculated from:

$$\Gamma = \Gamma_0 \exp\left(\frac{-E_d}{k_B T}\right) \tag{5.2}$$

where $\Gamma_0$ is the pre exponential factor. The diffusion constant depends on temperature, jump length, and the adatom and substrate vibrations [141, 143]. $T$ and $k_B$ are temperature and Boltzmann constant, respectively. $E_d$ is the energy barrier which is the energy difference between the maximum (saddle point) and the minimum (equilibrium site) of the potential curve along the diffusion pathway.

In the description of surface adatom diffusion within the transition-state theory (TST) [144] framework it is important to have information about the potential energy surface (PES).

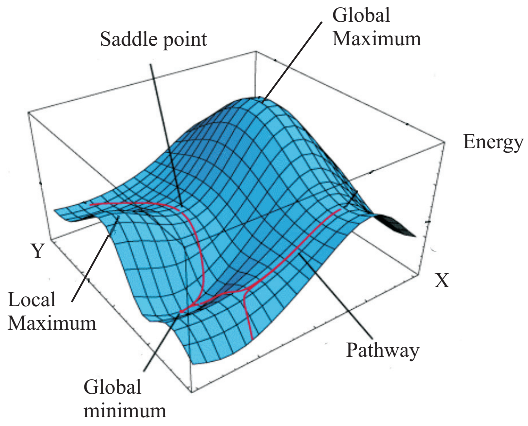

Fig. 5.9: Schematic of potential energy surface. $x$ and $y$ are coordinates of adatom and $z$ axis is adsorption energy.

In order to have a complete map of all binding sites and diffusion pathways one needs to calculate the ground state total energy of the adsorbate system for a dense mesh of adatom positions. This is the so-called potential energy surface.

The energy surface is mapped out in the following way. The adatom is placed at a number of positions $(x, y)$ on the surface. The dimer row is parallel to the $y$-axis, and the direction of the dimerization bond is along the $x$-axis. These positions form an equidistant grid with a spacing between the grid points of about 1 Å in $x$ and $y$ directions. Starting with the adatom above the surface, at each $(x, y)$ position the total energy is minimized simultaneously with respect to the electronic charge density and the remaining ionic degrees of freedom, i.e. the $x$ and $y$ coordinates of the adatom and the positions of the two inner layers are fixed.

The minimum of the energy with respect to the $z$-coordinate of the adatom and all coordinates of the substrate atoms is as follow:

$$E^{\mathrm{PES}}(X_{ad}, Y_{ad}) = \min_{\mathbf{R}} \min_{Z_{ad}} E^{\mathrm{tot}}(\mathbf{R}, \mathbf{Z}_{\mathrm{ad}}) - \mu_{\mathbf{ad}} \mathbf{E}^{\mathbf{bulk}}_{\mathbf{ad}} \tag{5.3}$$

Here **R** denotes the position of the substrate atoms, $\mu$ is chemical potential and $N$ is the number of each type of atom in the unit cell.

The global (local) minimum in the PES corresponds to the stable (meta-stable) binding positions of the adatom, and saddle points correspond to transition states for adatom diffusion.

In the description of an adatom on a surface within the framework of transition-state theory, it would be necessary to determine the energy barrier for a jump between two binding sites. One should locate the maximum energy along each possible path in the complete configuration space which connects the configurations of two binding sites. The minimum energy among these maxima is the energy barrier for diffusion and the total-energy function then has a saddle point at the corresponding configuration.

The minimum value of the energy barrier of different pathways between two minima is the so-called diffusion barrier.

We note that important binding sites and transition states could be missed in the so-defined PES, *e.g.*, sub-surface sites that cannot be reached by relaxing the adatom from above the surface. In this case, additional computational work has to be done to obtain the complete picture.

Usually, the pathway with the lowest energy barrier will be used most frequently, but other pathways may exist which have comparable barrier and contribute with less probability [145]. Therefore, the effective barrier should be measured by averaging over all possible pathways with respect to their probability.

Lastly,the combination of DFT calculations and kinetic Monte Carlo simulations describe and analyze epitaxial growth.

In order to have complete information about surface diffusion and sub-surface penetration barriers, two PES are mapped and several diffusion pathways are considered in the following part.

### 5.5.1 PES and Diffusion Pathway on The Surface

The potential energy surface for a Mn adatom *on* the Si(001) surface is mapped in Fig. 5.10. The energy minima were found by explicit energy minimization with respect to $x$ and $y$. The saddle points were pinpointed by interpolating the PES on a finer grid of points.

The binding position of the adatom, H, is the absolute minimum $on$ the surface. There is a local minimum on the $x$ axis which is 0.3 eV higher than the energy of the absolute minimum. There is a pathway connecting the absolute minima of two adjacent cells by passing through this point.

As was discussed before, the Mn atom binds most strongly at the hollow site (marked by H in Fig. 5.1), also called pedestal site by other authors, [124] located between two Si surface dimers. At this site, the Mn adatom makes bonds with all four neighboring surface Si atoms, while the Si–Si dimer bonds are elongated. The adatom in the global minimum (H) is 0.2 Å above the surface and the tilt angle slop of the buckled Si-dimers is reduced significantly.

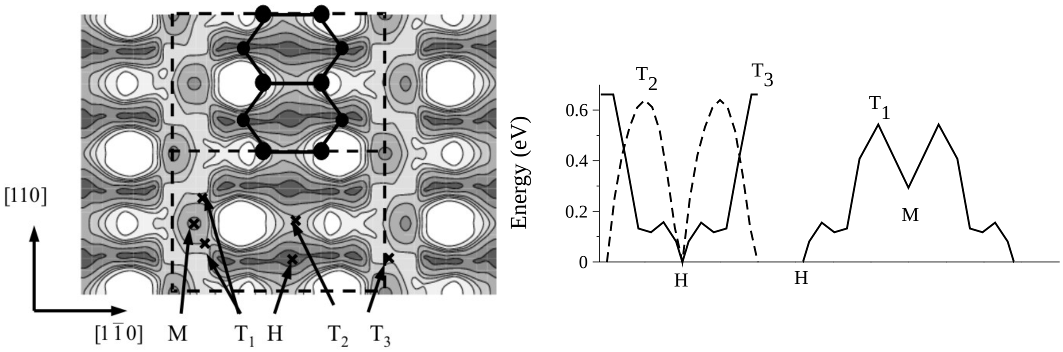

Fig. 5.10: The PES and diffusion pathway on the Si(001) surface. The diffusion barriers for hopping to the next on-surface minimum are in the range of 0.6 eV. H and M are global and local minimum, $T_1$, $T_2$ and $T_3$ are saddle points. The white region are maximum and the dark parts are minimum in the potential energy surface. The space between contour lines is 0.2 eV.

In the weaker binding site (M in Fig. 5.10), the Mn adatoms interacts with the (occupied) dangling bond of the upper Si atom in the surface Si dimer.

There are three diffusion routes for Mn on the surface:

1) An indirect pathway via the minimum M, passing twice through symmetry-equivalent saddle points $T_1$ with energy barrier of 0.55 eV.

2) A pathway which runs parallel to the dimer rows which crosses the dimer short bridge site ($T_2$).

3) A pathway perpendicular to the dimer rows that runs between two adjacent dimers in the neighboring rows ($T_3$).

The first outcome is that the diffusion barriers along pathway ($T_2$) and ($T_3$) are almost the same with 0.65 eV which indicates isotropic diffusion in parallel and perpendicular to the dimer rows. On the contrary, for diffusion of a Si atom this surface behaves anisotropic with 0.6 eV and 1.0 eV energy barrier along and perpendicular to the surface dimer rows, respectively [146].

### 5.5.2 PES and Diffusion Barrier for Penetration to The Sub-Surface (site $I_1$)

It is well known that Mn in bulk silicon is a mobile impurity which occupies preferentially interstitial sites. [147, 148] For this reason, it could be expected that sub-surface sites, in addition to on-surface sites, play a role for Mn adsorption and diffusion, and we consider this possibility in this Section.

The second-layer interstitial site below the Si dimer, $I_1$, is the most stable site for Mn, Fig. 5.1. With 3.8 eV adsorption energy it is actually lower in energy than any surface site. Now the question arises how Mn diffuses on this surface to reach the sub-surface site and how high the energy barrier for penetration to the sub-surface is.

Determining the diffusion pathway requires special care, because considerable relaxation of the neighboring Si atoms occurs along the pathway. For this reason, we plotted the PES for a Mn atom in a $[1\bar{1}0]$ plane perpendicular to the surface, which intersects both the hollow and the interstitial sites. We fix the Mn atom at a set of positions in this plane, and relax the substrate Si atoms in each case. The resulting PES, spanned by [110] and [001] vectors, is displayed in Fig. 5.11. It is seen that for the most favorable pathway the Mn adatom first moves slightly upward away from the hollow site. Thereby, the surface Si dimer is elongated, thus giving room for the Mn atom to find its way to the sub-surface interstitial site. The energy barrier for the penetration pathway H-T-$I_1$, crossing the transition state T, is about 0.3 eV measured from the hollow site, and about 1.2 eV for the reverse process (see Fig. 5.11-b).

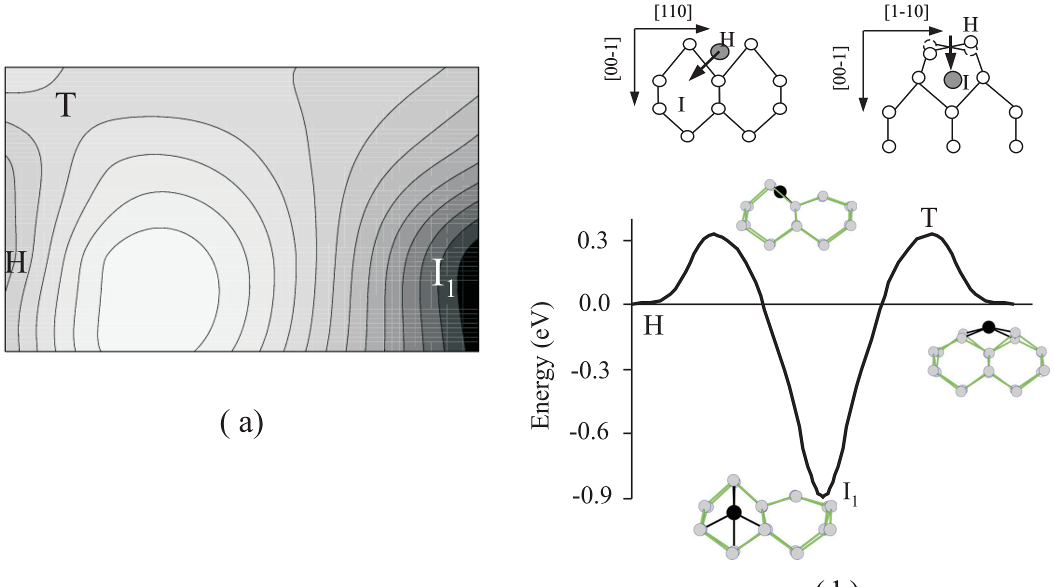

( a)

( b)

Fig. 5.11: PES plot and diffusion barrier for penetration to the sub-surface site (a). The energy barrier is about 0.3 eV. The dark region is the global minimum and the bright part is the place of maximum in the PES. Structure of minimum and saddle points are shown in figure (b). The space between contour lines is 0.125 eV.

In addition, one can consider the possibility that a Mn atom coming from the vacuum could directly reach the second-layer interstitial site, by normal incidence and breaking of the Si dimer. For these calculations, a $c(4\times 2)$ unit cell is used , in order to avoid spurious interactions between neighboring Si dimers being broken, which could occur if a $p(2\times 2)$ cell would be used for simulating this process. The calcula-

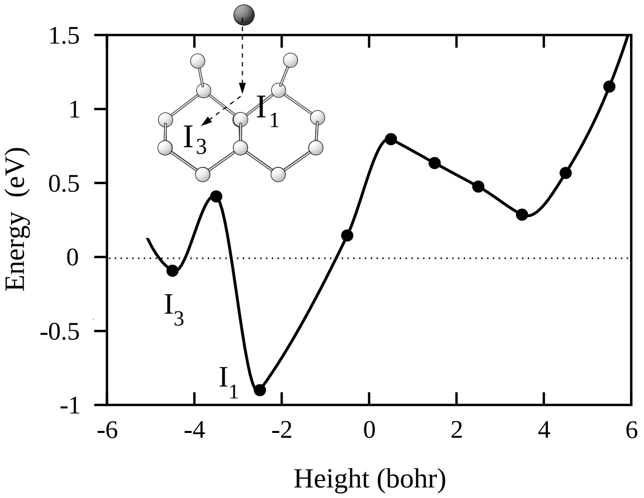

Fig. 5.12: Energy profile for a Mn atom approaching the Si(001) surface from the vacuum along the path shown in the left panel, breaking the Si dimer and inserting itself via the stable sub-surface site $I_1$ into the third-layer interstitial site $I_3$. The energy barrier for the last step, from $I_1$ to $I_3$, is about 1.3 eV.

tions show that the energy of this system first decreases when Mn approaches the surface, but then rises again by about 0.5 eV and goes through a maximum before decreasing finally to the binding energy in the interstitial site (Fig. 5.12).

The intermediate increase in energy is associated with the Mn atom breaking the Si-Si dimer bond. However, the energy gained by the Mn atom during approaching the surface is more than sufficient to overcome this energy barrier. Hence we conclude that a deposited Mn atom can reach the interstitial site both indirectly through the hollow site, or directly by breaking the Si dimer upon impact, if the site and angle of impact are appropriate, but the indirect approach is faster because of the lower barrier. The possibility of such a direct process was also demonstrated by calculations for Mn on GaAs(001). [138]

The results of Dalpian *et al.* are in good agreement with the present work, except for the energy barrier between the hollow site and the sub-surface interstitial site, which we find to be 0.3 eV while they reported a higher value of 0.96 eV .

The behavior of Mn on Ge (001) is similar to Si (001) [123]. The adatom penetrates to the 2nd layer interstitial site via the hollow site. Zhu *et al.* reported an energy barrier of 0.59 eV and the reverse process barrier is 1.22 eV, which is comparable with results for Si in this work. Also for Ge, the deeper layer interstitial and substitution sites are less stable than the 2nd layer interstitial site.

In deposition of Mn on GaAs(001) the interstitial site below the As dimer is also the most stable site for Mn on GaAs(001) [138]. Mn with 0.2 eV energy cost breaks the dimer and penetrates to the sub-surface. In GaAs the cave site is a stable site and the energy barrier to reach this position is almost zero. This site is located between two adjacent dimers above a Si atom in the fourth layer. In contrast to GaAs, the cave site is an unstable adsorption site for Mn on Si(001). The Mn atom moves up from this position to the surface site, $M$, which is a local minimum in the PES (see, fig. 5.1 and 5.10 ), without any barrier.

The present calculations show that there are high energy barriers for diffusion of Mn into deeper layers. To reach the third-layer site, Mn must overcome an energy barrier of 1.3 eV, measured from the second-layer interstitial site (Fig. 5.12).

Moreover, it is concluded that Mn atoms, even after penetrating to the sub-surface site, will diffuse mainly through the on-surface (H) site to find other Mn atoms for nucleation of some silicide, rather than through a bulk diffusion mechanism.

The diffusion barriers of Mn in Si bulk reported in the literature are around 1.3 eV [147] and 1.17 eV (theory) [137].

## 5.6 Effect of Adatom Interaction : Submonolayer, Overlayer, or Bilayer Structures

In a hierarchy of growth, the adsorption of Mn at higher coverage, in the range between 1/4 and 1 ML will be studied. With the choice of the $(2 \times 2)$ cell, this corresponds to adsorption of 2–8 Mn atoms per supercell.

For two Mn atoms, one possibility is the adsorption at adjacent interstitial and hollow sites. This geometry is found to be the most stable arrangement for a pair of Mn atoms in the present calculations. Other configurations that can be realized by two Mn atoms in the $p(2 \times 2)$ cell correspond to infinite chains of Mn adatoms. Chains in the [110] direction (along the dimers rows) can be formed in two ways, either by occupation of all on-surface hollow sites, or by occupation of all sub-surface interstitial sites.

It is found that the adsorption energy per Mn atom in an infinite chain is larger than for a single atom per unit cell for the hollow site, while for the interstitial site the infinite chain has a lower absorption energy compared to single Mn atoms. In other words, Mn adatoms in hollow sites interact attractively, whereas Mn atoms in the interstitial site show a repulsive interaction. This can be understood from the fact that Mn atoms in interstitial sites introduce tensile strain by widening the Si crystal lattice in their neighborhood, and hence two interstitial Mn atoms repel each other through these strain fields. However, a chain of interstitial Mn atoms is still lower in energy than the chain of hollow site Mn atoms; i.e., the trend for

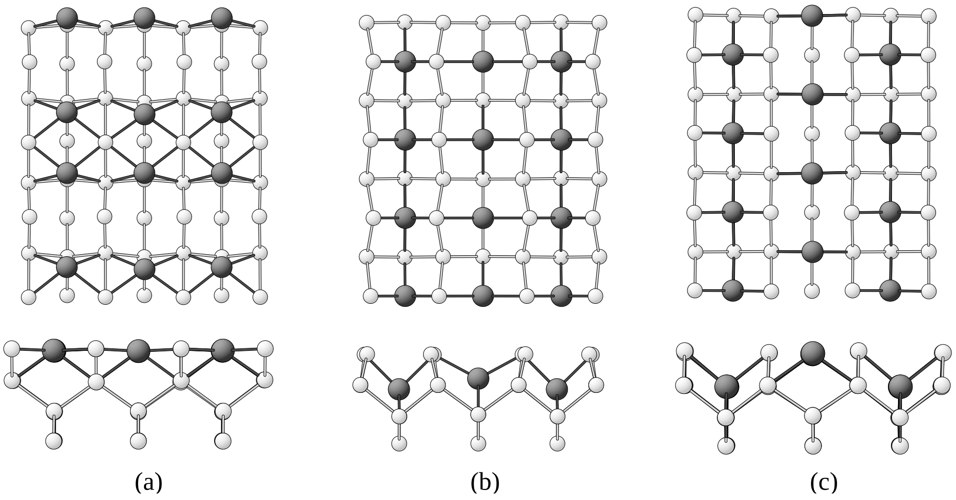

Fig. 5.13: Different possible structures for adsorption of 1/2 ML of Mn on Si(001), shown in top view (upper panels) and side view (lower panels). (a) relaxed structure resulting from Mn in on-surface sites only (b) in sub-surface sites (c) in sub-surface and cave sites.

occupying sub-surface positions persists.

Furthermore, chains of on-surface Mn atoms in $[1\bar{1}0]$ direction perpendicular to the Si dimer rows are considered. Alternately one Mn atom is in a hollow site, and one Mn atom is in a cave site. Although the adsorption energy per atom is less than the average adsorption energy of these two sites calculated separately (i.e., there is attractive interaction), this chain is energetically less favorable than any chain of Mn atoms running in [110] direction.

For coverage 3/8 ML, i.e., 3 Mn atoms per unit cell two possibilities are studied:
For on-surface adsorption a chain of Mn atoms in hollow sites, plus one Mn atom in a cave site is considered.
For sub-surface adsorption a chain of interstitial Mn atoms, plus one Mn atom occupying a hollow site on the surface is supposed to form.
As for the 1/4 ML case, the latter possibility, combining interstitial and hollow sites, is energetically more favorable. In both geometries, the Si dimers are still intact, albeit elongated.

For a coverage of 1/2 ML there are 4 Mn adatoms occupying both hollow sites and both cave sites of the unit cell. Starting from this geometry, the surface spontaneously transforms to a configuration where each of the Mn atoms has four in-plane bonds to neighboring Si atoms, formerly being part of Si dimers, which have been broken up due to bonding to the Mn atoms. In addition, each Mn atom establishes two bonds to second-layer Si atoms. This structure has a (1×1) periodicity, the same

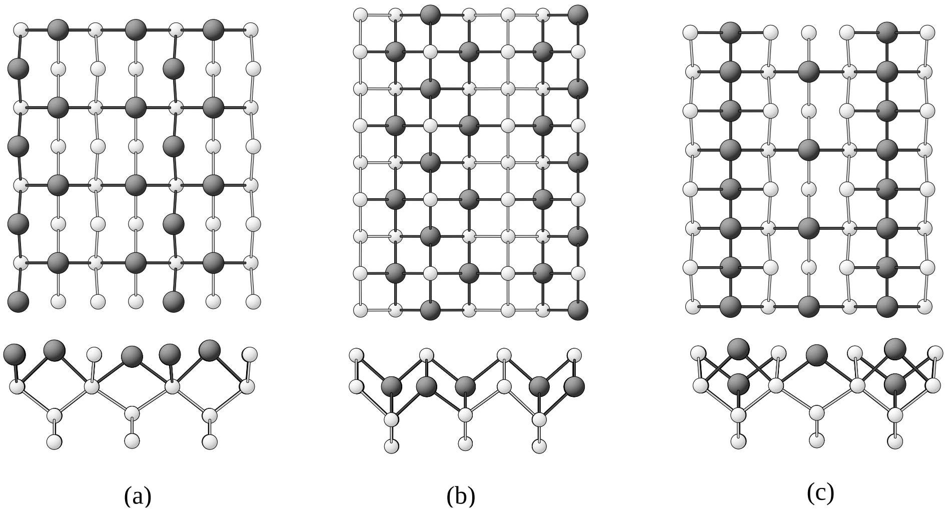

Fig. 5.14: Structures for adsorption of 3/4 ML of Mn on Si(001), shown in top view (upper panels) and side view (lower panels). (a) relaxed structure resulting topmost layer (b) sub-layer with Si-capping layer (c) from 1/2 ML in on-surface sites plus 1/4 ML in sub-surface sites.

as the underlying substrate. The energy of this structure can be lowered slightly if two neighboring Mn atoms move toward each other along the [110] direction, see Fig. 5.13-a. Due to this relaxation, the symmetry of the surface reconstruction is lowered from $(1 \times 1)$ to $(1 \times 2)$, with the long side of the unit cell now along the direction of the former Si dimer row. Alternatively, the case of sub-surface adsorption are also studied. This atomic configuration is obtained by relaxing a structure where Mn atoms are sitting in interstitial sites, and also at cave sites in the trenches between Si dimer rows, the latter Mn atoms either bonding to two third-layer Si atoms (see Fig. 5.13-b), or sitting directly above a third-layer Si atom (cf. Fig. 5.13-c). As a result of the calculations, it is found that at 1/2 ML coverage, on-surface Fig. 5.13-a and sub-surface Fig. 5.13-b adsorption yield the same energies within numerical accuracy, while the mixed structure shown in Fig. 5.13-c gives an energy lower by about 0.24 eV per adatom.

Upon further increasing the number of Mn atoms in the mixed Mn-Si layer, the system has the tendency to adsorb the additional Mn atoms by a mixed occupation of both sub-surface and on-surface site (cf. Fig. 5.14-c) rather than in the sub-surface layer, Fig. 5.14-b, and topmost layer, Fig. 5.14-a . This configuration, is also found to be energetically more favorable by about 0.06 eV per atom than an alternative when Mn substitutes for the atoms in the sub-surface layer.

For the magnetic coupling of Mn atoms in the same layer, the antiferromagnetic ordering is found to be energetically preferred by about 0.05 eV per atom compared to ferromagnetic ordering. For mixed structures with $\theta = 3/4$ ML, the energy difference between two possibilities where the dense Mn layer is the topmost layer or in the sub-surface is calculated. The first configuration is lower in energy by 0.11 eV.

Table 5.2: Average adsorption energies per Mn atom of ordered monolayer structures at various Mn coverages $\theta$ with respect to bulk Mn and bulk Si. The left column is for all Mn atoms occupying on-surface (H) sites, and the middle column is for all Mn atoms in sub-surface ($I_1$) sites, the right column is for structures where sub-surface ($I_1$) and on-surface (H) sites are alternatingly populated.

| Mn coverage (ML) | on surface eV/Mn | sub-surface eV/Mn | sub+on surface eV/Mn |
|---|---|---|---|
| $\theta = 1/8$ | 2.91 | 3.8 | — |
| $\theta = 2/8$ | 3.01 | 3.4 | 3.44 |
| $\theta = 3/8$ | 3.32 | 3.31 | 3.40 |
| $\theta = 4/8$ | 3.29 | 3.31 | 3.55 |
| $\theta = 6/8$ | 3.06 | 3.45 | 3.52 |

The results for adsorption of 1/8 ML up to 6/8 ML of Mn are summarized in Tab. 5.2, quoting the average adsorption energy per Mn atom. The mixed occupation of sub-surface and on-surface sites is found to be most favorable, and leads to a monotonous decrease of the energy per atom during the increase of coverage. In contrast, occupation of on-surface sites only is energetically less favorable. Hence, the former growth mechanism, alternating occupation of sub-surface and on-surface sites, is identified as the preferred mechanism for growth of MnSi islands on Si(001).

# Chapter 6

# Thin Film Growth on Si(001)

## 6.1 Introduction

There are a few experimental results about growth of manganese films on Si(001) [15, 16, 128, 149]. They all agree in this point that pure Mn films can not be grown on these surfaces but hetero-structure Mn-Si compounds are observed. Wang $et\ al.$ reported thin film formation of MnSi and $\mathrm{MnSi}_{1.7}$ at 400 and 600 °C by solid phase reaction on Si(001) [128]. Recently, in scanning tunneling microscope images, Lippitz $et\ al.$ observed two different 3D-islands that were grown by deposition at around 450 °C. These islands are a pancakes-stack-like island which is interpreted as MnSi and a hut-like structure which seems to be $\mathrm{Mn}_5\mathrm{Si}_3$. The regular Si-dimer reconstruction with (2×1) periodicity was also observed on the surface [16].

The Mn atoms in suitable chemical environments possess considerable magnetic moments. Moreover, both fcc-Mn and some MnSi compounds are closely lattice-matched with the Si(001) surface (within a few percent of the relevant lattice constants). Therefore, it is conceivable that Mn-silicide thin films could be grown on Si. It is intersting to discuss the stability of pseudomorphic Mn and MnSi thin films for growing ferromagnetic films on Si(001). The present work focuses on their atomic structure, thermodynamic stability, and magnetic properties.

It has been discussed in Chap. 2, that stable Mn bulk phases show either antiferromagnetic (AFM) ordering or complex spin structures [63], while the metastable ferromagnetic (FM) state emerges at an expanded volume. It is, therefore, conceivable that a ferromagnetic pseudomorphic fcc-Mn film, with a lattice constant slightly expanded to match the Si(001) surface, could be formed. Additional to such film the epitaxial structure of compounds is considered which is formally resulting from substitution of part of the Mn atoms in fcc-Mn by Si atoms. These films have locally a B2 structure of Mn-mono-silicide, which is not as stable as the natural B20 structure but it can be grown epitaxially under non-equilibrium condition with molecular beam epitaxy (MBE) [76]. Recently, the stability of such films has been theoretically studied by Wu *et al* [150].

The stability of thin films containing more than 1 ML of Mn is conveniently discussed in terms of their formation energy. Since the Si dimer reconstruction is lifted already after deposition of 1/2 ML of Mn, it is appropriate to use a Si(001)-$(1 \times 1)$ unit cell to study thicker films.
The formation energy is defined as

$$E^{\text{form}} = \frac{1}{2}(E^{tot} - \sum_i N_{\text{i}}\mu_{\text{i}}) - \gamma^{\text{surf}}_{\text{Si(001)}} \tag{6.1}$$

where $E_{\text{total}}$, $N$ and $\mu$ refer to the total energy per $(1 \times 1)$ supercell, the number of atoms in the $(1 \times 1)$ cell, and the chemical potential of the atomic species as calculated from bulk materials, respectively. $\gamma^{\text{surf}}_{\text{Si(001)}}$ is the surface energy of the clean reconstructed Si(001) surface, which is found to be 1.25 eV per $(1 \times 1)$ cell in this work.

Since the ground-state $\alpha$-Mn has a complicated structure [1], the total energy of $\gamma$-Mn has been calculated [63]. The chemical potential of Mn is obtained from our calculation for bulk Mn in the fcc-structure ($\gamma$-Mn) corrected by $-0.07$ eV/Mn, which is the energy difference per atom between $\alpha$-Mn and $\gamma$-Mn.

All calculations in this chapter are done using a $(1 \times 1)$ supercell with a $10 \times 10 \times 1$ **k**-point mesh for Brillouin zone integration.

In this section, two types of films are studied - either pure Mn or Mn-Si alloy films for up to 3 ML coverages are considered.

## 6.2 Coverage of 1ML on Si(001)

### 6.2.1 Thermodynamics, and Structural Stability

The foregoing calculations on Mn bulk established that the lattice constant for fcc-Mn is a=3.77 Å [2] which matches the Si(001)-(1×1) cell lattice of 3.88 Å quite well. The atomic density of the Mn layer is twice that of a Si layer and therefore 2 Mn atoms per cell are considered as one monolayer for a Si(1×1) cell.

For 1ML coverage several growth possibilities are simulated. They can be divided into two categories, namely, i) a dense Mn layer and ii) a sparse Mn bilayer with a 1:1 ratio of Mn and substrate Si atoms. The structures and formation energies for both pure Mn and Mn-Si films in a ferromagnetic and an antiferromagnetic phase are summarized in fig. 6.1.

---

[1] See section 3.4 of chapter 3.

[2] the experimental value is 3.72 Å [67].

The formation energy for the first structure, formed by a dense Mn sub-layer with a Si-capping layer on top, is calculated, (Fig. 6.1-a). The presence of the Si-capping layer greatly reduces the energy costs for formation of a dense film on the surface. This is due to the higher coordination of Mn atoms in the sub-layer to Mn and Si neighbors, compared to a dense Mn overlayer. Putting the dense Mn layer on the surface, rather than in the sub-surface region, leads to an increase of the formation energy from 0.567 eV to 1.687 eV.

For the sub-layer Mn-film, the parallel spin alignment is found to be thermodynamically more stable than an intralayer anti-parallel spin arrangement, while a change from FM to AFM interlayer coupling is observed for an Mn film on the surface.

The capping-Si layer structure shows a strong buckling of 0.43 Å for Si and 0.17 Å for Mn, respectively. The bonding between Si atoms in the topmost layer and Mn atoms in the sub-layer is rather weak, leading to long Si2-Mn1 and Si2-Mn2 bonds (2.67 Å and 2.78 Å). These bonds are however essential for the stability of the structure. This can be seen by removing a Si2 atom from the surface, which leads to an increase of the formation energy, $E_{\mathrm{form}}$, of 0.77 eV.

The dense Mn layer with a Si-capped structure is also more stable than structures with mixed Mn-Si occupation. Four different structures for Mn-Si mixed phases are shown in Fig. 6.1(b, c, d, f). The AFM phase is considered as an interlayer structure of opposite spin orientation.

In the MnSi bilayer structure, 50% of the Mn atoms in the sub-surface layer are interchanged with atoms of the Si overlayer (cf. Fig. 6.1-b). Though this structure can be considered as a sparse alternating Mn-layer perpendicular to the surface, its formation energy still rises by the order of hundreds of meV compared to Mn in the sub-layer. Formation of an intralayer AFM spin alignment is more stable than both FM and interlayer AFM spin arrangement by 0.122 eV / unit cell and 0.129 eV / unit cell, respectively. In this structure the shortest interlayer distance in the Mn-Si bilayer is about 1.71 Å . This value is smaller than Mn in the overlayer and Mn in the sub-layer by 15 % and 20 % , respectively . Furthermore, the roughness and surface corrugation in this structure are reduced.

| **One ML Mn on Si(001)(1x1) cell** | 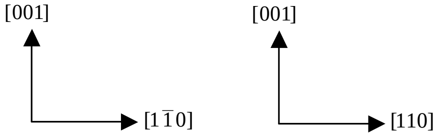 | **FM eV/cell** | **AFM eV/cell** |
|---|---|---|---|
| **Dense layer Mn with capped Si**<br>**(a)** | 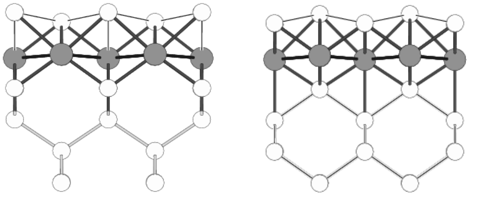 | **0.567** | 0.787 |
| **Bilayer mixed Mn-Si**<br>**(b)** | 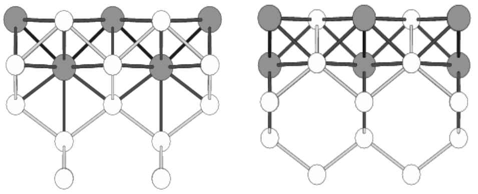 | 0.902 | 0.895 |
| **Bilayer Mn-I**<br>**(c)** | 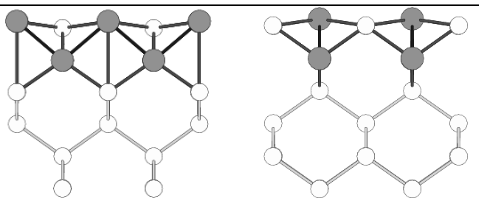 | 1.399 | 1.435 |
| **Bilayer Mn-II**<br>**(d)** | 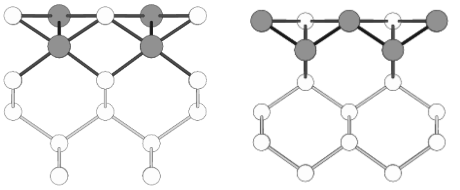 | 1.471 | 1.446 |
| **Dense overlayer Mn**<br>**(e)** | 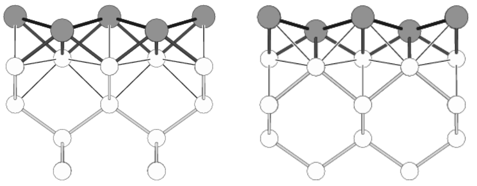 | 1.704 | 1.687 |
| **Bilayer Mn-III**<br>**(f)** | 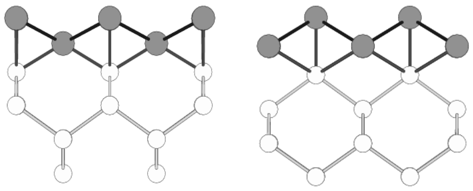 | 2.56 | 2.37 |

Fig. 6.1: Side view for two different directions of several configurations with 1 ML Mn coverage. Big black circles represent Mn and small white circles Si.

In addition, some other bilayer structures with
i) One diluted Mn layer and one dense Mn-Si layer on top, Fig. 6.1-c, d and
ii) Two diluted Mn overlayers, Fig. 6.1-f are considered.
In the later case, due to Mn-non-saturated bond and weak Mn-Mn bond is quite unstable and $E_{\mathrm{form}}$ in AFM phase is 2.37 eV. These results show that The adsorption in separate layers, i.e. one pure dense Mn monolayer is energetically more favorable than two intermixed layers.

The above allows the conclusion, that a Mn-dense layer with Si capping is the most stable structure (of the considered). For this reason we will concentrate on this arrangement of Mn and Si and study higher coverages of the dense atomic layer.

### 6.2.2 Electronic and Magnetic Structure

The different spin alignment between Mn-atoms in sub-layer and topmost layer was mentioned previously. Mn in the sub-layer has a ferromagnetic spin configuration, while the magnetic structure of Mn in the topmost layer is antiferromagnetic.

The origin of this magnetic transition, which is due to the structural transformation of Mn being moved from the topmost layer to the sub-surface layer, can be explained by an analysis of the orbital-projected density of states shown in Fig. 6.2.

In the Mn-DOS plots for both the overlayer and the sub-surface layer, a large exchange splitting[3] of almost 4 eV and 2 eV, respectively, is found. The $d$-band-widths of both the majority (minority) spin of Mn is narrower than in comparison to the bulk Mn which indicates the Mn-$d-d$ overlap is more than the Mn-$d$ and Si-$sp$ hybridization. The Mn $3d$-bands are broadened in the sub-layer structure and have a large overlap around the Fermi level, which reduces the spinpolarization at the Fermi level. The spin polarization ($P$) of carriers is about 30 % at the Fermi level, as estimated from the spin-resolved total DOS shown in Fig. 6.2. The spin polarization is defined by:

$$P = \frac{\rho_{\uparrow}^{\mathrm{F}} - \rho_{\downarrow}^{\mathrm{F}}}{\rho_{\uparrow}^{\mathrm{F}} + \rho_{\downarrow}^{\mathrm{F}}} \times 100\% \tag{6.2}$$

where $\rho_{\uparrow}^{\mathrm{F}}$ and $\rho_{\downarrow}^{\mathrm{F}}$ are the density of states for spin up and down at the Fermi level, respectively.

According to the itinerant $sp-d$ exchange model [151], in the Mn-Mn interaction two mechanisms are in competition over all interaction. These interactions can be

---

[3] The exchange splitting is measured by the difference between the position of the highest peak in the total DOS for spin up and spin down.

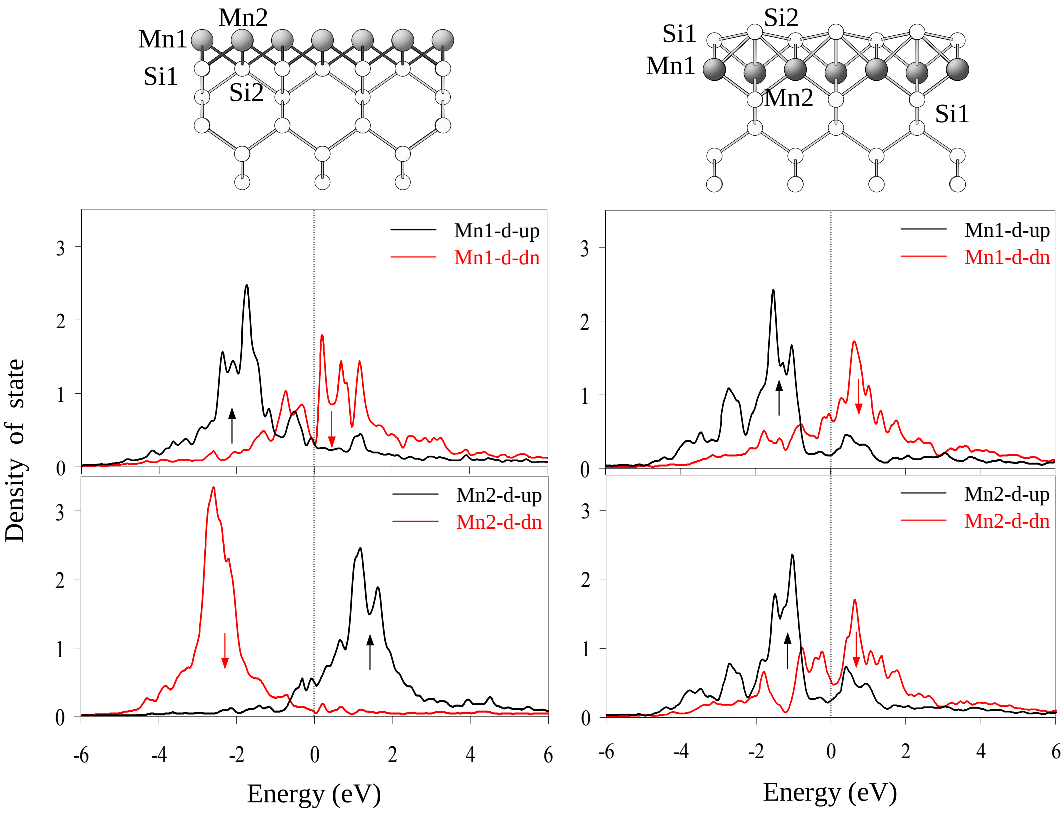

Fig. 6.2: Density of states for spin up and down $d$-orbitals of the Mn atoms in the a dense layer of the Mn-overlayer (left panel) and the Mn-sub-layer (right panel).

interpreted as the $d-d$ direct antiferromagnetic coupling and the $d-sp-d$ indirect intercation which the ferromagnetic coupling is more favorable.

There is AFM coupling between the Mn-sub-layer and its nearest neighbor Si. The Mn atoms interact with each other through the three Mn1-Si-Mn2 channels in the interface and capping layer. From itinerant $sp-d$ exchange model, the electron kinetic energy can be reduced by itinerant $sp-d$ exchange which this effect stabilizes the FM spin coupling between the Mn atoms [150].

The $sp-d$ exchange in the Mn-overlayer is not as big as Mn-sub-layer because there is only one Mn1-Si-Mn2 channel. Then direct $d-d$ exchange between Mn is more effective than the $sp-d$ exchange between Mn and Si. This direct the $d-d$ hopping makes an AFM Mn-Mn coupling. This is a qualitative explanation for the AFM - FM transition which is caused by the Si capping layer. Now the calculated results confirm this explanation also quantitatively. The Mn-sub-layer structure was found to have a FM ground state. The energy cost associated with a FM-AFM spin reverse is 0.22 eV / cell in the Mn-sub-layer which suggest that the $sp-d$ exchange mediated FM coupling is rather strong in Si-Mn on Si(001).

The same justification is valid for Mn-Si bilayer (which is kind of double layer mixed) structure for which the intralayer AFM coupling has lower energy. In this atomic geometry, there are two hopping channels for itinerant electrons in the $sp-d$ hybridized band but still the direct $d-d$ exchange prevails effect, because the Mn-Mn distance is as short as the Mn-Si distances.

Table 6.1: Spin moments (in $\mu_\mathrm{B}$) of the Mn-overlayer, sub-layer and mixed MnSi layer at their respective magnetic ground states. $\mathrm{Si}^\mathrm{S}$ is substrate atom, $\mathrm{Si}^\mathrm{I}$ is an atom in the interface and $\mathrm{Si}^\mathrm{T}$ is a Si-capping atom. Note that a non-negligible spin moment is induced on the Si atoms in surface and interface Mn.

| Structure | $(\mathrm{Si})^\mathrm{S}$ | $\mathrm{Si}_1^\mathrm{I}$ | $\mathrm{Si}_2^\mathrm{I}$ | $\mathrm{Mn}_1$ | $\mathrm{Mn}_2$ | $\mathrm{Si}_1^\mathrm{T}$ | $\mathrm{Si}_2^\mathrm{T}$ |
|---|---|---|---|---|---|---|---|
| Mn-overlayer | -0.04 | 0.01 | -0.042 | -3.68 | 2.04 | — | — |
| MnSi-bilayer* | 0.03 | — | 0.00 | -1.53 | 3.31 | 0.01 | — |
| Mn-sub-layer | 0.02 | -0.07 | — | 1.61 | 2.16 | -0.06 | -0.04 |

(*) refers to the Fig. 6.1-b

The lower coordination of Mn in the overlayer compared to the sub-layer increases the magnetic moments up to 40% from 2.16/1.61 $\mu_\mathrm{B}$ for sub-layer to 3.67/2.04 $\mu_\mathrm{B}$ for the topmost layer. The magnetic moments of the three top layer atoms in the discussed structures (shown in Fig. 6.1) are listed in Tab. 6.1. The induced magnetic moment in the Si atoms at the interface is larger than the one at the surface. Moreover, because of the strong Si-$3sp$ Mn-$3d$ hybridizations (also seen in Fig. 6.2), the Si *3p* state becomes spin-polarized. The down-spin component below or at the Fermi level is increased compared to the up-spin component, and thus the two capping $\mathrm{Si}_1^\mathrm{T}$ and $\mathrm{Si}_2^\mathrm{T}$ and the interface $\mathrm{Si}_1^\mathrm{I}$ have an induced negative spin moment.

Tab. 6.1 shows that the presence of a Si capping layer causes an interesting AFM-FM transition, thereby reducing the spin moment from 3.68 $\mu_\mathrm{B}$ and 2.04 $\mu_\mathrm{B}$ for Mn1 and Mn2 in the AFM structure to 2.16 $\mu_\mathrm{B}$ and 1.61 $\mu_\mathrm{B}$ for Mn1 and Mn2 in the FM Mn-sub-layer.

## 6.3 Coverage of 2ML on Si(001)

### 6.3.1 Thermodynamical and Structural Stability

The preceeding discussion showed that a structure with a dense Mn layer covered by a Si layer is generally preferred over all others. This point supports further calculations with higher Mn coverage for only some probable structures. For $\theta = 2\,\mathrm{ML}$

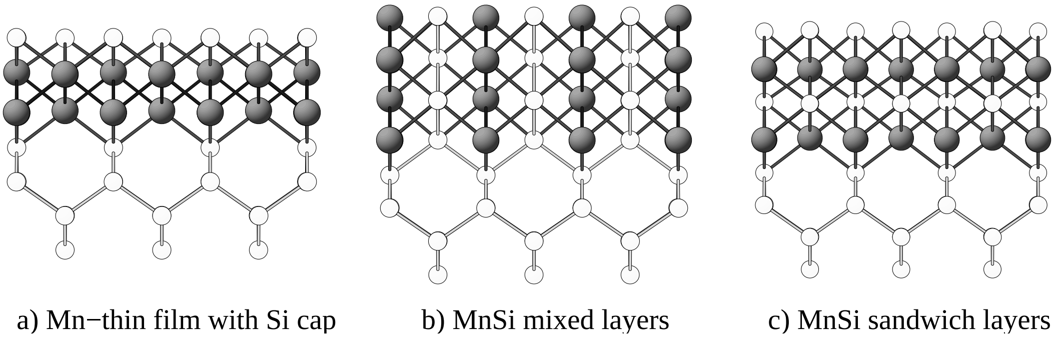
a) Mn−thin film with Si cap b) MnSi mixed layers c) MnSi sandwich layers

Fig. 6.3: Side view of structures with 2 ML coverage Mn / Si(001). Big black circles represent Mn atoms and small white circles represent Si atoms.

three structures with a FM, an interlayer AFM and an intralayer AFM magnetic configuration are studied (see Fig. 6.3):

1) A structure with a pure Mn-thin film and Si in the topmost layer.

2) A mixed MnSi layer structure with an 1:1 ratio of Mn and Si. The Mn and Si layers are alternating perpendicular to the surface. The atomic arrangements in this structure resembles the atomic positions in a [100] plane of the cesium chloride structure.

3) A sandwich MnSi layer structure with alternating Mn and Si layers in the [001] plane and a resolved Si-overlayer. This structure resembles the CsCl structure in direction parallel to the surface.

The most stable film is the MnSi sandwich with a negative $E_{\mathrm{form}}$, which indicates that the film is stable relative to decomposition into a clean silicon surface and bulk manganese. In Tab. 6.2, the calculated $E_{\mathrm{form}}$ in eV and the vertical interlayer distances in Å for all structures are shown.

In view of the strong (weak) intralayer (interlayer) FM coupling of the Mn layers in the above mentioned sandwich structures, the structures with $\geq 2$ ML Mn coverage are modeled by i) FM coupling (↑↑↑), ii) intra-layer FM and interlayer AFM coupling and iii) intra-layer AFM but inter-layer FM (↑↓↑) coupling.

The formation energy of the FM B2(001) structure is -0.507 eV, which is lower than both the AFM Mn-thin film and the MnSi film by more than 1 eV. In this structure Mn atoms at the interface have six (or seven) bonds with Si while Mn atoms in the inner layers are eightfold coordinated. The surface roughness at this coverage is reduced in comparison to similar structures with 1 ML Mn coverage and the average vertical distance between layers decreases from 1.7 Å at 1 ML coverage to 1.4 Å and 1.6 Å at 2 ML[4]. Therefore, from thermodynamic stability considerations

---

[4] These are the distances between layers from the interface to the surface.

Table 6.2: Formation energy (eV / cell) for different magnetic ordering and interlayer distances (Å) for the three structures with 2 ML coverage, shown in Fig. 6.3.

| Structure | FM | Interlayer AFM | Intralayer AFM | Intralayer distance(Å ) |
|---|---|---|---|---|
| Pure Mn with Si cap | — | 0.53* | 1.27 | |
| B2(001) film (mix) | 0.528 | 0.726 | 0.85 | 1.4 / 1.7 |
| B2(001) film (sandwich) | -0.507 | -0.444 | -0.164 | 1.4 / 1.6 |

(*) Reference [150]

and structure analysis, it follows that bonds in thicker layers are stronger and the structures become more stable.

The formation energy for a Mn-thin film and B2(001) film, shown in the Tab. 6.2, are positive. The average interlayer distances are 1.4 Å for the interface, $\sim 1.6 \pm 0.03$ Å for the inner layers and 1.7 Å for the surface. It is not sensitive to the thickness of the film in the B2(001) structure.

The results for the pure Mn film are just for the AFM phase, because self-consistent calculations did not support FM structures.

### 6.3.2 Magnetic Structure

The B2(001) structure has a FM metallic ground state with total spin polarization of about 50% at the Fermi level.

The interfacial-layer Mn atoms with sixfold (or sevenfold) coordination have an averaged magnetic moment of 1.90 $\mu_\mathrm{B}$ / layer. This value is the same as for the previously described ground state of this structure at 1 ML coverage. Due to the higher coordination of Mn atoms in the inner layer (eightfold coordination), the averaged magnetic moment is decreased to 1.11 $\mu_\mathrm{B}$ / layer. The $sp$-$d$ hybridizations induce an averaged magnetic moment of 0.02, -0.07 and -0.04 $\mu_\mathrm{B}$ at the Si atoms in the capping-layer , the middle layer and the first layer of the substrate, respectively.

Note that the $sp$-$d$ exchange mediated FM intralayer coupling is as strong as for the same structure at 1 ML coverage. The energy cost to orient the magnetic moment of the Mn atoms within two layers in opposite directions (interlayer AFM) is 16 meV / Mn and to revers it from parallel to antiparallel for Mn atoms in the same layer (intralayer AFM) is 86 meV / Mn [5].

Within the layer, the indirect $d$-$sp$-$d$coupling between Mn atoms is stronger than direct $d$-$d$ coupling, because within the two dimensional layer the itinerant $sp$-$d$ hybridized electrons mediate laterally between Mn atoms in the layer. On the other hand, the *d*-*d* coupling has dominant effect between Mn atoms in the subsequent layers. The formation energy indicates that, the FM interlayer coupling is weaker than the intralayer FM coupling. Therefore, one can conclude that *d*-*sp*-*d* coupling is always stronger than *d*-*d* coupling between Mn atoms. Additionally, the distances between Mn atoms play role for changing magnetic structure.

---

[5] At coverage of 2 ML there are four Mn atoms in the unit cell.

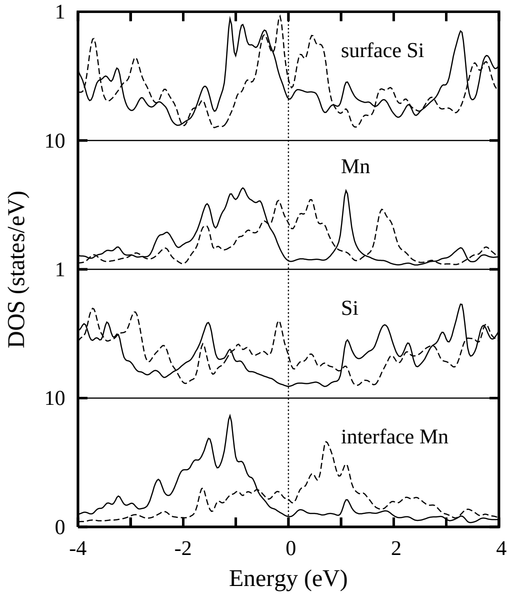

Fig. 6.4: The overlayer-resolved DOS of the FM 2(Si-Mn) / Si(001) film. The overlayers are shown from surface (top) to interface (bottom). Full lines show the majority spin, dashed lines the minority spin component. The considerable spin polarization of carriers at Fermi level (zero energy) is evident.

The nearest intralayer Mn-Mn distance is about 2.74 Å which is shorter than the Mn-Mn in-plane distance by 0.26 Å.

For pure Mn thin films, the Mn atoms on the surface have the large average magnetic moment of about $-3.2$ $\mu_\mathrm{B}$ / Mn due to the presence of the surface, while the spin moment of the interface Mn atoms is reduced to 1.5 $\mu_B$. The magnetic moment of a Mn atom with sixfold coordinations is bigger than for a Mn with sevenfold coordination, because the bondlengths are shorter for the sevenfold coordination.

At one monolayer coverage the interlayer AFM magnetic structure has lower formation energy, whereas $E_\mathrm{form}$ at 2 ML coverage for the FM state is lower than for the AFM state by 0.062 eV / Mn.

Fig. 6.4 shows the overlayer resolved density of states of the 2 ML B2(001) structure. In particular, the interface Mn layer has a spin polarization of up to 45 %. These findings make the ultrathin B2(001) films interesting candidates in the search for spintronic materials [152].

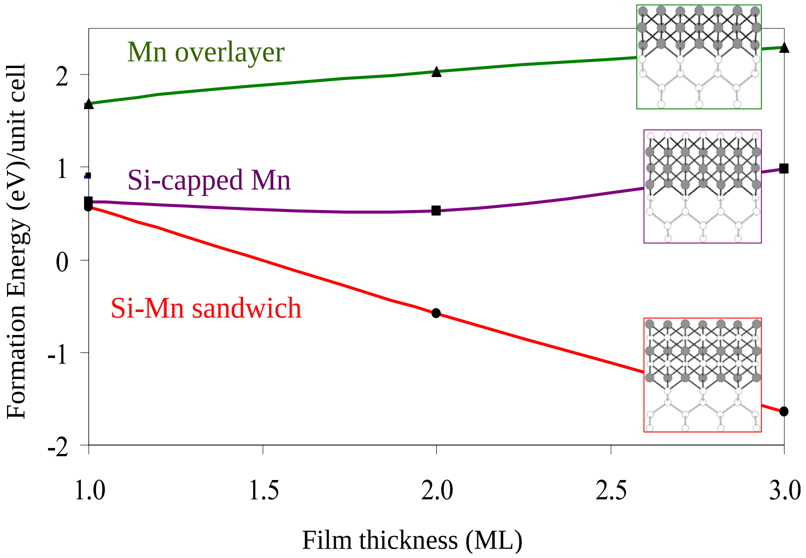

Fig. 6.5: Formation energy of pure Mn films and MnSi films in the B2(001) structure as a function of the film thickness. The zero of the energy scale refers to the surface energy of the clean reconstructed Si(001) surface. The green line corresponds to the pure Mn overlayer-film, the purple line corresponds to the Mn thin film with a Si capping layer and the red line to the MnSi sandwich film in the B2(001) structure.

## 6.4 Coverage of 3ML on Si(001)

### 6.4.1 Thermodynamical and Structural Stability

In order to find a common rule for the stability of film formation, the calculations for the B2 structure (sandwich Mn-Si film) and the pure Mn film are repeated for 3 ML Mn coverage [150, 152].

At $\theta = 3$ML, the most stable structure is the MnSi sandwich layers which has negative formation energy. The 3 ML B2(001) on Si(001) has a Mn-Si interlayer distance of 1.46 Å, 1.40 Å and 1.48 Å for the inner, middle and outer Mn layers, respectively.

The Mn film is found to be highly strained and the average Mn-Mn nearest distance in the layer is 2.74 Å and thereby longer than the Mn bulk value in the ground state [6] by almost 8%.

In Fig 6.5, the stability of films formation is shown as a function of film thickness.

As we have found earlier [150], a film with a B2 structure of alternating Mn and Si layers, terminated by a Si layer, has the lowest energy of all investigated candidate structures. In particular, it is much more stable than a film of pure Mn (filled triangles in Fig. 6.5), or a film of Mn capped by a Si monolayer (filled squares in Fig. 6.5). These findings can be rationalized by the fact that Mn–Si bonds are stronger than the average of Mn–Mn and Si–Si bonds; hence the system tends to maximize the number of Mn–Si bonds. In the sandwich films, the local coordination of a Mn atom is similar to the bonding in the cesium chloride (CsCl) crystal structure, i.e., each Mn atoms has eight Si neighbors. However, due to epitaxial strain, the local environment of a Mn atom does not have cubic symmetry, but is slightly distorted, and Mn–Si bond lengths vary by several percent within the film, being shortest in its interior and longer near the surface and interface. Negative values of $E_{\mathrm{form}}$ in Fig. 6.5 indicate that the film is thermodynamically stable with respect to decomposition into a clean Si surface and bulk Mn metal. This is the case for films formed by depositing 2 ML of Mn or more.

---

[6] The nearest Mn-Mn distance in fcc structure in the ground state (AFM phase) is 2.54 Å and in the FM state 2.67 Å .

### 6.4.2 Electronic and Magnetic Structure

In all magnetic structures of MnSi film, the magnetic moment of the central Mn layer almost vanishes (the calculated averaged spin moment is only about 0.1 $\mu_{\mathrm{B}}$ / Mn). The lack of magnetic moment in the central layer is due to strong Mn-$3d$ and Si-$3sp$ hybridizations which is caused by eight coordinations of Mn atom with Si and also the shortest Mn-Si interlayer distance of 1.40 Å. The intralayer distance is slightly elongated in comparison to interlayer distances of 1.46 Å for both the inner and outer Mn layers. All these interlayer distances are shorter than the one between Mn layers in the 1 ML Mn-Si structure and the interface (surface) Mn layer in the 2 ML Mn-Si. It is therefore not surprising that in the 3 ML sandwich Mn-Si structure, the spin moment of the interface (surface) Mn layer is reduced to 1.72 (0.91) $\mu_{\mathrm{B}}$.

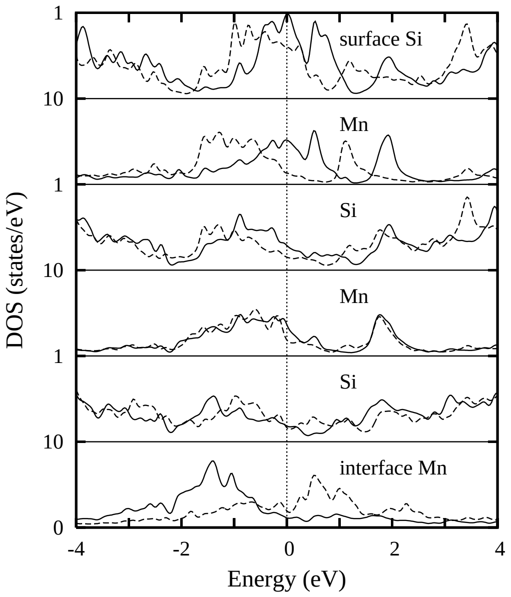

Fig. 6.6: The overlayer-resolved DOS of the interlayered AFM 3(Si-Mn) / Si(001) film. See Fig. 6.4 for other notes.

In addition, the induced spin moment of the sandwich-layer Si decreases to – 0.03 $\mu_{\mathrm{B}}$.

Moreover, the magnetic state with interlayer AFM coupling between the interface and surface Mn layers in the 3 ML B2(001) structure on Si(001) is calculated. It is found that besides the almost vanishing spin magnetic moment of the central Mn layer (–0.15 $\mu_\mathrm{B}$), the spin moment is 1.75 (–1.07) $\mu_\mathrm{B}$ for the interface (surface) layer Mn. This interlayer AFM structure has a little lower negative $E_\mathrm{form}$ of –1.53 eV and is the magnetic ground state. Note that the surface and interface of the 3 ML sandwich thin film can be regarded as a antiferromagnet (film) with a central magnetically dead layer.

For the 3 ML B2 structure, it is found that the surface and interface Mn layers are magnetically active, while the middle Mn layer becomes nearly nonmagnetic. This can be attributed to a stronger covalent bond between Mn and Si in the middle layer, which is indicated by the shorter Mn-Si bond length.

In contrast to the weak FM interlayer coupling in the 2 ML sandwich mentioned above, the 3 ML sandwich Mn-Si film shows an energetic preference for the magnetic moments of the surface Mn atoms and the interface Mn atoms to point in opposite directions. This AFM interlayer (structure B in Fig. 6.7) is lower in energy than the FM state and the nonmagnetic one by 15 and 120 meV / Mn, respectively [150]. Note, however, that the FM intralayer coupling persists also in the 3 ML B2(001) structure.

The AFM interlayer coupling (structure B in Fig. 6.7) between the interface and surface Mn layers is partly due to the almost vanishing but antiparallel spin moment of the middle Mn layer (to the interface Mn layer) with the smallest interlayer spacing and the strongest Mn-Si covalency. In a sense, such an AFM coupling could, via the almost non-magnetic intermediate Si-Mn-Si trilayer complex, have a superexchange origin. Furthermore, it follows that energy difference between parallel and antiparallel alignment of spin magnetic moment on neighboring in-layer Mn atoms is about 82 meV / Mn (see structure (A) and (C) in Fig. 6.7). This indicates once again the strong FM intralayer coupling in these sandwich films.

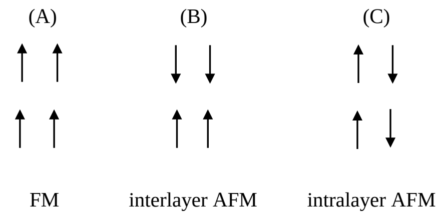

Fig. 6.7: Ferromagnetic (A), interlayer antiferromagnetic (B) and intralayer antiferromagnetic (C) structure of B2(001) / Si(001).

The spin moment of the middle-layer Mn in the 3 ML pure Mn / Si(001) structure, being around 1 $\mu_\mathrm{B}$, is smaller than the calculated bulk-phase value of 1.9 $\mu_\mathrm{B}$. This is not surprising, since the Mn film is found to be highly strained and the middle-layer averaged Mn-Mn nearest distance of 2.48 Å is shorter than the bulk value of

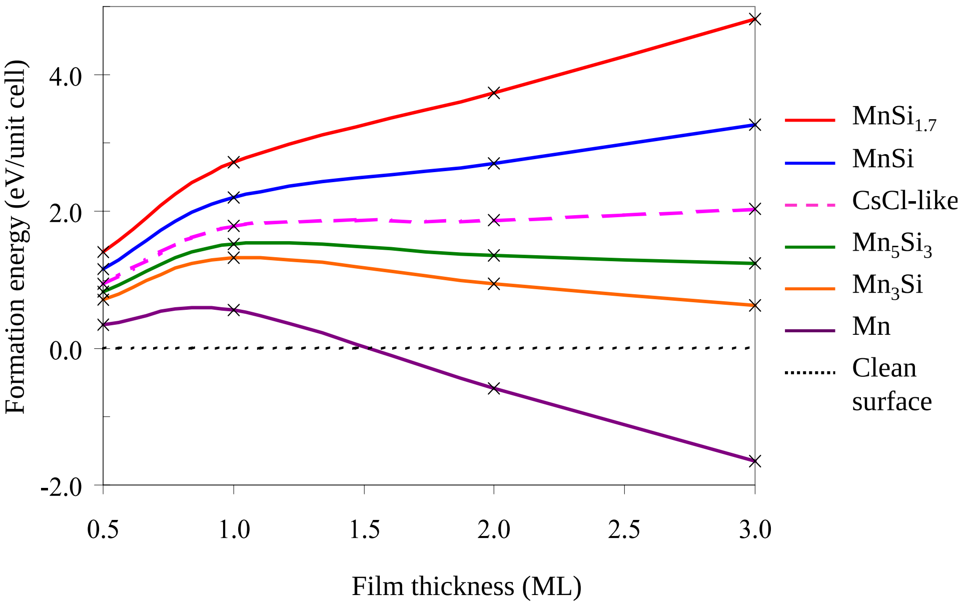

Fig. 6.8: Formation of films with B2 structure of Mn-mono-silicide on Si(001) in equilibrium with some Mn-silicide structures. The surface energy of the clean (001) reconstructed surface is considered as zero point. Formation of these films on the surface is unstable in equilibrium with Mn-poor compounds.

2.54 Å .

Fig. 6.6 provides the DOS plot for the 3 (Si-Mn) / Si(001) sandwich. It is evident that both the Mn and Si overlayers have a considerable spin polarization of carriers at the Fermi level, as we reported earlier for (Si-Mn) / Si(001) [150]. In particular, the interfacial Mn layer has a spin polarization of up to 27 % in the 3 (Si-Mn) / Si(001) sandwiches.

It is therefore concluded that the growth of Mn overlayers on the Si(001) surface is energetically rather unfavorable. The pure Mn films on Si(001) is unstable and it turns into the Mn-Si sandwich structures.

## 6.5 The Thermodynamic Stability

Most of the experiments indicate that Mn prefers to form a silicide when grown on Si surfaces. In 1985 the epitaxial growth of (001)MnSi$_{1.7}$ / Si(001) was reported by Lian *et al.* [15] and recently, Lippitz *et al.* observed that, MnSi and Mn$_5$Si$_3$ islands could be formed [16] . Also it was discovered by molecular beam epitaxy (MBE) that, some transition metal mono-silicides [7] ( CoSi, FeSi) can be crystallized in the

---

[7] These intermetallic compounds are isostructure with four Mn and Four Si atoms in a simple cubic structure with space group $P2_13$ and pearson symbol *cP*8.

CsCl structure on Si surfaces [76]. Moreover, among the known bulk phases of Mn silicides, $Mn_3Si$ in the $D0_3$ structure appears to be compatible with pseudomorphic thin film growth on Si(001) [8], but (as bulk compound) is known to be only weakly magnetic [154]. These results motivate us to calculate the film stability of the proposed structures in equilibrium with known Mn-silicide structures in this surface.

From the curves in Fig. 6.8, the sandwich films with CsCl structure are metastable relative to the Si-rich compounds (bulk MnSi or $MnSi_{1.7}$). The formation of a pseudomorphic CsCl-like structure is endothermic in equilibrium with bulk MnSi and $MnSi_{1.7}$. In contrast, film formation in equilibrium with Mn-rich compounds (or bulk Mn) are exothermic and become stable for thicker films. The negative $E_{\rm form}$ shows that multilayers [$n$(Si-Mn) / Si(001)] are thermodynamically stable against decomposition into the elements for $n \geq 2$. Note that in this curve , the formation energy of the CsCl-like films, $E_{\rm form}(\theta)$, decreases almost linearly with film thickness in the regime of multilayer-films. The almost linear decrease between 1 ML and 3 ML indicates that the interior of a 2–3 ML thick film has already properties similar to those of bulk MnSi in the CsCl structure.

However, as a consequence of the negative curvature, at small thickness a thin homogeneous film is unstable against decomposition into a thicker film that only partly covers the surface, plus a corresponding area of clean Si(001)[9].

We stress that the deposition of Mn on Si does *not* lead to the formation of a wetting layer, because the formation energy of thin films ($\leq$ 2 ML) is higher than that of the clean Si(001) surface. Moreover, a homogeneous film is less stable than three-dimensional islands on clean Si(001), see Sec. 7.7.1. Thus, MnSi on Si(001) is expected to grow in the Volmer-Weber growth mode. Since it is plausible that parts of the Si(001) surface remain uncovered, these surface areas can act as a continuous source for Si that feeds to growing MnSi islands during further deposition of Mn.

Moreover, it leads to the conclusion that interface growth depends very much on the substrate preparation: From our calculations, it is apparent that Mn adatoms bind very strongly to missing-dimer defects (and probably others defects and steps) on the Si(001) surface. We speculate that these binding sites, if present, could act as very efficient nucleation centers for three-dimensional island growth on MnSi. Only in the absence of these nucleation centers, two-dimensional film growth appears to be possible. Similar observations of a preparation-dependent interface growth were made in experiments of Co silicide formation on Si(001). [155]

---

[8] For $Fe_3Si$, this structure was inferred from LEED analysis, see Ref. [153].

[9] More details about conditions for island formation are given in chapter 7

# Chapter 7

# Epitaxial Growth of Mn on Si(111)

## 7.1 Introduction

There are a few reports and experiments concerning the adsoption of Mn on Si(111), where film growth with and without a Bi surfactant layer [18–21,156], surface structural phase transitions [157], as well as a non-metal-to-metal phase transition in 5-10 monolayers thick films [158] have been reported. Kumar *et al* observed with low-energy electron diffraction (LEED) that at low coverage silicide islands form which turn into a nearly closed film at higher coverage [22].

In the matter of morphology of Mn-silicide films, a Volmer-Weber-like growth mode is supposed in these reports.

## 7.2 Low Coverage Adsorption

There are a number of experimental and theoretical studies on the reconstructions of the bare Si(111) surface. It has been established that this surface has a (7×7) reconstruction of Takayanagi type[1] [117], which undergoes a phase transition to a high temperature phase, a (1×1) structure, at 870 °C. A host of other reconstructions of the clean Si(111) $(9\times9)$, $(5\times5)$, $(2\times2)$, $c(2\times4)$, and $(\sqrt{3}\times\sqrt{3})$ have been reported from scanning tunneling microscopy (STM) experiments [159].

Adsorption of Mn on Si(111) leads to the formation of a closed metallic film at a coverage of more than 5 ML and exhibiting a $(\sqrt{3}\times\sqrt{3})$ surface reconstruction [22].

The present calculations are performed in order to find the low coverage (for a coverage of 0.5 ML) adsorption site of Mn in the (1×1) surface unit cell. For simulating

---

[1] This model basically consists of 12 adatoms arranged locally in the (2×2) structure, nine dimers on the sides of the triangular subunits of the (7×7) unit cell and a stacking fault layer.

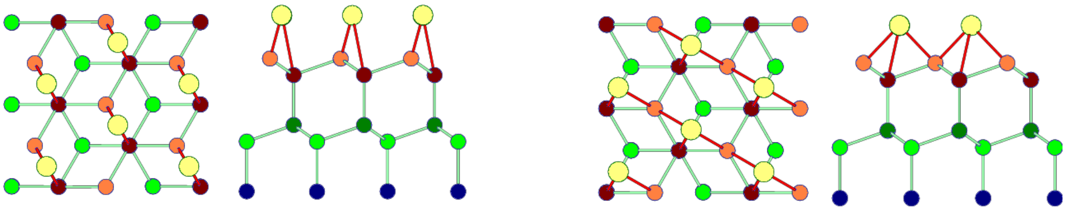

(top-side view) 1fold overlayer $(O_1)$ (top-side view) 3fold chain $(C_3)$

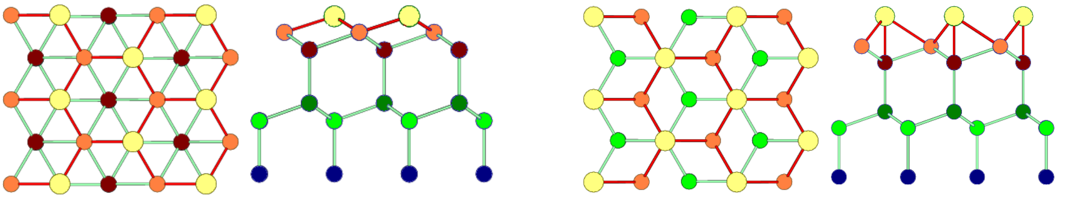

(top-side view) 3fold hollow $(H_3)$ (top-side view) 4fold atop $(T_4)$

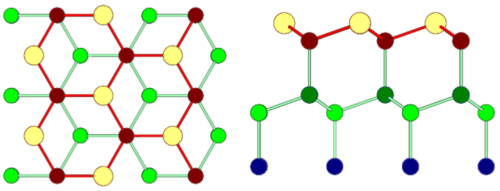

(top-side view) 3fold substitutional $(S_3)$

Fig. 7.1: Top-view (left figure in each structure) and side-view (right figure in each structure) for five configurations of Mn adsorbed on the Si(111) surface. The big yellow circles represent Mn atoms, while all the small circles depict Si atoms in different layers. $O_1$ is an overlayer site with one-fold coordination to a surface atom. $C_3$ is a 3-fold mono-atomic chain and $H_3$ is the 3-fold hollow sites. $T_4$ is a 4-fold atop site and $S_3$ is a 3-fold substitutional site.

silicide films a $(\sqrt{3} \times \sqrt{3})$ unit cell is used. There are two kinds of common adsorption sites on the (111)-(1×1) surface of the diamond crystal structure.

One of them is a four-fold atop site, $T_4$, which was proposed by Northrup [160]. In this model the adatom has four Si neighbors, three in the surface layer and one in the second layer directly below. Adsorption in this position can eliminate the surface dangling bonds.

The second one is a three-fold hollow site, $H_3$, in which the adatom forms just 3 bonds with the surface layer atoms. Such an arrangement leads to the disappearance of surface dangling bonds, as well.

In 1964, Lander and Morrison suggested that the hollow site, $H_3$, is the most stable adsorption site for adsorption of a Si-adatom on Si(111) [161]. Later on, in 1989, Kohmoto *et al.* [162] showed, following the analysis of reflective high electron energy diffraction (RHEED) intensity at 900 °C, that Si-adatoms are adsorbed in both the $T_4$ and the $H_3$ sites with a mixing ratio of about 4:1. This means that the $T_4$ position is more stable than the $H_3$ site.

Besides these two known sites (i.e. $T_4$ and $H_3$), we also calculated the adsorption energy in other positions, such as the overlayer site ($O_1$), the mono-atomic-chain site ($C_3$) and the substitutional site ($S_3$), all shown in Fig. 7.1. The substitutional sites $S_4$ and $S_6$, see Fig. 7.2, were considered as well. We point out that adsorption of a single Mn in a (1×1) cell coresponds to a 0.5 ML coverage.

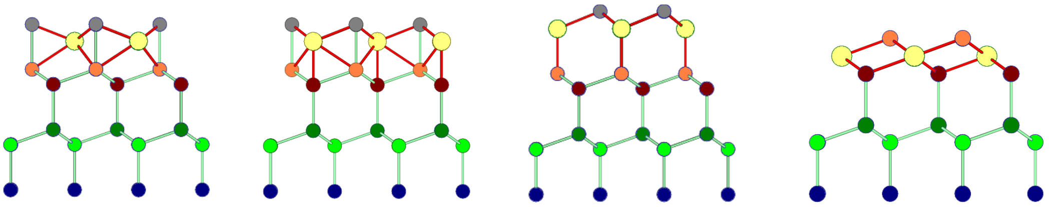

3-fold interstitial ($H_6^I$) 4-fold interstitial ($T_7^I$) 4-fold substitutional ($S_4$) 6-fold substitutional ($S_6$)

Fig. 7.2: Side view of structures with hollow, atop and substitutional site adsorption and a Si-covering layer. In most of the structures, the surface dangling bonds are saturated and the Mn atoms below the surface are highly coordinated.

As it was discussed in chapter 4, the bare Si surface in (111) orientation can be either the single-dangling-bond (shuffle-terminated faces), SDB, or the triple-dangling-bond (glide-terminated faces), TDB structure. Since the TDB surface is less stable than the SDB surface[2], it is not surprising that the released energy due to the adsorption on the TDB surface becomes larger than on the SDB surface.

Fig. 7.1 shows the configurations for Mn adsorbed at the topmost layer of either SDB or TDB. There are four possible adsorption sites on the SDB surface, the $O_1$,$C_3$, $H_3$ and $T_4$ sites, while only one adsorption site, called $S_3$, is found on the TDB surface. Mn in a $O_1$ binds to the corner of surface triangles with only one bond, so that one surface dangling bond per cell still remains. The energy gain from the adsorption in this position is 2.557 eV [3]. An adatom in the $C_3$ configuration is three-fold coordinated to the substrate atoms and sits on the side of substrate triangles. Adatoms and surface atoms form alternating mono-atomic chains and surface dangling bonds are completely saturated. This configuration is more stable than $O_1$ site by 0.174 eV. For adsorption of Mn at the topmost layer on the SDB surface, the $H_3$ is found to be favored over the $T_4$ site by 0.184 eV; the energy gained from the $H_3$

---

[2] The surface energy, $\gamma$, is 1.303 and 2.279 eV / (1×1) cell for the SDB and TDB, respectively.

[3] In order to calculate the adsorption energy, the total energy of the bare Si(111) surface and the total energy of the free Mn atom are considered as reservoirs, see eq. 5.1 chap.4.

site adsorption is 3.248 eV. The $S_3$ structure corresponds to the adsorption of Mn at the TDB surface. The adatom is substituted in the place of the substrate atom. The adsorption energy is 4.130 eV but formation energy of this structure is less than $H_3$ structure.

Since it was concluded from adsorption on Mn on Si(001) that the presence of a Si-capping layer increases the stability of the system, the effect of a capping layer on the Si(111) surface will be studied by adding a Si layer on top of the Mn layer, Fig. 7.2. The subsurface six-fold hollow site, $H_6^I$, and the seven-fold atop site, $T_7^I$, are interstitial sites. They resemble the $H_3$ and $T_4$ sites, but have an overlayer of Si on top. The adsorption energies are 4.271 eV and 4.537 eV, calculated with respect to the TDB surface. Similarly to the results for the (001) surface, the additional Si capping layer increases the stability in both cases.

In both $S_4$ and $S_6$ substitutional structures, one Si atom from the SDB surface is replaced by a Mn atom. The Si-bulk is considered to be the reservoir for the replacement.

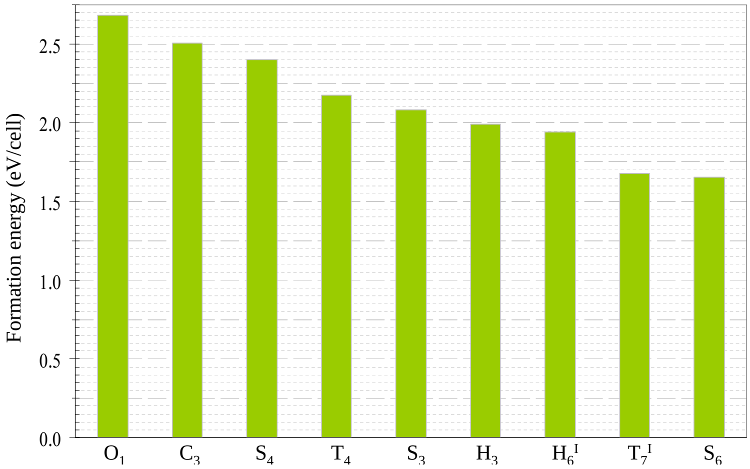

Fig. 7.3: Formation energy for all the considered structures in eV per (1×1) cell.The six-fold substitutional site, $S_6$ on the SDB surface with a Si capping layer is the most stable adsorption site for Mn on this surface.

The formation energies [4] for the different considered structures are listed in chart. 7.3. The lowest formation energy belongs to the position in which a single Mn atom sits in a six-fold substitutional site on the SDB surface with a Si-capping layer. The tendency of Mn atoms to penetrate into the subsurface region can be explained with an increased coordination of the adatoms and the formation of strong Mn-Si bonds.

The Si overlayer has also a considerable effect on the thermodynamic stability of

---

[4] For the calculation of the formation energy the total energy of the bulk phase of each constituent part is considered as a reservoir.

Table 7.1: The distance between Mn and Si in the first ($Si_1$) and the second ($Si_2$) substrate layer in Å , Mn magnetic moment and first layer Si magnetic moment (in $\mu_B$) for different adsorption sites of Mn on Si(111).

| site | Mn-$Si_1$ distance (Å ) | Mn-$Si_2$ distance (Å ) | Mn-spin moment ($\mu_B$) | $Si_1$-spin moment ($\mu_B$) |
|---|---|---|---|---|
| $O_1$ | 2.33 | 2.72 | 3.74 | -0.04 |
| $C_3$ | 2.45 | 2.62 | 3.60 | -0.04 |
| $H_3$ | 2.34 | 2.71 | 3.12 | -0.02 |
| $T_4$ | 2.58 | 2.34 | 3.51 | -0.04 |
| $S_3$ | 2.38 | — | 3.44 | -0.15 |
| $H_6^I$ | 2.45 | 2.66 | 3.24 | -0.09 |
| $T_7^I$ | 2.42 | 2.68 | 2.20 | -0.14 |
| $S_4$ | 2.29 | 2.38 | 2.45 | -0.24 |
| $S_6$ | 2.37 | 2.39 | 2.56 | -0.04 |

the atop positions ($T_4$). The capping layer increases the stability of this position (i.e. $T_7^I$ site) by almost 0.50 eV relative to the $T_4$ site, while the energy difference between $H_3$ and $H_6^I$ is just 0.05 eV.

The magnetic moment of Mn induces a small magnetic moment in opposite direction in the substrate atoms in these structures. The bonds lengths of Mn with the Si atoms of the first ($Si_1$) and second ($Si_2$) substrate layers, as well as the magnetic moments of the Mn and the $Si_1$ atoms are presented in the Tab. 7.1. The magnetic moment of the Si layer closest to the Mn layer has antiparallel coupling to the latter. The presence of a Si overlayer leads to a significant reduction of the magnetic moment of Mn, which is due to a large overlap between the Mn and Si orbitals, see Fig. 7.4. The DOS plot of configurations with a Si-overlayer, i.e. $S_6$, $H_6^I$ and $T_7^I$ (Mn-overlayer, i.e. $S_3$, $H_3$ and $T_4$ ) for the majority and the minority spin channel are shown on the left side (right side) plot of Fig. 7.4.

In DOS of the $T_4$ configuration, there is a sharp peak around -3.5 eV, while due to the stronger overlap between Mn-d and Si-sp orbitals in the $T_7^I$ position, the band width is broader compared to the $T_4$ structures. Furthermore, the Si-capping layer shifts some electrons in minority spin states of the $T_7^I$ structure to lower energy, below the Fermi level and also decreases the occupation number of states at the Fermi level. This results in the $T_7^I$ configuration becoming more favorable than the $T_4$ structure. Aditionally, the presence of the Si-capping layer in the $T_7^I$ structure shifts the position of the Fermi level of $T_4$ by +0.22 eV. This causes an increase of filled state in the minority spin channel which reduces magnetic moment and decreases the spin polarization [5] from 87% in $T_4$ to less than 20% in the $T_7^I$ structure.

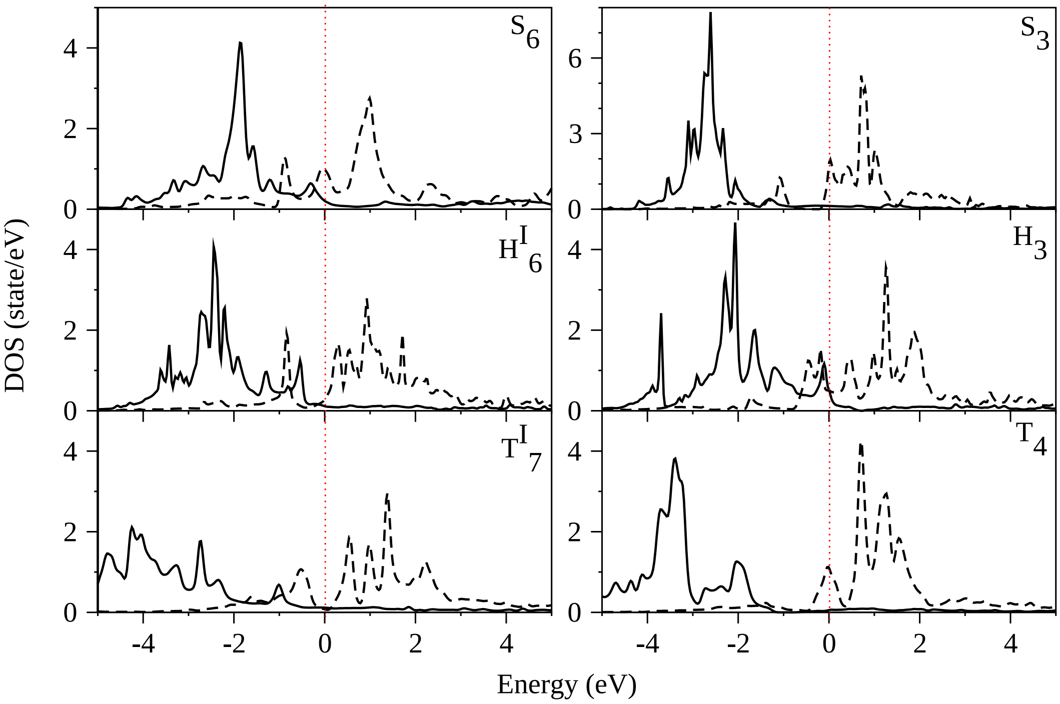

Fig. 7.4: Total density of states plot for Mn atom in $S_6$, $S_3$, $H_3$, $H_6^I$, $T_4$ and $T_7^I$ configurations. The solid (dashed) lines indicate the projection of the spin up(down) wave function onto the $d$ orbitals of manganese.

The presence of the Si-capping layer causes an energy gain in all configurations. We present a physical picture from analysis DOS plot which may leads to the stability these structures with Si-capping layer. In the structures with Si-capping layer (i.e. $S_6$, $H_6^I$ and $T_7^I$) the Fermi level in DOS plot moves forwards in the energy range, which causes an energy gain is obtained by transferring some electrons from the unoccupied state above the Fermi level to the occupied states below the Fermi level in both spin channels. Therefore, structures with a Si-capping layer are more favorable than structures with a Mn-over layer.

For the substitutional site, the spin polarization at the Fermi level for a Si-capping layer structure is lower compared to the Mn-overlayer configuration by almost 20%, while the Si-capping layer increases the spin polarization for the Mn interstitial site. A comparison of the DOS plots for the low coverage of Mn / Si(001) and Mn / Si(111) shows that the exchange splitting of Mn-$d$ orbitals in these structures is as large as the exchange splitting in a Mn-overlayer on Si(001), which is about 3-4 eV.

---

[5] Spin polarization is defined as: $\frac{\text{density of state(up)} - \text{density of state(dn)}}{\text{density of state(up)} + \text{density of state(dn)}}$

## 7.3 Morphology of Epitaxial Film on Si(111)

As discussed in Chap. 3, the cesium chloride (B2) and the nickel arsenide (AsNi) structures of Mn-mono-silicide do not exist as a bulk phase but there is a possibility that they could be grown epitaxially on a Si substrate [76]. The structure of these films is shown in Fig. 7.5. These structures are the two compatible epitaxial structures of Mn-mono silicide with the Si(111) substrate, having a small lattice mismatch of +2% for B2 and +7% for AsNi. In continuation of the topic of film growth on a Si substrate, the structural stability and magnetic properties of such films will be discussed in the following.

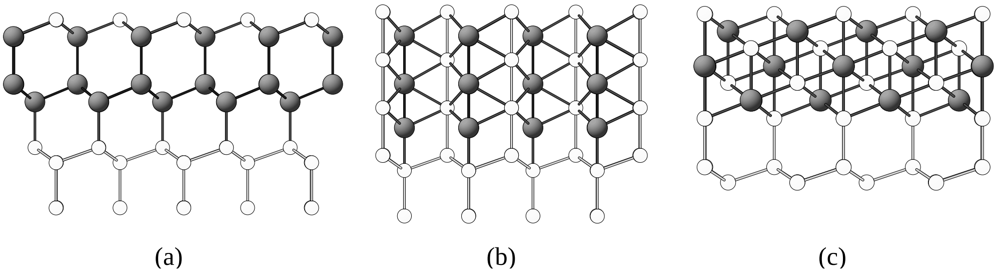

Fig. 7.5: The structures of a pure Mn film (a), a Mn-mono silicide with nickel arsenide structure (b) and a cesium chloride structure (c) are compared.

The formation energy and magnetic moments of the B2 and the AsNi structures for a coverage of $\theta = 1.5$ ML are compared to the pure Mn film in Tab. 7.2. Following the results for Si(001), according to which the Si-capping layer increases the stability of a film, a Si capping layer is considered in all film calculations.

The film with B2 structure is more stable than with AsNi structure by 1.3 eV/$(1 \times 1)$ cell. The formation energy of the film is calculated for equilibrium with bulk Mn and Si. Similar to the Mn/Si(001), the pure Mn-film is unfavorable, with a formation energy of more than 4 eV/$(1 \times 1)$ cell higher than for a film with a B2 structure.

Due to the surface and the distortion of the film from and ideal cubic B2 structure, a considerable magnetic moment (0.7 $\mu_\mathrm{B}$) is found for the Mn atom in the central layer. The vertical distance between layers is about 0.84 Å which is larger than for the bulk phase of B2 by maximum 5% . Mn in the surface and interface layer makes seven bonds with Si atoms at distances of 2.38-2.5 Å , while Mn in central layer has eight bonds to Si atoms.

The magnetic moments of Mn in the central layer of the AsNi structure is larger than its bulk value by 1.2 $\mu_\mathrm{B}$, which is due to the distortion of the structure compared to its bulk phase. The bonds between the Si-substrate and Mn-interface layer

Table 7.2: Formation energy, magnetic moment and spin polarization of different epitaxial structures of Mn-mono silicide on Si(111) at 1.5 ML coverage.

| Structure | Formation energy eV / cell | Interface magnetic moment $\mu_\mathrm{B}$ / layer | Surface magnetic moment $\mu_\mathrm{B}$ / layer | Central layer magnetic moment $\mu_\mathrm{B}$ / layer |
|---|---|---|---|---|
| Pure Mn | 5.1 | 2.6 | 3.8 | 3.8 |
| AsNi | 2.03 | 2.4 | 2.7 | 2.7 |
| CsCl(B2) | 0.73 | 1.5 | 1.9 | 0.7 |

are slightly shorter than Si and Mn bonds at the central layers, which leads to smaller magnetic moment for the Mn at the interface.

The ferromagnetic coupling is found to be the most favorable magnetic struture for all films. The magnetic moment at the interface and surface are given in Tab. 7.2. The interface spin polarization at the Fermi level is 4%, 37% and 59% for pure Mn, AsNi and B2 structure films, respectively. Si layers between Mn layers have antiferromagnetic coupling with Mn atoms with small magnetic moment of $\sim$ –0.2 (–0.05) $\mu_\mathrm{B}$ for AsNi (B2) structures.

In the following the stability and the magnetic structure of 3 ML of the B2 structure film on Si(111) will be compared to the similar film on the Si(001) surface

## 7.4 Comparison of B2 Structure of MnSi Film on Si(001) and Si(111)

The cutting of a B2 structure in the (111) direction is compatible with the Si(111) surface and can be suitably matched to it. In this structure Mn and Si layers of the film have the same atomic density as the substrate, therefore the thickness of such a film will be larger than for a film of B2(001) / Si(001) at the same coverage, Fig. 7.6.

The thermodynamic stability of a film with B2 structure on Si(111) is higher than on Si(001) by 0.12 eV / Mn atom. In addition to the B2 structure, the formation energy of a film with $\mathrm{Mn_3Si}$ structure is calculated. This structure contains three subsequent Mn-layers which are separated by one Si layer, see Fig. 7.6-c. The $\mathrm{Mn_3Si}$ structure on Si(111) is less stable than the B2 structure on the same surface by almost 0.14 eV / Mn atom. The magnetic moment of Mn at the surface and the interface is about 1.5 and 1.1 $\mu_\mathrm{B}$, respectively. The magnetic moment of Si in the central layer is almost zero but in the surface and interface a small negative magnetic moment of –0.06 and –0.01 on Si atoms appears. We discard this structure because of its higher

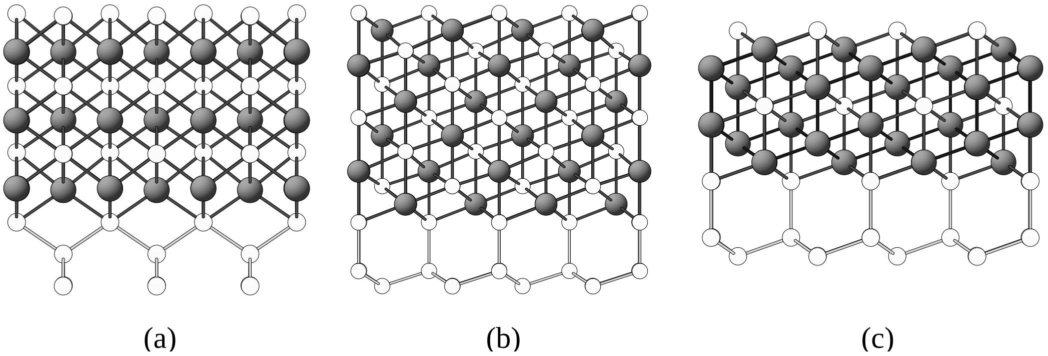

Fig. 7.6: B2 structure on Si(001) substrate (a) and Si(111) surface (b) and the film with $Mn_3Si$ structure on Si(111) (c) at coverage of 3 ML.

formation energy and continue with films with B2 structure.

The magnetic moments of Mn atoms at surface and interface are +1.8 $\mu_{\mathrm{B}}$ and –2.0 $\mu_{\mathrm{B}}$. The average magnetic moment at central layers is about –0.5 $\mu_{\mathrm{B}}$. It was found on B2 / Si(001) that, the spin magnetic moment of the central Mn layer almost vanishes (–0.15 $\mu_{\mathrm{B}}$),while for B2 / Si(111) surface the central layer and also the surface and interface Mn atoms have higher magnetic moments than in case of the Si(001) substrate.

With increasing Mn coverage the distances between Mn-layers decrease slightly which results in a decreasing magnetic moment in the central layer.

The interlayer distances between Mn and Si layers are smaller for the inner layers compared to the outer layers.

Moreover, the magnetic state with interlayer AFM and FM coupling between the interface and surface Mn layers are calculated. There are several similarities between B2(001) / Si(001) and B2(111) / Si(111):

The spin magnetic moment of the central Mn layer is small, while the surface and interface Mn layers are magnetically active with the spin moment of -2.0 (1.8) $\mu_{\mathrm{B}}$ for the interface (surface) layer Mn. The film formation of Mn-Si is more stable on the Si(111) compared to the Si(001) substrate.
This interlayer AFM structure is the magnetic ground state and has lower formation energy, $E_{\mathrm{form}} = -2.38\ \mathrm{eV}/(1 \times 1)$ cell, than FM order by 18 meV / Mn.
The magnetic moments in the central layers starting from the interface and going towards the surface are -0.75 , -0.46 , -0.24 and +0.17 $\mu_{\mathrm{B}}$ ,respectively (cf. Fig. 7.6). The central layer closest to the surface is magnetically almost inactive. The same argument as used in the case of the B2 film growth on a Si(001) substrate is valid here,

namely that a short Mn-Si bond length in the middle layer causes a strong covalent bond between Mn and Si, which reduces the already small magnetic moment of the central layer. Aditionally, the magnetic moment changes gradually over all these six layers from pointing downward in the interface to pointing upward at the surface.

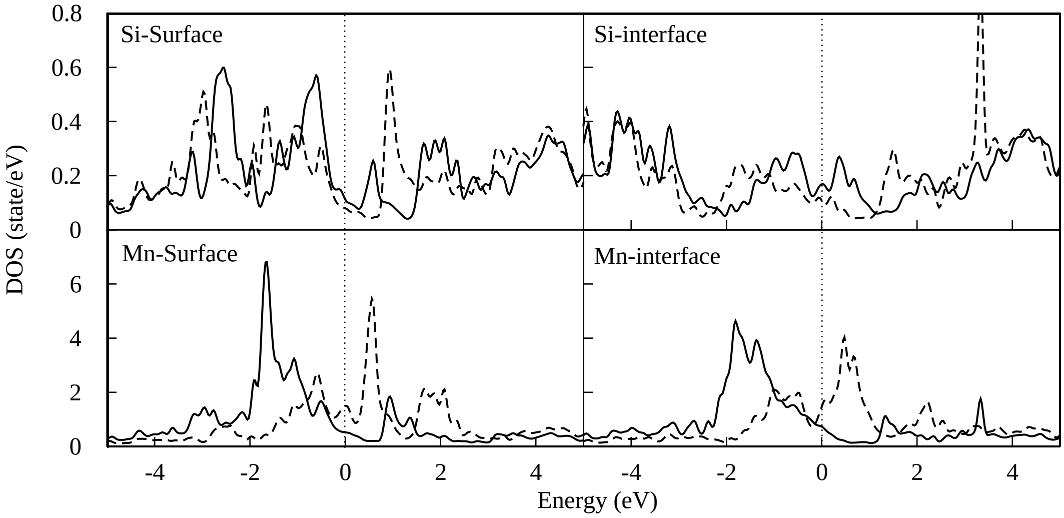

Fig. 7.7: DOS plot for the B2(111) structure on the Si(111) substrate at 3 ML coverage for Mn and Si atoms at interface and surface layer. Solid lines represent majority and dashed lines indicate minority spin channel, the dotted line shows the Fermi level.

The formation of a B2 structure film on Si(111), besides exhibiting a higher stability compared to the Si(001) case, also shows a high spin polarization of 33% and 49% at the interface and at the surface. This makes the growth of this structure on Si(111) more interesting than on Si(001).

Fig. 7.7 shows a DOS plot for B2(111) / Si(111). Clearly visible is the well defined peak for the majority spin DOS of Mn in the interface and surface layers and the Fermi level at the falling shoulder of the peak.

The thermodynamic stability of films with B2 structure on Si(111) and Si(001) as a function of coverage is shown in Fig. 7.8.
Here the formation energy of B2 film from 1-3 ML coverage in both Si surfaces are compared, red lines are B2(001) / Si(001) and black lines are B2(111) / Si(111). The dashed line which is considered as a zero reference is the surface energy of the bare surface. The formation energy of every structure consider in the case where it is in equilibrium with the bulk B20 structure of Mn-mono-silicide (circles), bulk B2 structure (triangles) and bulk Mn (squares) as reservoir.

According to this plot, the energy of film formation of B2 on Si(111) is smaller than on Si(001) in all coverages. The formation energy of the B2 film on both substrates is almost linear as a function of coverage.

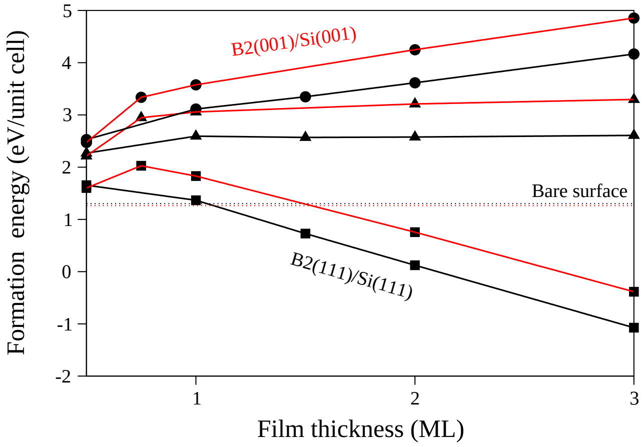

Fig. 7.8: Formation energy of film for B2 structure of Mn-mono-silicide on Si(001)(red lines) and Si(111)(black lines) substrates as a function of film thickness. Film formation is in equilibrium with bulk B20 structure of Mn-mono-silicide (circle signs), B2 structure of Mn-mono-silicide (triangle signs) and Mn (square signs). Surface energy of bare surface (dashed line) is considered as zero point.

As discussed before, the tendency of B2 / Si(001) film to transform to three-dimensional islands and the bare surface for low coverage ($\leq$ 2) makes formation of islands on this surface easier than on the Si(111) surface. However, on the other hand B2 / Si(111) film formation energy is always decreasing with increasing the film thickness.

This comparison between these surfaces can be formulated as below:

$$\begin{aligned} \Delta E &= \frac{1}{2}(\gamma_1 + \gamma_3) - \gamma_2 \\ &= \frac{(\gamma_3 - 2\gamma_2 + \gamma_1)}{2} \approx \frac{d^2\gamma}{d\theta^2} \end{aligned} \tag{7.1}$$

Here, $\gamma_i$ is the formation energy per area at $i$th ML coverage, and $\theta$ is the coverage. A positive value of $\Delta E$, which is the second derivative of the formation energy with respect to coverage, corresponds to the positive curveture of the curve. This means formation of a homogenous 2 ML film is stable againt decomposition to islands. Therefore there is a barrier against surface roughness and formation of islands.

For a negative value of $\Delta E$, the formation of a rough surface and areas with different film thicknesses are more favorable than a uniform film.

The formation energy of 2 ML is -0.51 eV / $(1\times1)$ cell which is higher than half of the sum of 1 ML and 3 ML by 0.03 eV / $(1\times1)$ cell. While in Si(111) formation of a uniform film with 2 ML coverage is more stable than 3 and 1 ML by 0.02 eV / $(1\times1)$ cell. Therefore one can conclude that from the thermodynamic point of view the formation of islands on Si(001) is easier and faster than on Si(111).

## 7.5 MnSi Surfaces

The low index Si(001) and Si(111) surfaces were studied in detail in Chap. 4. Here, the surface of MnSi in the B20(111) and B2(001) and (111) structures will be discussed.

- **B20(111) surface** The (111) surface of MnSi in the B20 structure has a in-plane hexagonal cell and four different surface terminations. The surfaces of the non-reconstructed $(1\times1)$ bulk-termination are considered in this work. These four terminations are the surface with Si-dense layer, Si-sparse layer, Mn-dense layer and Mn-sparse layer terminations, (cf. Fig. 7.5). The periodicity in $z$ direction is 12 layers, therefore the slab contains 12 layers of Mn and Si atoms. Since there is no inversion symmetry in the slab, there are two different surfaces, (111) and $(\bar{1}\bar{1}\bar{1})$, in both sides of the slab.

In these surfaces the top-most layer atomic configurations are exactly the same but the sub-surface layers are different. For example in Fig. 7.5, the top-most and the lowest layer of the slab are Si-dense layers but one of this surface connects to a Mn-dense layer below while below the other is a Mn-dilute layer. It is assumed that the surface energy of (111) and $(\bar{1}\bar{1}\bar{1})$ surfaces of the same type is very similar.

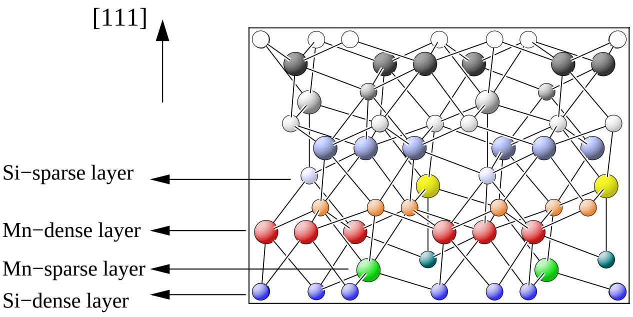

Fig. 7.9: Structure of four possible terminations of MnSi(111) in the B20 structure.

Since there are four $(1\times1)$ terminations, one needs to calculate the Gibbs free energy of each to find which one is the lowest-energy surface structure.

K. Reuter and M. Scheffler have described the formalism which combines thermodynamics and DFT total-energy calculations in order to determine the stable surface termination of compounds [163]. The most stable surface termination is the one that has lowest surface energy, defined as:

$$\gamma(T,p) = \frac{1}{A}(G(T,p) - \sum_i N_i \mu_i(T,p)) \tag{7.2}$$

Here $\gamma$ is the surface energy, $G$ is the Gibbs free energy of the slab, $N_i$ and $\mu_i$ are the number and chemical potential of the $i$th of the constituent parts of the compound. The calculated surface energies of the four possible terminations of MnSi(111) in the B20 structure as a function of chemical potential of Mn are shown in Fig. 7.10. In order to calculate the surface energies, the bulk B20 crystal structure is considered as reservoir.

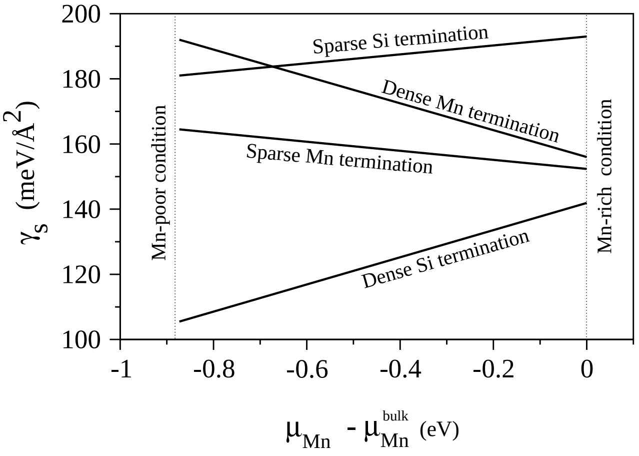

Fig. 7.10: Surface energy of the four terminations of MnSi(111) as a function of the chemical potential of Mn. The dotted vertical lines indicate the limit of the Mn chemical potential for Mn-rich and -poor conditions.

According to the phase diagram of the B20 structure, the dense-Si termination is the most stable termination over the whole Mn chemical potential range (see Fig. 7.10). The surface energy of B20 structure is about 62 meV / Å$^2$ (with respect to B2 crystal structure). The chemical potential of Mn in the Mn-poor limit corresponds to $\mu_{\mathrm{Mn}} = \mu_{\mathrm{MnSi}} - \mu_{\mathrm{Si}}$ and the high limit of $\mu_{\mathrm{Mn}}$ is taken as zero reference, and corresponds to the formation energy of bulk Mn. The lines belong to the Si (Mn) terminations and have positive (negative) slope, which indicates that the surface in Mn poor- (rich-) condition or equivalently in Si rich- (poor-) condition has more (less) stability.

Due to the increasing number of bonds, the magnetic moment of a Mn-dilute layer decreases from 2.8 $\mu_{\mathrm{B}}$ to about 1 $\mu_{\mathrm{B}}$ for a Mn-dense layer. The Mn atoms induce a small magnetic moment ($\sim$-0.05) in the topmost layer of Si atoms which have AFM coupling with the Mn atoms beneath.

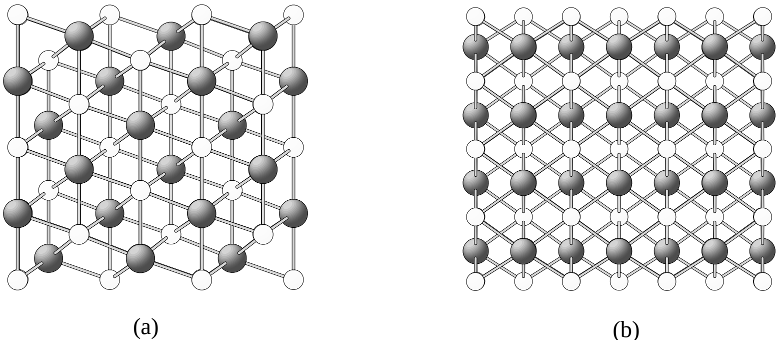
(a) (b)

Fig. 7.11: Side view of the Si-termination of MnSi in B2 structure for a (111) surface (a) and a (001) surface (b). Small white (big black) circles are Si (Mn) atoms.

- **B2 structure** The (111) and (001) surface planes of the B2 structure of MnSi with Si-termination are show in Fig. 7.5-a,b. The surface energy of B2(111)($1 \times 1$) is lower than that of B2(001) by 18.5 meV / Å$^2$ . The surface energy of B2(111) is about 39 meV / Å$^2$ more than surface energy of the B20 structure. The surface energies of all surfaces are summarized in Tab. 7.3 in Sec. 7.7. The B2(001) slab contains alternating planes of dense Mn and Si atoms with a lateral distance of 2 Å and vertical distances of 1.2-1.4 Å . In contrast, for the B2(111) surface the intralayer atomic distance is 4 Å with the vertical interlayer distances of 0.8-0.9 Å between Mn and Si.

Mn in both slabs with the B2 structure has eight bonds in the central layers, which is consistent with a small magnetic moment of 0.2 and 0.5 $\mu_\mathrm{B}$ for Mn in the (001) and the (111) slab, respectively. Due to the lack of a bond of Mn at the (111) surface , the magnetic moments of Mn atoms at the surface increase to 1.8 $\mu_\mathrm{B}$, while in the (001) surface the Mn atom still has eight bonds and a small magnetic moments of 0.2 $\mu_\mathrm{B}$.

## 7.6 MnSi Films with B20 Structure

In continuation of the work on film morphology, we study the stability of the natural structure of MnSi (B20). This structure is considered at low coverage (up to 4 / 3 ML). In the B20 structure 0.5 ML coverage corresponds to a $\sqrt{3} \times \sqrt{3}$ cell containing three Mn atoms. The structure for $\theta = 2/3$ ML in top view and side view is shown in fig. 7.12.

The formation energy of the films with B20 structure is always less than those with the B2 structure over all coverages. The formation energy of such films on Si(111) is compared with the corresponding formation energy of the films with the B2 struc-

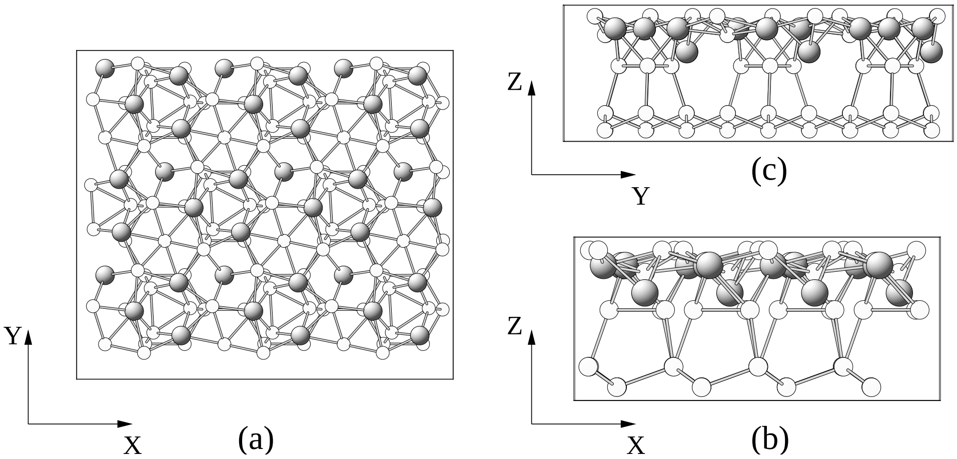

Fig. 7.12: Top view (a) and side view (b-c) of B20 of Mn-mono-silicide structure at coverage of $\theta$ = 2/3 ML.

ture for coverages from 0.5-1.5 ML in Fig. 7.13.

Similar to previous consideration, the stability of these films is calculated with respect to the reservoir of either bulk Mn (squares), or bulk MnSi in the B2 structure (triangles) or in the B20 structure (circles) of Mn-mono-silicide. The dashed lines represent B2 / Si(111) and the solid lines correspond to B20 / Si(111).

The energy of film formation of B20 / Si(111) with respect to bulk B20 is almost constant, about 1.1 eV / $(1 \times 1)$ unit cell, while its formation energy decreases with respect to bulk Mn and the B2 structure of Mn-monosilicide. However, the formation energy of the B20 film is still higher than the energy of the bare Si(111) surface.

The average magnetic moments at $\theta = 8/6$ ML coverage is about 2.3, 0.9 and 3.4 $\mu_{\rm B}$ at the surface, the central and the interface layers which are higher than the magnetic moment of a film with the B2 structure at similar coverage. The parallel spin moment coupling is considered for Mn atoms in-plane as well as between layers. With increasing of the film thickness the magnetic moments at surface and interface increase. According to the DOS plot, the film with B20 structure is a metallic film with the interfacial and surface spin polarization of more than 50%.

Finally, we come to the conclusion that thermodynamically formation of a homogenous wetting Mn-mono silicide film on the Si substrate is metastable and formation of islands of metallic Mn-mono-silicide with $(\sqrt{3} \times \sqrt{3})$R30° cell is favorable. Such an island has considerable magnetization and spin polarization at interface and surface.

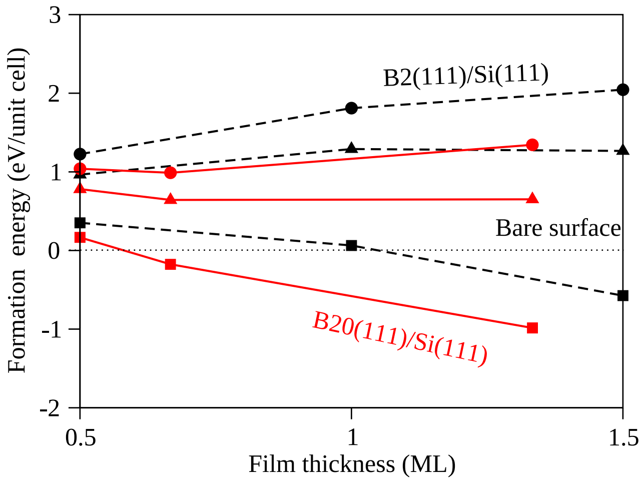

Fig. 7.13: Formation energy of ultrathin film for B2 (black lines) and B20 (red lines) structure of Mn-mono-silicide on Si(111) substrates as a function of film thickness. The energy of film formation is calculated by assuming equilibrium either with the B20 bulk structure of Mn-mono-silicide (circles), or the B2 structure of Mn-mono-silicide (triangles) or Mn bulk (squares). The surface energy of the bare Si(111)($1 \times 1$) surface (dotted line) is considered as zero point.

## 7.7 Growth Mode of Mn-Monosilicide in B2 Structures on Si Substrates

Studies of the surface morphology of epitaxial growth attract attention since their development help to explain the stability of nanostructures, islands or film formation on the surface.

Thin film growth usually falls into one of three broad categories: Frank van der Merwe (layer by layer growth), Volmer-Weber (island formation growth), and Stranski-Krastanov (layer growth followed by island formation), Fig. 7.7 [143]. This scheme of classification is well understood and works for the vast majority of systems investigated.

Quantitatively, each system adopts a unique growth mode depending on the relative magnitude of its surface and interface energies.

In a simple description, the growth mode can be attributed to the lattice match between the substrate and the film. Existence of a lattice mismatch creates strain in the film which leads to formation of three-dimensional (3D) islands (either Volmer-Weber or Stranski-Krastanov growth mode). Thermodynamically, this growth regime is more favorable than formation of a homogenous film. The small lattice mismatch between substrate and film causes first formation of a wetting layer and subsequently formation of islands on this wetting layer (Stranski-Krastanov growth mode). On the other hand, in the large lattice mismatch regime, the growth process will end up in the Volmer-Weber growth mode in which the islands form on the bare surface.

$$\Delta\gamma = \gamma_{\mathrm{film}} - \gamma_{\mathrm{substrate}} + \gamma_{\mathrm{interface}} \tag{7.3}$$

$$\begin{cases} \gamma_{\mathrm{substrate}} > \gamma_{\mathrm{film}} + \gamma_{\mathrm{interface}} & \mathrm{Frank-van\ der\ Merwe} \\ \gamma_{\mathrm{substrate}} < \gamma_{\mathrm{film}} + \gamma_{\mathrm{interface}} & \mathrm{Volmer-Weber\ /\ Stranski-Krastanov} \end{cases} \tag{7.4}$$

here, $\gamma_{subs}$, $\gamma_{film}$ and $\gamma_{inter}$ are the surface energy of the surface, the formation energy of a film and the interface energy per area.

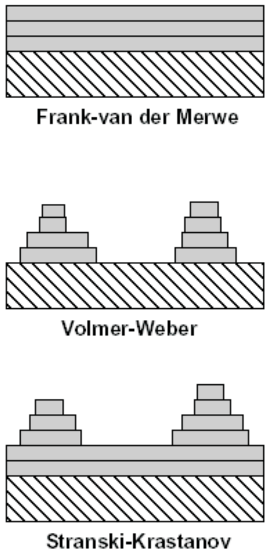

Fig. 7.14: Schematic illustration of different growth modes of heteroepitaxial growth.

If the energy of the film and of the interface per area is lower than the surface energy of the substrate, a layer-by-layer growth mode will be preferred, while a lower surface energy of the substrate would lead to formation of islands.

As it was discussed in Sec. 7.4 in the competition between island and film formation, it is more favorable at low coverage that islands form instead of a uniform epitaxial film on Si(001). It can be explained by the energy gain due to relaxation in an island which overcompensates the energy cost of increasing the surface energy by the side facets of the island [164]. However, since formation of island's facets costs energy, therefore island formation is not instantaneous and it will form only at certain coverage of adsorbate and island density. In order to study this surface roughness one needs to find the conditions for nucleation of islands and the optimum island size for a given coverage and island density. In the following part, the critical size for island formation will be calculated.

### 7.7.1 Formation of MnSi Nano-Structures on Si Substrates

The formation and stability of island and film were calculated for InAs/GaAs by Wang *et al.* [164]. They calculated the energy gain for an island assuming that islands form with a identical shape and size, in equilibrium with the wetting layer.

Since the lattice mismatch between the Si substrate and the B2 structure of MnSi is small (less than 2%), the formalism which is used in this work is a bit different. Here, the elastic energy density which is introduced by strain is neglected. We consider a pyramidal-shaped island of MnSi with a square or triangle base (with a base length of $a$) on the substrate.

The real island shapes are more complex, having complicated facets. However, already such a simple island shape allows a preliminary estimate of basic features of the island formation. It is supposed that the island which forms on Si(001) has four (111) facets and the tetrahedral island on Si(111) has three (001) facets, cf. Fig. 7.15.

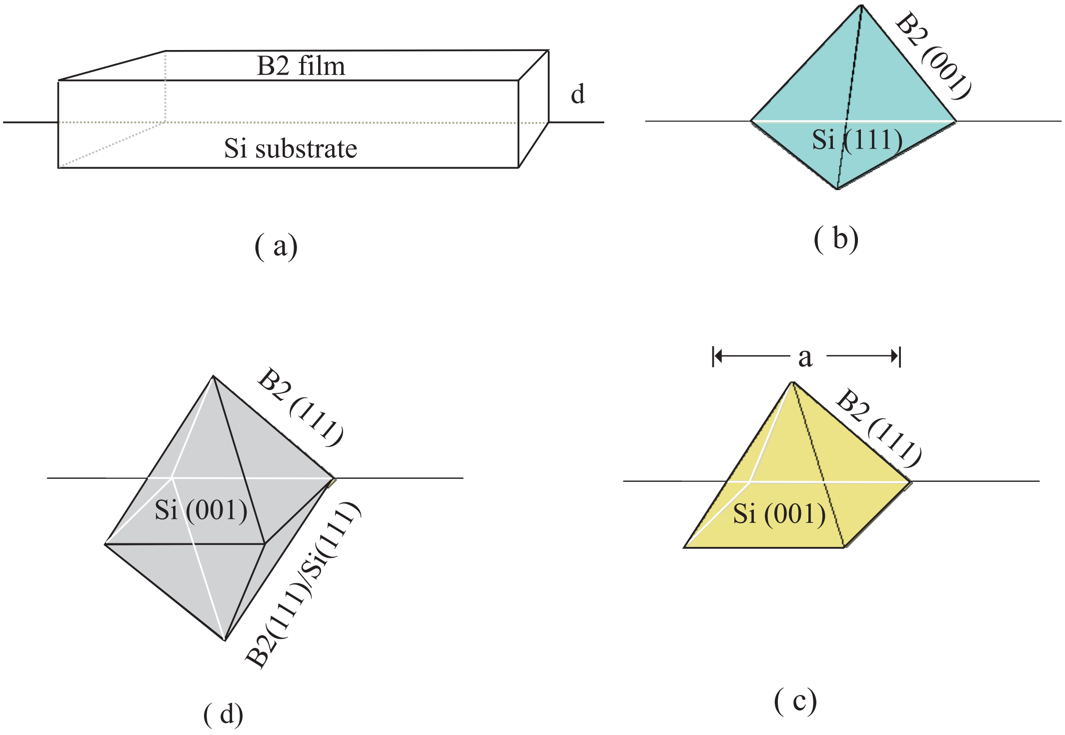

Fig. 7.15: Schematic illustration of film formation with thickness $d$ (a) and island formation with island base length $a$. On the Si(111) substrate, the tetrahedral-shaped-islands with B2(001) facets (b) will form and on the Si(001) substrate, the pyramid islands with B2(111) facets (c). The iceberg island (d) with B2 structure can form on both Si substrates.

Figure 7.15 schematically illustrates the island formation on the substrate surface. $d$ is the thickness of the film.

The equilibrium condition between film and island can be described as:

$$A_{\text{film}}\gamma_{\text{film}} = (A_{\text{film}} - A_{\text{interface}})\gamma_{\text{substrate}} + A_{\text{interface}}\gamma_{\text{interface}} + N \times A_{\text{facet}}\gamma_{\text{island}} \quad (7.5)$$

where $\gamma_{\text{film}} = \gamma_{\text{surface}} + \gamma_{\text{interface}}$ is the formation energy of the wetting layer per unit area. It consists of the surface energy of the wetting layer ($\gamma_{\text{surface}}$) and the interface energy per unit area ($\gamma_{\text{interface}}$). $\gamma_{\text{substrate}}$ and $\gamma_{\text{island}}$ are the surface energy of the bare substrate and the surface energy of the facet of an island. $A_{\text{film}}$ and $A_{\text{facet}}$ are the area of the wetting film and the facets, and $N$ is the number of facets.

In the present work all surface energies are evaluated with respect to being in equilibrium with a bulk of MnSi in a $B2$ (CsCl) structure (i.e., $\mu_{\text{Mn}} = \mu_{\text{MnSi}}^{\text{bulk}} - \mu_{\text{Si}}^{\text{bulk}}$). From mass conservation it can be deduced, that the volume of an island $V$ is given by:

$$\frac{V}{v_{\text{atom}}} = \frac{1}{6}\, a^3\, \frac{\tan\alpha}{v_{\text{atom}}^{\text{island}}} = A_{\text{film}} \times \frac{d}{v_{\text{atom}}^{\text{film}}} \quad (7.6)$$

where $\alpha$ is the angle between the island facets and the substrate (cf. Fig. 7.15) and $d$ is the thickness of the film [164]. $v_{\text{atom}}^{\text{island}}$ and $v_{\text{atom}}^{\text{film}}$ are atomic volume of MnSi in crystal structures of islands and film, respectively. Since crystal structure and bond lengths in B2 and B20 structures are different, therefore their islands have not the same volume. Thus $A_{\text{film}} = \frac{V}{d} \cdot v_{\text{atom}}^{\text{film}}/v_{\text{atom}}^{\text{island}}$. In this work, the film has only B2 structure and the islands have either B2 or B20 structures. According to the calculation in the Chap. 3 the volume of a Mn atom in B20 and B2 crystal structures is 23.04 and 21.84 Å$^3$, respectively.

Since the formation enthalpy of the B20 structure is lower than that of the B2 structure by $\sim$ 0.26 eV / formula unit, one should take into the account an extra term ($\epsilon = \Delta H \cdot V/v_{\text{atom}}^{\text{B20}}$) to eq. 7.5 for the B20 islands formation. The energy release to form a B20 island from a film with B2 structure is about 0.011 eV / Å$^3$.

The total energy difference between film and island formation per unit volume of a single island can be expressed as:

$$\begin{aligned}\Delta E/V = {} & \frac{(\gamma_{\text{substrate}} - \gamma_{\text{film}})}{d}(v_{\text{atom}}^{\text{film}}/v_{\text{atom}}^{\text{island}}) \\ & + [A_{\text{interface}}\,(\gamma_{\text{interface}} - \gamma_{\text{substrate}}) + N \times A_{\text{facet}}\,\gamma_{\text{island}}]/V - \epsilon \quad (7.7)\end{aligned}$$

A positive value of $\Delta E$ indicates that film formation with B2 structure of Mn mono-silicide is more stable than island nucleation, while a negative value favors the stability of islands.

The surface energy for a non-reconstructed $(1 \times 1)$ ideal surface termination at low index silicon surfaces as well as for MnSi surfaces in the B2 and B20 structures are given in Tab. 7.3. For Si surfaces the surface energy is compared to the surface energy calculated by Stekolnikov and Bechstedt (S-B) [6].

In order to a calculate the surface energy, bulk silicon and MnSi in B2 structure are considered as reservoirs. The surface energy of the Si(111) surface is less than that of the Si(001) but the B20(111) surface is the most stable surface. Therefore, formation of a wetting layer with the natural MnSi film should be more stable on Si(111) than an epitaxial film with B2 structure.

Table 7.3: Surface energy, $\gamma_{\mathrm{surface}}$ (meV/Å $^2$) of non-reconstructed Si and MnSi surfaces. Bulk MnSi in the B2 structure is considered as a reservoir for the chemical potential of Mn. The calculated surface energies from Stekolnikov and Bechstedt (S-B) [6] are for a Si(001)c$(4 \times 2)$ and a Si(111)$(7 \times 7)$ reconstruction.

| Surface | Present work GGA | Ref. | S-B work LDA |
|---|---|---|---|
| Si(001)$(1 \times 1)$ | 136 | Sec. 4.2.1 | 149 |
| Si(001)$(2 \times 2)$ | 84 | Sec. 4.2.3 | 88 |
| Si(111)$(1 \times 1)$ | 100 | Sec. 4.3 | 109 |
| Si(111)$(7 \times 7)$ | 81* | — | 85 |
| MnSi(B2)(001) | 118 | Sec. 7.5 | — |
| MnSi(B2)(111) | 101 | Sec. 7.5 | — |
| MnSi(B20)(111) | 62 | Sec. 7.5 | — |

(*) The surface energy of the reconstructed Si(111)$(7 \times 7)$ is extrapolated from the LDA calculation of S-B work.

In Tab. 7.4 the film thickness $(d)$ , facet area $(A_{\mathrm{facet}})$, volume of island $(V_{\mathrm{island}})$, energy of film formation $(\gamma_{\mathrm{film}})$ and interface energy $(\gamma_{\mathrm{interface}})$ per area for MnSi in B2 and B20 structure in Si(001) and Si(111) are given. The films thickness in Tab. 7.4 corresponds to 3 ML Mn coverage. The surface energies of Si(001) and Si(111) are compared to Stekolnikov and Bechstedt (S-B) work which was done using the LDA functional [6].

The film growth on Si(111) is more favorable than an Si(001) and formation of the B20 structure is easier than of the B2 structure. The interface energy of the B20 structure is the lowest value. However, the interface energy in Si(001) and Si(111) depends on the kind of island which forms on each substrate (cf. Tab. 7.5).

Table 7.4: Film thickness, $d$, facet area $A_{\text{facet}}$ energy of film formation per area, $\gamma_{\text{film}}$, and surface energy of the bare surface. For Si, the reconstructed surfaces are considered while for MnSi, the non-reconstructed surface is considered.

| Film | $d$ Å | $A_{\text{facet}}$ Å $^{2}$ | $\gamma_{\text{film}}$ meV / Å $^{2}$ | $\gamma_{\text{substrate}}$ meV / Å $^{2}$ | Ref. |
|---|---|---|---|---|---|
| B2(001) / Si(001) | 7.51 | $(\sqrt{3}/4)a^2$ | 219 | 88 | Sec. 6.4 |
| B2(111) / Si(111) | 8.87 | $(1/4)a^2$ | 200 | 85 | Sec. 7.4 |
| B20(111) / Si(111) | 8.00 | $(1/4)a^2$ | 148 | 85 | Sec. 7.6 |

There are three kinds of islands that can form on Si(001), the pyramid shape with 4 facets with B2 structure, the iceberg island with B2 structure and the iceberg island with B20 structure. In the pyramid island there is an interface between the B2(001) film and the bare surface of Si(001). In the iceberg island there are four interfacial facets which have B2 (B20) structure on Si(111).

Because the B20 structure is not compatible with Si(001), therefore the energy of such interface is not calculated and the formation of an iceberg island with B20 structure on Si(111) is discarded.

The interface of a pyramid island on Si(001) is a square with $a^2$ and iceberg islands have 4 facets with $(\sqrt{3}/4)$ $a^2$ area of each facet. The interface of a pyramid island on Si(111) has a triangle base shape with $(\sqrt{3}/4)$ $a^2$ area and the interface area of the iceberg island is three triangles.

The critical base lengths for nucleation of different kind of islands on both Si(001) and Si(111) are given in Tab. 7.5 for a given thickness of the film (which is mentioned above Tab. 7.4) .

As one can see from the values of the stable island size, formation of an iceberg island with B20 structure on Si(001) is faster than other kind of island on both surface orientations. On Si(001), islands form earlier than in Si(111), and the film on Si(111) is more stable than on Si(001). Additionally, the iceberg form of the island is more favorable than the pyramid shape and in Si(001) islands have B20 structure. The island size of the B20 structure on Si(001) with iceberg shape is only 15.0 Å which is almost 3 times the lattice constant of Mn-mono silicide in B20 crystal bulk[6]. Therefore this nano-structure on Si(001) can from rapidly, in contrast to formation of pyramid islands on Si(111), which should be rare, because the base length for island formation is about 30 times the lattice constant of Mn-mono silicide in the

---

[6] The lattice constant of B20 structure of Mn-mono silicide is 4.5 Å, see Sec. 3.4.1

Table 7.5: Area of interface and volume of islands, interface energy per area, $\gamma_{\text{interface}}$ and stable island size $a_0$ for island formation. Bulk MnSi in B2 structure is considered as reservoir for calculating the chemical potential of Mn.

| Film | | $A_{\text{interface}}$ Å $^2$ | $V_{\text{island}}$ Å $^3$ | $\gamma_{\text{interface}}$ meV / Å $^2$ | $a_0$ Å |
|---|---|---|---|---|---|
| B2(001) on Si(001) | Pyramid B2 | $a^2$ | $\frac{\sqrt{2}}{6}\,a^3$ | 101 | 52.0 |
| | Iceberg B2 | $\sqrt{3}\,a^2$ | $\frac{\sqrt{2}}{3}\,a^3$ | 99 | 28.0 |
| | Iceberg B20 | $\sqrt{3}\,a^2$ | $\frac{\sqrt{2}}{3}\,a^3$ | 86 | 15.0 |
| B2(111) on Si(111) | Pyramid B2 | $\frac{\sqrt{3}}{4}\,a^2$ | $\frac{1}{12\sqrt{2}}\,a^3$ | 99 | 133.2 |
| | Iceberg B2 | $\frac{3}{4}\,a^2$ | $\frac{1}{6\sqrt{2}}\,a^3$ | 101 | 71.3 |

B20 structure.

With island size larger than the stable value, $a_0$, $\Delta E$ has negative value which means that the growth of the islands become exothermic.

⋆ ⋆ ⋆ ⋆

## Chapter 8

# Conclusion and Outlook

When this project was started, it was not known how adsorbed Mn atoms behave and react on the most common and technologically important semiconductor, *i.e.* Si surfaces. All previous information about Mn / Si heterostructures was limited to just a few experimental reports about the growth mode of Mn on Si(111) [15,18–20]. The scope of this work consists of the comprehensive study of the morphology and the (epitaxial-)growth mode of manganese and some Mn-silicide heterostructures on the two most practical Si surfaces (*i.e.* Si(001) and Si(111)). The goal was to understand the thermodynamic and structural stability as well as magnetic behavior of the Mn / Si system. Since the quality of the metal-semiconductor interface is crucial for practical applications, one has to know about the growth mechanism of films as well as the magnetic properties and spin polarization of the surface and interface.

In order to explore the suitability and character of the films and their interface, we perform all-electron calculations in the density-functional theory framework (Sec. 2.3) which is a powerful practical tool to study the properties of materials. The calculations were based on the generalized gradient approximation (GGA-PBE) to the exchange correlation functional (Sec. 2.4) and the full-potential augmented plane wave (FP-APW+lo) method (Sec. 2.5.1 & 2.5.2)as implemented in the WIEN2k computer package (Sec. 2.8).

The third chapter represents an important contribution towards understanding bulk properties (such as the cohesive energy, bulk stability, Mn-Si interactions and magnetic properties) of some of the $\mathrm{Mn}_x\mathrm{Si}_y$ compounds which could be grown on Si surfaces. We perform systematic studies of the stability of different structures of bulk Mn-mono-silicide. We find that the CsCl structure has a cohesive energy only 0.25 eV per formula unit lower than that of the natural phase, the B20 structure, but is clearly more stable than the WC, NiAs or NaCl crystal structure.

Since surface diffusion and morphology of growth are directly related to the substrate, we studied surface reconstructions and thermodynamic stability of bare Si(001) and (111) surfaces (Chap. 5). The calculations on surface diffusion were done on the $(2 \times 2)$ surface reconstruction and the film growth is based on a $(1 \times 1)$ surface supercell.

The energetic stability, electronic and magnetic properties of different configurations of a Mn adatom on the Si substrate for low coverage (up to 1 ML) have been obtained as an early stage of epitaxial growth. We found that the most stable site is a second layer interstitial site, where the Mn atom is located beneath the Si surface dimers on Si(001), and an second layer hollow site on Si(111) (Sec. 5.3 & 7.2).

In a comprehensive calculation, we mapped out the potential energy surface (PES) for diffusion of a Mn adatom on Si(001) (Sec. 5.5). From the PES, we conclude that the energy barrier for the Mn atom to go to sub-surface interstitial site is 0.3 eV. From the calculated potential-energy surface for the Mn adatom $on$ the surface, it was found that the energy barrier for on-surface diffusion is 0.55 eV which is higher than the diffusion barrier for penetration to a sub-surface site.

A large number of calculations were performed to predict the morphology and stability of ultra-thin films of Mn / Si up to 3 ML (Chap. 6 & 7). We find that for ultrathin film growth of Mn on the Si substrate, the manganese-silicon multilayers with 1:1 stoichiometry (MnSi) are more stable than a pure Mn film.

Since the rather complex natural MnSi (B20 structure) appears to be incompatible with Si(001), we introduced the epitaxial formation of a novel structure which does not exist in bulk form. As a starting point, we compare various crystal structures of Mn-mono-silicide (CsCl, WC, NiAs, NaCl). The CsCl (B2) structure is found to be the most stable structure after the natural B20 structure. Films with B2 structure can be superior to natural monosilicides because of their good lattice match (within $\sim +2\%$) with Si(001). The B2 structure yields smaller strain than the B20 structure (with lattice mismatch of 3%) on the substrate.

In Section 7.4 we compare films of the B2 structure of Mn-mono-silicide on both Si(001) and Si(111) substrates. The film formation of the B2 structure on both substrates is thermodynamically stable with respect to bulk Mn. The B2 film on Si(111) is more stable than the equivalent film on Si(001), and their stability with film thickness increases monotonously.
Although the film with the proposed B2 structure has similar structure and lattice constant with the Si substrate, it is metastable against island formation of silicon-rich compounds.

The CsCl-like films show a layered magnetic structure with strong ferromagnetic coupling between the Mn atoms of each layer, and also sizable magnetic moments of $\sim 2\,\mu_B$ in the interface and surface layer. The B2 films on Si(111) show slightly larger magnetic moments than the films on Si(001); hence the Si(111) substrate is preferable for the preparation of magnetic films. The ferromagnetic coupling between the spin moment of Mn atoms is more favorable than antiferromagnetic coupling in this film structure in both surfaces. The calculated spin polarization of this structure at both (001) and (111) surfaces is about 30%. Hence we suggest that MnSi / Si heterostructures can be used for injection of a spin-polarized current from the metal into the semiconductor.

We find that on Si(111) the most stable Mn-mono-silicide has an atomic structure similar to the bulk B20 structure and shows a $(\sqrt{3} \times \sqrt{3})\ R30^\circ$ reconstruction at the surface, in agreement with experiment. Therefore, we judge that films with B20 structure of MnSi are the most interesting ones for possible spintronics applications (among the monosilicides studied here), and Si(111) is the preferred substrate for their growth.

Elaborate work was done to simulate an enormous number of configurations to gain insight into the formation of nanostructures of Mn-silicides on the Si substrate, but there are still some open questions about properties, shape, structure and size of these nanostructures. Beyond our thermodynamic approach, by using our DFT results and kinetic Monte Carlo, one could study the diffusion and nucleation processes to understand how the nanostructures form. The research in this thesis gave an idea about the possibility of applying Mn to fabricate magnetic metal-semiconductor heterostructures.

⋆ ⋆ ⋆ ⋆

# Zusammenfassung

In dieser Arbeit wurde das Ziel verfolgt, den Wachstummodus von Mn / Si Heterostrukturen zu verstehen. Dabei wurde besonders Wert auf die thermodynamische und strukturelle Stabilität und die magnetischen Eigenschaften eines solchen Systems gelegt. Da die Qualität der Metall-Halbleiter Schnittstelle für praktische Anwendungen entscheidend ist, muß man den Wachstumsmechanismus der Filme, sowie die magnetischen Eigenschaften, die Spinpolarisation der Oberfläche und Grenzfläche kennen.

Um die Eignung und den Charakter der Filme und ihrer Grenzfläche zu erforschen, führen wir All-Elektron-Berechnungen im Rahmen der Dichtefunktionaltheorie durch (Abschnitt 2.3) die ein geeignetes und leistungsfähiges Werkzeug für eine Studie des Eigenschaften dieser Materialien ist. Die Berechnungen basieren auf der Methode der generalisierten Gradientenapproximation (GGA-PBE) zum Austauschkorrelationsfunktional (Abschnitt 2.4) und der "full-potential augmented plane wave plus local-orbital (FP-APW+lo)" Methode (Abschnitt 2.5.1 & 2.5.2), wie sie im WIEN2k Paket (Abschnitt 2.8) implementiert ist.

Das dritte Kapitel stellt einen wichtigen Beitrag zum Verstädnis der Festkörper-Eigenschaften (Bindungsenergie, Stabilität, Mangan-Silizium Wechselwirkung, magnetische Eigenschaften) einiger der $\mathrm{Mn}_x\mathrm{Si}_y$ Verbindungen dar, die auf Silizium-Oberflächen aufgewachsen werden können. Wir führen systematische Studien der Stabilität der unterschiedlichen Polytypen von Manganmonosilizid durch. Unsere Rechnungen zeigen, daß die CsCl-Struktur eine Bindungsenergie hat, die um 0.25 eV pro Einheitszelle geringer ist als die der natürlichen Phase, der B20 Struktur, und stabiler ist als die WC, NiAs oder NaCl-Kristallstruktur.

Da Oberflächendiffusion und Wachstumsmorphologie direkt mit dem Substrat zusammenhängen, studierten wir Oberflächenrekonstruktionen und die thermodynamische Stabilität von diversen Si(001)- und (111)-Oberflächen (Kap. 5). Die Berechnungen auf Oberflächendiffusion erfolgten zum der $(2\times2)$-Oberflächen-Rekonstruktion, die Untersuchung des Filmwachstums basiert auf einer $(1 \times 1)$-Superzelle.

Die energetische Stabilität, die elektronischen und magnetischen Eigenschaften der unterschiedlichen Konfigurationen eines Mangan-Adatoms auf der Silizium-oberfläche bei niedriger Bedeckung (bis zu 1 ML) sind bedeutsam als frühestadium der Epitaxie. Wir fanden, daß die stabilste Bindungs Position ein Zwischengitterplatz in der zweiten Monolage ist, in dem das Mangan-Atom unter den Oberflächen-Dimeren der Si(001)-Oberfläche liegt. Auf der Si(111)-Oberfläche ist der stabiste Bindungsplatz ein Lochplatz in zweiten Monologe (Abschnitt 5.3 & 7.2).

In einer umfassenden Berechnung erstellten wir die Potential-Energieoberfläche (PES) für Diffusion eines Mangan-Adatoms auf Si(001) (Abschnitt 5.5). Es ergibt sich, daß der Potentialbarriere für das Mn-Atom auf einen Zwischengitterplatz zu gelangen bei 0.3 eV liegt. Aus der errechneten Potentialoberfläche für das Mangan-Adatom *auf* der Oberfläche wurde die Diffusionsbarriere zu 0.55 eV bestimmt. Dieser Wert liegt höher als die Barriere für die Diffusionsbarriere unter die Oberfläche.

Viele Berechnungen wurden durchgeführt, um Morphologie und Stabilität von ultradünnen Film von Mn / Si bis zu 3 ML vorauszusagen (Kap. 6 & 7). Wir fanden, daß bei ultradünnem Filmwachstum von Mangan auf dem Silizium-Substrat das Mangan-Silizium-Mehrlagensystem mit 1:1 Stöchiometrie (MnSi) stabiler ist als ein reiner Mangan-Film.

Da das natürliche MnSi (Struktur B20) mit Si(001) Structurell inkompatibel zu sein scheint, schlagen wir die Herstellung einer neuartigen Struktur durch Epitaxie vor, die nicht als Volumenkristallform existiert. Als Ausgangspunkt vergleichen wir verschiedene Kristallstrukturen von Manganmonosilizid wie CsCl, WC, NiAs, NaCl. Die CsCl (B2) ist die stabilste Struktur nach der natürlichen B20 Phase. Filme mit der B2 Struktur könnten natürlichen Monosiliziden wegen ihrer guten Gitterpassung ($\sim +2\%$) mit Si(001) überlegen sein. Außerdem zeigt die B2-Struktur eine kleinere Verspannung als die B20-Struktur (mit Gitterfehlpassung von $3\%$) auf dem Substrat.

In Abschnitt 7.4 vergleichen wir die B2-Struktur von Manganmonosilizid auf Si(001) und Si(111). Die Bildung der Filme mit B2-Struktur auf beiden Substraten ist thermodynamisch stabil in Bezug auf daselementare Mangan und Silizium.

Der Film (B2) auf Si(111) ist stabiler als ein gleichartiger Film auf Si(001), und interessanterweise erhöht sich die Stabilität monoton mit der Schichtdicke.
Obgleich der Film mit unserer vorgeschlagenen B2-Modellstruktur ähnliche Struktur- und Gitterparameter wie das Siliziumsubstrat hat, ist er metastabil gegen Inselbildung aus Verbindungen mit hohem Siliziumgehalt.

Die Filme mit CsCl-Stuktur zeigen eine magnetische Schichtstruktur mit starker ferromagnetischer Kopplung zwischen den Mangan-Atomen jeder Schicht und auch beträchtliche magnetische Momente von $\sim 2\,\mu_B$ in der Granzflächen- und Deck-

Schicht. Die B2-Filme auf Si(111) zeigen etwas größere magnetische Momente, folglich ist dieses Substrat eher geeignet um magnetische Filme herzustellen. Die ferromagnetische Kopplung dominiert in dieser Filmstruktur bei beiden Oberflächen. Die errechnete Spinpolarisation dieser Struktur an (001)- und (111)-Oberflächen sind ungefähr 30%, also ausreichend für Strominjektion vom Metall zum Halbleiter.

Jedoch finden wir, daß auf Si(111) das stabilste Manganmonosilizid eine Atomstruktur hat, die ähnlich der B20 Struktur ist und eine $(\sqrt{3} \times \sqrt{3})\ R30^\circ$ Rekonstruktion der Oberfläche zeigt, in Übereinstimmung mit dem Experiment.
Folglich denken wir, daß MnSi-Filme mit einer B20 Struktur am interessantesten (unter den hier studierten Monosiliziden) für mögliche spintronische Anwendungen sind. Si(111) ist das am besten geeignete Substrat für die Herstellung der Filme.

⋆ ⋆ ⋆ ⋆

# Appendix A

## A-1 Convergence Test for Bulk Si

The calculations in this work are performed using the full-potential augmented plane wave plus local orbital method (Sec. 2.5.1 & 2.5.2) as implemented in WIEN2k computer code (cf. Sec. 2.8).

In order to obtain adequate accurate results and save as well computer time, one should first optimize the parameters which have a significant effect on the results. Here we present the convergence test for parameter which were used in the bulk Si and Si(001) surface calculations.

The main parameters which should de determined are the energy cutoff for the plane waves and the number of **k**-points in the irreducible part of the first Brillouin zone (1 BZ). In the surface calculations, additionally one needs to test the vacuum thickness and number of the layers in the slab. As it discused in Sec. 2.7, the surfaces of slabs should not have interaction with each other through the vacuum or the slab. On the other hand, the vacuum should not be very thick as this would make the calculations slow.

The calculations are done with the lattice constant of 5.47 Å for Si. The APW basis set is taken as follows: $R_{\mathrm{Si}}^{\mathrm{MT}}$ = 2.1 bohr, the maximum number of angular mometa for the wave function inside the muffin tin spheres up to $l_{\max}^{\mathrm{wf}}$ = 12. The results for the convergence test of the cohesive energy of Si bulk are shown in Fig. A-1.

Facilitate the comparison between plots, we compare cohesive energies. The energy of Si-atom is calculated in such way that we determine the total energy of and a single atom in a big box in size of $(20 \times 20 \times 20)$ bohr, for one **k**-point in the 1BZ and for a sufficiently big energy cutoff (here we took 16.4 [Ry]). In contrary to bulk, the calculation for the free atom is very slow which is due to the large size of the box which increases the size of the interstitial region.

We compare results for the **k**-point set of $(5\times5\times5)$, $(6\times6\times6)$, $(7\times7\times7)$, $(8\times8\times8)$ and $(10\times10\times10)$ and as well as for $RK_{\max}$ from 6 to 8.5 (bohr.Ry$^{1/2}$) which corresponds to $\mathrm{E}_{cut}^{pw}$ from 8 to 16.4 [Ry].

Finally, a (8×8×8) Monkhorst-Pack grid in the Brillouin-zone which corresponds to 29 **k**-points in the irreducible part of the Brillouin-zone and the energy cutoff of 12.8 [Ry] ($i.e.$ $RK_{\max}$ = 7.5 (bohr.Ry$^{1/2}$)) are chosen for bulk Si calculations. The differences in the cohesive energy for calculations using a higher number of **k**-points and larger $\mathrm{E}_{cut}^{pw}$ than above are smaller than 3 meV / atom.

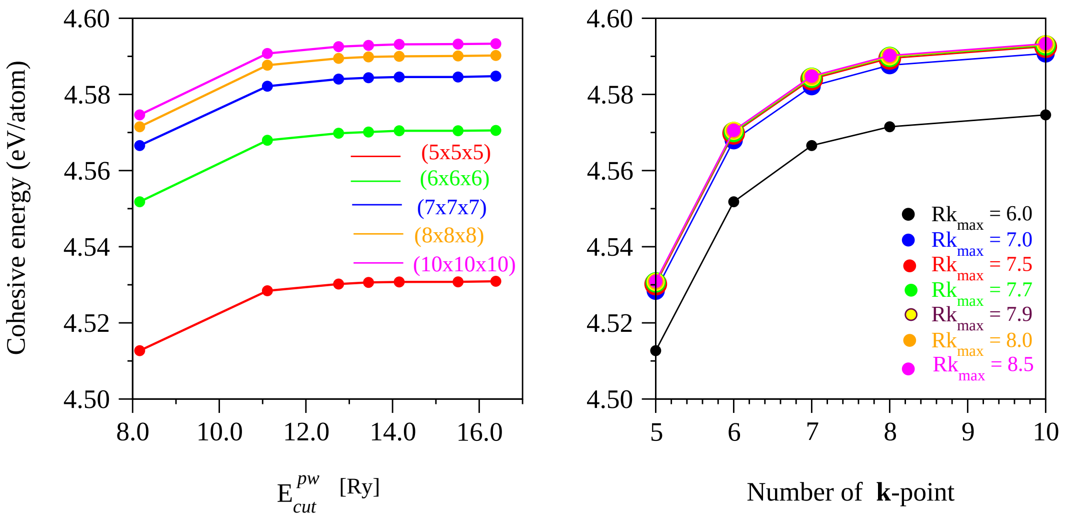

Fig. A-1: The cohesive energy as a function of (a) the cutoff of wave function, (b) the number of **k**-points in the 1BZ.

## A-2 Convergence Test for The Si(001) Surface

The surface calculations are performed using a supercell containing a slab with inversion symmetry. The slab is oriented in $z$ direction. The atoms in the two middle Si-layers are fixed at their bulk positions. All atoms in the remaining top and bottom layers are allowed to relax in each of the three directions ($x$,$y$,$z$). The geometry is relaxed until the residual forces on any atom are smaller than 30 meV / Å.

Before starting with the surface calculations, we perform tests concerning the energy cutoff, the number of **k**-points in the irreducible part of the first Brillouin zone (1 BZ), the vacuum thickness and the number of layers in the slab for an unreconstructed surface to determine the optimal parameters needed for the subsequent calculations. The values used for any of these parameters have a significant effect on the results.

Some details of the mentioned tests are as follows.

The convergence of the surface free energy (see Eq. 4.1 ) with respect to the plane wave energy cutoff, $E^{pw}_{cut}$ is shown in Fig. A-2 (a) for the unrelaxed surface. In order to calculate the surface energy for each calculation, the energy values for both surface and bulk Si are taken using the same $E^{pw}_{cut}$. Choosing an energy cutoff of 13.8 Ry ensures an accuracy of about 0.6 meV / Å$^2$ . The number of **k**-points needed for an accuracy of 0.7 meV / Å , corresponds to a $(8 \times 8 \times 1)$ Monkhorst-Pack grid in a $(1 \times 1)$ surface unit cell. To obtain the bulk cohesive energy of silicon, a $(8{\times}8{\times}8)$ **k**-point set is used. The dependence of the surface free energy on the **k**-points is displayed in Fig. A-2 (b).

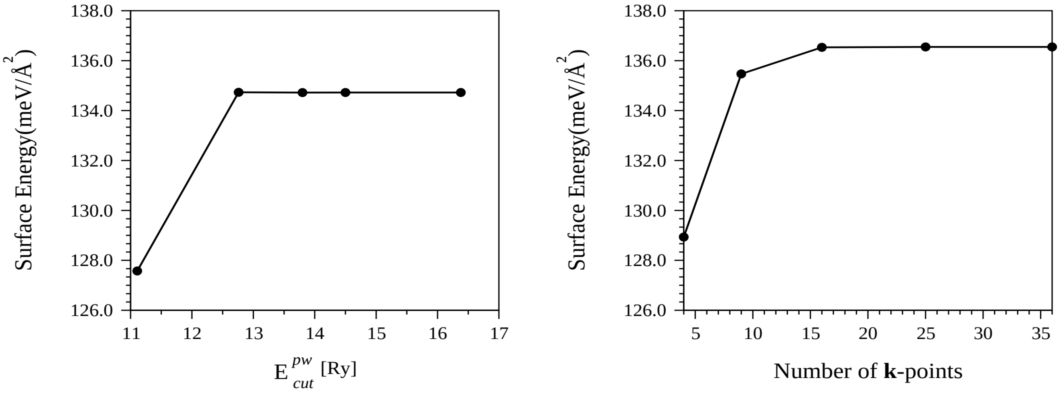

(a) (b)

Fig. A-2: The surface free energy versus (a) the energy cutoff, (b) the number of **k**-points in the 1BZ for a slab of six Si layers and a vacuum of 15 Å.

The results of the convergence test concerning the number of Si layers in the slab and the vacuum thickness at $E_{cut}^{pw}$=13.8 Ry and with the $(8 \times 8 \times 1)$ **k**-point set in a $(1 \times 1)$ surface unit cell are shown in Fig. A-3. Using an 8 layer Si-slab and 14 Å vacuum thickness are sufficient to achieve an accuracy about 0.3 meV / Å$^2$ and 0.5 meV / Å$^2$ in the surface free energy convergence with respect to the slab and the vacuum thickness, respectively.

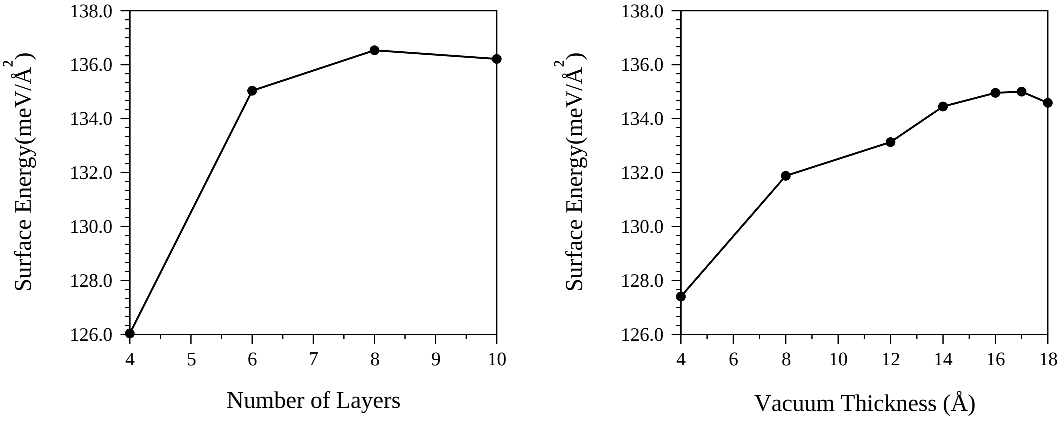

(a) (b)

Fig. A-3: The surface energy as a function of the number of layers in the slab (a) and the vacuum thickness (b), using $E_{cut}^{pw}$=13.8 Ry and a $(8 \times 8 \times 1)$ **k**-point set.

★ ★ ★ ★

# Appendix B

## Bulk $Mn_3$Si

The cubic crystal structure of $Mn_3$Si and its iso-structures, e.g. $Fe_3$Si and $Fe_2$MnSi, is called $DO_3$ type structure. Their crystals are equivalent to the $L2_1$ structure of the Heusler compounds[1] $X_2YZ$ [165] Fig. B-4-a. Metallic $Mn_3$Si crystallizes as $Mn_I$-$Mn_{II}$-Si with space group $Fm3\mathrm{m}$ and has complex spin configuration which depends on the temperature. Despite of its complex magnetic structure, $Mn_3$Si is an itinerant electron antiferrimagnet with incommensurate magnetic structure [154, 166] at 25 K. At this temperature, it has in-plane magnetic moments of $\mu_I$ = 1.7 $\mu_B$ and $\mu_{II}$ = -0.19 $\mu_B$ [154]. The crystal structure can be described in terms of an fcc Bravais lattice with Si atoms at the fcc lattice sites and Mn atoms occupying all of the octahedral and tetrahedral sites of the lattice. The Si and $Mn_I$ atoms are located at (0, 0, 0) and ($\frac{1}{2}$, $\frac{1}{2}$, $\frac{1}{2}$), respectively, while the $Mn_{II}$ atoms occupy ($\frac{1}{4}$, $\frac{1}{4}$, $\frac{1}{4}$) and ($\frac{3}{4}$, $\frac{3}{4}$, $\frac{3}{4}$) sites. The $Mn_I$ sites are surrounded by eight $Mn_{II}$ nearest neighbors and the nearset neighbors of $Mn_{II}$ are four $Mn_I$ and four Si atoms.

The calculations for non-magnetic, ferromagnetic and antiferromagnetic types of ordering are performed and the results are compared with those from the literature. The ferromagnetic ordering is described as a sequence of ferromagnetic planes $Mn_{II}$-$Mn_I$-$Mn_{II}$, separated by a Si plane, all equidistant with $d = 1.4$ Å . In the antiferromagnetic phase, it is assumed that the magnetic moments of the $Mn_I$ and the $Mn_{II}$ have an antiparallel coupling.

The calculations concerning the structural, electronic and magnetic properties are done with the GGA functional, an energy cutoff of $E_{\mathrm{cut}}$=13.6 Ry and $17 \times 17 \times 17$ **k**-points in the Brillouin zone.

## B-1 Structural and Magnetic Properties

The energy vs. volume plots are shown in Fig. B-4-b as green, red, blue curves for nonmagnetic (NM), ferromagnetic (FM) and antiferromagnetic (AFM) ordering, respectively. As these curves show, the AFM spin configuration has the lowest energy. At a compressed volume of -14 % the system becomes non-magnetic.

---

[1] The Heusler alloys have half metallic behavior: The Fermi level lying in the band gap in the minority spin channel and the electronic bandstructure of majority spin, like metallic bandstructure, crosses Fermi level which cause higher mobility and conductivity in this channel.

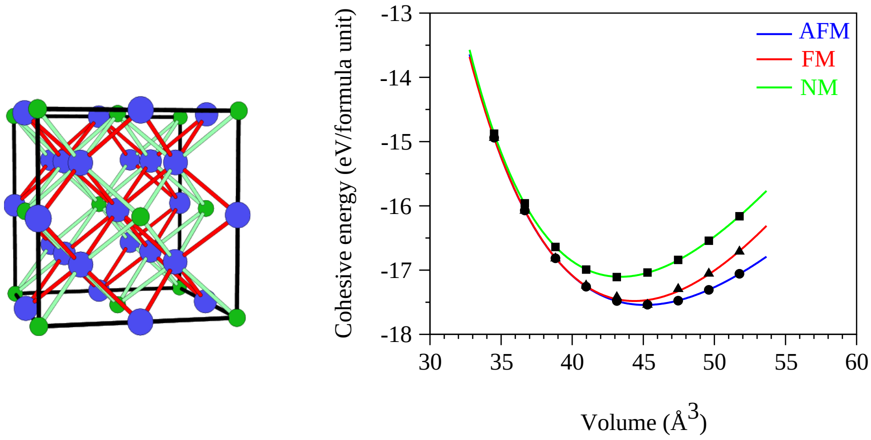

(a)

(b)

Fig. B-4: Crystal structure of $Mn_3Si$ in the fcc lattice (a). The green small circles are Si and big blue circles are Mn. Energy-volume curves for non-magnetic, ferromagnetic and antiferromagnetic structures for $Mn_3Si$ (b). The antiferromagnetic structure has the lowest energy curve.

Therefore one can conclude a magnetic phase transition to the non-magnetic phase at the compressed volume.

The stability of the AFM phase can be explained by direct $d-d$ coupling between $Mn_I$ and $Mn_{II}$, which lowers the energy in the antiparallel spin alignment. The calculated and experimentally observed lattice constants and magnetic moments for this crystal are summarized in Table B-1.

Table B-1: Formation enthalpy ($\Delta H$) (cf. Eq. **??**), lattice parameter ($a_0$) and magnetic moments ($m_I$, $m_{II}$) of $Mn_I$ and $Mn_{II}$ in different layers for $Mn_3$ Si.

| $Mn_3Si$ fcc | Phase | $\Delta H$ [eV/formula unit] | $a_0$ [Å] | $m_I$ [$\mu_B$] | $m_{II}$ [$\mu_B$] |
|---|---|---|---|---|---|
| Present work (GGA) | AFM | 1.15 | 5.65 | 2.15 | -0.30 |
| | FM | 1.093 | 5.62 | 2.58 | 0.83 |
| | NM | 0.72 | 5.59 | — | — |
| LMTO(LSDA)$^{(a)}$ | AFM | — | 5.63 | 2.06 | -0.43 |
| EXP.$^{(b)}$ | AFM | — | 5.72 | 1.7 | -0.19 |

(a) Ref. [167]
(b) Ref. [154]

The results for the magnetic moments are similar to LMTO results [167], and are overestimated compared to experimental magnetic moments, but both method pre-

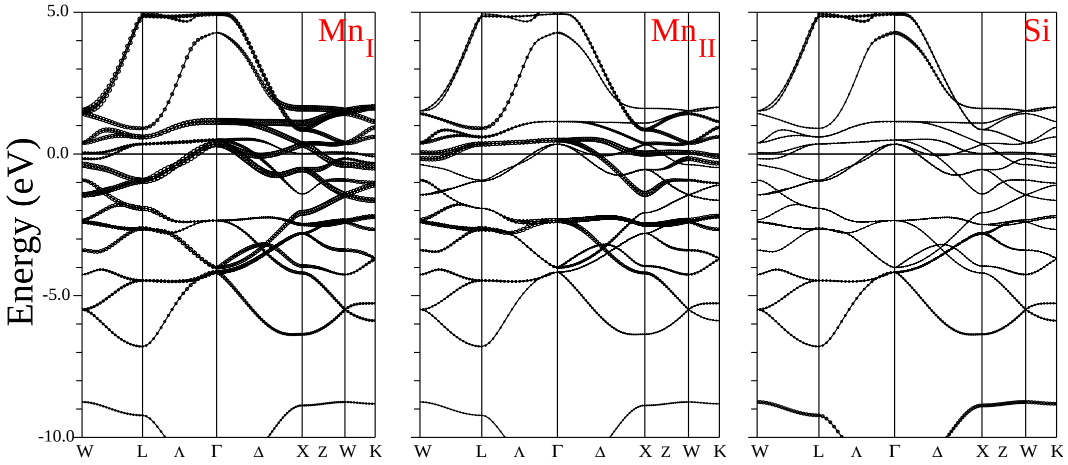

(a) (b) (c)

Fig. B-5: Band structure of non-magnetic $Mn_3Si$ shows metallic behavior. The contributions of $Mn_I$ (a), $Mn_{II}$ (b) and Si (c) atoms are shown separately.

dict antiferrimagnetic ordering.

## B-2 Electronic Properties

The electronic properties are studied by analyzing the band structures of non-magnetic, Fig. B-5, and antiferromagnetic $Mn_3Si$, Fig. B-6. Figures (a), (b), and (c) in Fig. B-5 show the bands weighted with their projection onto the atomic orbitals of $Mn_I$, $Mn_{II}$ and Si, respectively in the non-magnetic structure. Their corresponding AFM band structures, Fig. B-6, show the majority (a-c) and minority (d-f) spin channels. [The thickness of the bands of each atom indicates the contribution of the specific atom to the particular band.]

In all graphs the $Mn_I$ atoms considerably contribute around the Fermi level, whereas the Si p-states are far from the Fermi level.This means the magnetic ordering has no effect on the character of the p-bands.

A comparison of the band structures of NM and AFM at their equilibrium volume show that, the bands below -3 eV and above 1 eV are identical for both magnetic structures. As an example, the bands around the Fermi level at the $\Gamma$ point are considered, c.f. Fig. B-6. Both the NM phase and the majority spin channel of the AFM phase exhibit metallic behavior. There is an exchange splitting of the Mn 3$d$-electron states in the magnetic structure and the $\Gamma_{12}$ level is shifted below the $\Gamma_{25}$ band due to polarization. The $Mn_{II}$, which has $O_h$ symmetry, tends to be polarized strongly far away from the Fermi level which results in an indirect gap of about 0.5 eV in the minority spin channel. The Fermi level touches the top of the valence band at the point $\Gamma$. For this reason, this material does not belong to the group of half-metal compounds.

The bands in the energy range of -3 to 1 eV have mainly $d$-character. The $\Gamma_{12}$ and

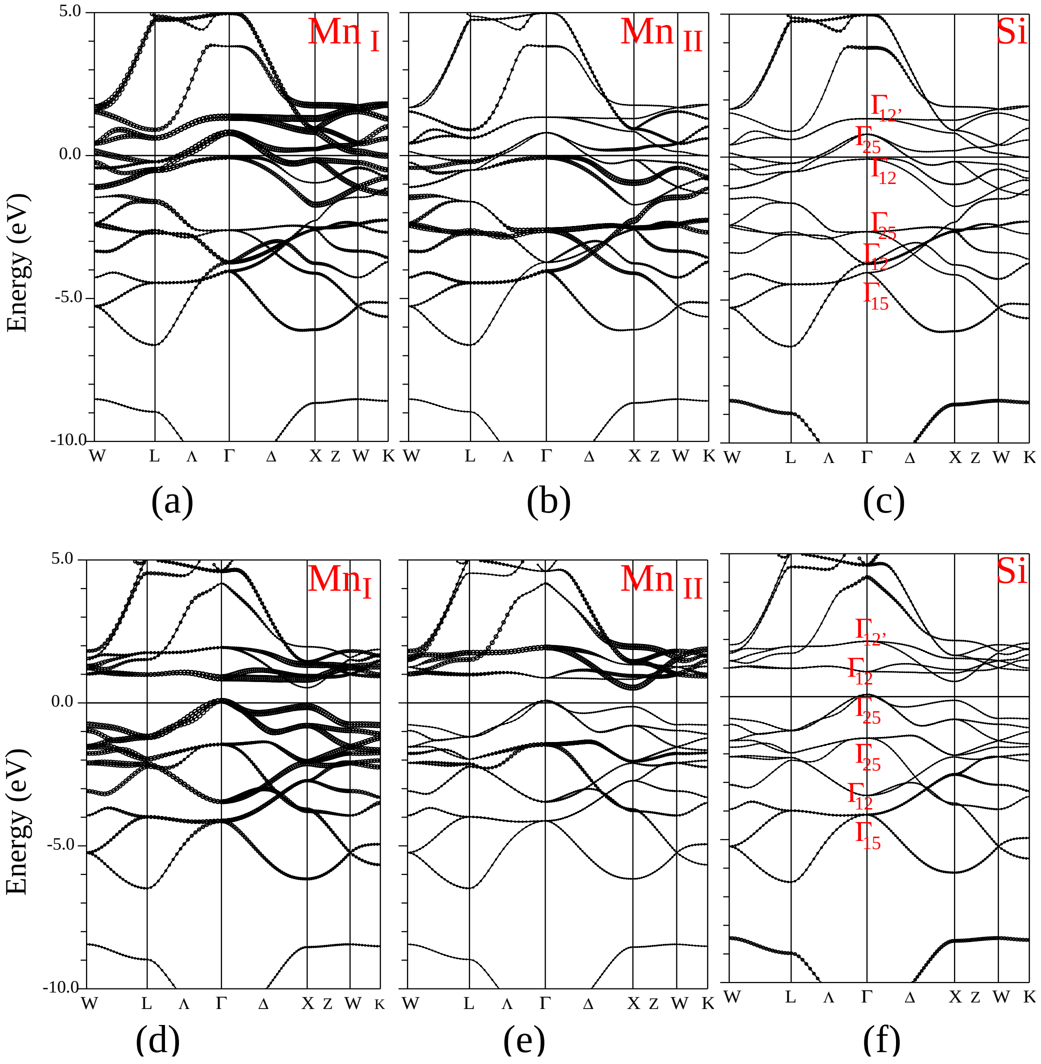

Fig. B-6: Band structures for Mn$_{I}$, Mn$_{II}$ and Si atoms in majority spin direction (a, b, c)and for minority spin channel (d, e, f) of Mn$_3$Si in the AFM phase. The majority spin band structure has the Fermi level crosses the top of the conduction band at the high symmetry point Γ which produce a few hole in this band.

$\Gamma_{15}$ bands have $e_g$ and $t_{2g}$ symmetry of the $d$-orbitals, respectively [168].

The lower $e_g$ and $t_{2g}$ level belong to Mn$_I$ sites and the $\Gamma_{12}$ and $\Gamma_{25}$ levels, which have the same symmetry of $d$-Mn$_{\text{II}}$ are near to the Fermi level, see Figs. B-5 and B-6. Therefore the energy level of $d$-Mn$_{\text{I}}$ is lower than $d$-Mn$_{\text{II}}$. The $d$-orbitals of Mn atoms, which possess similar symmetry will overlap, thereby broadening these bands. The obvious differences between the polarized and non-polarized band structure can be seen in the $\Gamma_{12}$, $\Gamma_{25}$ and $\Gamma_{12'}$ levels. There is a strong separation between in the minority spin channel of $\Gamma_{12}$, $\Gamma_{25}$ into antibonding and bonding states, respectively. The $\Gamma_{12}$ which is located above $\Gamma_{25}$ band is shifted to lower energy and ends up below the Fermi level in the majority spin channel. It is also remarkable that contributions of $d$-Mn$_{\text{II}}$ in on $\Gamma_{12'}$ band becomes negligible. Therefore the latter band is rather flat in spinpolarized calculations.

Figure B-7 illustrates the density of states for total and constituent parts of the crystal in the FM and AFM magnetic phases using the tetrahedral integration method [169, 170].

The $\Gamma_{12}$ and $\Gamma_{25}$ levels below and above the Fermi level in the spinpolarized band structure lead to two clear peaks in the DOS plot of Mn$_{\text{II}}$ atoms, Fig. B-7.

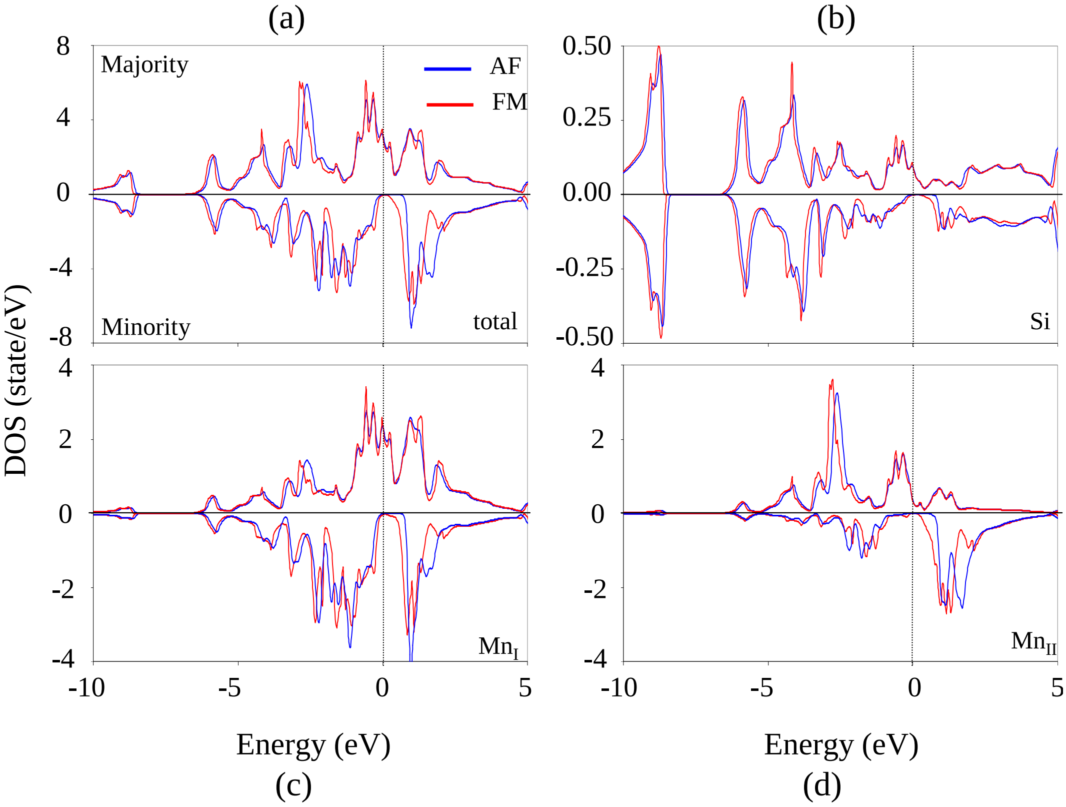

Fig. B-7: The DOS plot of $Mn_3Si$ for both ferromagnetic and antiferromagnetic phases. The plots are total density of states of $Mn_3Si$ (a), Si (b), Mn$_{\text{I}}$ (c), and Mn$_{\text{II}}$ (d). The minority spin channel has character similar to a semiconductor.

The band gap in the total dop of AFM ordering is about 0.75 eV which is larger than than in the FM oder by 0.50 eV. According to Tab. B-1, the magnetic moments in the both Mn$_{rmI}$ and Mn$_{rmII}$ of the parallel spin structure are larger than in the antiparallel alignment. There are large spinpolarizations at the Fermi level for both the FM and the AFM structure.

According to the DOS, the multi-peak Mn$_{\mathrm{I}}$ DOS spreads out in the energy range with considerable intensity. The DOS of Mn$_{\mathrm{II}}$ is relatively localized and has two significant peaks: one of them is fully occupied and the other is unoccupied. The exchange splitting of Mn$_{\mathrm{II}}$ is larger than for the Mn$_{\mathrm{I}}$ atoms. Consequently, a gap will be opened in the minority spin channel.

⋆ ⋆ ⋆ ⋆

# Appendix C

## Theory of Scanning Tunneling Microscopy (STM)

Scanning tunneling microscopy (STM), which was introduced by Binnig and Rohrer at 1982, is an experimental technique for studying surfaces. In this technique the electronic structure of surfaces is probed, by utilizing the quantum mechanical phenomenon of tunneling. Theories of scanning tunneling microscopy aim to help understand experimental findings and thereby gain a deeper understanding of surfaces.

The principle of STM is to bring a sharp metallic tip close (a few Å) to the surface. With applying of a bias voltage between tip and sample a tunneling current (0.01 nA-50 nA) will flow between them. The Image contrast represents the difference in the tip-surface current at different surface sites. In this work the constant current mode of STM is used.

In the constant current regime of operation the position of the tip above the surface is adjusted such, that the tunneling current remains constant. The measured height of the tip above the surface is transformed in pixel intensity rendering a two-dimensional image of the surface. The tunneling current is highly influenced by the distance between sample-tip and the electronic structure of the sample.

STM yields information about empty and filled states of the sample. At negative tip bias empty states of the sample are probed, since the Fermi level of the tip lies higher than the Fermi level of the sample (cf. Fig. C-8-a). At positive tip bias the situation is reverse - the Fermi level of sample lies higher and the current flows from the filled sample states to the tip, i.e. the filled states of the sample are probed, Fig. C-8-b .

There are several theories on STM [171–173] containing different levels of sophistication. The most simple theory by Tersoff and Hamman [174, 175] is based on a perturbation approach as described by the Bardeen transfer-Hamiltonian [176]. This model shows that the tunneling current is proportional to the surface local density of states at the Fermi level energy and at a given tip position. The tip is modeled as a locally spherical potential well where it approaches nearest to the surface. The effect of the tip on the tunneling current is neglected in this model.

The tunneling current is proportional to :

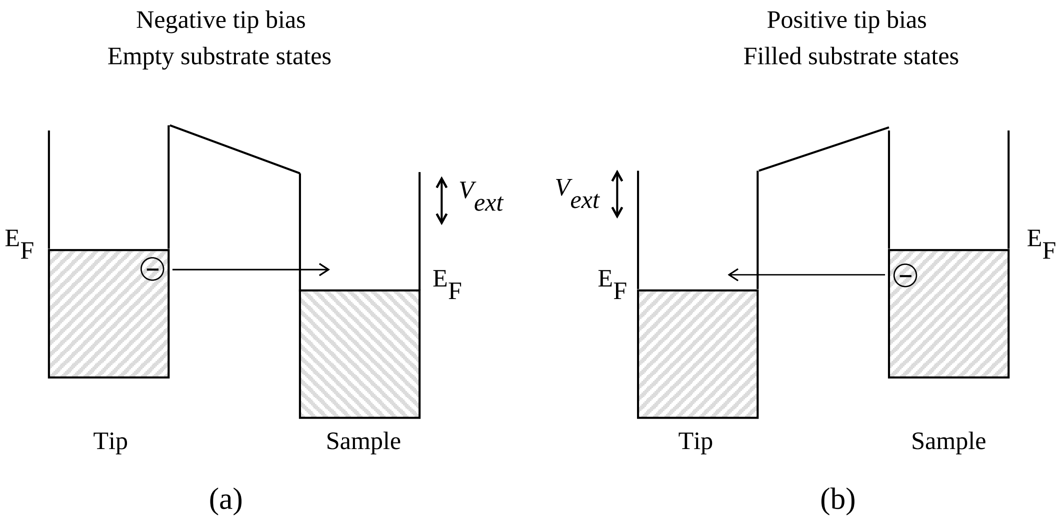

Fig. C-8: The negative tip bias probes empty substrate states (a) and positive tip bias probes filled states of the substrate (b).

$$I(R) \propto \sum_{E_n=E_F-eV}^{E_F} |\psi(\vec{\mathbf{R}}, E_n)|^2 = eVn(\vec{\mathbf{R}}, E_F) \tag{C-1}$$

where $I$ is the tunneling current, $E_n$ the eigenstates of the crystal electrons, $E_F$ the Fermi level, $V$ the bias voltage. The probability of an electron in the state $\psi$ at $E_\psi$ to tunnel into a state $\chi$ at $E_\chi$ is given by the "Fermi golden rule"

$$W = \frac{2\pi}{\hbar}|M|^2\delta(E_\psi - E_\chi) \tag{C-2}$$

The tunneling matrix ( Bardeen matrix), $M$, is given by an integral over the separation surface $S$ between sample and tip.

$$M = \int_S (\chi^*\nabla\psi - \psi\nabla\chi^*) \cdot d\vec{\mathbf{S}} \tag{C-3}$$

The probability of tunneling is large for electrons close to the Fermi level having lower barrier.

$\delta(E_\psi - E_\chi)$ means that an electron can only tunnel if there is an unoccupied state with the same energy at the other side. In case of positive (negative) tip potential the occupied (unoccupied) states generate the current. Therefore by applying the alternating voltage, a completely different image scan be detected.

Thus, by applying a bias voltage $V$ and considering the tip as a small perturbation of the system, the tunneling current at low bias and temperature is defined as:

$$I = \frac{4\pi e}{\hbar}\int_0^{eV} \rho_s(E_F - eV + \varepsilon)\rho_t(E_F + \varepsilon)|M|^2 d\varepsilon \tag{C-4}$$

Hence the current is given by combinations of the local density of states of the sample and the tip, weighted by tunneling matrix, $M$.

The clean Si(001) surface has been extensively studied by STM [98, 105, 106]. In STM images of the $(2 \times 1)$ structure, the silicon dimer appears symmetric at room temperature due to the time averaging of the flipflop motion of the buckled dimers. Low temperature images show the stable configurations to be the $c(4\times2)$ and $p(2\times 2)$ structures consisting of asymmetric dimer rows [110, 177]. At low temperature ( 4.2 K), it has been demonstrated that a phase change between the $c(4 \times 2)$ and the $p(2 \times 2)$ can be induced by controlling the sample bias voltage [106].

⋆ ⋆ ⋆ ⋆

# Bibliography

[1] Figure is taken from the presentation of Prof. M. Scheffler in the density-functional theory workshop at Los Angeles, (2005).

[2] M. Krause et al., Submitted to Phys. Rev. B.

[3] C. Kittel, *Introduction to Solid State Physics*, 5th ed. (Wiley, New York (1983).

[4] A. G. Beattie and J. E. Schirber, Phys. Rev. B **1**, 1548 (1970).

[5] N. Moll, M. Bockstedte, M. Fuchs, E. Pehlke, and M. Scheffler, Phys. Rev. B **52**, 2550 (1995).

[6] A. A. Stekolnikov and F. Bechstedt, Phys. Rev. B **72**, 125326 (2005).

[7] G. Uhlenbeck and S. Goudsmit, Nature **117**, 264 (1926).

[8] M. N. Baibich et al., Phys. Rev. Lett. **61**, 2472 (1988).

[9] G. Binash, P. Grünberg, F. Saurenbach, and W. Zinn, Phys. Rev. B **39**, 4828 (1989).

[10] J.-P. Ansermet, J. Phys.:Condens. Matter **10**, 6027 (1998).

[11] M. A. M. Gijs and G. E. Bauer, Advances in Physics **46**, 285 (1997).

[12] J. Bass and W. P. Pratt, J. Magn. Magn. Mater. **200**, 274 (1999).

[13] M. Julliere, Phys. Lett. **54A**, 225 (1975).

[14] J. S. Moodera, L. R. Kinder, T. M. Wong, and R. Meservey, Phys. Rev. Lett. **74**, 3273 (1995).

[15] Y. C. Lian and L. J. Chen, Appl. Phys. Lett. **48**, 359 (1986).

[16] H. Lippitz, J. J. Paggel, and P. Fumagalli, Surf. Sci. **575**, 307 (2005).

[17] K. Schwinger, C. Müller, A. Mogilatenko, J. Paggel, and P. Fumagalli, J. Appl. Phys. **97**, 103913 (2005).

[18] M. M. R. Evans, J. C. Glueckstein, and J. Nogami, Phys. Rev. B **53**, 4000 (1996).

[19] T. Nagao, S. Ohuchi, Y. Matsuoka, and S. Hasegawa, Surf. Sci. **419**, 134 (1999).

[20] G. Ctistis, U. Deffke, J. Paggel, and P. Fumagalli, J. Magn. Magn. Mater. **240**, 420 (2002).

[21] G. Ctistis, U. Deffke, K. Schwinger, J. Paggel, and P. Fumagalli, Phys. Rev. B **71**, 35431 (2005).

[22] A. Kumar, M. Tallarida, M. Hansmann, U. Starke, and K. Horn, J. Phys. D: Appl. Phys. **37**, 1083 (2004).

[23] E. Fermi, Z. Phys. **48**, 73 (1928).

[24] L. H. Thomas, Proc. Cambridge Philos. Soc. **23**, 542 (1927).

[25] P. Hohenberg and W. Kohn, Phys. Rev. **136**, B 864 (1964).

[26] R. O. Jones and O. Gunnarsson, Rev. Mod. Phys. **61**, 689 (1989).

[27] G. P. Parr and W. Yang, *Density-Functional Theory of Atoms and Molecules*, Oxford University Press (1994).

[28] R. M. Dreizler and E. K. U. Gross, *Density Functional Theory*, Springer-Verlag (1990).

[29] W. Kohn and L. J. Sham, Phys. Rev. **140**, A 1133 (1965).

[30] E. Wigner, Phys. Rev. **46**, 1002 (1934).

[31] L. Hedin and B. I. Lundqvist, J. Phys. C **4**, 2064 (1971).

[32] J. P. Perdew and Y. Wang, Phys. Rev. B **45**, 13244 (1992).

[33] D. M. Ceperley and B. J. Adler, Phys. Rev. Lett **45**, 566 (1980).

[34] J. P. Perdew, K. Burke, and M. Ernzerhof, Phys. Rev. Lett **77**, 3865 (1969).

[35] J. C. Slater, Phys. Rev. **51**, 846 (1937).

[36] T. L. Loucks, *Augmeted Plane Wave Method: a guide to performing electronic structure calculations*, Benjamin, New York (1967).

[37] E. Sjöstedt, L. Nordström, and D. J. Singh, Solid Stat Commun. **114**, 15 (2000).

[38] K. Schwarz, P. Blaha, and G. K. H. Madsen, Comp. Phys. Commun. **147**, 71 (2002).

[39] O. K. Andersen, Phys. Rev. B **12**, 3060 (1975).

[40] D. D. Koelling and G. O. Arbman, J. Phys. F: Metal Phys. **5**, 2041 (1975).

[41] M. Weinert, E. Wimmer, and A. J. Freeman, Phys. Rev. B **26**, 4571 (1982).

[42] E. Wimmer, H. Krakauer, M. Weinert, and A. J. Freeman, Phys. Rev. B **12**, 864 (1981).

[43] H. Krakauer, M. Posternak, and A. J. Freeman, Phys. Rev. B **19**, 1706 (1978).

[44] N. W. Ashcroft and N. D. Mermin, Harcourt Brace College Publishers (1976).

[45] A. Baldereschi, Phys. Rev. B **7**, 5212 (1972).

[46] S. Froyen, Phys. Rev. B **39**, 3168 (1988).

[47] D. J. Chadi and M. L. Cohen, Phys. Rev. B **8**, 5747 (1973).

[48] K. Cho and J. Joannopoulos, Phys. Rev. Lett. **71**, 1387 (1993).

[49] H. J. Monkhorst and J. D. Pack, Phys. Rev. B **13**, 5188 (1976).

[50] M. Posternak, H. Kraukauer, A. J. Freeman, and D. D. Koelling, Phys. Rev. B **21**, 5601 (1980).

[51] P. Blaha, K. Schwarz, P. Sorantin, and S. B. Trickey, Comp. Phys. Commun. **59**, 399 (1990).

[52] P. Blaha, K. Schwarz, and J. Luitz, WIEN2k, A Full Potential Linearized Augmented Plane Wave Package for Calculating Crystal Properties, Karlheinz Schwarz, Techn. Universität Wien, Austria. **ISBN 3-9501031-1-2.** (1999).

[53] R. Yu, D. Singh, and H. Kraurauer, Phys. Rev. B **43**, 6411 (1991).

[54] F. D. Murnaghan, Proc. Nat. Acad. Sci. USA **30**, 244 (1944).

[55] D. M. Ceperley and B. J. Alder, Phys. Rev. Lett. **45**, 566 ((1980)).

[56] M. I. McMahon and R. J. Nelmes, Phys. Rev. B **47**, 8337 (1993).

[57] Please refer to the lecture script of Prof. Matthias Scheffler, ”www.fhi-berlin.mpg.de/th/lectures.html”.

[58] Y. Wang, J. P. Perdew, and E. Engel, Phys. Rev. Lett. **66**, 508 (1991).

[59] I. Lee and R. M. Martin, Phys. Rev. B **56**, 7179 (1997).

[60] J. R. Chelikowsky and M. L. Cohen, Phys. Rev. B **10**, 5095 (1974).

[61] J. W. Grover and P. Handler, Phys. Rev. B **9**, 2600 (1974).

[62] A. J. Bradley and J. Thewlis, Proc. R. Soc. A **115**, 465 (1927).

[63] D. Hobbs and J. Hafner, J. Phys.: Condens. Matter **13**, L681 (2001).

[64] M. O’Keeffe and S. Anderson, Acta Cryatallogr. A **33**, 914 (1977).

[65] H. Nakamura, K. Yoshimoto, M. Shiga, M. Nishi, and K. Kakurai, J. Phys.: Condens. Matter **9**, 4701 (1997).

[66] B. Canals and C. Lacroix, Phys. Rev. B **61**, 11251 (2000).

[67] M. Eder, J. Hafner, and E. G. Moroni, Phys. Rev. B **61**, 11492 (2000).

[68] M. Körling and J. Häglund, Phys. Rev. B **45**, 13293 (1992).

[69] R. W. G. Wyckoff, *Crystal Structure*, volume 1 (1963).

[70] L. Pauling and A. M. Soldate, Acta. Cryst. **1**, 212 (1948).

[71] L. F. Mattheiss and D. R. Hamann, Phys. Rev. B **47**, 13114 (1993).

[72] Y. Ishikawa, K. Tajima, P. Bloch, and M. Roth, Solid State Commun. **19**, 525 (1976).

[73] T. Moriya, Solid Stat. Commun. **26**, 438 (1978).

[74] Y. Ishikawa, G. Shirane, and J. A. Trarvin, Phys. Rev. B **16**, 4956 (1977).

[75] C. Thessieu, C. Pfleiderer, A. N. Stepanov, and J. Flouquet, J. Phys.: Condens. Matter **9**, 6677 (1997).

[76] H. von Känel, C. Schwarz, S. Goncalves-Conto, and E. Müller, Phys. Rev. Lett. **74**, 1163 (1995).

[77] T. Jeong and E. Pickett, Phys. Rev. B **70**, 75114 (2004).

[78] O. Nakashini, A. Yanase, and A. Hasegawa, J. Magn. Magn. Mater. **15-18**, 879 (1986).

[79] L. Vočadlo, G. Price, and I. Wood, Acta Crystallogr. Sect. B: Struct. Sci. **55**, 484 (1999).

[80] P. Mohn and E. Wohlfarth, J. Phys. F: Met. Phys. **17**, 2421 (1987).

[81] O. Gunnarsson, J. Phys. F: Met. Phys. **6**, 587 (1976).

[82] P. James, O. Eriksson, B. Johansson, and I. Abrikosov, Phys. Rev. B **59**, 419 (1999).

[83] S.Kaul, J. Phys. Condens. Matter **11**, 7597 (1999).

[84] E. Stoner, Proc R. Soc A **154**, 656 (1936).

[85] H. Wu, P. Kratzer, and M. Scheffler, Phys. Rev. B **72**, 144425 (2005).

[86] K. Murata and S. Doniach, Phys. Rev. Lette. **29**, 285 (1972).

[87] A. Shick, W. Pickett, and C. Fadley, Phys. Rev. B **61**, 9213 (2000).

[88] J. MacLaren, T. Schulthess, H. Butler, R. Sutton, and M. McHenry, J. Appl. Phys. **85**, 4833 (1999).

[89] C. B. Duke, Chem. Rev. **96**, 1237 (1996).

[90] R. E. Schlier and H. E. Farnsworth, J. Chem. Phys. **30**, 917 (1959).

[91] J. E. Rowe and H. Ibach, Phys. Rev. Lett **32**, 421 (1974).

[92] Y. J. Chabal, S. B. Christmann, E. E. Chaban, and M. T. Yin, J. Vac. Sci. Thechnol. A **1**, 1241 (1983).

[93] F. J. Himpsel, P. Heimann, T. C. Chiang, and D. E. Eastmann, Phys. Rev. Lett **45**, 1112 (1980).

[94] R. M. Tromp, R. G. Smeenk, and F. W. Saris, Phys. Rev. Lett **46**, 9392 (1981).

[95] J. A. Appelbaum and D. R. Hamann, Surf. Scie. **178**, 21 (1974).

[96] D. J. Chadi, Phys. Rev. Lett. **43**, 43 (1979).

[97] M. Aono, Y. Hou, C. Oshima, and Y. Ishizawa, Phys. Rev. Lett **49**, 567 (1982).

[98] R. M. Tromp, R. J. Hamers, and J. D. Demuth, Phys. Rev. Lett **55**, 1303 (1985).

[99] P. Krüger and J. Pollmann, Phys. Rev. Lett **74**, 1155 (1995).

[100] A. Ramstad, G. Brocks, and P. Kelly, Phys. Rev. B **51**, 14504 (1995).

[101] J. Dabrowski and M. Scheffler, Appl. Surf. Sci. **56**, 15 (1992).

[102] G. Jayaram, P. Xu, and L. Marks, Phys. Rev. Lett. **71**, 3489 (1993).

[103] N. Jedrecy et al., Surf. Scie. **230**, 197 (1990).

[104] H. Over, J. Wasserfall, and W. Ranke, Phys. Rev. B **55**, 4731 (1996).

[105] R. J. Hamers, R. M. Tromp, and J. D. Demuth, Phys. Rev. B **34**, 5343 (1986).

[106] K. Sagisaka, D. Fujita, and G. Kido, Phys. Rev. Lett. **91**, 146103 (2003).

[107] R. Uhrberg, G. Hansson, and S. Flodström, Phys. Rev. B **24**, 4684 (1981).

[108] R. Hamers and U. Kohler, J. Vac. Sci. Technol. A **7**, 2854 (1989).

[109] J. E. Rowe and H. Ibach, Phys. Rev. Lett **31**, 102 (1973).

[110] R. Wolkow, Phys. Rev. Lett. **68**, 2636 (1992).

[111] G. Hwang, Surf. Sci. **465**, L789 (2000).

[112] K. Inoue, Y. Morikawa, K. Terakura, and M. Nakayama, Phys. Rev. B **49**, 14774 (1994).

[113] L. Johansson, R. Uhrberg, P. Martensson, and G. Hansson, Phys. Rev. B **42**, 1305 (1990).

[114] N. Roberts and R. Needs, Surf. Sci. **236**, 112 (1990).

[115] B. Chen and D. Haneman, Phys. Rev. B **51**, 4258 (1995).

[116] A. Scholze, W. G. Schmidt, and F. Bechstedt, Phys. Rev. B **53**, 13725 (1996).

[117] K. Takayanagi, Y. Tanishiro, M. Takahashi, , and S. Takahashi, J. Vac. Sci. A **3**, 1502 (1984).

[118] D. Haneman, Rep. Prog. Phys. **50**, 1045 (1987).

[119] R. Phaneuf, E. Williams, and N. Bartelt, Phys. Rev. B **38**, 1984 (1987).

[120] Y. N. Yang and E. D. Williams, Phys. Rev. Lett. **72**, 1862 (1994).

[121] A. Stekolnikov, J. Furthmüller, and F. Bechstedt, Phys. Rev. B **65**, 115318 (2002).

[122] J. Wilson, J. Todd, and A. Sutton, J. Phys.:Condens. Matter **2**, 10259 (1990).

[123] W. Zhu, H. Weitering, E. Wang, E. Kaxiras, and Z. Zhang, Phys. Rev. Lett. **93**, 126102 (2004).

[124] G. M. Dalpian, A. J. R. da Silva, and A. Fazzio, Phys. Rev. B **68**, 113310 (2003).

[125] G. M. Dalpian, A. J. R. da Silva, and A. Fazzio, Surf.Sci. **688**, 566 (2004).

[126] M. Bolduc et al., Pys. Rev. B **71**, 33302 (2005).

[127] T. Dietl, H. Ohno, F. Matsukura, J. Cibert, and D. Ferrand, Science **287**, 1019 (2000).

[128] J. Wang, M. Hirai, M. Kusaka, and M. Iwami, Appl. Surf. Sci. **113-114**, 53 (1997).

[129] B. Z. Liu, M. V. Katkov, and J. Nogami, Surf. Sci. **453**, 137 (2000).

[130] M. M. R. Evans and J. Nogami, Phys. Rev. B **59**, 7644 (1998).

[131] J. C. Glueckstein, M. M. R. Evans, and J.Nogami, Surf. Sci. **415**, 80 (1998).

[132] A. P. Horsfield, S. D. Kenny, and H. Fujitani, Phys. Rev. B **64**, 245332 (2001).

[133] S. Hagai and T. Ohno, J. Appl. Surf. Sci. **166**, 149 (2000).

[134] B. D. Yu, Y. Miyamoto, and O. Sugino, Phys. Rev. B **58**, 3549 (1998).

[135] F. Beeler, O. K. Andersen, and M. Scheffler, Phys. Rev. B. **41**, 1603 (1990).

[136] H. H. Woodbury and W. G. Ludwig, Phys. Rev. **117**, 102 (1960).

[137] Y. Kamon, H. Harima, A. Yanasei, and H. Katayama-Yoshida, Phys. B. **308-310**, 391 (2001).

[138] S. C. Erwin and A. G. Petukhov, Phys. Rev. Lett. **89**, 227201 (2002).

[139] S. Higai and T. Ohno, Appl. Surf. Sci. **166**, 149 (2000).

[140] H. J. W. Zandvliet, Surf. Sci. **377–379**, 1 (1997).

[141] R. Gomer, Rep. Prog. Phys. **53**, 917 (1990).

[142] E. Penev, *On the theory of surface diffusion in InAs/GaAs(001) heteroepitaxy*, PhD thesis, 2002.

[143] P. Ruggerone, C. Ratsch, and M. Scheffler, Chem. Phys. of Solid Surf. **8**, 490 (1997).

[144] G. H. Vineyard, J. Phys. Chem. Solids **3**, 121 (1957).

[145] A. Klay and M. Scheffler, The physics of semiconductors, Number 1031, World Scientific, Singapore, 1996.

[146] A. P. Smith et al., J. Chem. Phys. **102**, 1044 (1995).

[147] E. R. Weber, Appl. Phys. A **30**, 1 (1983).

[148] D. Gilles, W. Bergholz, and W. Schroeter, J. Appl. Phys. **59**, 3590 (1986).

[149] S. Teichert et al., J. Cryst. Growth **227-228**, 882 (2001).

[150] H. Wu, M. Hortamani, P. Kratzer, and M. Scheffler, Phys. Rev. Lett. **92**, 237202 (2004).

[151] J. Kanamori and K. Terakura, J. Phys. Soci. Jap. **70**, 1433 (2001).

[152] M.Hortamani, H. Wu, P. Kratzer, and M. Scheffler, accepted in Phys. Rev. B (2005).

[153] U. Starke et al., Europhys. Lett. **56**, 822 (2001).

[154] C. Pfleiderer, J. Boeuf, and H. Lohneysen, Phys. Rev. B **65**, 172404 (2002).

[155] H. L. Meyerheim, U. Döbler, and A. Puschmann, Phys. Rev. B **44**, 5738 (1991).

[156] U. Deffke et al., J. Appl. Phys. **96**, 3972 (2004).

[157] S. M. Shivaprasad, C. Anandan, S. Azatyan, Y. Gavriljuk, and V. Lifshits, Surf. Sci. **382**, 258 (1997).

[158] S. Kawamoto, M. Kusaka, M. Hirai, and M. Iwami, Surf. Sci. **242**, 331 (1991).

[159] R. S. Becker, J. A. Golovchenko, G. S. Higashi, and B. S. Swartzentruber, Phys. Rev. Lett. **57**, 1020 (1986).

[160] J. E. Northrup, Phys. Rev. Lett. **53**, 683 (1984).

[161] G. V. Hansson, R. Z. Bachrach, R. S. Bauer, and P. Chiaradia, Phys. Rev. Lett. **46**, 1033 (1980).

[162] S. Kohmoto and A. Ichimiya, Surf. Sci. **223**, 400 (1989).

[163] K. Reuter and M. Scheffler, Phys. Rev. B **65**, 35406 (2001).

[164] L. G. Wang, P. Kratzer, M. Scheffler, and N. Moll, Phys. Rev. Lett **82**, 4042 (1999).

[165] R. de Groot and F. Mueller, Phys. Rev. Lett. **50**, 2024 (1983).

[166] S. Tomiyoshi and H.Watanabe, J. Phys. Sco. Jpn. **39**, 295 (1975).

[167] S. Fujii, S. Ishida, and S. Asano, J. Phys. Soc. Jpn. **64**, 185 (1995).

[168] R. Smoluchowski, L. Buockaert, and E. Winger, Phys. Rev. **50**, 58 (1936).

[169] J. Janak and O. Andersen, Solid State Commun. **9**, 1963 (1971).

[170] J. Rath and A. Freeman, Phys. Rev. B **11**, 2109 (1975).

[171] J. Tersoff, Phys. Rev. B **40**, 11990 (1989).

[172] H. Kageshima and M. Tsukada, Phys. Rev. B **46**, 6928 (1992).

[173] G. Briggs and A. Fisher, Surf. Sci. Rep. **33**, 1 (1999).

[174] J. Tersoff and R. Hamann, Phys. Rev. Lett. **50**, 1998 (1983).

[175] J. Tersoff and R. Hamann, Phys. Rev. B **31**, 805 (1985).

[176] J. Bardeen, Phys. Rev. Lett. **6**, 57 (1961).

[177] T. Yokoyama and K. Takayanagi, Phys. Rev. B **61**, 5078 (2000).

⋆ ⋆ ⋆ ⋆

# Acknowledgment

At the end of my thesis I would like to thank those people who made this thesis possible.
First of all I wish to express my sincere gratitude to Prof. Dr. Matthias Scheffler who gave me the chance to work in his group at the Fritz-Haber Institute. I think it was the best thing which could happen to me. I would like to thank him for his continuous support, for his attempt to provide a nice environment which always felt like home to me, for giving self-confidence, for giving me the chance to participate in conferences and workshops as well as contact other people working in the same field.
I am also deeply indebted to Prof. Dr. Peter Kratzer for his courtesy and tolerance for teaching me the way of thinking, for giving me a deep understanding of science and specifically physics, to answer all my questions and help me whenever I was in need, and to guide this thesis in the correct way. It has been my great pleasure to work with him.
I would like also to express my appreciation to Prof. Dr. Paul Fumagalli for his advice and very useful discusions.
I am grateful to members of the institute and the Freie university for their comradeship and supporting; especially Dr. Mira Todorova, Dr. Jens Oliver Müller, Dr. Karsten Reuter, Thomas Hammerschmidt, Jutta Rogal, Dr. Hua Wu, Dr. Andreia Luisa da Rosa, Dr. Hakim Meskine, Dr. Angelos Michaelides, Dr. Jens Paggel, Dr. Holger Lippitz, and Dr. Kai Schwinge.
My special thanks go to my dear friends Dr. Daryoush Shayesteh Afshar, Dr. Norbert Pfänder, Hediyeh and Payam Kaghazchi.
Finally, I would like to thank my family for their support. I am greatly indepted to my brother, Dr. Amir Hortamani who was the first to encourage me. Above all, I would like to express my full gratitude to my parents Maliheh and Mehdi and my sisters, Maryam and Mozhgan.

I dedicate this thesis to my family.

⋆ ⋆ ⋆ ⋆

# CURRICULUM VITAE

## PERSONAL DETAILS:

| | |
|---|---|
| Name: | Mahboubeh Hortamani |
| Address: | Fritz-Haber-Institute of the Max-Planck-Society,<br>Theory Department<br>Faradayweg 4-6, 14165 Berlin, Germany<br>Phone: +49-30-8413 4820, Fax: +49-30-8413 4701<br>Email: hortaman@fhi-berlin.mpg.de |
| Birthday: | 24th of July 1976, Esfahan, Iran |

## EDUCATION:

| | |
|---|---|
| 08 / 2002–06 / 2006 | Ph.D. at the Fritz-Haber-Institute, Theory Department |
| 09 / 2000 – 08 / 2002 | Teaching, Esfahan, Iran |
| 01 / 2001 – 02 / 2002 | Master-thesis at the Esfahan University of Technology, Iran |
| 09 / 1999 – 01 / 2001 | Master degree at the Esfahan University of Technology |
| 09 / 1998 – 09 / 1999 | Teaching, Esfahan, Iran |
| 09 / 1994 – 09 / 1998 | Bachelor degree at the Kashan University, Esfahan, Iran |
| 09 / 1994 | High school diploma, Esfahan, Iran |

# PUBLICATIONS

- M.Hortamani, I. Mertig, P. Kratzer, and M. Scheffler, *Exchange interactions, Curie and Nèel temperature of bulk and layered Mn-mono-silicide: An ab initio calculation*, In print
- M.Hortamani, P. Kratzer, and M. Scheffler, *Formation and stability of Mn-mono-silicide islands on Si(001) and Si(111) surfaces*, In print (8 pages)
- M. R. Krause, A. J. Stollenwerk, J. Reed, V. P. LaBella, M.Hortamani, P. Kratzer, and M. Scheffler, *Observation of subsurface Mn on the Si(001)-($2\times1$) reconstructed surface*, Submitted to Phys. Rev. B
- M.Hortamani, H. Wu, P. Kratzer, and M. Scheffler, *First-principles calculations for initial adsorption and thin film growth of manganese on Si(001)*, Accepted to Phys. Rev. B (11 pages)
- P. Kratzer, S.J. Hashemifar, H. Wu, M. Hortamani, and M. Scheffler, *Transition-metal silicides as novel materials for magnet-semiconductor heterostructures*, Submitted to J. Appl. Phys.
- H. Wu, M. Hortamani, P. Kratzer, and M. Scheffler, *First-principles study of ferromagnetism in epitaxial Si-Mn thin films on Si(001)*, Phys. Rev. Lett. 92, 237202 (2004)
- M.Hortamani, *Ab initio Calculation Hyperfine Interaction in Fe and $YFe_2$*, Technical university, Esfahan, Iran, January 2002
- M. Hortamani and H. Akbarzadeh, *Hyperfine Interaction in $YFe_2$*, Conf. Proc. The Physical Society of Iran, 2001
- M. Hortamani and H. Akbarzadeh, *Structural, Electronic Properties and Hyperfine Interaction in Iron*, Conf. Proc. The Physical Society of Iran, 2001